



Friedrich-Alexander-Universität  
Naturwissenschaftliche Fakultät



# **Energy Storage in Derivatized Norbornadiene/Quadricyclane as Molecular Solar Thermal System Investigated by XPS**

Energiespeicherung in derivatisiertem  
Norbornadien/Quadricyclan als molekulares solarthermisches  
System untersucht mittels XPS

Der Naturwissenschaftlichen Fakultät  
der Friedrich-Alexander-Universität Erlangen-Nürnberg  
zur  
Erlangung des Doktorgrades Dr. rer. nat.

vorgelegt von

**Felix Hemauer**

Als Dissertation genehmigt von der Naturwissenschaftlichen Fakultät  
der Friedrich-Alexander-Universität  
Erlangen-Nürnberg

Tag der mündlichen Prüfung: 3. Mai 2024

Vorsitzende des

Promotionsorgans:

Prof. Dr. Svetlana Tsogoeva

Gutachter:

Prof. Dr. Christian Papp

Prof. Dr. Jörg Libuda

---

## Kurzfassung

Der notwendige Wandel zu erneuerbaren Energiequellen geht Hand in Hand mit passenden Energiespeicherlösungen. Molekulare solarthermische (MOST) Systeme kombinieren die Nutzung von Sonnenenergie mit der unmittelbaren Speicherung der gewonnenen Energie in chemischer Form. Durch Bestrahlung wird eine energiearme Verbindung in ihr energiereiches Photoisomer umgewandelt, wobei die gespeicherte Energie bei Bedarf katalytisch freigesetzt werden kann.

Das Molekülpaar Norbornadien (NBD) und Quadricyclan (QC) erscheint vielversprechend für MOST-basierte Anwendungen. Eine geeignete Derivatisierung des Molekülgerüsts ermöglicht die Optimierung der Umwandlungs- und Speichereigenschaften. Die Überlappung des Absorptionsprofils von NBD mit dem Spektrum der Sonne bestimmt insbesondere die Gesamteffizienz und erfordert neuartiges Moleküldesign. Dabei ist nicht nur die Ausbeute der Photoumwandlung von NBD zu QC für die generelle Anwendbarkeit entscheidend, sondern es sollte auch die Rückreaktion von QC zu NBD auf kontrollierte und effiziente Weise erfolgen.

Im Rahmen dieser Arbeit wurden verschiedene 2,3-disubstituierte NBD-Derivate und deren dazugehörige QC-Isomere auf modellkatalytischen Oberflächen (Pt, Ni, Au) mittels Synchrotronstrahlung-basierter Röntgenphotoelektronenspektroskopie (XPS) untersucht. Im Einzelnen umfasste die Derivatisierung Cyano-Gruppen, Phenylester-Substitution und Ester-substituiertes oxa-NBD/QC unterschiedlicher Größe. Aus Untersuchungen der Adsorption bei niedrigen Temperaturen und anschließenden Temperatur-programmierten Experimenten konnten Informationen über die jeweiligen Systeme auf molekularer Ebene gewonnen werden, welche Rückschlüsse auf thermisch-induzierte Oberflächenreaktionen erlaubten. Der Schwerpunkt wurde auf die Bedingungen und den Umfang der energiefreisetzenden Cycloreversion-Reaktionen der QC-Derivate gesetzt, womit die Realisierbarkeit der verschiedenen Kombinationen aus Molekülen und Katalysatoren beurteilt werden konnte.

---

---

## Abstract

The indispensable transition to renewable energy sources goes hand in hand with appropriate energy storage solutions. Molecular solar thermal (MOST) systems combine the utilization of solar power with the direct storage of the gained energy in a chemical manner. Upon irradiation, an energy-lean compound is converted into its energy-rich photoisomer, whereby the release of the stored energy can be catalytically triggered on demand.

The molecule pair norbornadiene (NBD) and quadricyclane (QC) appears promising for MOST-based applications. By suitable derivatization of its molecular framework, the conversion and storage properties are optimized. In particular, the overlap of the absorption profile of NBD with the solar spectrum defines the overall efficiency and requires novel molecular design. Not only the photoconversion yield from NBD to QC is essential for the general applicability, but also the back reaction from QC to NBD must occur in a controlled and efficient way.

In this thesis, several 2,3-disubstituted NBD derivatives and their corresponding QC isomers were surveyed on model catalyst surfaces (Pt, Ni, Au) by synchrotron radiation-based X-ray photoelectron spectroscopy (XPS). Specifically, the derivatization included cyano moieties, phenyl-ester substitution, and ester-substituted oxa-NBD/QC of various size. Investigations on the adsorption at low temperatures and subsequent temperature-programmed experiments allowed for information on the respective systems on the molecular level, which enabled the deduction of thermally induced surface reactions. The focus was set on the conditions and the extent of the energy-releasing cycloreversion reactions of the QC derivatives, by which the feasibility of the different molecule and catalyst combinations was assessed.

---

---

# Table of Contents

<b>1</b>	<b>Introduction</b>	<b>1</b>
<b>2</b>	<b>Fundamentals</b>	<b>12</b>
2.1	X-ray Photoelectron Spectroscopy (XPS) .....	12
2.2	Synchrotron Radiation .....	18
<b>3</b>	<b>Experimental Section</b>	<b>22</b>
3.1	Synchrotron Apparatus.....	22
3.2	Hemispherical Electron Energy Analyzer .....	24
3.3	Data Acquisition and Evaluation.....	25
<b>4</b>	<b>Results of Publications</b>	<b>28</b>
4.1	Contribution of the Authors .....	28
4.2	Dicyano-NBD/QC on Ni(111) <sup>[P1]</sup> .....	30
4.2.1	XP spectra of the C 1s region.....	30
4.2.2	XP spectra of the N 1 region.....	33
4.2.3	Supporting DFT calculations .....	35
4.3	PENBD/PEQC on Pt(111) and Ni(111) <sup>[P2]</sup> .....	37
4.3.1	PENBD/PEQC on Pt(111) .....	37
4.3.2	PENBD/PEQC on Ni(111) .....	40
4.3.3	Comparison of PENBD/PEQC on Pt(111) and Ni(111) .....	43
4.4	PENBD/PEQC on Au <sup>[P3]</sup> .....	45
4.4.1	Monolayer conversion with XPS in UHV.....	45
4.4.2	Complementary IRRAS experiments .....	48
4.5	O-NBD/QC and exO-NBD/QC on Pt(111) <sup>[P4]</sup> .....	51
4.5.1	XPS results of O-NBD/QC.....	52
4.5.2	XPS results of exO-NBD/QC .....	56
4.5.3	Catalytic behavior in the liquid phase .....	59
4.6	Review: Surface Science Studies of NBD/QC Derivatives <sup>[P5]</sup> .....	62
<b>5</b>	<b>Summary</b>	<b>67</b>

---

---

<b>6</b>	<b>Zusammenfassung</b>	<b>71</b>
<b>7</b>	<b>Bibliography</b>	<b>75</b>
	<b>Appendix</b>	<b>91</b>
	A.1 Publication [P1] – (CN) <sub>2</sub> -NBD/QC on Ni(111).....	91
	A.2 Publication [P2] – PENBD/PEQC on Pt(111) and Ni(111).....	91
	A.3 Publication [P3] – PENBD/PEQC on Au.....	91
	A.4 Publication [P4] – O-NBD/QC and exO-NBD/QC on Pt(111).....	92

---

# 1 Introduction

*“Conservation means development as much as it does protection. I recognize the right and duty of this generation to develop and use the natural resources of our land; but I do not recognize the right to waste them, or to rob, by wasteful use, the generations that come after us.”*

– Theodore Roosevelt, New Nationalism (1910)

The environmental, economic, and social consequences of climate change are attributable to anthropogenic contributions to the atmospheric warming.<sup>[1-6]</sup> Already in 1896, Arrhenius stated a direct link between the ground temperature and the concentration of CO<sub>2</sub> in air.<sup>[7, 8]</sup> With a relative increase of 1.5% in comparison to the preceding year, the global CO<sub>2</sub> emissions accounted for 36.1 billion tons in 2022; the largest fraction of this breaks down into power production (39.3%), followed by the industry sector (28.9%), transportation (21.9%), and residential consumption (9.9%).<sup>[9]</sup> While the energy consumption rate was about 13.5 TW at the beginning of this century, an estimate of 43.0 TW is predicted for the year 2100.<sup>[10]</sup>

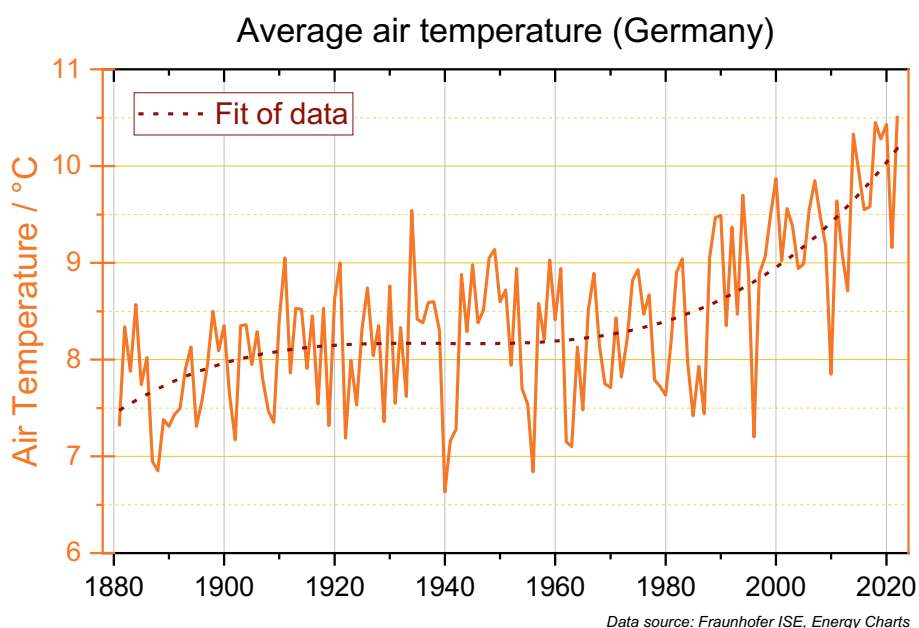


**Figure 1.1:** Development of average air temperature in Germany since 1881; the increase of the mean value is indicated by the fit of the data. Figure created with permission and data from Fraunhofer ISE.<sup>[11]</sup>

This ever-growing energy demand has to be satisfied in a climate-neutral manner in order to counteract the current temperature rise; Figure 1.1 clearly illustrates the increase of the mean value of the average air temperature in Germany since the beginning of the weather records in 1881. International attempts, such as the Paris Agreement of 2016<sup>[12]</sup> and beyond,<sup>[13]</sup> aim to limit the emission of greenhouse gases and mitigate the impacts of climate change.<sup>[14-16]</sup>

The primary energy consumption in Germany in 2022 comprised only 17.2% of renewable energy sources, whereas more than 78% was supplied by fossil fuels (i.e., mineral oil, natural gas, hard coal, and lignite).<sup>[17]</sup> Next to the depletion of hydrocarbon-based energy sources,<sup>[18]</sup> their phasing-out is tightly interwoven with climate change<sup>[19]</sup> and improves the air quality,<sup>[20]</sup> with associated health benefits.<sup>[21]</sup> At the same time, the utilization of nuclear power takes only a minor share due to safety concerns and economic reasoning,<sup>[22]</sup> and has currently no prospect in Germany.<sup>[23]</sup> Therefore, the structural transition to renewable energy sources is indispensable to accomplish a carbon-neutral infrastructure.<sup>[24, 25]</sup>

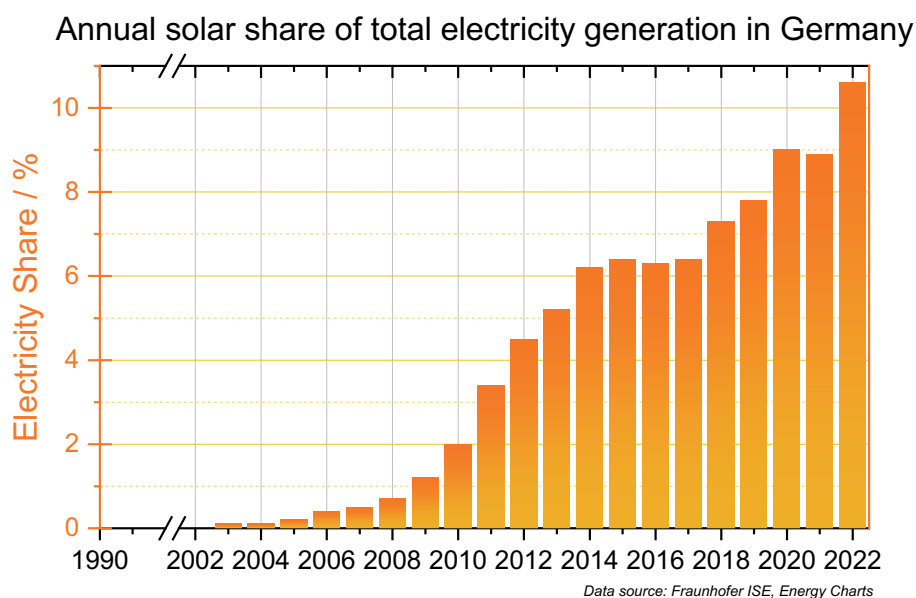


**Figure 1.2:** Depiction of increasing annual solar share of total electricity generation (public and industrial power plants) in Germany since 1990. Figure created with permission and data from Fraunhofer ISE.<sup>[11]</sup>

In a global perspective, the use of solar energy appears most viable, as the total solar irradiance is at least  $1360.8 \text{ W m}^{-2}$ ,<sup>[26]</sup> exceeding the worldwide power demand by far. The utilization of solar power requires suitable conversion technologies, which can take the form of a solar fuel in a thermal or electric manner, using different materials.<sup>[27, 28]</sup> Especially, the field of photovoltaics, including silicon-based<sup>[29]</sup> and organic solar cells,<sup>[30]</sup> led to large-scale applications. Substantial advances have been achieved,<sup>[31]</sup> resulting in enhanced efficiencies

of up to 26.8% for silicon single-junction cells.<sup>[32]</sup> As a consequence, the annual solar share of the total electricity generation in Germany increased from virtually zero to above 10% in the course of the last 20 years (see Figure 1.2). Still, there are technical limitations and intrinsic and external hindrances, e.g., the effect of temperature, dust, humidity, and shading on the overall performance;<sup>[33]</sup> moreover, the thermal stability and the degradation over time, leading to an expanding source of hazardous waste, have to be addressed.<sup>[34]</sup>

However, the main drawback of solar energy is the intermittent character of its power flux; this issue also concerns other renewable energy sources, *inter alia*, onshore and offshore wind energy, unlike to the constant base load, generated by nuclear power or fossil fuels on demand.<sup>[35]</sup> The diurnal pattern of solar power is illustrated in Figure 1.3, in which its average total net electricity generation is compared to the load during a calendar week in Germany in 2022.

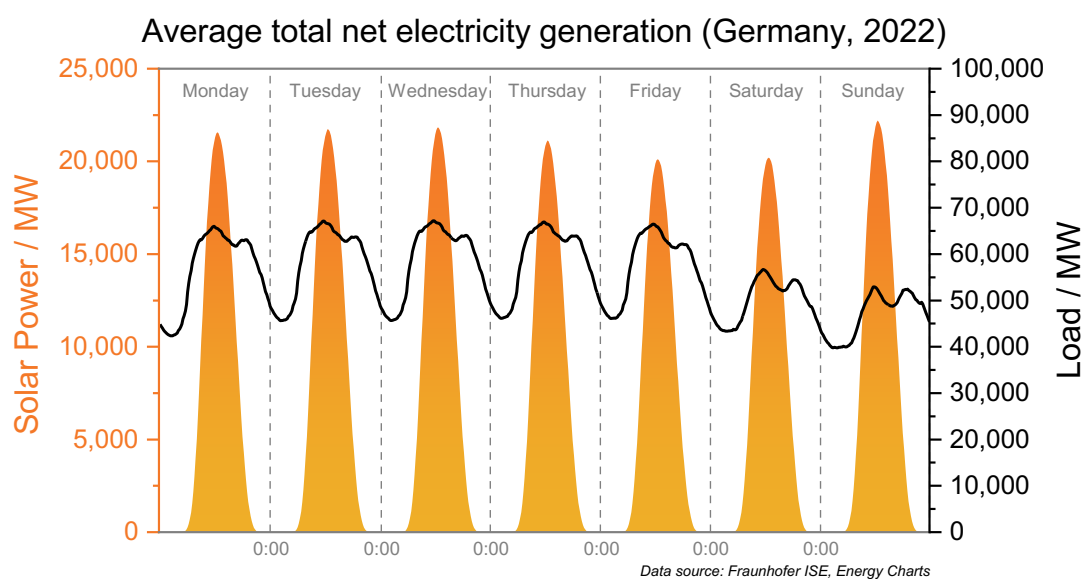
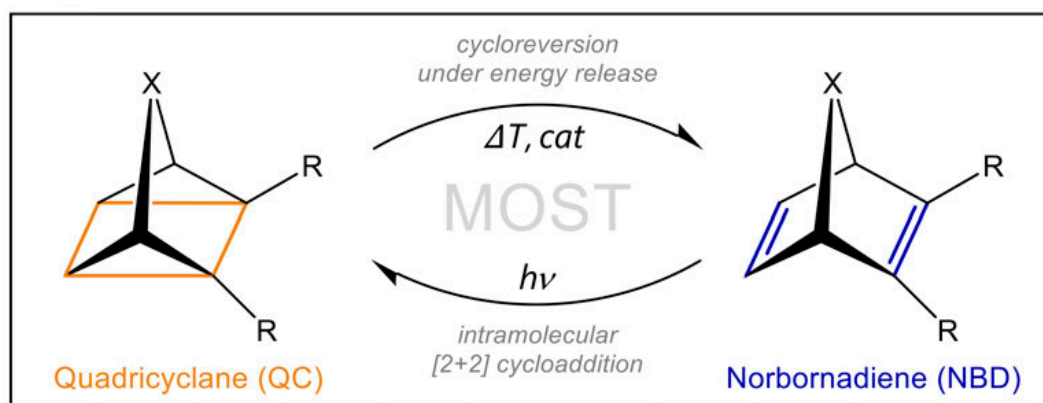


**Figure 1.3:** Visualization of fluctuation and mismatch of generated solar power and load during one week; the values are averaged for 2022 in Germany. Figure created with permission and data from Fraunhofer ISE.<sup>[11]</sup>

Self-explanatory, solar power peaks around midday, matching the highest energy demand throughout a day, whereas the second apex of the load in the evening hours does not coincide well. Besides, geographical factors influence the availability of solar power, and weather and seasonal effects restrict its utilization, predominantly in the winter months. As a result, the emerging mismatch between energy supply and consumption gives the necessity of energy storage solutions, in which the surplus of energy is stored and then released at will in energy-deficient periods.<sup>[36, 37]</sup> For this purpose, battery technologies are well-developed and readily available.<sup>[38-40]</sup> Yet, environmental and safety aspects arise during production, operation, and

recycling of many types of batteries, which depend on the general composition and the respective cycle life;<sup>[41]</sup> these challenges also involve the depletion of natural resources, and affect the ecological and social sustainability.<sup>[42, 43]</sup> Alternatively, novel and complementary concepts for energy storage in chemical compounds are therefore proposed.<sup>[44, 45]</sup>

One such new approach are so-called molecular solar thermal (MOST) energy storage systems,<sup>[46-56]</sup> in which the direct light harvesting and storing of the gained energy is possible in single-photon single-molecule processes. MOSTs are based on couples of photoisomers, representing a discharged and loaded energy state. The irradiation with light of suitable wavelengths causes a conversion reaction to a higher-lying metastable energy state, e.g., in form of a strained molecular framework. Triggering the back reaction to the initial isomer, in a catalytic, thermal, or electrochemical manner, then releases the stored energy on demand, i.e., the energetic difference between both molecules. Thus, the formed photoswitchable systems make use of the light-induced rearrangement of chemical bonds. In literature, various compound classes have been suggested as potential energy storage materials: among others, the (E/Z)-isomerization of stilbenes<sup>[57-60]</sup> or azobenzenes<sup>[61-66]</sup> and derivatives thereof, the formation of anthracene dimers,<sup>[67-69]</sup> or the interconversion of organometallic fulvalene-tetracarbonyl-diruthenium complexes<sup>[70-74]</sup> are reported. This thesis focuses on the chemistry of norbornadiene (NBD) and its energy-rich counterpart quadricyclane (QC)<sup>[75-79]</sup> (see Scheme 1.1), as this molecule pair exhibits the most promising properties.



**Scheme 1.1:** Overview of the energy storage in a molecular solar thermal (MOST) system; in a photoconversion reaction, the energy-lean norbornadiene (NBD) is converted into the strained quadricyclane (QC), whereas the back reaction under energy release is triggered thermally or catalytically.

For the general feasibility of MOST applications, several requirements have to be fulfilled:<sup>[80-82]</sup> First of all, the energy storage density of the considered molecular system should be maximized; for this reason, a highly exothermic reaction profile in combination with a small

molar mass is favorable. For the unsubstituted NBD/QC pair, a reasonable storage density of  $0.97 \text{ MJ kg}^{-1}$  is achieved, as the reaction enthalpy amounts to  $89 \text{ kJ mol}^{-1}$  at a mass of  $92.14 \text{ g mol}^{-1}$ .<sup>[83-85]</sup> Besides, for the photoconversion into the strained isomer, a high quantum yield and the sufficient overlap of the parent compound with the excitation wavelengths is essential; since the spectral distribution of the direct solar radiation has the highest intensities between 300 and 800 nm (peaking at  $\sim 500 \text{ nm}$ ),<sup>[86]</sup> according absorption features are necessary in this range for an efficient utilization of solar power. Moreover, the conversion must exhibit a photochromic character, i.e., the energy-rich photoisomer must not absorb visible light to a greater extent in order to avoid unwanted photo-induced follow-up reactions. The quantum yield of NBD to QC is only about 5%;<sup>[87]</sup> however, the use of appropriate photosensitizers,<sup>[77, 88-90]</sup> which should not be quenched in the system,<sup>[91]</sup> gives values close to unity, e.g., above 90% for acetophenone.<sup>[92]</sup> The photoconversion works thereby through triplet sensitization from the sensitizer to NBD.<sup>[93, 94]</sup> Further, the isomerization can be facilitated catalytically by semiconductor materials<sup>[95, 96]</sup> or transition metal complexes.<sup>[97, 98]</sup> Concerning the absorption behavior of NBD, unfortunately, there are no significant contributions to wavelengths above 300 nm;<sup>[99, 100]</sup> instead, its absorption onset is found at 267 nm.<sup>[101]</sup> Nonetheless, through derivatization of the NBD framework, the desired bathochromic shift of the absorption bands towards lower energies can be achieved. Numerous derivatives have been suggested and surveyed in literature, whereby some examples will be listed later in the text. In general, there is a trade-off between overlap of the absorption features with the solar spectrum and the molecular weight of the compounds. Recently, also a dependence of the absorption and conversion processes on solvent effects was described.<sup>[102]</sup> Regarding the overall efficiency, the storage densities should exceed that of solar water heating ( $0.2 \text{ MJ kg}^{-1}$  for  $\Delta T = 50 \text{ K}$ ) to be a useful MOST system.<sup>[77]</sup>

There are also a number of criteria for the energy-releasing cycloreversion reaction from QC back to NBD. Naturally, both molecules need to be stable over a long period; in particular, the half-life of the metastable QC isomer is essential. The Woodward–Hoffmann selection rules for concerted cycloaddition reactions<sup>[103, 104]</sup> state the back conversion to NBD as a formally forbidden  $[\pi 2_s + \pi 2_s]$  ring opening.<sup>[105]</sup> This explains the observed high activation barrier of roughly  $140 \text{ kJ mol}^{-1}$ ,<sup>[106]</sup> resulting in an unexpected high stability of the strained QC ( $t_{1/2} > 14 \text{ h}$  at  $140 \text{ }^\circ\text{C}$ ).<sup>[107, 108]</sup> As the energy release must only occur readily when required, the likelihood of spontaneous back reactions to the released isomer should be

minimized, i.e., a high resistance of the energy-rich compound to storage under increased temperatures or the exposure to visible light sources. Self-evidently, a quantitative conversion without the formation of by-products is necessary for both isomerization reactions. A closed energy-storage cycle, with the operation of as many charge and release steps as possible, is prerequisite both for economic aspects and sustainability reasons. This comprises a minimized degradation over time and the prevention of catalyst fouling. Moreover, as for any large-scale process in chemistry, the turnover numbers and the development of the involved infrastructure should be optimized, including availability, costs for syntheses, transportation, and environmental considerations. All in all, the introduced NBD/QC molecule pair appears promising to meet the, in part contrasting, requirements for potential MOST energy storage materials.

The synthesis of the first NBD derivatives dates back to the introduction of the Diels–Alder reactions in the first half of the last century.<sup>[109]</sup> In 1951, the formation of unsubstituted NBD from acetylene and cyclopentadiene was described in a patent by Hyman.<sup>[110]</sup> Thereafter, the reactivity of bridged polycyclic compounds was explored<sup>[111, 112]</sup> and synthetic routes of NBDs became available.<sup>[113, 114]</sup> Since QC was not accessible through chemical preparation,<sup>[115-117]</sup> photochemical approaches<sup>[118]</sup> yielded the discovery of QC derivatives.<sup>[99, 119]</sup> The photo-conversion to unsubstituted QC was achieved in an analogous way,<sup>[120]</sup> facilitated by the use of appropriate sensitizers.<sup>[107]</sup> As outlined before, the insufficient absorption of NBD in the visible light range led to a plethora of derivatives with a redshift of their absorption onset. Different molecule classes are defined according to their substitution pattern. As compared to tetrasubstituted molecules, disubstituted derivatives seem encouraging due to their lower molecular weight in comparison. In addition, the functionalization of the bridgehead demonstrated to increase quantum yields and kinetic stabilities.<sup>[121]</sup> Further, hetero-NBDs are expected to display enhanced storage profiles<sup>[122]</sup> and are synthetically well-known.<sup>[123]</sup> Other systems consist of an array of linked NBD units<sup>[124, 125]</sup> or employ different MOST molecules in hybrid compounds.<sup>[126, 127]</sup>

In particular, substitution with electron-donating and -withdrawing moieties are of interest due to the formation of push-pull systems by extension of the  $\pi$ -conjugation or through-space interactions. Overall, the symmetric<sup>[82, 100, 128]</sup> as well as asymmetric 2,3-disubstitution of NBD gave numerous derivatives with advantageous properties for possible MOST applications. Especially, Moth-Poulsen *et al.* promoted this area of research in the

course of the last years.<sup>[101, 102, 129-133]</sup> For the assessment of suitable derivatives, quantum mechanical modelling gives important predictions of desirable trends. Next to first-principle calculations to gain specific insights into optical and thermal properties of the proposed molecules,<sup>[134]</sup> a screening of kinetically stable derivatives of a vast number of NBD compounds is possible by means of tight binding methods<sup>[135]</sup> and machine learning-based techniques.<sup>[136]</sup>

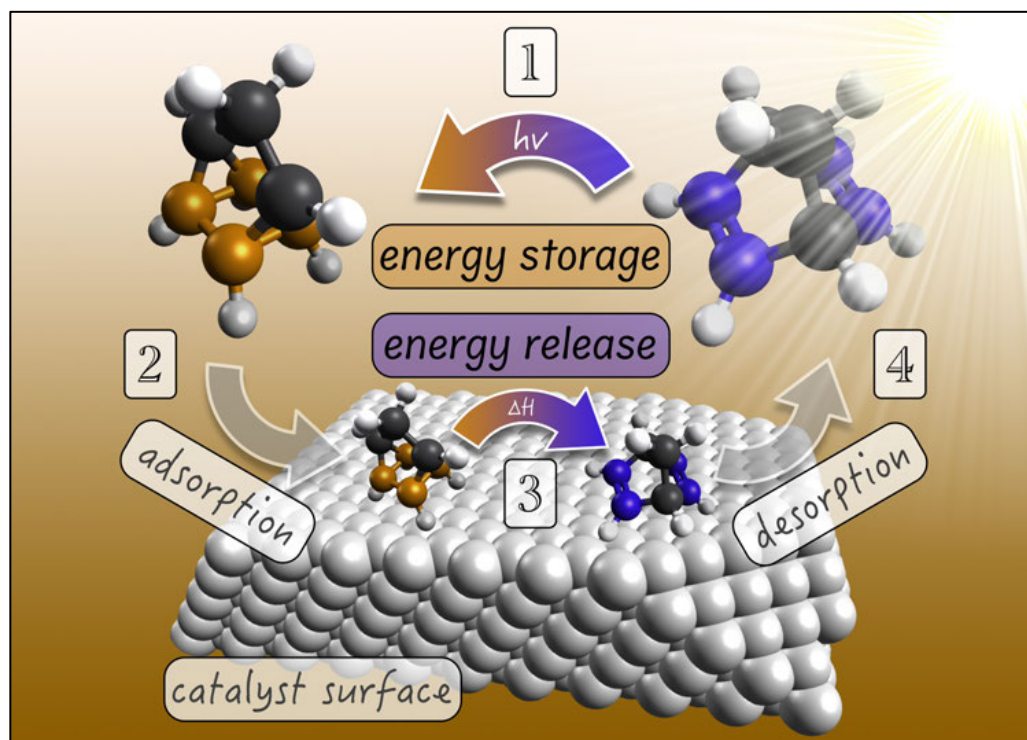
Not only a sophisticated molecular design of NBD is crucial but also the control of the energy release. The energetic barrier for the back conversion of the energy-rich QC can be overcome in a thermal way. Early investigations on this caloric pathway<sup>[106]</sup> yielded the respective heat of isomerization.<sup>[83]</sup> However, since the stored energy is generally needed in energy-deficient periods, heat as trigger reduces the overall efficiency. The rearrangement of cyclic organic molecules<sup>[137]</sup> is also catalyzed by the use of various transition metals in solution,<sup>[108, 138]</sup> influenced by diverse ligands.<sup>[139]</sup> Hereby, different intermediate states<sup>[140]</sup> facilitate the isomerization, e.g., the resulting complexation changes the symmetry constraints during the concerted reaction,<sup>[141]</sup> furthermore, oxidative-addition pathways<sup>[142]</sup> and Lewis acid type of reactions<sup>[143]</sup> are described. The cycloreversion to NBD can also be initiated in an electrochemical way. Upon oxidation of QC (0.91 V vs. SCE),<sup>[144]</sup> the energetic barrier for the interconversion between the radical species is lowered drastically.<sup>[145, 146]</sup> Yet, the proceeding redox-mediated chain reaction<sup>[147]</sup> leads to unwanted side reactions and electrode fouling.<sup>[148]</sup> This lack of control in the mechanism is approached in photoelectrochemical experiments in a well-defined environment. Eventually, by appropriate coupling of the MOST system to a suitable semiconductor electrode, it might become possible to gain the stored energy in form of electricity instead of heat.<sup>[149]</sup>

Although a process analysis in 1983 proved the general technical feasibility of NBD/QC as MOST energy storage solution, economic assessments stated insufficient profitability, primarily due to low collector efficiencies.<sup>[76]</sup> Nevertheless, advances in molecule and catalyst design tackled the intrinsic limitations of the system, whereas a simulated efficiency limit of up to 21% was estimated.<sup>[150]</sup> That is, improvements in the macroscopic heat release were achieved,<sup>[151-153]</sup> which could be used for thermal power processes in industry or domestic heating. A maximum temperature gradient of 63 °C has been reached so far, whereupon corresponding outdoor testing demonstrated the proof of concept under operation conditions.<sup>[153]</sup> Aside from that, for example, Dreos *et al.* developed high-performing NBD derivatives, which absorb up to 10% of the incoming solar light and still display high storage

densities (up to  $577 \text{ kJ kg}^{-1}$ ); besides, their viscosities enable a pumping without the use of additional solvents.<sup>[131]</sup> Depending on the technical adaptations, the incorporation of NBD derivatives into processable matrices is also possible, creating energy storage coatings, e.g., for window tinting<sup>[154]</sup> or UV shielding.<sup>[155]</sup> Hybrid concepts combine MOST molecules with solar water heating systems<sup>[156]</sup> or phase-change materials<sup>[157]</sup> to increase the efficiencies for short- and long-term energy storage. In combination with a microfabricated thermoelectric generator, the released heat of a MOST system can also be directly transformed into electricity, giving power densities of up to  $1.3 \text{ W m}^{-3}$  in first laboratory-scaled devices.<sup>[158]</sup>

In total, the synthetic possibilities allow for various potential implementations, as the derivatives now feature absorption profiles towards 590 nm, high storage densities of up to  $250 \text{ Wh kg}^{-1}$ , and adjustable storage times (1h to 18 years) as needed.<sup>[79]</sup> In addition, the up-scaling of NBD syntheses was shown to be viable using continuous flow chemistry.<sup>[159]</sup> In order to fulfill individual requirements of NBD-based devices, an understanding of the particular systems on the molecular level is necessary. Fundamental research helps in the assessment of different molecule and catalyst combinations, supports the search for further design, and promotes the specific optimization of single parameters. The utilization of heterogeneous catalysis concepts is preferential for the transition to large-scale applications. Next to a straightforward separation of the reaction product, the facile recycling and the wide range of applicable catalyst materials is of advantage.

Surface science techniques deliver mechanistic insights into the occurring phenomena at interfaces, necessary for improvements of the catalytic activity.<sup>[160]</sup> Experiments in ultra-high vacuum are conducted under controlled and ordered conditions, from which, ideally, the knowledge transfer to more complex real-life scenarios is achievable. In this context, information on the energy release during the cycloreversion from the respective QC to NBD is obtained. Moreover, adsorption and desorption processes of the molecules are investigated, the interaction strength with the surface determined, and thermal stability limits and decomposition pathways identified. Scheme 1.2 illustrates the catalytic cycle utilizing a single crystal surface as heterogeneous catalyst: (1) The photoconversion of NBD to QC stores the solar energy in a chemical manner, (2) the energy-rich QC is adsorbed onto the catalyst material, (3) the energy-releasing cycloreversion reaction is triggered yielding NBD on the surface, and (4) the desorption of the energy-lean NBD from the catalyst for an ideal total reversibility and closed energy storage and release cycle.



**Scheme 1.2:** Illustration of the molecular pair NBD/QC in heterogeneously catalyzed applications: (1) Solar power is harvested through the isomerization of energy-lean NBD into energy-rich QC. (2) The adsorption onto a suitable catalyst surface enables the (3) cycloreversion reaction back to NBD, whereby the stored energy is released on demand as heat. (4) Subsequent desorption of NBD gives ideal reversibility of the cycle.

First surface science investigations of NBD were carried out by Muetterties *et al.* on Pt(111), on which a high sticking coefficient was determined and the evolution of hydrogen and benzene was detected, when heating to temperatures above 520 K.<sup>[161]</sup> The regioselective removal of the bridging carbon was concluded, as the incorporation of the CH<sub>2</sub> bridgehead into the desorbing benzene molecules was excluded in experiments with isotopic labeling.<sup>[162]</sup> Infrared reflection absorption spectroscopy measurements of the same system by Hostetler *et al.* indicated an unexpected  $\eta^2:\eta^1$  adsorption geometry upon adsorption at 130 K. Hereby, only one C=C double bond coordinates to the surface, while the CH<sub>2</sub> bridgehead forms an agostic interaction with the platinum surface. At elevated temperatures above 260 K, the cleavage of this agostic C-H bond takes place, yielding a norbornadienyl species that is stable until 450 K. As reported before, the thermally induced decomposition gives benzene and hydrocarbon fragments on the surface via a retro-cyclization.<sup>[163]</sup> Bauer *et al.* confirmed the previously found adsorption geometry of NBD on Pt(111) in a subsequent combined surface science study, supported by DFT calculations. In addition, the surface chemistry of QC was investigated for the first time directly. The multimethod approach of XPS, UPS, and IRRAS determined a high catalytic activity of platinum for the cycloreversion reaction, so that all QC

is instantly converted to NBD upon contact with the surface. Temperature-programmed experiments supported the formation of norbornadienyl above 190 K, with a comparable stability range; however, this time, no benzene and methylidyne was detected as reaction product at higher temperatures.<sup>[164]</sup> Besides, a comprehensive electrochemical characterization of NBD/QC was conducted, whereby IR experiments using Pt(111) as working electrode showed the reaction rates to be potential-dependent.<sup>[149]</sup> Photoelectrochemical IRRAS investigations followed the light-induced conversion to QC, with the use of the sensitizing Michler's ketone, as well as the electrochemically triggered back reaction to NBD, again on a Pt(111) electrode. Thereby, a high selectivity for both isomerization reactions was stated after quantification of the results.<sup>[165]</sup>

The molecule pair NBD/QC was also surveyed on a less reactive Ni(111) surface, on which a flat binding motif ( $\eta^2:\eta^2$ ) of NBD was suggested by DFT and supported by NEXAFS measurements. Synchrotron radiation-based XPS and UPS spectra enabled a spectroscopic distinction of both valence isomers on nickel upon adsorption at 120 K. The energy-releasing cycloreversion reaction occurred, in contrast to Pt(111), in a controlled manner when heating, and was completed at 175 K. A comparable decomposition onset was monitored at 190 K, yielding benzene and methylidyne species and, above 300 K, C-H fragments and carbide.<sup>[166]</sup> Follow-up studies of 2,3-dibromo-NBD/QC on Ni(111), as first model system of simple derivatives, indicated the partial dissociation of the bromine moieties during exposure to the surface. Adsorption geometries were likewise resolved by DFT calculations, whereas spectroscopic findings indicated the conversion from QC to NBD derivative at 170 K. Yet, due to the less stable C-Br bond, the reaction towards parent NBD was proposed to a significant extent. Above 190 K, the decomposition pathways were analogous to unsubstituted NBD on Ni(111).<sup>[167]</sup>

In this thesis, the surface chemistry of norbornadiene (NBD) and quadricyclane (QC) derivatives is investigated by synchrotron radiation-based X-ray photoelectron spectroscopy (XPS). The adsorption of newly-designed molecules on single crystal surfaces, Ni(111) and Pt(111), or a prepared gold film was followed *in situ*, whereby the spectroscopic fingerprints of the respective isomers were identified. When possible, the adsorption geometries were determined, or probable binding motifs proposed, and the interaction strength with the surface assessed. Temperature-programmed XPS experiments (TPXPS) allowed for the deduction of reaction pathways of both QC and NBD derivatives. Next to the evaluation of the feasibility as MOST system, through the successful observation of the cycloreversion reaction from the energy-rich to the energy-lean released molecule, information on thermal stability boundaries, desorption processes, and decomposition reactions was gained.

In the following, Chapter 2 gives a brief introduction into the fundamentals of the applied methodology, with the focus set on the basics of X-ray photoelectron spectroscopy as surface science technique (Chapter 2.1), and a general description of synchrotron radiation (Chapter 2.2), as all data were acquired at a corresponding facility. The experimental setup is described in Chapter 3, whereby the used “synchrotron apparatus” (Chapter 3.1) and the functionality of a hemispherical electron energy analyzer (Chapter 3.2) are addressed, after which the data evaluation (Chapter 3.3) is illustrated. The results of the publications are presented in Chapter 4, with a listing of the single author contributions (Chapter 4.1). The molecule pair 2,3-dicyano-substituted NBD/QC, (CN)<sub>2</sub>-NBD/QC, on Ni(111) is discussed in Chapter 4.2, supported by DFT calculations. Thereafter, the promising asymmetrically derivatized 2-carbethoxy-3-phenyl compounds, phenyl-ester-NBD/QC (PENBD/PEQC), are surveyed on different surfaces; specifically, the comparison between Pt(111) and Ni(111) is shown in Chapter 4.3. In a collaboration, the high activity of a gold surface for the conversion of PEQC to PENBD was confirmed in XPS and IRRAS measurements (Chapter 4.4). The first surface studies of hetero-NBD derivatives on Pt(111), namely ester-derivatized oxanorbornadiene (oxa-NBD), in particular, 2,3-(bismethylester)-oxa-NBD (O-NBD) and 2,3-(bisbenzylester)-oxa-NBD (exO-NBD), and their respective photoisomers (O-QC/exO-QC) are subject of Chapter 4.5. Chapter 4.6 refers to the review article on surface science studies of NBD/QC molecules. Finally, the main findings are summarized in English (Chapter 5) and in German (Chapter 6).

## 2 Fundamentals

### 2.1 X-ray Photoelectron Spectroscopy (XPS)

The surface chemistry of the considered molecules was investigated using *X-ray photoelectron spectroscopy* (XPS) as primary method in this thesis. By means of this photoemission technique, the elemental composition can be identified in a quantitative manner. Moreover, information on the chemical environment is accessible, so that XPS is also referred to as *electron spectroscopy for chemical analysis* (ESCA).<sup>[168]</sup> Utilizing synchrotron radiation (see Section 2.2) yields spectroscopic data with high resolution and surface sensitivity with short acquisition times. Thereby, adsorption processes are observable *in situ*, while the thermal evolution is monitored in temperature-programmed XPS (TPXPS) experiments.<sup>[169]</sup>

As implied by its name, XPS is based on the photoelectric effect, which describes the emission of electrons upon interaction of electromagnetic radiation with matter. Historically,<sup>[170, 171]</sup> in 1887, Hertz was the first to discover that light facilitated spark formation between metal surfaces.<sup>[172]</sup> The subsequent experimental systematization was carried out, *inter alia*, by Hallwachs<sup>[173]</sup> and Lenard.<sup>[174, 175]</sup> In 1905, Einstein gave a quantum mechanical explanation,<sup>[176]</sup> wherefore he received the Nobel Prize in 1921. The technical advances, especially promoted by Siegbahn and his group,<sup>[177-180]</sup> unveiled the potential as powerful spectroscopic analysis tool. Having developed instruments with sufficiently high resolutions for feasible measurements, the Nobel Prize was awarded to Siegbahn in 1981. Further technical improvements extended the application fields of XPS, such that it is nowadays a widespread and indispensable method in various scientific disciplines; detailed descriptions are found in associated literature.<sup>[181-191]</sup>

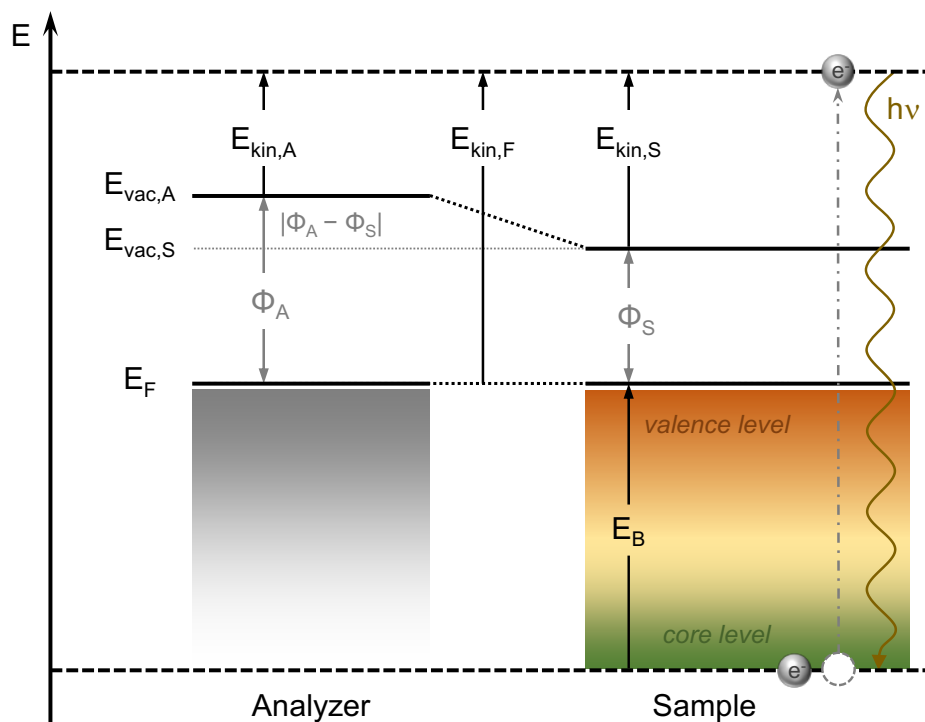
The basic principle of XPS comprises the measurement of the kinetic energy  $E_{kin}$  of the emitted photoelectrons. Due to energy conservation, the following simple relation is deduced for the photoelectric emission, valid if the energy of the irradiating light  $h\nu$  is high enough to release the bound electron:

$$E_{kin} = h\nu - E_B, \quad (2.1)$$

where  $h$  is the Planck constant,  $\nu$  the frequency of the light, and  $E_B$  the binding energy of the electron; here, the vacuum level is the reference for the energies, as applicable for free atoms and molecules. Considering solids, the electronic properties are defined by the Fermi level, to which the energies are then referred to. The resulting equation for the binding energy is consequently:

$$E_B = h\nu - E_{kin,S} - \phi_S, \quad (2.2)$$

with  $\phi_S$  as work function of the sample, i.e., the energetic difference between the Fermi level and vacuum; this value is specific for the particular specimen and often difficult to determine. However, by conductively connecting the sample and the electron energy analyzer, the Fermi levels align. The kinetic energy is measured within the analyzer with a distinct work function  $\phi_A$ , which is accessible by suitable calibration.



**Scheme 2.1:** Depiction of the energetic levels during an X-ray photoelectron spectroscopy measurement: The incoming photon possesses an energy of  $h\nu$ , while  $E_B$  describes the binding energy of the electron; the Fermi levels  $E_F$  of the analyzer and sample align; due to different work functions  $\Phi$ , the vacuum levels of analyzer and sample differ by  $|\phi_A - \phi_S|$  resulting in the respective kinetic energies of the photoelectron  $E_{kin}$ .

Therefore, the binding energy is obtained as:

$$E_B = h\nu - E_{kin,A} - \phi_A. \quad (2.3)$$

The schematic measurement arrangement and its corresponding energy landscape during the photoemission process are illustrated in Scheme 2.1. Since the emission of an electron leads to an ionization of the system, the energetic difference between initial neutral state and the charged final state has to be considered for the binding energy:<sup>[183]</sup>

$$E_B = E^{N-1}(final) - E^N(initial) , \quad (2.4)$$

whereby  $N$  amounts to the number of electrons in the system; the convention denotes a positive value as bound state. In a simplified assumption, according to the Koopman's theorem,<sup>[192]</sup> the remaining electrons do not react to the formed core hole (*frozen orbital approximation*); in this case, the binding energy corresponds to the negative Hartree-Fock orbital energy. More realistic approaches include these interactions, which yields an energetic relaxation of the orbitals giving generally lower apparent binding energies, as follow:

$$E_B = E_0 - E_R - E_C , \quad (2.5)$$

so that the experimentally measured binding energy  $E_B$  is composed of the subtraction of relaxation contributions  $E_R$  and correlation terms between initial and final state  $E_C$  from the Koopman's energy  $E_0$ . In molecules or for solids, in addition, extra-atomic relaxation effects  $\Delta E_{ER}$  might be considered, e.g., the additional polarization screening or charge transfer by neighboring atoms. Either way, the formation of core holes causes two competing follow-up processes, depending on the atomic number and binding energy of the emitted electron. In this way, the lifetime of the core hole determines the natural linewidth in XPS, as a consequence of the uncertainty principle;<sup>[193]</sup> note that the measured peak shape is also broadened by instrumental factors, discussed later in the text. For low binding energies of the core hole, i.e., the K-shell decay for lighter elements ( $Z < 30$ ), the occurrence of the Auger decay is more probable. Here, one electron of a higher shell fills up the core hole, thereby creating again a hole, and transfers the corresponding energetic difference onto another electron that is then emitted with the remaining kinetic energy. The transitions are labeled by the core hole level, the filling electron, and the emitting one; if the core hole and one electron originates from the same shell, the term *Coster-Kronig* transition<sup>[194]</sup> is used, and *super Coster-Kronig* for all three electrons coming from the identical shell, resulting in shorter half-lives of the core holes. An additional effective potential is used to describe the Coulomb interaction between the two core holes in the final state. The characteristics of the Auger effect are utilized in a separate spectroscopic technique, named Auger electron spectroscopy (AES).<sup>[195]</sup>

In the case of higher initial binding energies and heavier elements ( $Z > 30$ ), the phenomenon of X-ray fluorescence takes place predominantly. The core hole is again filled by a higher-lying electron, and the difference in energy is emitted as electromagnetic radiation, specifically, X-rays this time. Derived X-ray fluorescence (XRF) methods<sup>[196]</sup> are commonly applied for elemental analyses.

Since the measured binding energies are element-specific, XPS naturally provides information on the chemical composition of a sample.<sup>[197]</sup> Utilizing common excitation energies up to 2 keV, in the soft X-ray range, the first electron shells are readily accessible for the majority of elements; in particular, the K-shell, i.e., the 1s core level region, is oftentimes of interest for lighter elements. However, not only knowledge about elemental concentrations is gained, but XPS is also sensitive to the chemical state of the considered atom and its surrounding. The resulting variation in the binding energies  $\Delta E_{Chem}$ , referred to as *chemical shift*,<sup>[198, 199]</sup> can be resolved with sufficient energy resolution and allows for the spectroscopic distinction of different chemical species. Contributions prior to the photoemission event are so-called initial state effects, which include the reaction of core level orbitals to changes of the charge density distribution, thus, being primarily influenced by the local chemical environment of the atom that is emitting the photoelectron. Next to the oxidation state, the specific bonding situation, and the electronegativity of adjacent atoms are decisive. A prominent example is the XP spectrum of ethyl trifluoroacetate,<sup>[200]</sup> in which a clear separation of the peaks associated to the four carbon atoms is visible and the assignment to the different moieties within the molecular framework is straightforward due to their chemical identity. Similarly, for surface atoms, the lower coordination yields a surface core level shift ( $\Delta E_{SCLS}$ ). Phenomena after the excitation of the photoelectron are named final state effects and also influence the detected XP spectra. The relaxation, in form of an energetic lowering of the system as a result of the formed core hole, was already described above. In addition, multiple excitation processes are possible, since the initial and final state are not eigenstate of the same Hamiltonian in photoemission leading to different final state configurations.<sup>[201]</sup> Most prominent are additional satellites in the spectrum at higher binding energies. These originate from the initial ionization and the further simultaneous excitation of another electron into higher-lying states (*shake-up*), or the emission of this second electron resulting in a double ionization (*shake-off*).<sup>[202]</sup> Moreover, vibrational excitations<sup>[203]</sup> cause corresponding satellites, according to the Franck–Condon principle,<sup>[204]</sup> and are especially

applicable for the identification of small surface species by their vibrational signature.<sup>[205]</sup> Besides, molecular systems with unpaired spins consequently feature a multiplet splitting; in solids, plasmonic excitation or that of electron-hole pairs can occur. Extrinsic losses on the way to the detector, mainly through inelastic scattering, yield low-energy secondary electrons, which account to a stepwise increase of the background towards higher binding energies. This typical appearance of an XP spectrum is depicted in Figure 2.1, in which the survey spectra of clean Pt(111) and Ni(111) surfaces with their labeled peaks are plotted. The expected binding energies ranges for the in this thesis employed core levels, namely C 1s, N 1s, and O 1s region, are highlighted.

In summary, XPS enables the precise chemical characterization of various specimen, whereby the obtained data from molecules might even be deconvoluted to single atomic contributions within the structure; in any case, the measured X-ray photoelectron spectra serve as characteristic spectroscopic fingerprints of the investigated systems.

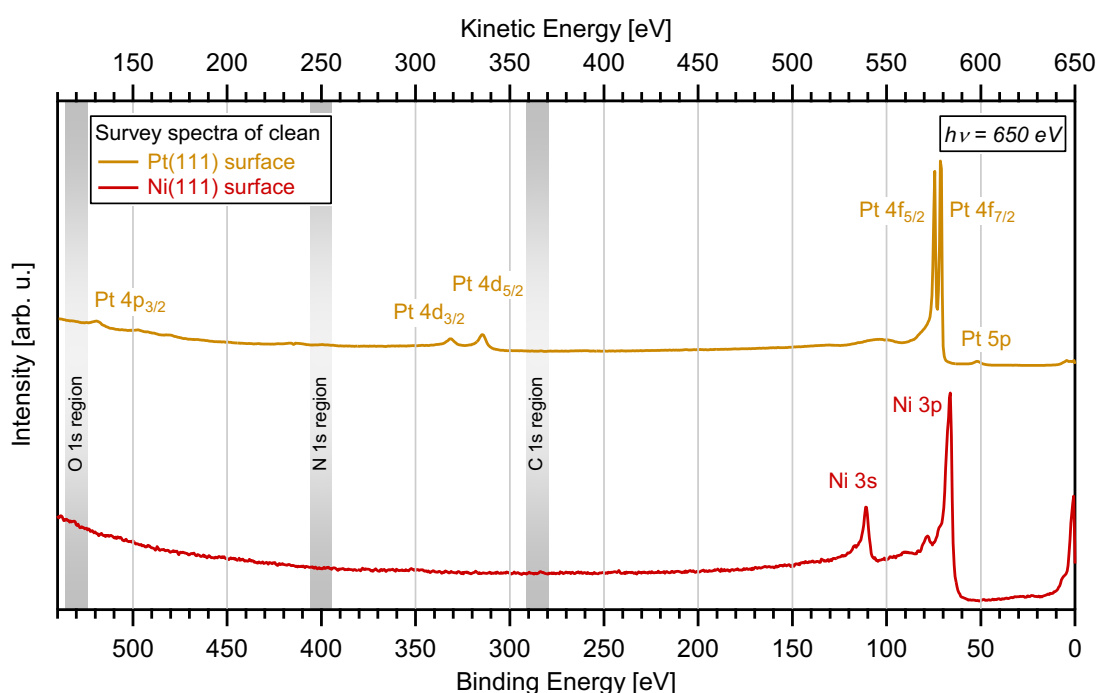


**Figure 2.1:** XP survey spectra of clean single crystal surfaces, Pt(111) and Ni(111), acquired at a photon energy of 650 eV; elemental peaks are denoted as well as regions (1s core level) of relevant adsorbate contributions (carbon, nitrogen, and oxygen) highlighted.

Photoelectron spectroscopy (PES) methods are predestined for surface science research due to their general advantage of a very high surface sensitivity,<sup>[206]</sup> which is based on the short inelastic mean free path of electrons. As charged particles, they exhibit strong interactions with matter, reaching on average only a few atomic layers (5-30 Å) before they

lose their energy. A correlation between the inelastic mean free path and the kinetic energy of electrons was established by Seah and Dench; their proposed *universal curve*, agreeing to compilations of experimental measurements, displays a minimum at about 100 eV.<sup>[207]</sup> Therefore, tuning the kinetic energy of the photoelectrons, applicable at synchrotron facilities, enables the enhancement of the surface sensitivity. Besides, the detection angle  $\vartheta$  influences the information depth through geometrical reasoning. The attenuation obeys the Beer–Lambert law, as follows:

$$I = I_0 \times \exp \left[ \frac{-d}{\lambda_M(E_{kin}) \times \cos(\vartheta)} \right], \quad (2.6)$$

whereby  $I_0$  describes the initial intensity,  $d$  the escape depth,  $\lambda_M(E_{kin})$  the energy-dependent inelastic mean free path of the emitted electrons, and  $\vartheta$  the detection angle with respect to the surface normal.

Furthermore, XPS is inherently a quantitative method, since the measured intensities are directly proportional to the atom density of an element within the specimen but are not affected by its chemical environment.<sup>[208, 209]</sup> In theory, the signals can be derived by the photoemission probability.<sup>[186]</sup> However, the photoelectric cross section of the particular orbital and the overall instrument response, including the detection efficiency of the spectrometer and the angular asymmetry of the emission,<sup>[210]</sup> additionally influence the count rates. Similarly, the photon flux on the sample area has to be considered. In practice, the calibration of the surface amount is performed by suitable reference measurements (see Section 3.3), as some of these parameters are difficult to determine. Yet, attenuation of the photoelectrons and the occurrence of photoelectron diffraction effects,<sup>[211-213]</sup> i.e., the energy- and orientation-dependent scattering of the emitted electrons by neighboring atoms, yielding intensity modulations, might lead to slight uncertainties in the determination of the surface coverages. In total, XPS proved as suitable surface science technique to gain fundamental information on molecular systems, so that the spectroscopic data acquired within the scope of this thesis contributed to the elucidation of the surface chemistry of the investigated organic molecules on single crystal materials.

## 2.2 Synchrotron Radiation

As outlined in the previous Section 2.1, synchrotron radiation<sup>[214]</sup> features several advantages and was thus utilized for the herein discussed measurements. Next to a large continuous and adjustable energy range, especially its high intensity and spectral brightness, also referred to as brilliance, is favorable, i.e., the photon flux per solid angle and unit area for a fixed relative energy bandwidth (0.1%).<sup>[215]</sup> Moreover, the generated radiation is extremely collimated, monochromatized, and exactly calculable, with a defined degree of polarization and pulsed time structure. Various specific experimental methods can be performed at synchrotron radiation facilities,<sup>[216]</sup> e.g., near edge X-ray absorption fine structure (NEXAFS)<sup>[217]</sup> measurements that require the scanning of the excitation energy. Likewise, XPS experiments benefit from the enhanced light source under controlled conditions; as both spatial and spectral resolution is increased, an improved signal-to-noise ratio is obtained, and the acquisition times are significantly lowered. In addition, the tunability of the excitation energy enables the optimization for the cross section of element-specific core levels as well as depth profiling due to a variable surface sensitivity at different kinetic energies. Whereas the technical operability of synchrotron radiation was already demonstrated in the middle of the last century, and the progression of the specifications is still ongoing, the basic theoretical considerations date back even further.<sup>[218, 219]</sup> In the following, a brief description of the underlying physical principles will be given.

According to electrodynamics, the acceleration of charged particles yields the emission of electromagnetic radiation.<sup>[220]</sup> Here, non-relativistic particles display almost negligible power outputs. For velocities close to the speed of light  $c$ , relativistic effects must be taken into account, so that the radiation power  $S$  is expressed for circular acceleration as:<sup>[221]</sup>

$$S = \frac{q^2 c}{6\pi\epsilon_0} \frac{1}{(m_0 c^2)^4} \frac{E^4}{R^2}, \quad (2.7)$$

with the charge  $q$  and mass  $m_0$  of the accelerated particle, the dielectric constant of the vacuum  $\epsilon_0$ , the energy  $E$ , and the bending radius  $R$  of the trajectory. Formula 2.7 reveals the strong dependence of the radiation power reciprocally on the mass and directly on the energy, to the fourth power. Thereby, the use of electrons is not only reasoned by their comparably

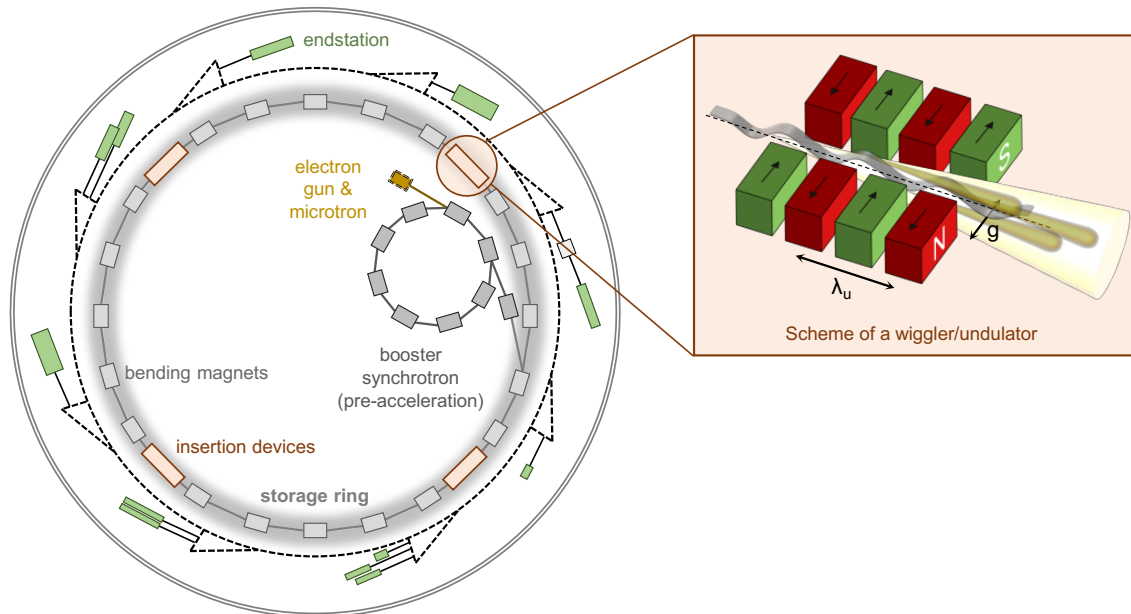
facile generation but also based on efficiency issues. Correspondingly, the energy loss  $\Delta E$  per each full turn is defined by:<sup>[221]</sup>

$$\Delta E = \oint S dt = \frac{e^2}{3\epsilon_0(m_0c^2)^4} \frac{E^4}{R}, \quad (2.8)$$

whereby for high-energetic electrons, the value amounts to approximately:

$$\Delta E [\text{keV}] = 88.5 \frac{E^4 [\text{GeV}^4]}{R [\text{m}]}. \quad (2.9)$$

For comparison, BESSY II in Berlin is operated at a maximum energy of 1.7 GeV, whereby the circumference of the booster synchrotron is 96 m and that of the affiliated actual storage ring 240 m. The general layout for synchrotron facilities is depicted in Scheme 2.2.



**Scheme 2.2:** Representation of a synchrotron radiation-facility consisting of an electron gun with microtron, a booster synchrotron as pre-accelerator, and the storage ring with corresponding insertion devices (see scheme of a wiggler/undulator); experiments are conducted at the respective endstations.

Electrons, emitted by an electron gun, are first linearly pre-accelerated to several million electron volts (MeV). Due to the oscillation of the electric field, the electrons are separated in temporally shifted bunches, which are adaptable for particular applications (*single-bunch* or *multi-bunch* modes). The acceleration to their expected energy is achieved in a dedicated booster synchrotron, after which they are transferred to the outer storage ring. Here, the operation in a quasi-stationary situation at a fixed energy is targeted, whereby the circular path is formed by bending magnets that act a perpendicular force on the electrons. The above-described energy decay through the emission of radiation and extrinsic scattering losses is

compensated by energy gains from radio frequency (RF) electric fields; these cavities are installed in the linear sections of the ring between the focusing and bending magnets. The electron bunches exhibit lifetimes in the order of several hours. Additionally, regular injections of electrons can be applied to keep the ring current constant (*top-up mode*).<sup>[222, 223]</sup>

Early synchrotron radiation sources only utilized bending magnets, whereby the large opening angle leads to a horizontally spread emission profile, especially disadvantageous for the requirement of small beam dimensions.<sup>[221]</sup> The next generation facilities employ *insertion devices* (IDs), namely multipole wigglers and undulators,<sup>[224]</sup> for radiation production, which are implemented between bending magnets that are still necessary for the deflection to a circular beam. Using IDs, the resulting brilliance has been increased by multiple magnitudes. The setup of a wiggler/undulator consists of an array of short dipole magnets with alternating polarity; the field along the axis is characterized by the period length  $\lambda_u$  and the gap distance  $g$  (see Scheme 2.2). The differentiation between a wiggler and an undulator is mainly attributed to the maximum beam deflection from the axis  $\varphi$ , i.e., the deflection angle per half pole. By multiplication of this parameter with the beam energy  $\gamma$ , the so-called strength parameter  $K$  is obtained, as follows:<sup>[219]</sup>

$$K = \gamma \times \varphi = \frac{ecB_0}{m_0c^2} \frac{\lambda_u}{2\pi} = 0.934 B_0 [T] \lambda_u [cm], \quad (2.10)$$

where, in addition,  $e$  is the elementary charge,  $m_0$  the particle mass,  $c$  the speed of light, and  $B_0$  the magnetic field. For  $K \lesssim 1$ , the insertion device is referred to as undulator, while values of  $K \gg 1$  describe wiggler magnets.<sup>[224]</sup> The emission spectra of wigglers are the composed superposition of the radiation of the individual poles, which number  $N$  thus determines the enhancement factor.<sup>[215]</sup> In undulators, the oscillating beam deflection is much smaller yielding more collimated radiation with higher brightness. For these conditions, also interference phenomena of the source points of light generation affect the observed radiation spectrum. Depending on the  $K$ -factor, only features of the fundamental peak and contributions of the first few harmonics are produced. Therefore, in contrast to wigglers, coherent light can be obtained for very small undulator parameters. Ideally, for a number of  $N$  periods, the brightness of the undulator light is a function of  $N^2$ ,<sup>[224]</sup> with a spectral width proportional to  $N^{-1}$ .<sup>[219]</sup> As outlined in the beginning, emitted radiation is also polarizable by adjusting the trajectory within the insertion device. According to requirements, next to linear polarization in the horizontal plane, variable motifs, e.g., vertical or elliptical,<sup>[225]</sup> are possible. On the way

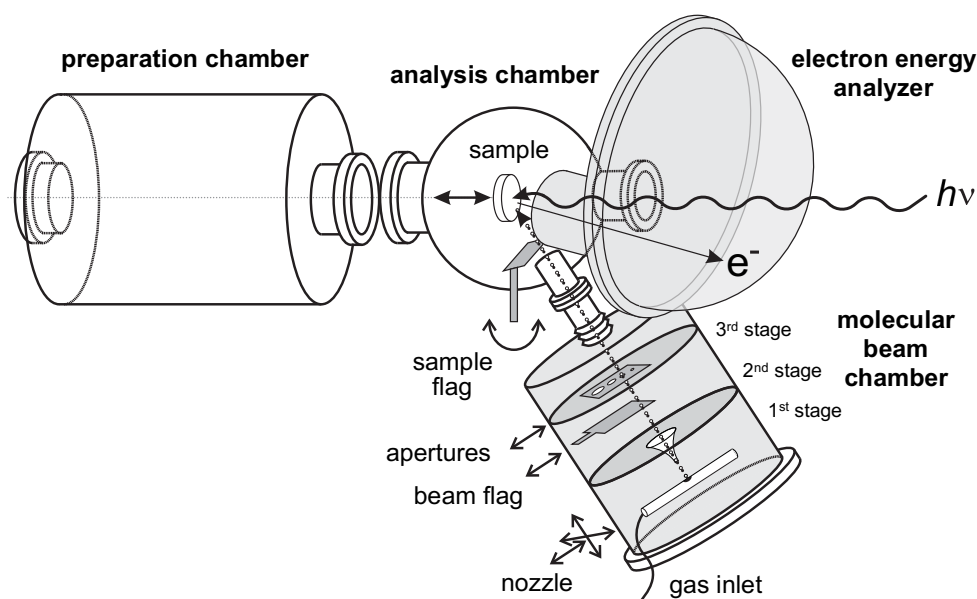
to the endstation of a beamline, where the experiments are conducted, the synchrotron radiation passes a monochromator and is eventually focused by a series of gratings, mirrors, and slits to a certain spot size.<sup>[226]</sup>

The numerous advantages of XPS experiments at a synchrotron radiation source were specified above, so that the *in situ* measurements for this thesis were performed at BESSY II (Berliner Elektronenspeicherring-Gesellschaft für Synchrotronstrahlung mbH) of HZB (Helmholtz-Zentrum Berlin für Materialien und Energie GmbH) in Berlin. For that, a transportable UHV apparatus was connected to respective open port beamlines, whereby the experimental setup is described in the next Section 3.1.

## 3 Experimental Section

### 3.1 Synchrotron Apparatus

For all XPS measurements, a transportable custom UHV apparatus was utilized. Its initial operation is described by Denecke *et al.*,<sup>[227]</sup> whereby a detailed description of the setup and characterization is given in the Ph.D. thesis of M. Kinne.<sup>[228]</sup> Mainly, the apparatus comprises the requirements for applications at synchrotron facilities as well as experiments based on laboratory sources. The overall layout is depicted in Scheme 3.1. Next to the separation into an analysis and preparation chamber, supersonic molecular beam techniques are implemented. In this way, time- and temperature-resolved investigations of surface processes are possible by *in situ* measurements.



**Scheme 3.1:** Setup of synchrotron apparatus comprising the preparation chamber, analysis chamber (with electron energy analyzer), and molecular beam chamber. Not true to scale; adapted from M. Kinne.<sup>[228]</sup>

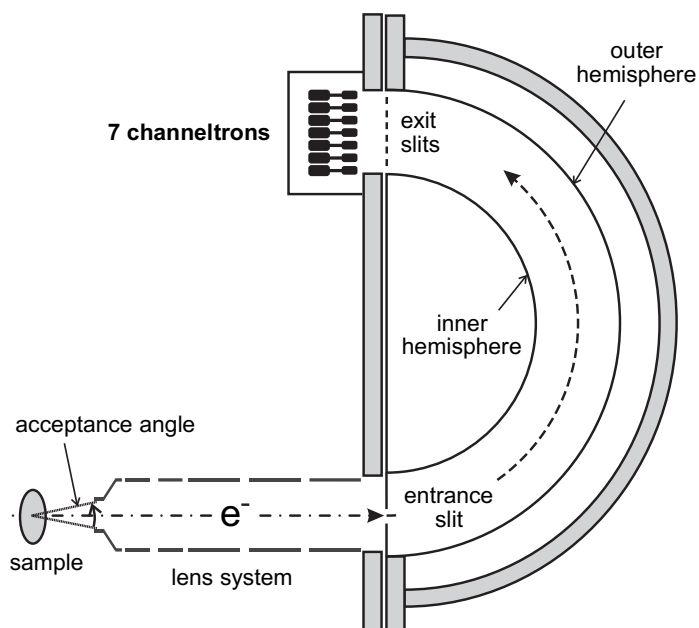
A multi-stage vacuum pumping system generates and maintains ultra-high vacuum (UHV) conditions that are necessary for a sufficiently high mean free path of the emitted photoelectrons towards the detector, and to ensure clean substrate surfaces on the needed timescale of the experiments. The *analysis chamber* is equipped with a hemispherical photoelectron energy analyzer (EA 125 U7 HR, Omicron), a partial electron yield detector for

NEXAFS (home-built),<sup>[229]</sup> and a quadrupole mass spectrometer (Prisma QME 200, Pfeiffer) for residual gas analyses or temperature-programmed desorption (TPD) experiments. As the apparatus is specifically designed for the operation at synchrotrons, a fluorescent screen simplifies the rough adjustment of collimated radiation on the sample. Besides, the attachment of a laboratory X-ray source (Mg & Al anodes) allows for measurements beyond beamtimes. Moreover, the utilization of a gas discharge lamp gives radiation in the UV range, e.g., employing He I emission. Separated by a gate valve, the *preparation chamber* houses an ion sputter gun (IQE 11/35, Specs), low-energy electron diffraction (LEED) optics (ErLEED, Specs), electron beam evaporators (Focus) for metal deposition, and a quartz crystal microbalance (SQC-160, Inficon) in order to monitor the deposition rate; with these facilities, cleaning of the surface and various sample preparation routes are feasible.

Arranged in an angle of 45° from underneath the analyzer, the *supersonic molecular beam* achieves local sample pressures of up to  $1 \times 10^{-5}$  mbar, while still maintaining a low background pressure by differential pumping. The adiabatic expansion of gases through a molybdenum nozzle generates the beam, which is then aligned by a skimmer and apertures on the way to the analysis chamber; a beam flag controls the on/off switching, and a sample flag in the analysis chamber allows for indirect exposure of the sample. In addition, a regular dosing system is connected to both chambers via a microcapillary array doser; for compounds with very low vapor pressure, an evaporator for organic molecules can be attached directly at the analysis chamber, yielding a facile exposure of the surface to the substances. Transferring and positioning of the sample is possible through an xyz-manipulator, enabling the further variation of both azimuthal and polar angle, i.e., rotary motion as well as tilting by up to 90° of the sample holder; thereon, the crystals are mounted by affixed tantalum wires. Temperature readings are provided by independent thermocouples (type K), spot-welded to the sample. A cryostat reaches temperatures of about 95 K with liquid nitrogen cooling, whereas heating is conducted resistively up to 1500 K. Hereby induced fields, however, deflect the photoelectron paths, so that an additional bifilar coiled tungsten filament behind the crystal enables radiative heating with minimized disturbances; in this way, temperature-programmed experiments were carried out up to 550 K.

### 3.2 Hemispherical Electron Energy Analyzer

The utilized analyzer, EA 125 U7 HR, commercially available by Omicron, detects the photoelectrons and determines their respective kinetic energy. The hemispherical setup of the device is illustrated in Scheme 3.2. The general function principle will be sketched shortly, whereby detailed considerations concerning the spectrometer design can be found elsewhere.<sup>[230, 231]</sup>



**Scheme 3.2:** Drawing of the electron energy analyzer Omicron EA 125 U7 HR; adapted from M. Kinne.<sup>[228]</sup>

Basically, the dispersion of the photoelectrons follows the geometrical layout of the electric field between the two concentric hemispherical electrodes. Depending on the kinetic energy, the electrons are forced on certain trajectories, and thus filtered accordingly.<sup>[232]</sup> Only electrons possessing a distinct pass energy  $E_p$  are focused along the equipotential surface, when the following relation for the applied voltages  $V_i$  and radii  $r_i$  of the hemispheres  $i$  is fulfilled:<sup>[233]</sup>

$$\Delta V = V_2 - V_1 = \frac{1}{e} E_p (r_2/r_1 - r_1/r_2), \quad (3.1)$$

whereby  $e$  is the elementary charge. For this specific setup, the mean radius of the electron trajectories amounts to 12.5 cm. Prior to entering the hemisphere, the photoelectrons, emitted from the sample within the acceptance angle of the analyzer, are focused and decelerated onto the entrance slit by a preceding lens system with a tunable magnification. As deduced in Equation 3.1, electrons with the set pass energy  $E_p$  reach the middle exit slit

and impinge on the channeltron (Burle) behind yielding a pulse of  $10^7$  to  $10^8$  secondary electrons; this signal is amplified and processed further. For slightly lower or higher energies, the trajectories of the electrons end at one of the outer slits. Here, the maximum energetic difference is about 10% of  $E_p$ . Electrons with more deviating kinetic energies exhibit greater deflections and are therefore not counted. The measurements were performed in constant analyzer energy (CAE) mode, i.e., the value of the pass energy  $E_p$  is kept constant, so that the energy range of the requested spectrum is obtained by scanning the retardation potential of the lens system. Next to intrinsic and instrumental factors, the chosen pass energy and slit sizes determine the total resolution.

### 3.3 Data Acquisition and Evaluation

All synchrotron radiation-based XPS experiments were conducted at BESSY II of HZB during multi-bunch top-up mode, at a constant ring current close to 300 mA. The in Section 3.1 described “Sync”-apparatus was used as end station at different open port beamlines, namely UE56/2-PGM1, UE56/2-PGM2, or U49/2-PGM1, with their corresponding specifications.<sup>[234]</sup> The spectra were recorded in normal emission, i.e., in an angle of  $0^\circ$  with respect to the surface normal, while the angle of the incident light was  $50^\circ$ . Depending on the beamlines, the parameters of the gratings and slit sizes were adjusted as needed. The excitation energies (1<sup>st</sup> or 3<sup>rd</sup> harmonic) were chosen according to the core levels of interest, 380 eV for C 1s, 500 eV for N 1s, and 650 eV for O 1s regions; normally, a CAE between 5 to 20 eV was used, yielding following spectral resolutions: 150-180 meV (C 1s), 220 meV (N 1s), and 250 meV (O 1s). The X-ray spot size was determined by experimental properties of the beamline, whereby the sample was shifted to a new position after every acquired spectrum to avoid or minimize beam damage or radiation-induced reactions due to the high photon flux of the synchrotron.

The thereafter presented experiments utilized a Ni(111) or Pt(111) single crystal (MaTeck) as substrate. The removal of surface contaminations was achieved by ion bombardment ( $\text{Ar}^+$ ,  $E = 1.0$  keV,  $I_s \sim 2$ -10  $\mu\text{A}$ ), with subsequent annealing step to 1200 K for surface reconstruction. Possibly remaining carbonaceous residues were eliminated by  $\text{O}_2$  dosage (10-20 sccm, direct or indirect) at 800-850 K and flashing to 1150-1200 K. Prior to each adsorption experiment, the cleanness of the respective substrate was assured by XPS check spectra. For the preparation of a well-ordered Au surface, a thin gold film was deposited on Pt(111) by

calibrated evaporation of 30 Å gold onto the crystal, followed by annealing at 770 K for 10 min; this surface structure is known to behave in photoemission experiments equivalent to Au(111).<sup>[235-237]</sup> The investigated organic molecules were synthesized and provided by the Chair of Organic Chemistry II at FAU in Erlangen. Freeze-pump-thaw cycles were carried out as an additional purification procedure before their direct exposure to the catalyst surface through the vapor pressure of the substances. Here, the final coverages of the various molecules can vary slightly, since different pumping speeds, sticking coefficients, and deviating base or dosing pressures complicate identical absolute exposures.

The adsorption at low temperatures between 110 and 150 K was followed *in situ* in dedicated experiments, in which the base pressure-corrected exposure is expressed in Langmuir [*L*], whereby  $1 L = 10^{-6} \text{ Torr} \times 1 \text{ s}$ .<sup>[238]</sup> Thereafter, the corresponding temperature-programmed experiments<sup>[169, 239]</sup> were started with a linear heating rate up to 550 K, having a typical value of  $\beta = 0.5 \text{ K/s}$ , and above by resistive heating. The acquisition time of one spectrum, determined by the binding energy range, the step size, and the dwell time, was adjusted as required.

The data evaluation and calibration of the surface coverage is demonstrated in Figure 3.1, whereby the software IGOR Pro 6.22A (WaveMetrics) was used for processing and presenting. As outlined in the fundamentals (see Section 2.1), the XP spectra are “Fermi corrected” by measuring and fitting the corresponding Fermi edge (insert in Figure 3.1a). The increase of the base line towards higher binding energies (see Section 2.1) is treated with the subtraction of a linear background (Figure 3.1b). Further applicable background corrections are described in literature.<sup>[240, 241]</sup> In a series of spectra, the background intensity can vary due to damping or decaying ring current, which is accounted for by rescaling the data to the first spectrum. Finally, the analysis of the spectra is carried out in a quantitative manner by introduction of a suitable fit model with single peak contributions to match the envelope of the measured data points (Figure 3.1c). The broadening of the linewidths of the obtained signals is defined by natural and instrumental factors (see Section 2.1). Since many effects lead to an asymmetry towards higher binding energy side, a convolution of Doniach-Šunjić profiles<sup>[242]</sup> and Gaussian functions is applied. In total, every fitted peak is characterized by its position, Gaussian width, Lorentzian width, and asymmetry factor, with customizable constraints.

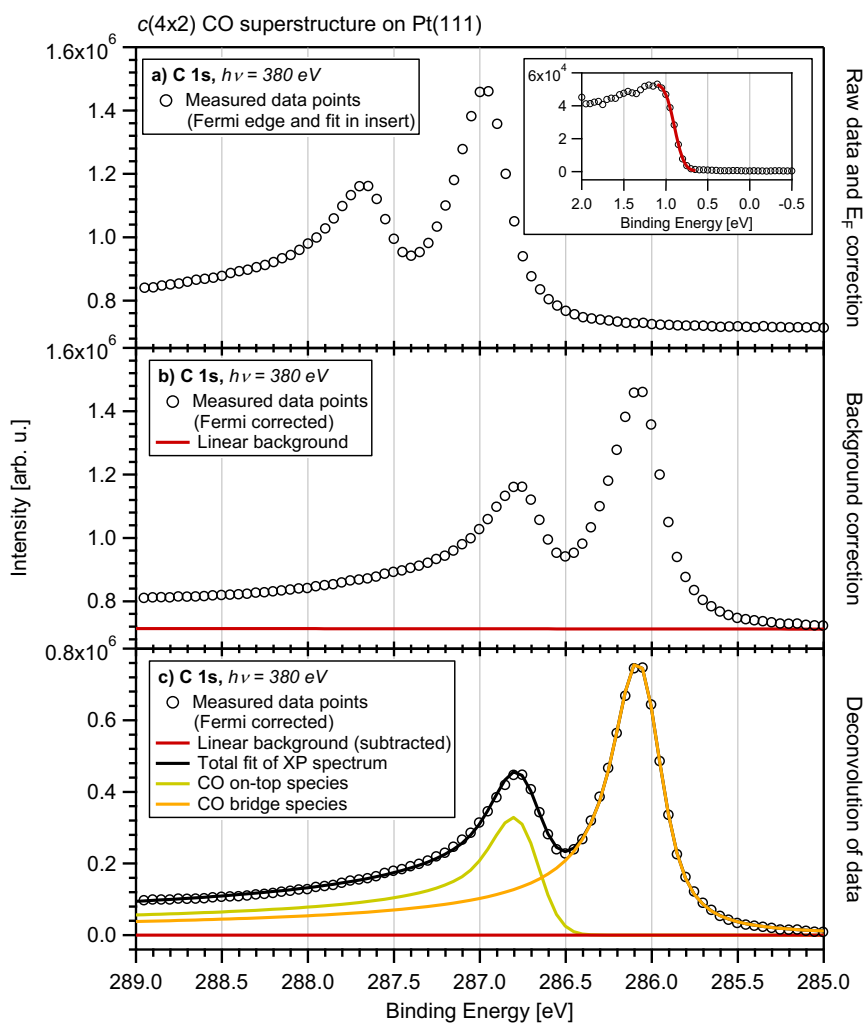


**Figure 3.1:** (a) Measured XPS data of the  $c(4 \times 2)$  CO superstructure on Pt(111) at low temperature ( $T = 120$  K) at beamline UE56/2-PGM1 (BESSY II) after a dosage of 2.2 L (2 sccm, indirect); Fermi edge with according fit is shown in insert. (b) Fermi corrected data points and corresponding linear background. (c) Reproduction of XP spectrum (Fermi and background corrected) by suitable peak contributions of on-top and bridge site species.

The quantitative nature of XPS, as discussed in Section 2.1, gives the advantage to ascertain the amounts of respective surface species. In practice, the reference to a system with well-known coverage for the identical measurement setup is convenient. Thus, the calibration factors were determined by means of following structures, whereby 1 monolayer (ML) corresponds to one adsorbed atom per surface atom: A saturated graphene layer on Ni(111)<sup>[243-245]</sup> contains two carbon atoms for every nickel atom resulting in a coverage of 2 ML. On Pt(111), the  $c(4 \times 2)$  superstructure of carbon monoxide (CO)<sup>[246-248]</sup> occupies 0.5 ML, with molecules adsorbed equally at on-top and bridge sites<sup>[249]</sup> (see Figure 3.1c). For molecules containing heteroatoms, the nitrogen or oxygen coverage was defined by considering the respective stoichiometric ratio of the chemical formula. Overall, the utilized experimental setup allowed for high-resolution XPS data during adsorption and thermal evolution of sophisticated organic compounds for potential energy storage applications.

## 4 Results of Publications

In the following, the results of the accepted publications in terms of this cumulative thesis are highlighted. Herein, the surface chemistry of differently substituted norbornadiene (NBD) and quadricyclane (QC) molecule pairs as possible molecular solar thermal (MOST) energy storage systems is addressed on model catalysts.

### 4.1 Contribution of the Authors

The described investigations follow initial studies of unsubstituted NBD/QC on Pt(111)<sup>[164]</sup> and Ni(111)<sup>[166]</sup> and of first derivatization with dibromo-NBD/QC on Ni(111)<sup>[167]</sup> by U. Bauer. In general, the acquisition of the measured XPS data at BESSY II was achieved by support from the co-workers within the synchrotron group of Prof. Papp. As the resulting journal articles, labeled as [P1] – [P4] (see Appendix), originated from collaborations with other work groups, a description of the single contributions is listed hereafter.

#### Journal Articles

**[P1]** *Surface Chemistry of the Molecular Solar Thermal Energy Storage System 2,3-Dicyano-Norbornadiene/Quadricyclane on Ni(111)*

F. Hemauer, U. Bauer, L. Fromm, C. Weiß, A. Leng, P. Bachmann, F. Düll, J. Steinhauer, V. Schwaab, R. Grzonka, A. Hirsch, A. Görling, H.-P. Steinrück, and C. Papp

– <https://doi.org/10.1002/cphc.202200199>

#### Contributions:

Authorship, XPS measurements (supported U. Bauer), data evaluation, manuscript (except DFT part); molecule syntheses by Chair of Organic Chemistry II (Prof. Dr. A. Hirsch); DFT calculations by Chair of Theoretical Chemistry (Prof. Dr. A. Görling).

**[P2]** *Surface Studies on the Energy Release of the MOST System 2-Carboxy-3-Phenyl-Norbornadiene/Quadricyclane (PENBD/PEQC) on Pt(111) and Ni(111)*

F. Hemauer, V. Schwaab, E. M. Freiberger, N. J. Waleska, A. Leng, C. Weiß, J. Steinhauer, F. Düll, P. Bachmann, A. Hirsch, H.-P. Steinrück, and C. Papp

– <https://doi.org/10.1002/chem.202203759>

#### Contributions:

Authorship, XPS measurements, data evaluation, manuscript; molecule syntheses by Chair of Organic Chemistry II (Prof. Dr. A. Hirsch).

**[P3]** *Au-Catalyzed Energy Release in a Molecular Solar Thermal (MOST) System: A Combined Liquid-Phase and Surface Science Study*

R. Eschenbacher<sup>+</sup>, F. Hemauer<sup>+</sup>, E. Franz, A. Leng, V. Schwaab, N. J. Waleska-Wellnhofer, E. M. Freiberger, L. Fromm, T. Xu, A. Görling, A. Hirsch, H.-P. Steinrück, C. Papp, O. Brummel, and J. Libuda

– <https://doi.org/10.1002/cptc.202300155>

Contributions:

Shared authorship, XPS measurements, data evaluation (XPS part), manuscript (XPS part); molecule syntheses by Chair of Organic Chemistry II (Prof. Dr. A. Hirsch); DFT calculations by Chair of Theoretical Chemistry (Prof. Dr. A. Görling); PEC-IRRAS and IRRAS parts by Chair of Interface Research and Catalysis (Prof. Dr. J. Libuda).

**[P4]** *Surface science and liquid phase investigations of oxanorbornadiene/oxaquadracyclane ester derivatives as molecular solar thermal energy storage systems on Pt(111)*

F. Hemauer, D. Krappmann, V. Schwaab, Z. Hussain, E. M. Freiberger, N. J. Waleska-Wellnhofer, E. Franz, F. Hampel, O. Brummel, J. Libuda, A. Hirsch, H.-P. Steinrück, and C. Papp

– <https://doi.org/10.1063/5.0158124>

Contributions:

Authorship, XPS measurements, data evaluation (XPS parts), manuscript (except PC-IRRAS part); molecule syntheses by Chair of Organic Chemistry II (Prof. Dr. A. Hirsch); PC-IRRAS part by Chair of Interface Research and Catalysis (Prof. Dr. J. Libuda).

## Review Article

**[P5]** *The Norbornadiene/Quadracyclane Pair as Molecular Solar Thermal Energy Storage System: Surface Science Investigations*

F. Hemauer, H.-P. Steinrück, and C. Papp

– <https://doi.org/10.1002/cphc.202300806>

Contributions:

Authorship, manuscript.

## 4.2 Dicyano-NBD/QC on Ni(111)<sup>[P1]</sup>

The derivatization of the norbornadiene/quadricyclane (NBD/QC) framework aims to optimize efficiencies and energy storage properties, as described in the introduction. The feasibility of promising molecular design on different catalyst materials is assessed by surface-sensitive probes. Herein, synchrotron radiation-based X-ray photoelectron spectroscopy (XPS) experiments were conducted to elucidate the surface chemistry of interesting NBD/QC derivatives. The investigation of the molecule pair 2,3-dicyano-norbornadiene/quadricyclane, (CN)<sub>2</sub>-NBD/QC, emerged as follow-up study of the spectroscopic characterization of first NBD/QC derivatives, namely the 2,3-dibromo-substituted system, Br<sub>2</sub>-NBD/QC.<sup>[167]</sup> Since latter molecules displayed partial dissociation upon adsorption on Ni(111), even at low temperatures of about 115 K, a higher stability of the attached cyano moieties and controlled energy release from the strained (CN)<sub>2</sub>-QC to (CN)<sub>2</sub>-NBD was anticipated. Moreover, in comparison, the storage density is considerably higher due to a smaller molecular weight ( $M_r = 142.16$ ), while the favorable redshift of the absorption onset of (CN)<sub>2</sub>-NBD was determined to be at least ~40 nm in relation to unsubstituted NBD.<sup>[99, 100, 151]</sup> In the following, information on the reaction behavior of (CN)<sub>2</sub>-NBD and (CN)<sub>2</sub>-QC on Ni(111) is presented in dedicated temperature-programmed XPS (TPXPS) experiments. As the introduced cyano groups contain nitrogen, the C 1s as well as the N 1s regions are addressed. These results<sup>[250]</sup> are published in [P1], whereby complementary DFT calculations were performed by L. Fromm (group of Prof. Görling), which regarded different adsorption geometries and their respective contributions to calculated core level shifts. The used molecules were synthesized and provided by C. Weiß and A. Leng (group of Prof. Hirsch).

### 4.2.1 XP spectra of the C 1s region

To begin with, the findings in the C 1s region are discussed. The adsorption experiment of (CN)<sub>2</sub>-NBD on Ni(111) at 130 K is depicted as waterfall plot in Figure 4.1a. Upon exposure of the clean single crystal to (CN)<sub>2</sub>-NBD, the *in situ* observation of the growing characteristic line shape of its XP spectra was monitored, yielding a final carbon coverage of 0.26 ML. This submonolayer range was chosen, since the reactions proceed at the catalyst surface; additional experiments with multilayer exposures are provided in the corresponding Supporting Information of [P1]. Fitting of the data led to the proposal of an according reaction model. The spectrum of (CN)<sub>2</sub>-NBD was reproduced by four peaks (see Figure 4.1c, green). The

complexity of the adsorbed molecule did not allow for an assignment to single carbon atoms. However, the spectral appearance is a unique fingerprint of the respective surface species. Notably, in contrast to  $\text{Br}_2\text{-NBD}$ ,<sup>[167]</sup> a non-dissociative adsorption was concluded and confirmed by DFT calculations and in the complementary N 1s region (see below). Analogously, the adsorption of  $(\text{CN})_2\text{-QC}$  on Ni(111) at 130 K is shown in Figure 4.1f. Here, a carbon coverage of 0.40 ML was achieved. The fit of the data points required again four peaks, yet with deviating peak positions, widths, and intensities. Thus, a clear spectroscopic distinction of both valence isomers was found upon adsorption on Ni(111) at low temperatures. Also for  $(\text{CN})_2\text{-QC}$ , there were no indications for dissociation of the molecules at contact with the surface. Information on adsorption geometries and a reconciliation of the experimental spectra with calculated core level shifts is addressed below in the DFT section.

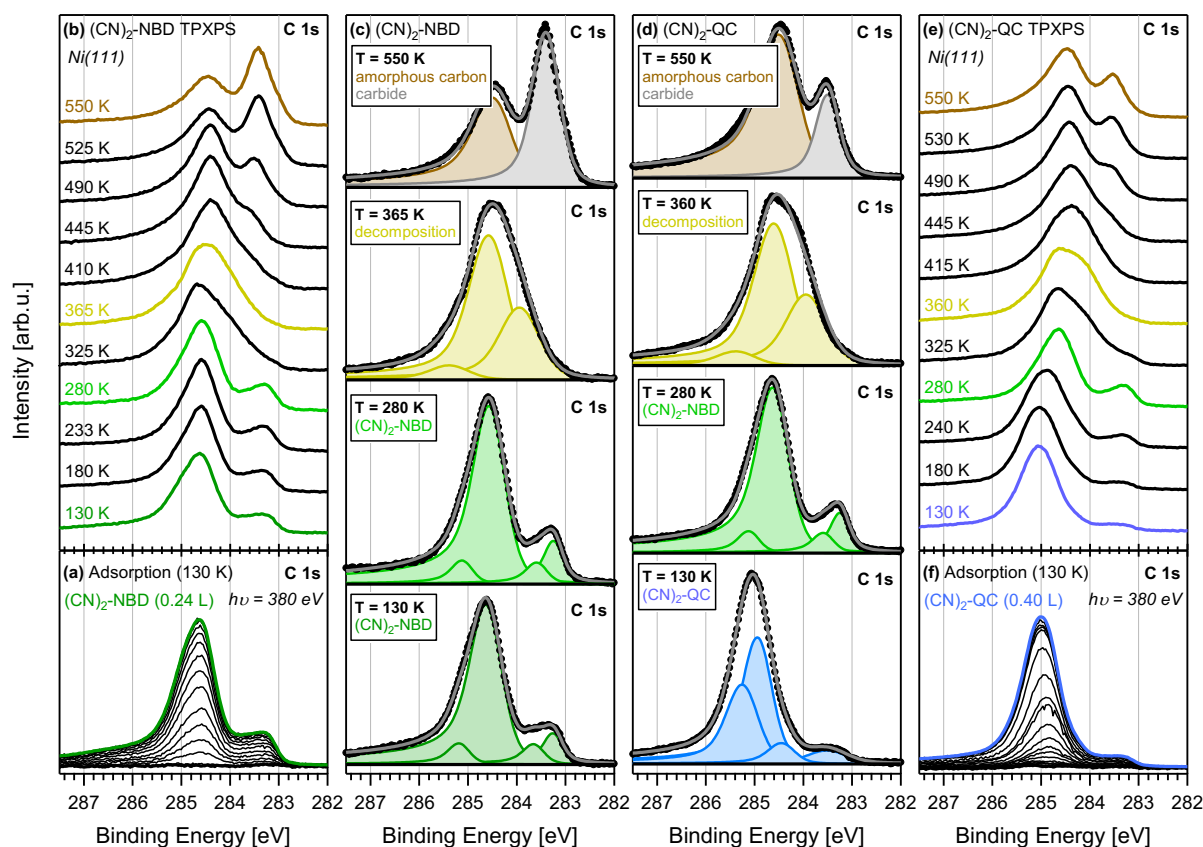


**Figure 4.1:** (a, f) C 1s spectra during exposure of Ni(111) to  $(\text{CN})_2\text{-NBD}$  and  $(\text{CN})_2\text{-QC}$  at 130 K; (b, e) Selected XP spectra of the respective temperature-programmed experiment (TPXPS) up to 550 K; (c, d) Representative surface species with corresponding fit model (color-coded). Whereas a spectroscopic distinction is possible upon adsorption (see 130 K), the identical spectral appearance at elevated temperatures (see 280 K) indicates the quantitative cycloreversion from  $(\text{CN})_2\text{-QC}$  to  $(\text{CN})_2\text{-NBD}$ . Reprinted with permission from Ref. [250]. Copyright (2022) John Wiley and Sons.

Selected spectra of the temperature-programmed XPS (TPXPS) experiments of  $(\text{CN})_2\text{-NBD}$  and  $(\text{CN})_2\text{-QC}$  are depicted in Figure 4.1b and 4.1e as waterfall plots, respectively. Representative surface species at comparable temperatures, with corresponding color-coded fits, are displayed in Figure 4.1c and 4.1d. The quantitative description of the thermal evolution considering all analyzed data in the C 1s region is given in Figure 4.2a and 4.2b as function of temperature. Starting with  $(\text{CN})_2\text{-NBD}$ , no spectral changes were observed up to 170 K. Only when heating higher, minor increases in intensities, especially for the peak at lowest binding energy, reflected a rearrangement<sup>[206, 251]</sup> of  $(\text{CN})_2\text{-NBD}$  into its thermodynamically most favored adsorption geometry. The decomposition onset of the molecular framework was determined at 290 K, when the broadening of the spectral line shape indicated the formation of C-H fragments<sup>[252-254]</sup> (see Figure 4.1c, yellow). Compared to unsubstituted NBD<sup>[166]</sup> and  $\text{Br}_2\text{-NBD}$  on Ni(111),<sup>[167]</sup> the derivatization with cyano substituents increased the thermal stability by almost 100 K. Heating to above 400 K yielded amorphous carbon<sup>[255-258]</sup> and carbide<sup>[243, 259, 260]</sup> (see Figure 4.1c, brown and gray).

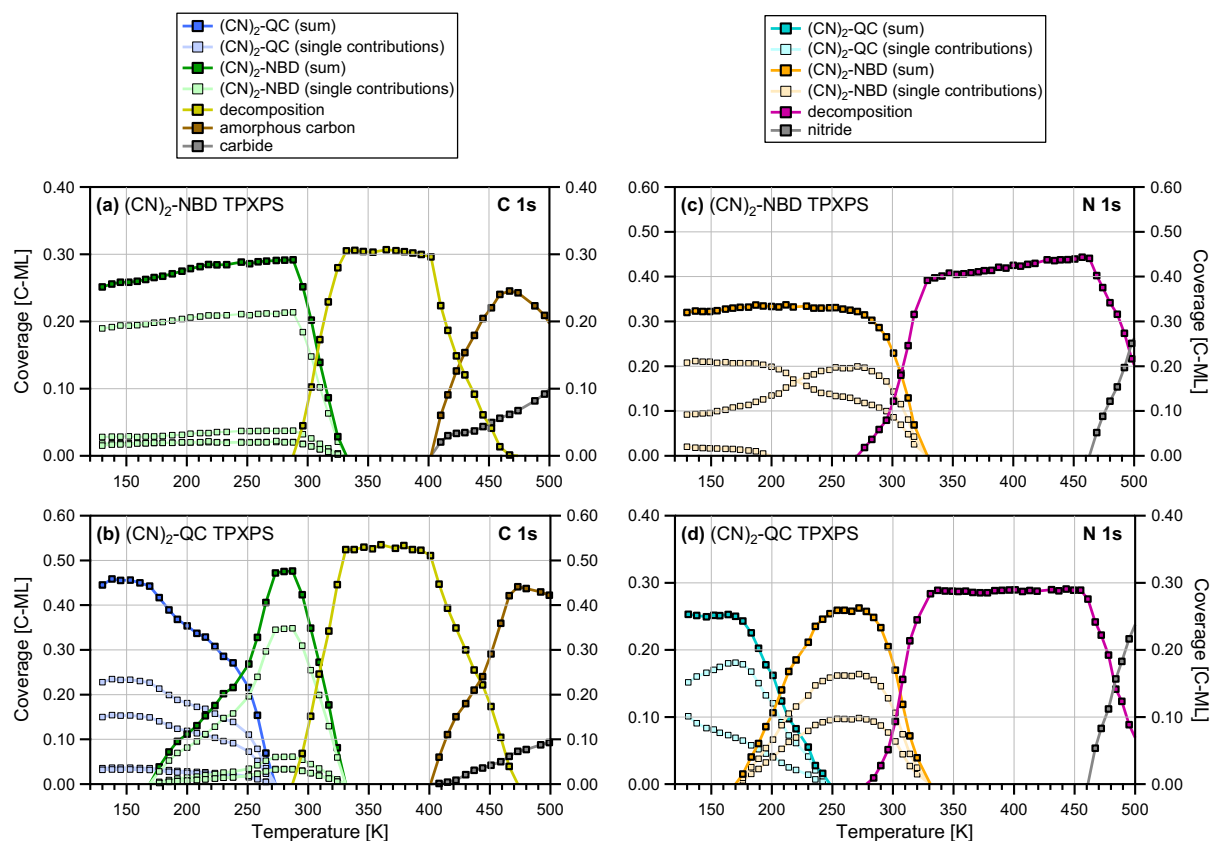


**Figure 4.2:** Quantitative description of surface species (coverage in monolayers) during TPXPS experiments of  $(\text{CN})_2\text{-NBD}$  and  $(\text{CN})_2\text{-QC}$  on Ni(111) as function of temperature (with a heating rate of 0.5 K/s): analysis in (a, b) C 1s region and (c, d) N 1s region; single contributions to the respective signal are depicted in light colors. Reprinted with permission from Ref. [250]. Copyright (2022) John Wiley and Sons.

In the case of (CN)<sub>2</sub>-QC, the spectra kept unchanged with the fixed fit parameters until reaching a temperature of 175 K. Above, the spectral appearance assimilated that of the (CN)<sub>2</sub>-NBD experiment, so that contributions of (CN)<sub>2</sub>-NBD evolved up to ~270 K at the expense of (CN)<sub>2</sub>-QC species (see Figure 4.2b). By comparison of the spectra at 280 K (see Figure 4.1c and 4.1d, green), the same fit parameters could be applied within the measurement accuracy. Therefore, the energy release in the cycloreversion reaction from the strained (CN)<sub>2</sub>-QC to (CN)<sub>2</sub>-NBD was found to proceed, between 175 and 260 K, in a quantitative manner without the detection of any side products. Thus, it was concluded that identical surface species existed on the surface, resulting in an equivalent decomposition pathway for the (CN)<sub>2</sub>-QC experiment at elevated temperatures. Note that the additional measurements with multilayer coverages verified the complete conversion from (CN)<sub>2</sub>-QC to (CN)<sub>2</sub>-NBD.

#### 4.2.2 XP spectra of the N 1s region

Next, results from the complementary N 1s region address the adsorption and reaction behavior of (CN)<sub>2</sub>-QC and (CN)<sub>2</sub>-NBD on Ni(111). Figure 4.3a depicts the XP spectra during exposure of Ni(111) to (CN)<sub>2</sub>-NBD at 130 K, yielding a total carbon coverage of 0.32 ML. The fit model (see Figure 4.3c, orange) required three peaks, which was unexpected as the two nitrogen atoms are arranged symmetrically in the molecular framework. Since multilayer formation was excluded, the multiple peaks indicated the existence of various adsorption sites and/or geometries. A non-dissociative adsorption was assured due to the absence of spectral features for cyanide fragments<sup>[261, 262]</sup> or atomic nitrogen.<sup>[263-265]</sup> Comparable amounts (0.25 ML) of the energy-rich isomer, (CN)<sub>2</sub>-QC, were adsorbed on Ni(111) at 130 K (see Figure 4.3f). Two peaks were used to describe the characteristic line shape this time (see Figure 4.3e, turquoise), while the necessity of more than one peak is again ascribed to diverse geometries and sites on the surface. Similar to the C 1s region (see above), the distinction of both molecules, (CN)<sub>2</sub>-NBD and (CN)<sub>2</sub>-QC, was possible on the base of the different spectral appearances at low temperatures.

Thermally induced reactions were also monitored in the N 1s region in the course of the respective TPXPS experiments. The corresponding waterfall plots, displaying selected spectra, are shown in Figure 4.3b and 4.3e, while Figure 4.3c and 4.3d illustrate the employed fit model. The quantitative analysis of the spectra gives the coverage of the representative surface species as function of temperature in Figure 4.2c and 4.2d. For (CN)<sub>2</sub>-NBD, the intensities of

the fitted peaks changed upon heating: At  $\sim 190$  K, the peak at lowest binding energy has vanished, while the middle peak became the most intense peak above 230 K (see Figure 4.2c). Whereas the total surface coverage stayed constant until 270 K, the two remaining peaks exhibited shifts by 70 meV towards lower binding energies (see Figure 4.3c, light orange). These spectral transformations were attributed to the rearrangement step, as proposed in the C 1s region. Since the nitrogen atoms are part of the attached cyano moieties, conformational changes are expected to be more pronounced in the N 1s region. Having heated to  $\sim 280$  K, the evolution of a new asymmetric peak (see Figure 4.3c, purple) marked the beginning decomposition, which is in good agreement to the C 1s data. The detachment of the cyano groups was suggested in this temperature range.<sup>[261, 262, 266, 267]</sup> Above 470 K, a broader contribution (see Figure 4.3c, gray) was assigned to nitride as product of further fragmentation.<sup>[252, 263, 264]</sup>

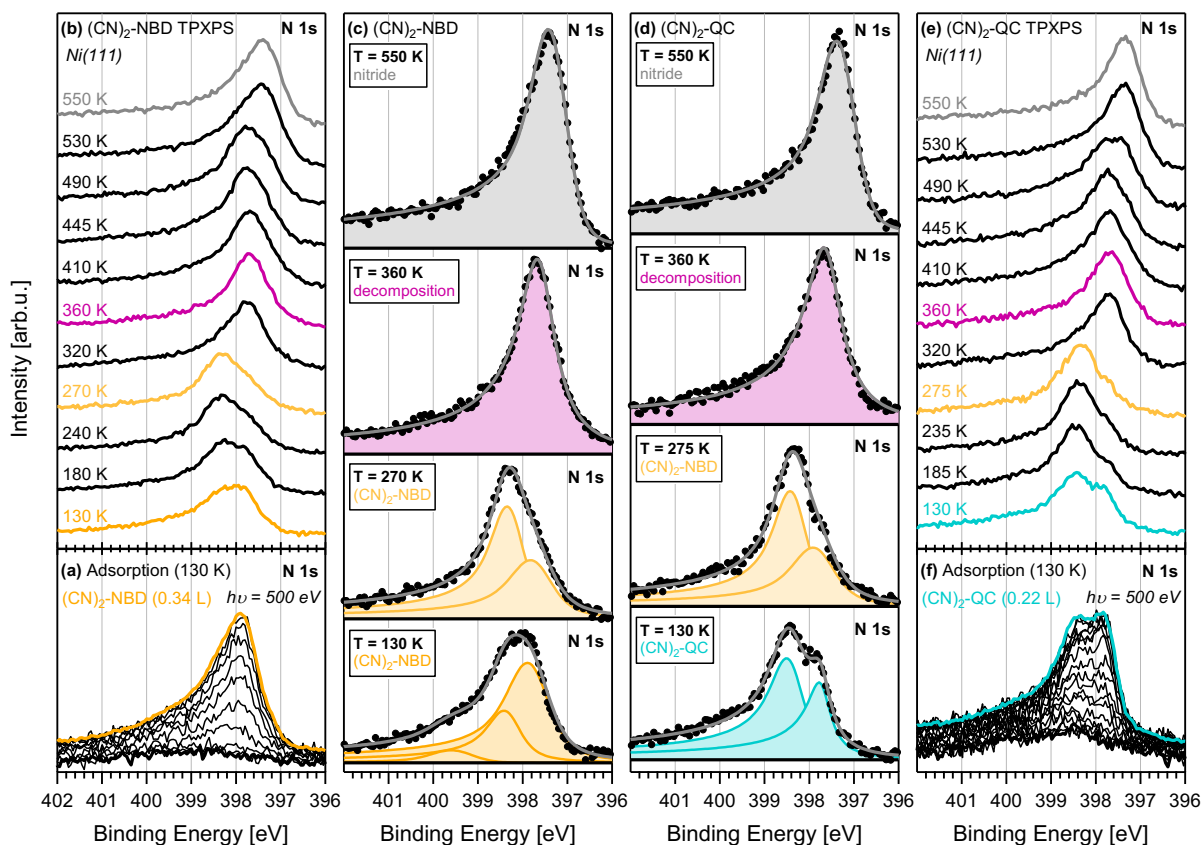


**Figure 4.3:** (a, f) N 1s spectra during exposure of Ni(111) to  $(\text{CN})_2\text{-NBD}$  and  $(\text{CN})_2\text{-QC}$  at 130 K; (b, e) Selected XP spectra of the respective temperature-programmed experiment (TPXPS) up to 550 K; (c, d) Representative surface species with corresponding fit model (color-coded). Whereas a spectroscopic distinction is possible upon adsorption (see 130 K), the identical spectral appearance at elevated temperatures (see 270/275 K) indicates the quantitative cycloreversion from  $(\text{CN})_2\text{-QC}$  to  $(\text{CN})_2\text{-NBD}$ . Reprinted with permission from Ref. [250]. Copyright (2022) John Wiley and Sons.

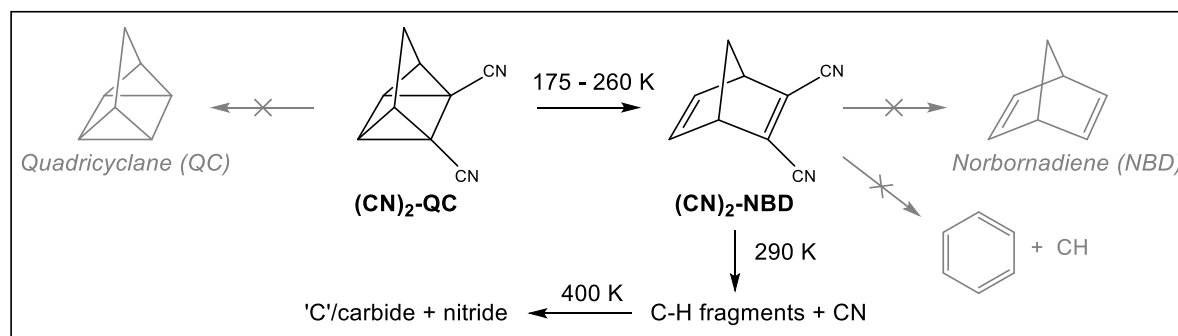
Considering the thermal evolution of (CN)<sub>2</sub>-QC, the overall coverage remained constant up to 170 K, while the peak at higher binding energy increased at the expense of that a lower binding energy. Above this temperature, the more narrow signal could be fitted with the identical fit parameters as for the (CN)<sub>2</sub>-NBD experiment (see Figure 4.3d, light orange). Thus, the back conversion from (CN)<sub>2</sub>-QC to (CN)<sub>2</sub>-NBD was confirmed in the N 1s region. The cycloreversion was completed at 250 K, yielding, upon further heating, the same decomposition species as for the (CN)<sub>2</sub>-NBD experiment.

#### 4.2.3 Supporting DFT calculations

Supporting DFT calculations were performed in order to gain insights into the adsorption geometries and to reveal the contributions to the respective spectral fingerprints. Due to previous results on the unsubstituted NBD/QC system,<sup>[164, 166]</sup> two different binding motifs were considered for the interaction of (CN)<sub>2</sub>-NBD with Ni(111): Next to a flat ( $\eta^2 : \eta^2$ ) geometry, where the two double bonds of NBD bind to the surface, a side-on ( $\eta^2 : \eta^1$ ) geometry describes the binding of the CH<sub>2</sub> bridgehead and only one double bond; moreover, different relative positions of the motifs to the surface were regarded. Unlike to Br<sub>2</sub>-NBD,<sup>[167]</sup> the smaller and more flexible cyano substituents allowed for a stronger interaction of the C=C double bonds with the surface. The highest adsorption energies were found for a “flat-like” adsorption of (CN)<sub>2</sub>-NBD (up to 4.0 eV), exceeding the values for the side-on geometry (~2.1 eV); the cyano moieties were preferential in a bridge position. The most stable structure of (CN)<sub>2</sub>-NBD involved the binding of the C=C bond with the cyano groups to a single surface atom, while the other side was bound to two nickel atoms. The adsorption at low temperature in the XPS experiments presumably caused the random sticking in one of the possible geometries to the surface. Supplying energy when heating, the activation barriers for the transition into the most stable adsorption motif could be overcome, explaining the initial rearrangement step that was observed in the evaluation of the TPXPS data.

For the more compact (CN)<sub>2</sub>-QC, the absence of double bonds in the molecular framework provided mainly interactions of the cyano moieties with the surface, which were preferably bound to nickel atoms at on-top sites. In contrast to (CN)<sub>2</sub>-NBD, both orientations revealed similar adsorption energies (1.8 eV): In the flat ( $\eta^2 : \eta^2$ ) motif, the hydrogen atoms of the four-membered ring displayed weak dispersion interactions with the surface, whereby the side-on ( $\eta^2 : \eta^1$ ) geometry showed a similar effect including the CH<sub>2</sub> bridgehead. The calculation of

relative core level shifts corroborated the spectral distinction of  $(\text{CN})_2\text{-QC}$  and  $(\text{CN})_2\text{-NBD}$  by means of their experimental XPS line shapes.



**Scheme 4.1:** Deduced reaction pathway of  $(\text{CN})_2\text{-QC}$  on Ni(111): energy release in quantitative cycloreversion to  $(\text{CN})_2\text{-NBD}$  between 175 and 260 K. Fragmentation of molecular framework above 290 K, with no formation of benzene and methylidyne; subsequent decomposition into carbon, carbide, and nitride species above 400 K. Reprinted with permission from Ref. [250]. Copyright (2022) John Wiley and Sons.

In conclusion, the surface chemistry of the molecule pair  $(\text{CN})_2\text{-NBD}$  and  $(\text{CN})_2\text{-QC}$  was investigated by high-resolution XPS measurements and DFT calculations. Upon adsorption on Ni(111) at 130 K, both molecules featured a unique spectroscopic fingerprint that enabled a distinction of the surface species, which was supported by simulated XP spectra. Whereas  $(\text{CN})_2\text{-NBD}$  adsorbed preferably in a flat ( $\eta^2 : \eta^2$ ) geometry,  $(\text{CN})_2\text{-QC}$  had similar adsorption energies for flat ( $\eta^2 : \eta^2$ ) and side-on ( $\eta^2 : \eta^1$ ) motifs. Upon heating, the rearrangement of  $(\text{CN})_2\text{-NBD}$  into its thermodynamically most stable geometry was suggested. The reaction pathway of  $(\text{CN})_2\text{-QC}$  is shown in Scheme 4.1: The conversion to  $(\text{CN})_2\text{-NBD}$  was triggered at 175 K and completed at 260 K with no side product formation. Above 290 K, the decomposition of the molecular framework occurred, yielding CH-fragments and detached cyano moieties. Finally, carbon structures, carbide, and nitride residues remained above 400 K. This study illustrated the advantages of the used dicyano-substituted derivatives, which achieved a quantitative energy release and offered a high thermal stability of the energy-lean isomer.

Adapted with permission from Ref. [250]. Copyright (2022) John Wiley and Sons.

### 4.3 PENBD/PEQC on Pt(111) and Ni(111)<sup>[P2]</sup>

The phenyl-ester substitution of the NBD/QC framework, yielding the valence isomers 2-carbethoxy-3-phenyl-norbornadiene/quadricyclane, referred to as PENBD and PEQC, was found to exhibit favorable properties upon characterization that qualifies the molecule pair for potential applications as MOST system. PENBD showed a bathochromic shift of its absorption onset to 359 nm, while the photoconversion proceeded quantitatively at a sufficient quantum yield ( $\Phi_{310nm} = 71\%$ ) without any sensitizer.<sup>[268]</sup> The formed PEQC displayed a pronounced thermal stability (half-life of 450 days at 25 °C), especially compared to similar push-pull substituted derivatives. Still, a high energy storage capacity of 367.5 kJ kg<sup>-1</sup> was achieved with an exothermic reaction profile ( $\Delta H = 88.3$  kJ mol<sup>-1</sup>) and a reasonably low molecular weight ( $M_r = 240.30$ ).<sup>[269]</sup> For this reason, the surface chemistry of this promising system PENBD/PEQC was assessed in synchrotron radiation-based XPS measurements. Herein, Pt(111) and Ni(111) were chosen as respective model catalytic surfaces, on which previous NBD/QC systems have already been investigated.<sup>[164, 166, 167, 250]</sup> Due to the ester substituent, the C 1s and O 1s regions gave complementary insights into the adsorption and reaction behavior. In the experiments, submonolayer coverages enabled the observation of surface reactions without the influence of physisorbed layers. These results<sup>[270]</sup> are published in [P2], whereby the molecule syntheses were carried out by A. Leng and C. Weiß (group of Prof. Hirsch).

#### 4.3.1 PENBD/PEQC on Pt(111)

First, the adsorption of PENBD and PEQC on Pt(111) is addressed, which revealed a high catalytic activity for the unsubstituted NBD/QC system.<sup>[164]</sup> Figure 4.4a depicts the exposure of the surface to the energy-rich PEQC at 125 K. The waterfall plot illustrates the growth of the characteristic line shape of the species, yielding a final carbon coverage of 0.39 ML. Fitting of the measured data points required four peaks, with a fixed relative intensity ratio (see Figure 4.4c, red). The overlapping peaks did not allow for an explicit deconvolution of the XP spectrum to single carbon atoms within the molecular structure. Nevertheless, contributions at higher binding energies were suggested to stem from the oxygen atoms of the ester group.<sup>[271]</sup> In addition, the binding energy range of unsubstituted QC<sup>[164]</sup> and benzene on Pt(111)<sup>[272]</sup> coincided with the remaining peaks. For the energy-lean PENBD, the adsorption of a comparable amount (0.25 ML) on Pt(111) at 125 K is shown in Figure 4.4f. Although the

obtained line shapes of both isomers appeared quite similar, the fit model of PENBD needed different parameters; specifically, deviating intensity ratios had to be employed, the peak widths differed, and also the positions were shifted to lower binding energies by up to 200 meV (see Figure 4.4d, blue). The assignment of the signals was deduced, as before, from the superposition of the influences by the ester moiety, the phenyl substituent, and the NBD subunit. Altogether, the molecular adsorption of PENBD and PEQC was monitored *in situ* in the C 1s region, whereby a spectroscopic distinction was possible by means of the corresponding line shapes of the spectra.

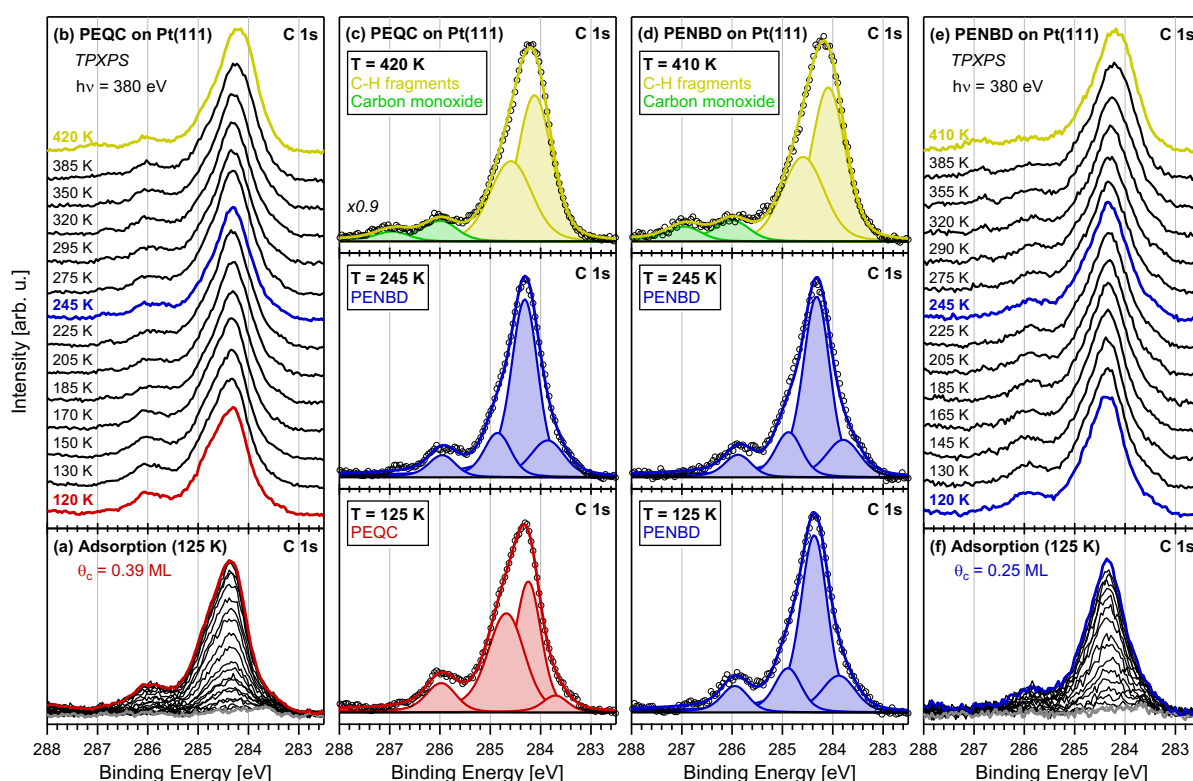


**Figure 4.4:** (a, f) C 1s spectra during exposure of Pt(111) to PEQC and PENBD at 125 K; (b, e) Selected XP spectra of the respective temperature-programmed experiment (TPXPS) up to 420 K; (c, d) Representative surface species with corresponding fit model (color-coded). Whereas a spectroscopic distinction is possible upon adsorption (see 125 K), the identical spectral appearance at elevated temperatures (see 245 K) indicates the quantitative cycloreversion from PEQC to PENBD. Note different scaling factor in (c). Reprinted with permission from Ref. [270] under license CC BY 4.0 DEED. Copyright (2023) John Wiley and Sons.

The thermal evolution of the molecular pair was followed in dedicated temperature-programmed XPS (TPXPS) experiments. Figure 4.4b and 4.4e display spectra at selected temperatures, while the representation of the fitted surface species (color-coded) is shown in Figure 4.4c and 4.4d, respectively. The quantitative analysis of the TPXP spectra of PEQC is given in Figure 4.5, with the schematic description of the proposed reaction pathway on Pt(111). Up to 140 K, no changes in the spectral appearance were observed. Having heated

further, the shoulder at higher binding energy declined and the maximum of the spectrum gained in intensity. That is, the line shape assimilated towards that of PENBD, indicative of the onset of the cycloreversion from the strained PEQC to PENBD. In the temperature range between 140 and 230 K, the amount of PEQC was decreasing at the expense of formed PENBD, while the total surface coverage stayed constant (see Figure 4.5).

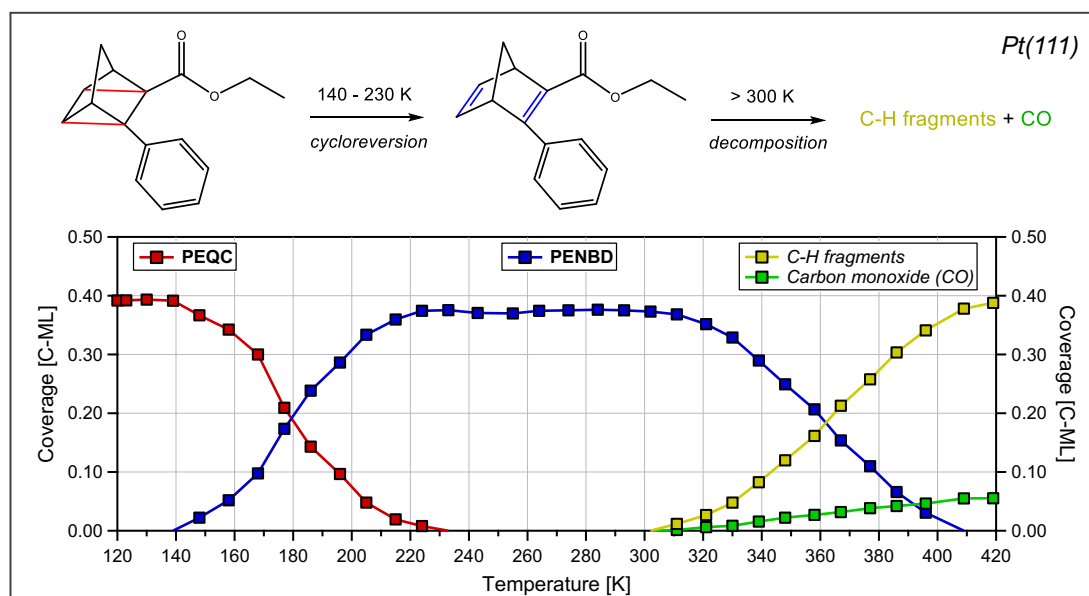


**Figure 4.5:** Quantitative description of the surface species (coverage in monolayers) during the TPXPS experiment of PEQC on Pt(111) in the C 1s region as function of temperature (with a heating rate of 0.5 K/s): energy release in quantitative cycloreversion to PENBD between 140 and 230 K; decomposition of molecular framework above 300 K, resulting in C-H fragments and carbon monoxide (CO). Reprinted with permission from Ref. [270] under license CC BY 4.0 DEED. Copyright (2023) John Wiley and Sons.

At 245 K, the same fit parameters could be applied as for the equivalent spectrum of the PENBD experiment (see Figure 4.4c and 4.4d, blue). Thus, identical surface species were present on the surface, and a quantitative conversion was concluded as no side products were detectable. Unlike to unsubstituted QC on Pt(111),<sup>[164]</sup> where the cycloreversion to NBD took place instantaneously upon adsorption at 125 K due to the high catalytic activity, the reaction proceeded in a controlled manner at higher temperatures for PEQC. As PENBD was the sole surface species above 230 K, the subsequent decomposition route was found to be analogous to the PENBD experiment. Here, the thermal stability limit was determined at 300 K, contrasting the degradation of unsubstituted NBD on Pt(111) at already 190 K.<sup>[164]</sup> The different reaction behavior indicated the adsorption in a geometry deviating from the side-on motif, for which a norbornadienyl species was formed. Above 300 K, unspecified C-H fragments<sup>[164, 169]</sup> were obtained as dissociation products (see Figure 4.4c, yellow); the amount of evolved

carbon monoxide (CO)<sup>[246]</sup> agreed with the stoichiometric formation of two equivalents (see Figure 4.4c, green).

The experiments in the O 1s region corroborated the stability limit of the molecular framework of PENBD, since no fragmentation of the ester moiety was observed at low temperatures. The formation of carbon monoxide (CO) was monitored at bridge and on-top sites<sup>[246]</sup> at elevated temperatures, which supports the reaction pathway deduced from the C 1s data. However, the coadsorption of water<sup>[273]</sup> upon exposure of Pt(111), and the low oxygen content, impeded to draw conclusions on the cycloreversion reaction. Moreover, the oxygen atoms in the ester substituent are remote from the carbon bonds that were involved in the rearrangement reaction. In general, the poor signal-to-noise ratio did not allow for an unambiguous spectral distinction of both valence isomers, PENBD and PEQC, in the O 1s spectra. Nonetheless, two peaks with almost identical height were assigned to the two oxygen atoms in different chemical environment.<sup>[271]</sup>

#### 4.3.2 PENBD/PEQC on Ni(111)

Analogously, adsorption and temperature-programmed experiments were conducted on Ni(111), which was found to be less reactive than Pt(111) for the unsubstituted NBD/QC system but catalytically active in terms of a controlled energy release at higher temperatures;<sup>[166]</sup> besides, next to the successful triggering of the conversion reaction, a high thermal stability was achieved for dicyano-substituted NBD/QC on Ni(111).<sup>[250]</sup> Within the scope of this study, the same molecule pair, PENBD and PEQC, was directly compared on both Pt(111) and Ni(111). The adsorption of PEQC on Ni(111) at 115 K is depicted in Figure 4.6a, whereby the carbon coverage amounted to 0.29 ML; note small intensities prior to dosage (gray spectrum) due to preadsorption of residual PEQC in the chamber. Four peaks were needed to reproduce the characteristic line shape (see Figure 4.6c, red), while their relative intensities were kept constant. As before, no explicit assignment to single carbon atoms was possible but the spectroscopic fingerprint was determined. The contributions to the measured signal were reconciled by comparison with spectra of unsubstituted NBD<sup>[166]</sup> and benzene on Ni(111),<sup>[274]</sup> plus considering the influence of the ester moiety. Although the binding energy positions of PEQC are comparable on Pt(111) and Ni(111), the relative intensities and the peak widths differed considerably. The exposure of Ni(111) at 120 K to PENBD yielded a carbon coverage of 0.42 ML. Small amounts of carbide<sup>[259]</sup> were detected from the beginning and

treated as a constant contribution throughout the experiment (see Figure 4.6d, brown). The overall line shape of PENBD, possessing two marked maxima, differed substantially from that of PEQC. In the fit model, four peaks with fixed intensity ratio were utilized, which were positioned up to 800 meV towards higher binding energies (see Figure 4.6d, blue). In contrast to the adsorption on Pt(111), both isomers exhibited a very different spectral appearance. Due to the similar molecular structures, the existence of various adsorption geometries was suggested, which are discussed later in the O 1s section.

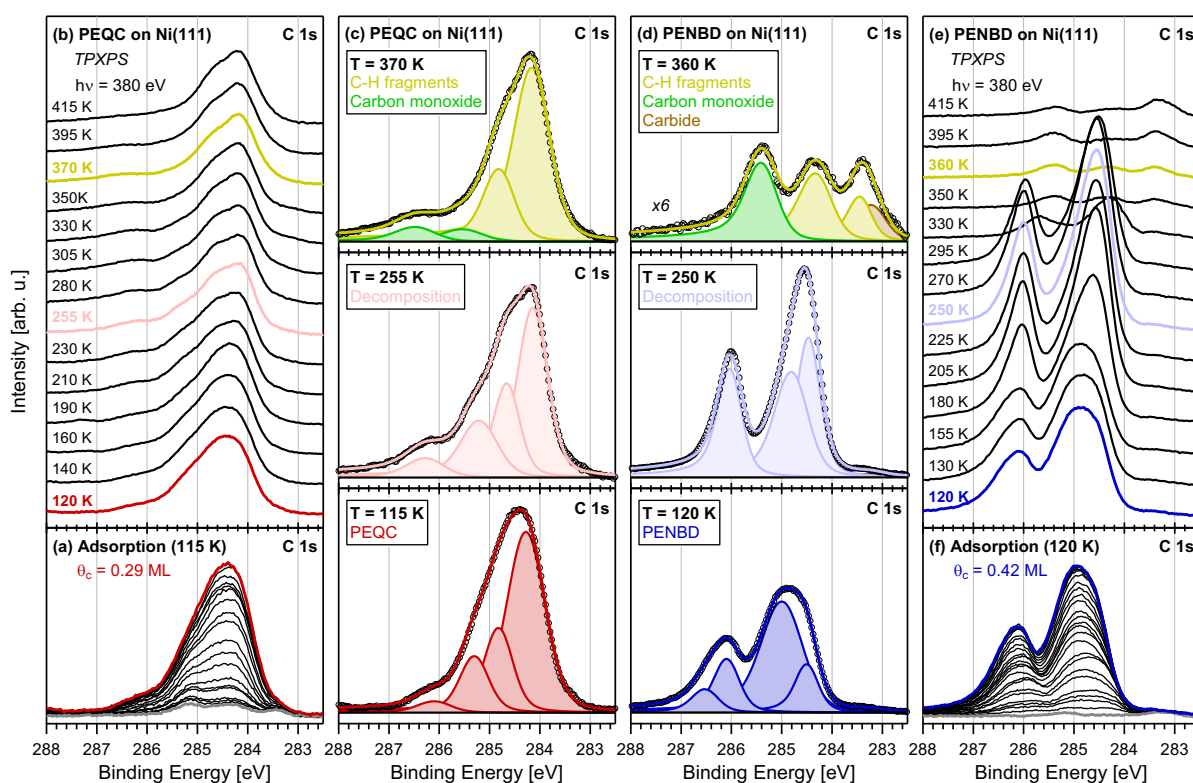


**Figure 4.6:** (a, f) C 1s spectra during exposure of Ni(111) to PEQC and PENBD at 115/120 K; (b, e) Selected XP spectra of the respective temperature-programmed experiment (TPXPS) up to 415 K; (c, d) Representative surface species with corresponding fit model (color-coded). A spectroscopic distinction is possible upon adsorption (see 115/120 K); the absence of spectral features of PENBD in the PEQC experiment indicates no cycloreversion to PENBD at any temperature. Note different scaling factor in (d). Reprinted with permission from Ref. [270] under license CC BY 4.0 DEED. Copyright (2023) John Wiley and Sons.

Selected TPXP spectra of PENBD and PEQC are plotted in Figure 4.6b and 4.6e, respectively. The corresponding fitted surface species (color-coded) are depicted in Figure 4.6c and 4.6d. For PEQC, major changes in the spectra became visible only above 180 K, when the peak positions shifted to lower binding energies and the narrowing of the line shape required for other signals, especially pronounced for the peak at lowest binding energy (see Figure 4.6c, light red). This was attributed to the rearrangement of the molecules into more stable adsorption motifs, as observed for  $(\text{CN})_2\text{-NBD}$ ,<sup>[250]</sup> and/or the early onset of a decomposition

reaction,<sup>[275, 276]</sup> which would be similar to unsubstituted NBD<sup>[166]</sup> and Br<sub>2</sub>-NBD on Ni(111).<sup>[167]</sup> By comparison of both temperature-programmed experiments of PENBD and PEQC, the acquired spectra deviated profoundly. That is, different surface species were present at any temperature, excluding the energy release in a cycloreversion reaction from PEQC to PENBD on Ni(111). Above 270 K, the fragmentation of the molecular framework<sup>[254, 277]</sup> and the formation of two equivalents of carbon monoxide (CO), in bridge and on-top positions,<sup>[278]</sup> was monitored (see Figure 4.6c, yellow and green). In the case of PENBD, intact molecules were found up to 160 K. At higher temperatures, the occurrence of the first reaction step was deduced from a new spectral appearance with three fitted peaks (see Figure 4.6d, light blue). The decomposition of PENBD, presumably with the detachment of the ester moiety,<sup>[279]</sup> was observed as a distinct shift in the O 1s region (see below). Unlike to unsubstituted NBD<sup>[166]</sup> and Br<sub>2</sub>-NBD,<sup>[167]</sup> no benzene or methylidyne were formed as intermediates.<sup>[205, 274]</sup> Note that for the appearance of new surface species, different attenuation and photoelectron diffraction conditions resulted in the observation of varying total coverages.<sup>[206, 251]</sup> Having heated to 280 K, the pronounced desorption of almost 90% of the surface coverage set in, which was due to a weakly bound adsorption geometry (see O 1s section). Above 340 K, small amounts of C-H fragments and CO, at bridge site, were remaining (see Figure 4.6d, yellow and green).

The experiments in the O 1s region gave complementary information on the adsorption and reaction properties. In these measurements, comparable amounts were adsorbed on Ni(111) at 120 K. The collected data were evaluated analogously to the previous investigations. For both PENBD and PEQC, the coadsorption of water during exposure of the surface was unavoidable, yielding a corresponding peak<sup>[280, 281]</sup> that vanished above the desorption temperature between 140 and 180 K.<sup>[281]</sup> Apart from this, the PEQC spectrum featured two distinct peaks, with equal area, attributed to the two oxygen atoms of the ester moiety, namely the carbonyl (C=O) and ether (C–O–C) oxygen.<sup>[271, 279, 282]</sup> The O 1s spectrum of PENBD was fitted with three peaks at a fixed intensity ratio of 1 : 2 : 1, ascribed to different binding fashions that were enabled through the flexible ester moiety:<sup>[283, 284]</sup> The two peaks with identical area displayed the situation of one binding and non-binding oxygen atom, while the middle peak described the binding of both oxygen atoms resulting in a similar chemical environment.<sup>[282]</sup> In general, the peak positions of PENBD were shifted to lower binding energies compared to PEQC. That is, PENBD exhibited a stronger interaction of the oxygen atoms with the Ni(111) surface, whereas PEQC was proposed not to bind via its oxygen

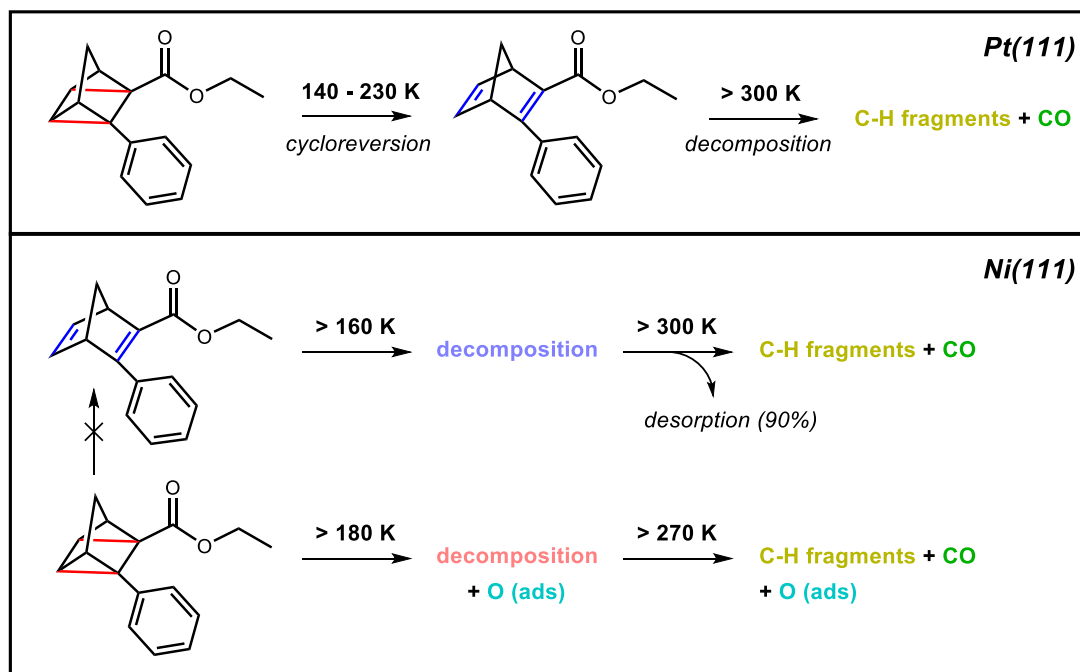
atoms.<sup>[282]</sup> These different adsorption motifs explained the very distinct spectral appearance of the molecule pair in both core level regions. Besides, the extensive desorption for PENBD above 270 K originated from the weak Ni-oxygen interaction.<sup>[285]</sup> The TPXPS experiment of PEQC in the O 1s region revealed a narrow peak at low binding energies above 180 K, which was characteristic for atomic oxygen.<sup>[275, 278, 286]</sup> Therefore, the remaining peaks indicated the decomposition of PEQC, while CO contributions (at bridge site)<sup>[278]</sup> emerged at 280 K, in agreement with the findings of the C 1s spectra. For PENBD, at 160 K, a marked shift of 1.3 eV towards lower binding energy corresponded to the spectral changes in the C 1s region. As this reaction involved the oxygen atoms, the detachment or fragmentation of the ester group was suggested.<sup>[276]</sup> The formation of CO in bridge position was confirmed above 280 K as well as the pronounced desorption, leaving about 16% of the initial surface coverage (in C 1s experiment: 13%, see above).

#### 4.3.3 Comparison of PENBD/PEQC on Pt(111) and Ni(111)

The surface chemistry of PENBD and PEQC was investigated by high-resolution XPS on different model catalytic surfaces. Their exposure to the molecules at low temperatures was followed *in situ*, whereby both isomers were spectroscopically differentiated, and qualitative information on the adsorption geometries was derived. Temperature-programmed experiments allowed for the determination of stability limits and to check if the energy release from the strained PEQC to PENBD was triggered. On Pt(111), it was suggested that the species occupied a similar adsorption geometry. In the case of Ni(111), distinct configurations were deduced on the surface: PEQC was predicted to interact predominantly by its QC subunit and the phenyl substituent, whereas, for PENBD, the orientation of its ester moiety towards the surface was expected, implying a weaker “oxygen-bound” motif.

The reaction pathways on either surface are depicted in Scheme 4.2. The Pt(111) surface was found to initiate the cycloreversion reaction from PEQC to PENBD starting at 140 K, with a quantitative conversion at 230 K. Above 300 K, the decomposition into C-H fragments and CO took place, marking the stability limit of the energy-lean isomer, which exceeds that of unsubstituted NBD by more than 100 K.<sup>[164]</sup> In contrast, Ni(111) showed no catalytic activity for the back conversion to PENBD. Instead, individual fragmentation routes of PENBD and PEQC were observed, when heating above 160 and 180 K, respectively. Notably, for PENBD on Ni(111), about 90% of the surface coverage has desorbed above 300 K, which was attributed

to the weak surface interaction of the adsorbed species. That is, only residual amounts of C-H fragments and CO remained at higher temperatures. The TPXPS experiment of PEQC stated further the formation of atomic oxygen above the decomposition onset.



**Scheme 4.2:** Deduced reaction pathways of PEQC and PENBD: (top) On Pt(111), energy release in quantitative cycloreversion to PENBD between 140 and 230 K; decomposition above 300 K yields C-H fragments and carbon monoxide (CO). (bottom) On Ni(111), no cycloreversion from PEQC to PENBD but degradation above 160 and 180 K, respectively; subsequent fragmentation above 270 K for PEQC, and pronounced desorption above 300 K for PENBD. Reprinted with permission from Ref. [270] under license CC BY 4.0 DEED. Copyright (2023) John Wiley and Sons.

In conclusion, this study demonstrated that the adsorption behavior and reactivity of derivatized NBD/QC molecules depends crucially on the used catalyst material. Utilizing Pt(111), the energy release from PEQC was induced in a controlled and quantitative manner; moreover, a high thermal stability limit was determined in the experiments. On Ni(111), the cycloreversion to PENBD was not detected; yet, the found correlation between adsorption geometries and desorption processes was ascertained to be of importance in heterogeneous catalysis for the design of reversible MOST cycles.

*Adapted with permission from Ref. [270] under license CC BY 4.0 DEED. Copyright (2023) John Wiley and Sons.*

## 4.4 PENBD/PEQC on Au<sup>[P3]</sup>

The promising molecule pair 2-carbethoxy-3-phenyl-norbornadiene/quadricyclane (PENBD/PEQC) regarding MOST applications, whose surface chemistry has been discussed on Pt(111) and Ni(111) before (see Section 4.3),<sup>[270]</sup> is now addressed on a gold surface as catalyst material. Previous liquid-phase studies on asymmetrically substituted cyano derivatives<sup>[287]</sup> showed an unprecedented catalytic activity of Au(111) for the energy-releasing cycloreversion reaction to the respective NBD derivative; in direct comparison to Pt(111), the reaction rates of the back conversion were more than two orders of magnitude higher under identical conditions. Besides, investigations on a functionalized NBD/QC system, which was anchored by an appropriate platform on Au(111),<sup>[288]</sup> revealed the direct cycloreversion to the energy-lean isomer in a single monolayer in UHV environment. The authors concluded the electronic coupling to the gold states of the substrate as requirement for the catalytic effect. These findings agreed with the single-triplet mechanism proposed by Schlimm *et al.* for enhanced isomerization kinetics on gold, wherein a mediated intersystem crossing was found to be crucial in the relaxation process.<sup>[289]</sup> That is, the facile triggering of the energy release on gold is also of interest in terms of the MOST storage cycle for the established PENBD/PEQC pair. In the following, the reaction behavior of PENBD and PEQC on Au(111) is surveyed in a combined liquid-phase and surface science study. Thereby, the determined catalytic activity was put into context with the deduced mechanistic insights. These results<sup>[290]</sup> are published in [P3]. In particular, infrared reflection absorption spectroscopy (IRRAS) experiments in UHV, performed by R. Eschenbacher (group of Prof. Libuda), and photoelectrochemical IRRAS (PEC-IRRAS) data, acquired by E. Franz (group of Prof. Libuda), complemented the synchrotron radiation-based XPS measurements. The calculations of the IR spectra were conducted by L. Fromm (group of Prof. Görling), and the molecules were synthesized by A. Leng (group of Prof. Hirsch).

### 4.4.1 Monolayer conversion with XPS in UHV

As first used surface science method, high-resolution XPS measurements are addressed to gain information on the monolayer conversion in UHV. The utilized substrate was a PVD-prepared gold film on Pt(111) that was known to yield well-defined structures and behaved identically to Au(111) in photoemission.<sup>[235-237]</sup> Its respective exposure to submonolayer coverages of PENBD and PEQC was followed *in situ* in the C 1s and O 1s region, and aimed to

determine the catalytic activity of the gold surface upon direct contact. Figure 4.7a depicts the XP spectra in the C 1s region after adsorption of comparable amounts of PENBD (0.32 ML, blue) and PEQC (0.24 ML, red) at 110 K in dedicated experiments. Notably, no significant differences were detectable in their spectral line shapes within the measurement accuracy. In both cases, next to a relatively broad main signal of the spectrum, a distinct shoulder developed at higher binding energies, with minor intensities at greater values. Although the complexity of the adsorbed species did not allow for a deconvolution to single carbon atoms, the absence of heteroatoms in the NBD/QC subunit and phenyl group suggested the contribution to the main peak, while the carbon atoms adjacent to the oxygen atoms of the ester moiety resulted in positions at higher binding energies. The comparison of the rescaled spectra of PENBD and PEQC (see Figure 4.7a) indicated equivalent species on the surface.

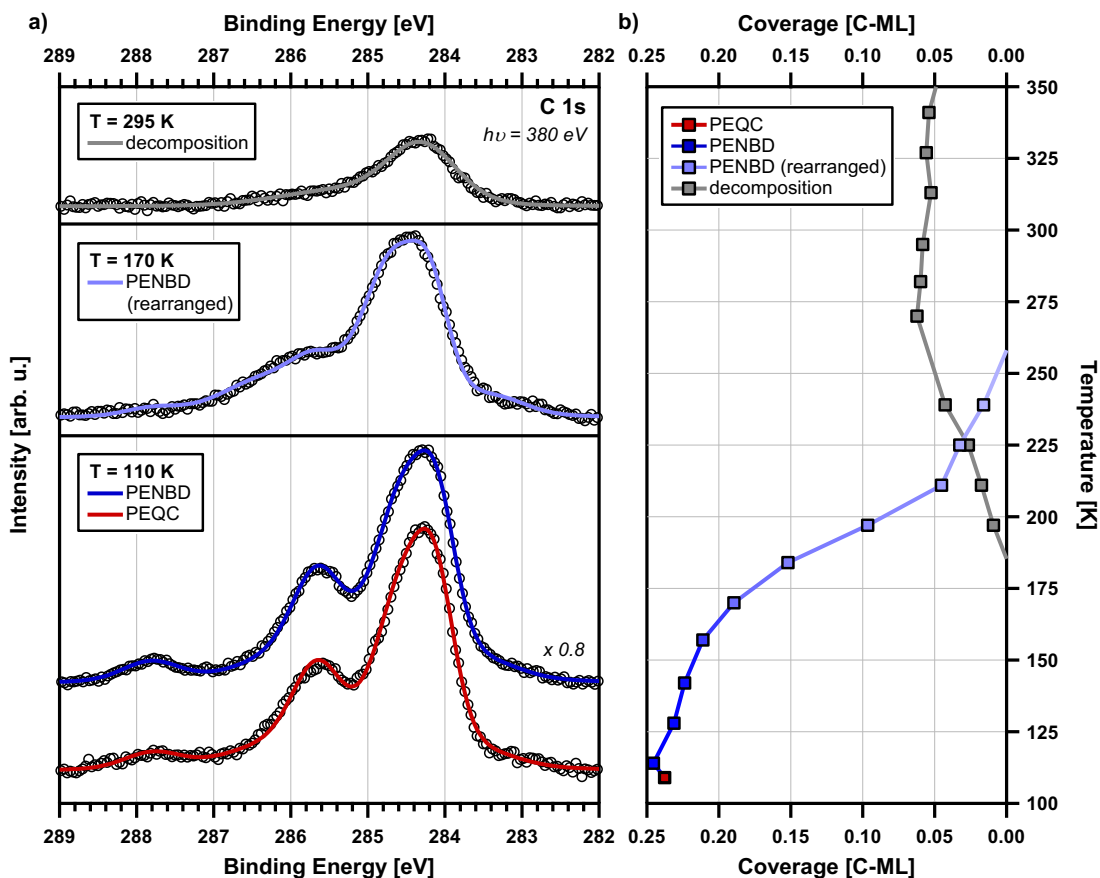


**Figure 4.7:** (a) C 1s spectra after exposure of Au/Pt(111) to PEQC and PENBD at 110 K, and representative XP spectra at elevated temperatures (170 and 295 K); the identical spectral appearance (rescaled) after adsorption indicates the instantaneous cycloreversion from PEQC to PENBD upon contact with the gold surface. (b) Quantitative description of the surface species (coverage in monolayers) during the TPXPS experiments of PEQC in the C 1s region as function of temperature (with a heating rate of 0.5 K/s): induced rearrangement step of PENBD upon heating, and desorption of PENBD up to 250 K, leaving minor residues on the surface (promoted by defects in the gold film). Reprinted with permission from Ref. [290] under license CC BY 4.0 DEED. Copyright (2023) John Wiley and Sons.

That is, no PEQC was spectroscopically detected on gold, even at an adsorption temperature of 110 K, but the instantaneous cycloreversion from the strained PEQC to PENBD was catalytically triggered. This observation was corroborated by experiments in the complementary O 1s region (see Figure 4.8a). Herein, the adsorption of both isomers yielded the same spectral appearance as well. This confirmed the assumption of gold being highly catalytically active for the isomerization to the energy-lean NBD derivative, as already stated for the above-mentioned NBD/QC systems on Au(111).<sup>[287, 288]</sup> Since a likewise conversion behavior was monitored, the triplet-singlet reaction mechanism, introduced by Schlimm *et al.*,<sup>[289]</sup> was again used as underlying explanation: This pathway via mixing of molecular and gold states facilitated the cycloreversion reaction and also minimized the occurrence of side products.

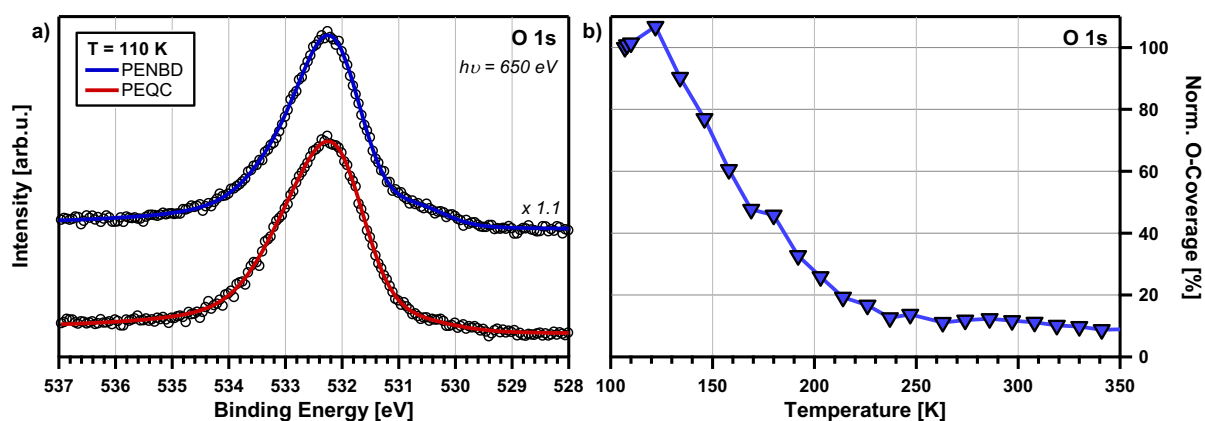


**Figure 4.8:** (a) O 1s spectra after exposure of Au/Pt(111) to PEQC and PENBD at 110 K; the identical spectral appearance (rescaled) after adsorption indicates the instantaneous cycloreversion from PEQC to PENBD upon contact with the gold surface. (b) Quantitative description of the surface species (normalized coverage) during the TPXPS experiments of PENBD in the O 1s region as function of temperature (with a heating rate of 0.5 K/s): decline of PENBD up to 240 K; a contribution by water desorption cannot be completely excluded. Reprinted with permission from Ref. [290] under license CC BY 4.0 DEED. Copyright (2023) John Wiley and Sons.

Furthermore, temperature-programmed experiments were conducted to describe the thermal evolution of PENBD. Figure 4.7a shows C 1s spectra at selected temperatures (110, 170, and 295 K), when representative surface species were present. The quantitative analysis of the PEQC experiment is illustrated in Figure 4.7b, which gives the amount in carbon coverage as function of temperature. Above 135 K, first spectral changes were noticeable: The main peaks exhibited a shift of  $\sim 150$  meV towards lower binding energies, while the shoulder at higher binding energy side broadened and lost in intensity (see Figure 4.7a, light blue). This was ascribed to a rearrangement step of the molecules on the surface to occupy thermodynamically more stable adsorption motifs,<sup>[250, 270]</sup> in particular, various geometries

were suggested for the flexible ester substituent, since the differences between 110 and 170 K mainly affected the features at higher binding energies. Up to 150 K, a decrease of less than 10% of the total carbon coverage was observed, whereas heating to 210 K led to the pronounced molecular desorption of PENBD (see Figure 4.7b). An analogous behavior is depicted in Figure 4.8b for the normalized oxygen coverage of PENBD plotted against the temperature; yet, impurities of co-adsorbed water<sup>[291]</sup> could not be completely excluded, so that the decline was possibly influenced by its desorption above 140 K.<sup>[292, 293]</sup> Having reached 250 K, no contributions of intact PENBD were detected anymore; instead, starting at 190 K, the spectra were described by an asymmetric peak (see Figure 4.7a, gray), which was attributed to fragmentation products, in line with carbide structures on polycrystalline gold.<sup>[294]</sup> Note the small remaining absolute amount, with about 20% of the initial coverage. Under-coordinates sites, such as defects of the prepared gold film, facilitated this decomposition<sup>[295]</sup> yielding minor residues on the surface.

#### 4.4.2 Complementary IRRAS experiments

The surface chemistry of PENBD on Au(111) at multilayer coverages was assessed in IRRAS experiments under UHV conditions. Time-resolved IRRAS spectra, collected during exposure to PENBD at 110 K, enabled the binding motif of the molecules to be derived due to the assignment of characteristic bands, which were corresponding to the calculated spectra,<sup>[296]</sup> and the consideration of the metal surface selection rule (MSSR).<sup>[297-299]</sup> At low coverages, an intact adsorption in upright-standing geometry was deduced, whereby the continuous deposition of PENBD led to intensity changes and the formation of new bands, indicative of a reorientation of the adsorbates. Subsequently, the growth of the multilayer proceeded in a random manner. Upon irradiation, the adsorbed PENBD multilayer was quantitatively photo-converted to PEQC, which was found to be stable in form of a frozen multilayer film, with no electronic coupling to the Au(111) surface. Next, the cycloreversion back to PENBD was investigated by means of temperature-programmed IRRAS (TP-IRRAS). Up to 150 K, no spectral changes became visible; when heating higher, modifications in the film morphology were proposed. In the temperature range between 224 and 232 K, the energy release from PEQC was monitored in the isomerization reaction to PENBD. It was suggested that, upon heating, the mobility of the species within the film was increased, so that the PEQC molecules reached the gold surface, which initiated the instantaneous back conversion (see XPS part).

The onset of the multilayer desorption was determined at 232 K, that of the remaining monolayer at 240 K.

Information on the kinetics of the energy release and the reversibility were obtained by PEC-IRRAS experiments in the liquid phase. The reaction rate depended on the applied potential, as demonstrated in a previous study.<sup>[287]</sup> The measurements were performed at  $-0.7 V_{fc}$  and in a thin-layer configuration (25  $\mu\text{m}$ ), so that the diffusion to the bulk solution was impeded.<sup>[300]</sup> As the  $\nu(\text{CO})$  stretching band exhibited the highest intensity and displayed a shift in the course of the isomerization between PENBD and PEQC, it was utilized as spectroscopic marker for the photoconversion and cycloreversion. Other than minor influences by the solvent (acetonitrile),<sup>[301]</sup> stable conditions were observed if the sample was not irradiated. During irradiation, the photoconversion from PENBD to PEQC was proven due to the formation of the characteristic bands of PEQC at the expense of that of PENBD. Since Au(111) acted as catalyst for the back conversion to PENBD, a steady state was reached after  $\sim 50$  s. Having switched off the LED, the cycloreversion was followed to proceed in a quantitative manner (after  $\sim 150$  s) without any indications for side products. Thus, a very high catalytic activity of gold was also attested in the liquid phase. Featuring comparable half-lives for the photoconversion and back reaction, the energy release rate was concluded to be similar to that of the previously investigated asymmetric cyano derivative.<sup>[287]</sup> In order to assess the reversibility of the isomerization between PENBD and PEQC, the irradiation experiment was cycled for 100 times. Within the detection limits, no degradation was monitored but the selective and full back conversion to PENBD in each cycle. Regarding the long-term stability, the catalytic effect did not decline over time; instead, for increased cycling, a lower band intensity in the steady state implied a slightly higher activity, which was presumably caused by the reductive removal of impurities.

In conclusion, the multi-method approach in this study comprised the complementary behavior of the molecule pair PENBD/PEQC on gold in UHV and in the liquid phase. A combination of XPS and IRRAS experiments delivered information on the catalytic activity for the energy release, the overall reversibility as well as mechanistic insights and reactions kinetics. Gold was found to effectively trigger the back conversion from PEQC to PENBD, whereby an applied external potential was demonstrated to control the reaction rate in the liquid-phase measurements. The UHV investigations confirmed the very high catalytic activity of the gold surface, even at cryogenic temperatures of 110 K. For that, a singlet-triplet mechanism,

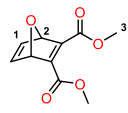
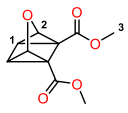
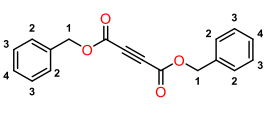
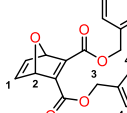
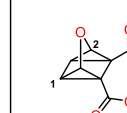
proposed for previous photoswitches,<sup>[288, 289]</sup> explained the spontaneous isomerization. This required a direct electronic coupling to the substrate, so that PEQC was only stable in the multilayer. Above 220 K, the increased mobility within the film yielded PENBD, as the molecules came in contact with the surface. The desorption of the multilayer was determined at 232 K. From the submonolayer experiments, the rearrangement of PENBD into more stable adsorption geometries was suggested to start at ~135 K, while the molecules desorbed up to 250 K; minor residues remained in the XP spectra due to decomposition to a small extent at defects in the gold film. The PEC-IRRAS experiments stated full reversibility for the system within 100 measured cycles; no side product formation occurred and also the catalytic activity did not diminish but actually increased slightly over time.

---

*Adapted with permission from Ref. [290] under license CC BY 4.0 DEED. Copyright (2023) John Wiley and Sons.*

## 4.5 O-NBD/QC and exO-NBD/QC on Pt(111)<sup>[P4]</sup>

The utilization of hetero-NBD/QC systems is of interest due to several reasons: First, the introduction of a heteroatom at the bridgehead position was expected to result in deviating adsorption geometries and reaction pathways on the catalyst surfaces. The methylene bridgehead was found to be particularly involved in the decomposition routes of unsubstituted NBD and derivatives thereof on different catalyst materials; on Pt(111), the agostic C-H interaction with the surface induced the early onset of the fragmentation of NBD,<sup>[163, 164]</sup> while the detachment of the bridging carbon yielded the formation of benzene as dissociation product for NBD and Br<sub>2</sub>-NBD on Ni(111).<sup>[166, 167]</sup> Therefore, a structural modification at this position might allow for higher thermal stability limits of the respective energy-lean isomers. Moreover, the appropriate functionalization of the bridgehead was demonstrated to achieve enhanced quantum yields of the photoconversion and also increased the half-life of the corresponding metastable state.<sup>[121]</sup> In addition, the incorporation of heteroatoms in the NBD framework was anticipated to influence the maximum energy storage density of the considered system.<sup>[122]</sup> As the photochemistry of oxanorbornadiene (oxa-NBD) has already been of interest several decades ago,<sup>[123]</sup> investigations on the surface chemistry of ester-substituted oxa-NBD/QC molecule pairs on Pt(111) are presented in the following. Specifically, synchrotron radiation-based XPS experiments in UHV were supplemented by measurements in the liquid phase by photochemical infrared reflection absorption spectroscopy (PC-IRRAS). Thereby, information on the respective adsorption motifs and reaction behavior of 2,3-bis(methylester) derivatives was deduced as well as the influence of an extended 2,3-bis(benzylester)-substitution was studied. Besides, the selectivities and associated reaction rates of the energy-releasing cycloreversion from the particular QC derivative were determined.

Molecule 1 (O-NBD)	Molecule 2 (O-QC)	Molecule 3 (dibenzyl acetylenedicarboxylate)	Molecule 4 (exO-NBD)	Molecule 5 (exO-QC)
				
C <sub>10</sub> H <sub>10</sub> O <sub>5</sub> M <sub>r</sub> = 210.19	C <sub>10</sub> H <sub>10</sub> O <sub>5</sub> M <sub>r</sub> = 210.19	C <sub>18</sub> H <sub>14</sub> O <sub>4</sub> M <sub>r</sub> = 294.31	C <sub>22</sub> H <sub>18</sub> O <sub>5</sub> M <sub>r</sub> = 362.38	C <sub>22</sub> H <sub>18</sub> O <sub>5</sub> M <sub>r</sub> = 362.38

**Scheme 4.3:** Depiction of synthesized hetero-NBD molecules and their corresponding QC isomers; specification of chemical formulas with molecular weight; note that dibenzyl acetylenedicarboxylate is a reaction intermediate towards exO-NBD/QC. Reprinted with permission from Ref. [302]. Copyright (2023) AIP Publishing.

These results<sup>[302]</sup> are published in [P4], whereby the PC-IRRAS part was contributed by Z. Hussain and E. Franz (group of Prof. Libuda). The molecule syntheses were carried out by D. Krappmann (group of Prof. Hirsch); the analysis of the crystal structure of exO-NBD was provided by F. Hampel (group of Prof. Dube). An overview and labeling of the utilized molecules is illustrated in Scheme 4.3, which comprises the molecular structures, chemical formulas, and molar masses.

#### 4.5.1 XPS results of O-NBD/QC

Both the C 1s and O 1s regions will be described for the XPS findings; the exposures were chosen to yield comparable surface coverages of the molecules in the submonolayer range. To begin with, the valence isomers O-NBD/QC are regarded as structurally simplest derivatives in this study. The C 1s spectra acquired during exposure of Pt(111) at 150 K to the energy-lean O-NBD are depicted in Figure 4.9a, resulting in a carbon coverage of 0.70 ML; note minor amounts of preadsorption (gray spectrum) due to residual O-NBD in the chamber. The evaluation of the data was conducted by introducing an appropriate fit model. The characteristic line shape of O-NBD, featuring two distinct intensity maxima and smaller contributions at higher binding energies, acted as spectroscopic fingerprint for the specific surface species and was reproduced by five peaks whose relative intensity ratio was kept fixed (see Figure 4.9c, blue). The complex molecular structure did not allow for the assignment of the signals to individual carbon atoms. Nonetheless, the attribution of carbon atoms that are in vicinity to oxygen to the higher binding energy side was reasonable.<sup>[271]</sup> That is, the proportion of the four peaks at higher binding energies coincided with the number of carbon atoms being directly bound to at least one oxygen atom; the highest intensities at lower binding energies agreed with the XP spectrum of unsubstituted NBD on Pt(111).<sup>[164]</sup> The analogous experiment for the strained isomer O-QC is shown in Figure 4.9f, whereby a total carbon coverage of 0.77 ML was obtained. The broader signals of its line shape required six fitted peaks this time (see Figure 4.9d, orange). Compared to the spectrum of O-NBD, next to small deviations in the employed widths and binding energy positions, the most apparent differences concerned the relative intensity ratios. Therefore, a clear distinction of both molecules with their spectral characteristics was possible in the C 1s region. In sum, no indications for dissociation processes upon adsorption at 150 K were observed for O-NBD and

O-QC. Moreover, the energy release from O-QC was not triggered instantaneously at low temperatures, unlike to unsubstituted NBD on Pt(111).<sup>[164]</sup>

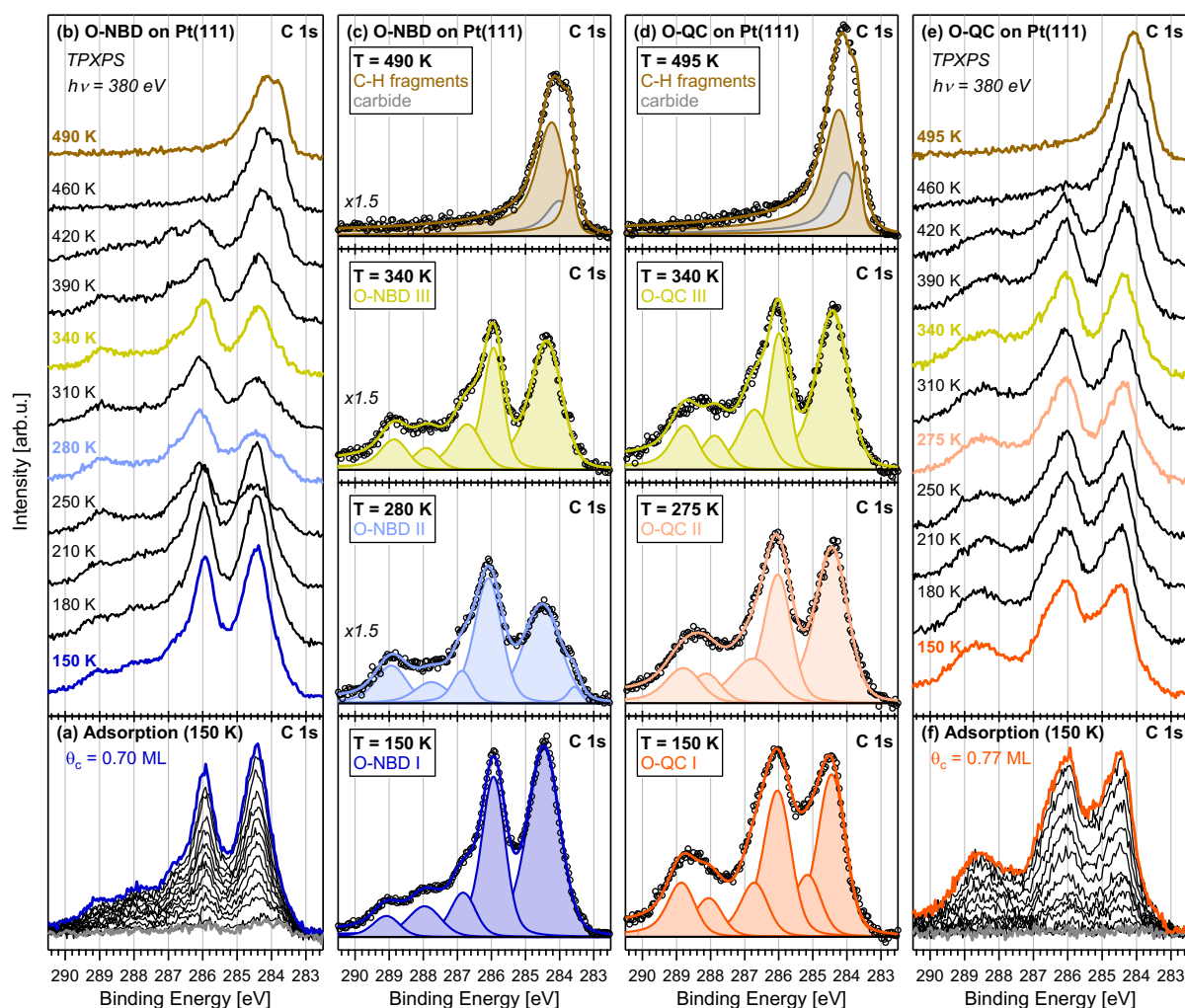


**Figure 4.9:** (a, f) C 1s spectra during exposure of Pt(111) to O-NBD and O-QC at 150 K; (b, e) Selected XP spectra of the respective temperature-programmed experiment (TPXPS) up to 495 K; (c, d) Representative surface species with corresponding fit model (color-coded). Whereas a spectroscopic distinction is possible upon adsorption (see 150 K), the identical spectral appearance at elevated temperatures (see 340 K) indicates the quantitative cycloreversion from O-QC to O-NBD. Note different scaling factors in (c). Reprinted with permission from Ref. [302]. Copyright (2023) AIP Publishing.

Temperature-programmed XPS (TPXPS) measurements were conducted to follow the respective reaction pathways on the catalyst surface. Figure 4.9b and 4.9e illustrate spectra of the O-NBD and O-QC experiment at selected temperatures, respectively. Representative surface species are depicted with their corresponding color-coded fits in Figure 4.9c and 4.9d. The analysis of the data enabled the quantification of the amounts, so that Figure 4.10 gives the coverages of the particular species as function of temperature. In the case of O-NBD, equivalent spectra were monitored up to 200 K. Having heated to 235 K, molecular desorption of about 46% of the initial coverage was detected (see Figure 4.10a). In the same temperature

range, minor spectral changes, which mainly affected the relative intensities, were ascribed to a rearrangement step of O-NBD to more stable adsorption geometries, as already suggested for other NBD derivatives.<sup>[250, 270]</sup> This surface intermediate, O-NBD II (see Figure 4.9c, light blue), was steady until 310 K. Beyond, another reorientation was deduced from a subtle different spectral appearance, caused by other damping conditions and photoelectron diffraction effects.<sup>[206, 251]</sup> At 340 K, O-NBD III (see Figure 4.9c, yellow) represented the species with the highest adsorption energy in this picture. The decomposition onset of the molecular framework was determined at 390 K, which exceeded that of unsubstituted NBD<sup>[164]</sup> and similar ester-substituted NBD derivatives on Pt(111).<sup>[270]</sup> This degradation yielded unspecified C-H fragments<sup>[164, 169]</sup> (see Figure 4.9c, brown), while additional carbide formation<sup>[303, 304]</sup> (see Figure 4.9c, gray) was found above 480 K.

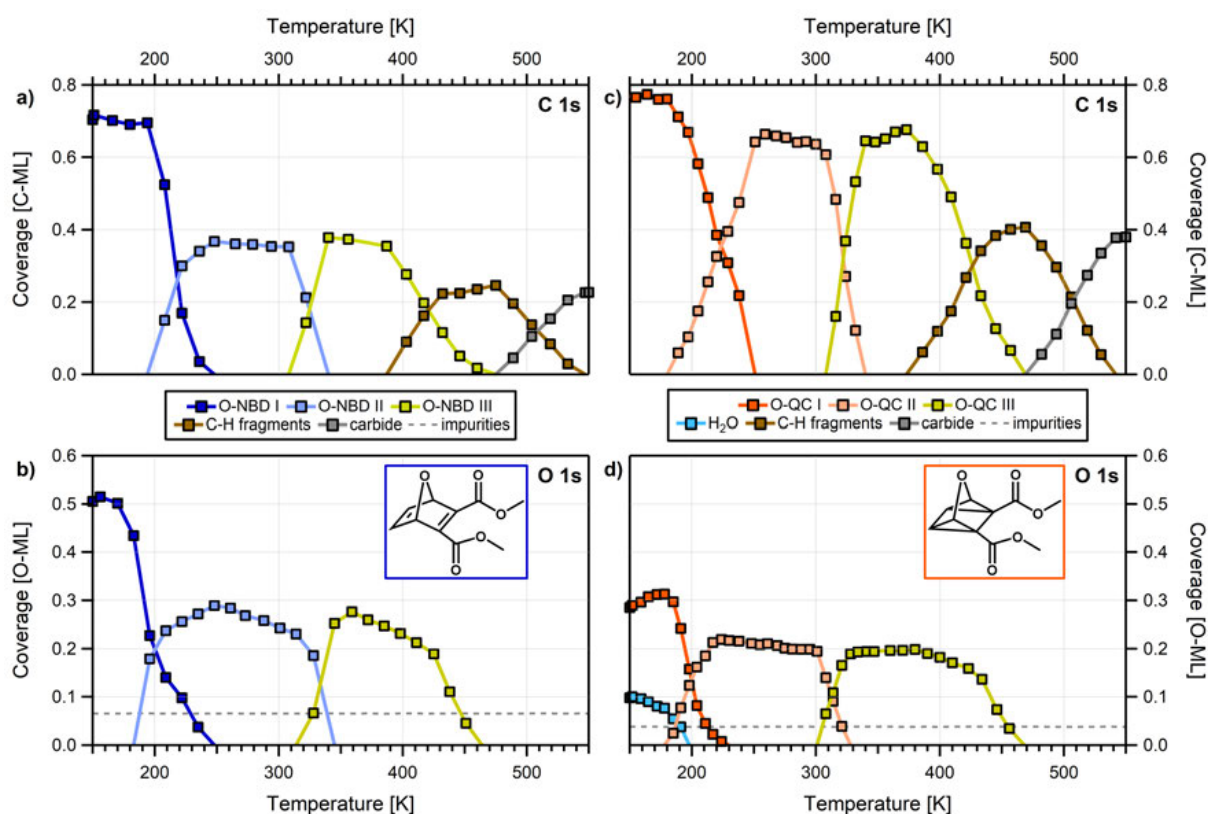


**Figure 4.10:** Quantitative description of the surface species (coverage in monolayers) during the TPXPS experiments of O-NBD and O-QC on Pt(111) as function of temperature (with a heating rate of 0.5 K/s): analysis in (a, c) C 1s region and (b, d) O 1s region. Reprinted with permission from Ref. [302]. Copyright (2023) AIP Publishing.

For the energy-rich O-QC, a stable adsorption motif was assumed from the beginning, since desorption took place to only a small extent of  $\sim 13\%$  (see Figure 4.10c). Still, above 180 K, slight changes in the spectra became apparent, by which the peak at second lowest binding energy position was not necessary anymore (see Figure 4.9d, light orange). Thus, this O-QC II

species described likewise the situation after rearrangements of the molecules. Heating to 310 K induced the transition of the line shape towards that observed in the dedicated O-NBD experiment at equal temperatures (see Figure 4.9d, yellow). Within the accuracy of the measurements, the same fit parameters could be employed; small deviations of the relative intensities for the peaks at higher binding energies were expected to stem from the flexibility of the associated ester groups.<sup>[283, 305]</sup> The identical spectral appearance implied the initiated cycloreversion from O-QC to O-NBD, which proceeded from 310 to 340 K in a quantitative manner without side reactions (see Figure 4.10c). Heating higher, an analogous decomposition was demonstrated as for O-NBD. As a result, alike to unsubstituted QC<sup>[164]</sup> and other derivatives,<sup>[270]</sup> Pt(111) was proven to be catalytically active towards the energy release in a first hetero-NBD/QC system; here, the isomerization was triggered at comparably high temperatures. The catalytic activity will be assessed in complementary liquid-phase measurements (see below).

Furthermore, the adsorption and reaction behavior was also studied in supplementary experiments in the O 1s region. As before, the adsorption of O-NBD and O-QC on Pt(111) at 150 K was monitored *in situ*, respectively. For O-NBD, the obtained spectra were fitted with three peaks exhibiting an intensity ratio of 1 : 2 : 2, which is in line with the chemically different oxygen atoms in the molecular structure. While the two peaks at higher binding energies were ascribed to the carbonyl (C=O) and ether (C–O–C) oxygens,<sup>[270, 271, 306]</sup> the third peak was due to the oxygen atom within the oxa-NBD subunit. The low binding energy position of latter one suggested its orientation towards the surface,<sup>[270, 271, 307]</sup> resulting in a “side-on” geometry, similar to unsubstituted NBD on Pt(111).<sup>[164]</sup> In the case of O-QC, an equivalent fit model was used; yet, compared to O-NBD, the peak positions were shifted by up to 0.7 eV towards lower binding energies, indicative of a stronger interaction of the oxygen atom of the oxa-QC subunit with the substrate.<sup>[270, 271, 307]</sup> Besides, the unavoidable coadsorption of water during exposure to O-QC, which originated from the additional photoconversion step in its synthesis, gave rise to another peak for water on Pt(111), in agreement with literature.<sup>[273]</sup>

The thermal evolution in the O 1s region corroborated the rearrangement and reaction steps deduced from the C 1s experiments. Concerning O-NBD, first spectral changes occurred at ~200 K, whereupon a similar decrease in its coverage was detected as in the C 1s spectra. Above ~320 K, a reordering of the surface species into the most stable geometry of O-NBD was attested in the O 1s measurements. Having heated to 450 K, no oxygen-containing

fragments were monitored, except for minor impurities prior to the dosage. The temperature-programmed experiment of O-QC in the O 1s region revealed the desorption of the coadsorbed water upon heating to above 180 K.<sup>[273]</sup> In the suggested fit model, the introduction of a new surface species starting at ~190 K agreed with the C 1s experiment. Only for temperatures above 310 K, the O 1s spectra of O-NBD and O-QC could be fitted with the same peak widths; although the binding energy positions deviated slightly, by less than 0.3 eV, the existence of identical surface species appeared reasonable. That is, the findings in the O 1s region confirmed that the cycloreversion reaction from O-QC to O-NBD proceeded quantitatively on Pt(111).

#### 4.5.2 XPS results of exO-NBD/QC

Next, the surface chemistry of the extended ester-substituted derivatives exO-NBD/QC is discussed. The adsorption of exO-NBD on Pt(111) at 115 K is shown in Figure 4.11a, which depicts the *in situ* growth of the spectra up to the final carbon coverage of 0.36 ML. The line shape was reproduced by five peaks at a fixed intensity ratio (see Figure 4.11c, blue). Again, the spectral appearance was utilized as characteristic fingerprint, whereby more detailed information on single contributions was not accessible. Nonetheless, the area of the three peaks at highest binding energies corresponded to the number of carbon atoms that are directly bound to oxygen; the remaining two peaks represented the sp<sup>2</sup> carbon atoms of the NBD subunit and the phenyl moieties. In general, the comparison to the XP spectra of unsubstituted NBD<sup>[164]</sup> and benzene on Pt(111)<sup>[272]</sup> reconciled the acquired spectrum of exO-NBD, when considering the contributions of the ester groups<sup>[271]</sup> and the oxygen atom of the oxa-NBD subunit. The waterfall plot of the exposure of Pt(111) at 115 K to the energy-rich exO-QC is given in Figure 4.11f, yielding a carbon coverage of 0.41 ML. The fit model of the obtained spectrum included five peaks at similar positions of exO-NBD but with deviating relative intensities, especially at lower binding energies (see Figure 4.11d, orange). As before, the spectrum was replicable when taking the individual molecular moieties into account.<sup>[164, 271, 272]</sup> Thus, both valence isomers were demonstrated to adsorb molecularly on Pt(111) at low temperatures, while being distinguishable in terms of their spectral line shapes.

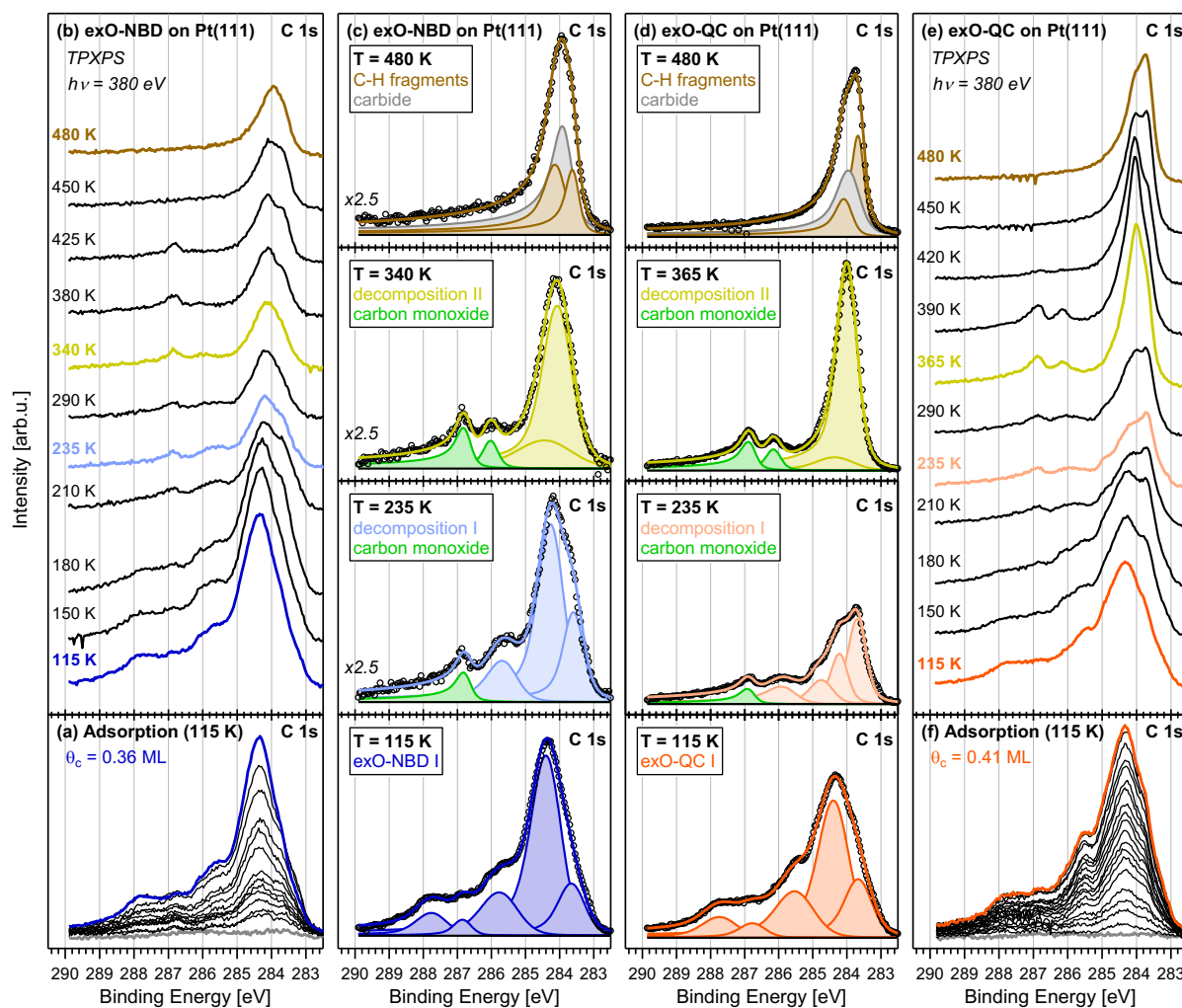


**Figure 4.11:** (a, f) C 1s spectra during exposure of Pt(111) to exO-NBD and exO-QC at 115 K; (b, e) Selected XP spectra of the respective temperature-programmed experiment (TPXPS) up to 480 K; (c, d) Representative surface species with corresponding fit model (color-coded). A spectroscopic distinction is possible upon adsorption (see 115 K); the absence of spectral features of exO-NBD in the exO-QC experiment indicates no cycloreversion to exO-NBD at any temperature. Note different scaling factors in (c). Reprinted with permission from Ref. [302]. Copyright (2023) AIP Publishing.

The respective reaction pathways of exO-NBD/QC were deduced in temperature-programmed experiments. Figure 4.11b and 4.11e show selected C 1s spectra at representative temperatures. In the course of the exO-NBD measurements, pronounced molecular desorption set in directly after starting the heating ramp; up to 200 K, about 60% of the carbon coverage has desorbed, analogous to the behavior of O-NBD but to a greater extent and at lower temperatures. That is, an overall weak adsorption energy was determined for exO-NBD. It was suggested that with increased size of the derivative, the most favorable adsorption sites were not occupied; instead a random sticking of the molecules in various motifs occurred,<sup>[308]</sup> whereby heating induced the surface species to desorb before a rearrangement could take place.<sup>[309]</sup> Above 135 K, the emerging peak for carbon monoxide (CO) at on-top sites<sup>[246]</sup> (see

Figure 4.11c, green) marked the decomposition onset of the molecular framework. As two equivalents of CO were formed from each exO-NBD molecule, the remaining fragments were attributed to cleaved oxa-NBD and benzyloxy-like species<sup>[310]</sup> (see Figure 4.11c, light blue). Heating to above 250 K gave rise to CO also in bridge position<sup>[246]</sup> (see Figure 4.11c, green); its quantification amounted to two additional equivalents, so that the dissociation into phenyl moieties<sup>[310, 311]</sup> was proposed next to the thermally stable oxa-NBD subunit (see Figure 4.11c, yellow). Starting at 370 K, further fragmentation into unspecified residues<sup>[164, 169]</sup> was monitored (see Figure 4.11c, brown), while the CO peaks have disappeared above 470 K,<sup>[312]</sup> and carbide structures<sup>[303, 304]</sup> were observed simultaneously (see Figure 4.11c, gray). For exO-QC, an analogous decomposition pathway was concluded. The early desorption between 125 and 220 K of about 49% of the surface species implied a lower adsorption energy compared to the smaller O-QC derivative (see above). As for exO-NBD, the formation of CO<sup>[246]</sup> (see Figure 4.11d, green) began at 135 K and indicated the dissociation of the molecular framework (see Figure 4.11d, light orange).<sup>[313, 314]</sup> Beside the cleaved oxa-QC subunit, the same degradation products were expected as for the exO-NBD experiment, whereby the second fragmentation step occurred at 270 K (see Figure 4.11d, yellow). Since the signals overlapped, it could not be ascertained if the cycloreversion from the oxa-QC to the oxa-NBD subunit proceeded. However, the liquid-phase investigations of the molecule pair (see below) stated a successfully triggered isomerization under these conditions.

Complementary experiments of exO-NBD/QC were carried out in the O 1s region. The exposure of Pt(111) at 115 K to the derivatives achieved the molecular adsorption of comparable amounts, respectively. The O 1s spectrum of exO-NBD was reproduced by three peaks with an intensity ratio of 1:2:2, which suited the number of oxygen atoms in equivalent chemical environment. Likewise to the above-described O-NBD, the peaks at higher binding energies were ascribed to the oxygen atoms of the ester moiety.<sup>[270, 271, 306]</sup> The oxygen atom of the oxa-NBD subunit was again found at lower binding energy position. Equally, the adsorption in a “side-on”-like geometry<sup>[164, 166, 167, 250]</sup> was suggested, wherein the oxygen atom of the oxa-NBD subunit points towards the surface. In the case of exO-QC, the obtained line shaped resembled that of exO-NBD, with exception of a less distinct shoulder at lower binding energy side. The used fit model was identical apart from slightly different widths of the peaks. That is, the derivatives exhibited adsorption motifs of the same kind. Moreover,

minor water impurities<sup>[273]</sup> in the experiment of exO-QC originated from its synthesis, as observed for the O-QC derivative.

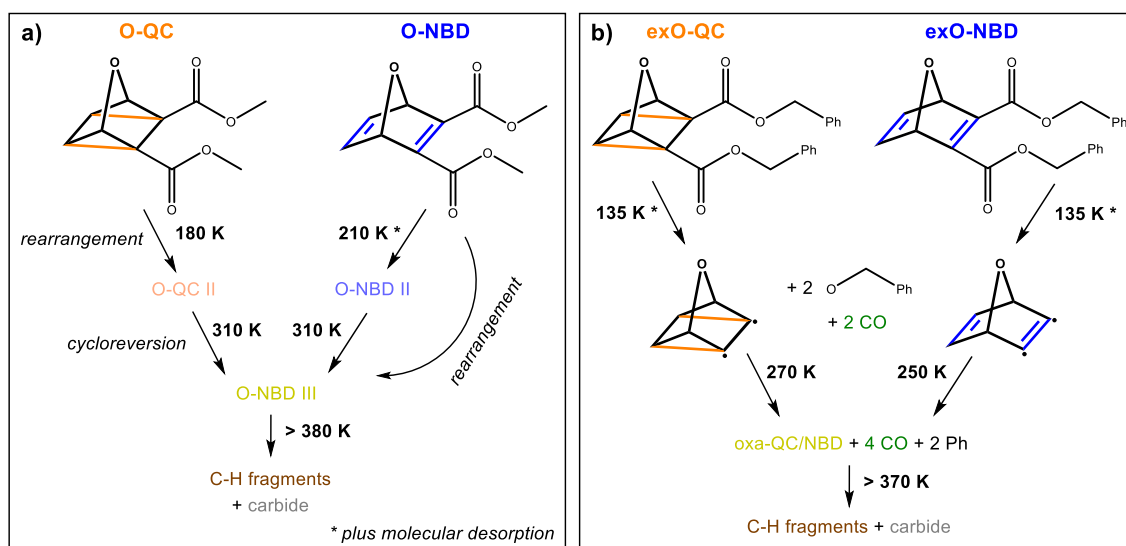
The TPXPS data in the O 1s region supported the reaction pathways, derived on the basis of the C 1s experiments. For exO-NBD, the significant decrease of the oxygen coverage upon heating to 180 K corresponded to the previously stated desorption behavior. Above 145 K, the emerging CO, at on-top sites,<sup>[246]</sup> and the remaining dissociation products<sup>[310]</sup> were also monitored in the O 1s spectra. Having heated to 250 K, the additional formation of CO in bridge positions<sup>[246]</sup> was supported, whereby the CO species desorbed completely above 460 K.<sup>[312]</sup> Regarding exO-QC, the contributions of the coadsorbed water vanished up to 200 K.<sup>[273]</sup> Besides, the same trend for molecular desorption as in the C 1s measurements was confirmed. In addition, the found stability boundaries and decomposition products were corroborated by the detection of CO and oxygen-containing residues in the O 1s experiments in equivalent temperature ranges.

#### 4.5.3 Catalytic behavior in the liquid phase

The catalytic activity of Pt(111) for the energy release of the hetero-QC derivatives was also assessed in liquid-phase experiments under more realistic conditions by PC-IRRAS. Characteristic IR bands of the respective molecules were determined through transmission IR spectra in a KBr matrix, acquired beforehand. The photoconversion to the O-QC and exO-QC isomer was achieved by irradiation with an UV LED ( $\lambda_{\max} = 275$  nm), whereby the complete isomerization was proven by NMR. Thus, particular bands acted as spectroscopic marker for the identification of the species in the *in situ* PC-IRRAS experiments.<sup>[165]</sup> The time-resolved measurements on Pt(111) were performed with a solution of 10 mM O-NBD/exO-NBD in acetonitrile (MeCN) in a thin-layer configuration of few microns, so that diffusion to the bulk was impeded.<sup>[300, 315]</sup> After the measurement of a reference spectrum, time-resolved spectra (resolution of 0.5 s) were collected for 1500 s, while the thin layer was irradiated for 80 s after 1 s. That is, the formation and consumption of specific IR bands, which were assigned by means of the transmission spectra, indicated the isomerization between the respective NBD and QC derivatives. Upon irradiation, the photoconversion from O-NBD to O-QC was monitored; having turned off the UV LED, the cycloreversion to O-NBD was deduced from the recurrence of its according IR bands. Analogously, the extended exO-NBD/QC pair was photoswitchable and revealed the subsequent back conversion. To exclude diffusion effects

and a thermal trigger but affirm the catalytic activity of Pt(111) for the cycloreversion, blank experiments with inert HOPG<sup>[296, 316]</sup> were conducted, on which the decrease of the features of the QC derivatives was significantly slower.

To determine the reaction rates of the cycloreversion reactions and the corresponding selectivities, the data was evaluated quantitatively. After calibration and detection of the extinction coefficients, the concentrations of the respective species were calculated. During irradiation of O-NBD, its amount and that of the photoisomer O-QC leveled off after  $\sim 50$  s, indicative of a complete conversion. Thereafter, a rate constant of  $k = 5.3 \times 10^{-4} \text{ s}^{-1}$  was found for the decrease of the concentrations on Pt(111), with the cycloreversion itself as rate-determining step.<sup>[317]</sup> A selectivity of  $> 99\%$  was obtained for the reaction from O-QC to O-NBD. Likewise, the photoconversion from exO-NBD to exO-QC was attested; the observed reaction rate for the back conversion was comparable with  $k = 6.3 \times 10^{-4} \text{ s}^{-1}$  at a selectivity of 98%. In contrast to the UHV results (see above), both oxa-NBD/QC derivatives displayed a similar behavior, which was attributed to a passivation of the Pt(111) surface by carbonaceous species that were present under ambient conditions. Thereby, the overall activity was reduced but also the suppression of decomposition pathways equally increased the selectivity for both molecule pairs.



**Scheme 4.4:** Deduced reaction pathways on Pt(111): (a) For the molecule pair O-NBD/O-QC, rearrangement steps upon heating and energy release in quantitative cycloreversion to O-NBD above 310 K; decomposition starting at 380 K yields C-H fragments and carbide. (b) For exO-NBD/exO-QC, observation of molecular desorption and no cycloreversion reaction before fragmentation above 135 K under detachment of substituents and formation of carbon monoxide (CO); subsequent degradation at 250 or 270 K, and final decomposition above 370 K. Reprinted with permission from Ref. [302]. Copyright (2023) AIP Publishing.

In conclusion, this study investigated the surface chemistry of hetero-NBD/QC derivatives on Pt(111). Synchrotron radiation-based XPS experiments gave qualitative information on the adsorption motifs: A spectroscopic distinction of the molecules was possible after adsorption at low temperatures, whereby a “side-on” geometry was suggested for all compounds. Based on the desorption processes, O-NBD was expected to exhibit lower adsorption energies than O-QC; an even weaker interaction with the substrate was concluded for the benzyl-extended molecules. Moreover, the respective reaction pathways were deduced upon heating (see Scheme 4.4): For O-NBD, the rearrangement into its most stable adsorption motif was observed between 210 and 310 K. O-QC also showed a reordering step above 180 K, while the energy release in the cycloreversion to O-NBD occurred within 310 to 340 K. The decomposition, starting at 380 K, yielded C-H fragments and eventually carbide. In the case of the exO-NBD/QC pair, the thermal stability was given only until 135 K. The dissociation resulted in the formation of CO and benzyloxy-like species. At higher temperatures, the fragmentation into phenyl species took place, followed by C-H residues and carbide structures. Complementary liquid-phase experiments determined the reaction rates of the cycloreversion and assessed the selectivities, which were similar for both systems. The less pronounced differences in the liquid phase were explained by the passivation of the surface. Nevertheless, Pt(111) was demonstrated to be catalytically active for the energy release from the oxa-QC derivatives with a very high selectivity.

---

*Adapted with permission from Ref. [302]. Copyright (2023) AIP Publishing.*

## 4.6 Review: Surface Science Studies of NBD/QC Derivatives<sup>[P5]</sup>

In the context of the presented work, a review article<sup>[318]</sup> about surface science investigations on the NBD/QC system and its derivatives was published as [P5]. It comprises a brief historical description from the first synthesis of NBD<sup>[109-114]</sup> to the utilization of its photoisomerization to QC<sup>[99, 107, 117-120, 319, 320]</sup> as novel energy storage possibility and the development of derivatives with optimized properties for potential molecular solar thermal (MOST) applications.<sup>[46, 50, 51, 54, 79]</sup> To overcome intrinsic and technical limitations concerning the overall efficiency,<sup>[150]</sup> studies on the reaction behavior, in particular the heterogeneously catalyzed energy release, on model surfaces give crucial insights for a knowledge-driven improvement of molecule and catalyst design.<sup>[160]</sup> The focus was set on experiments under well-controlled UHV conditions and photochemical liquid-phase measurements. That is, information on adsorption geometries and reaction mechanisms was obtained, assessing the feasibility of the cycloreversion from the respective QC derivative to its NBD isomer and identifying competing processes, especially, desorption and decomposition routes. Besides, various fields of application were demonstrated with the unique light-harvesting and storage characteristics of actual NBD-based devices.<sup>[56]</sup>

Several compound classes are known to act as molecular photoswitches.<sup>[321]</sup> However, the essential requirements for an applicability as MOST system<sup>[80-82]</sup> led to the selection of the NBD/QC molecule pair:<sup>[76-79, 85, 158]</sup> While exhibiting a reasonable energy storage density<sup>[83-85]</sup> and a pronounced stability of its photoisomer,<sup>[105-108]</sup> unsubstituted NBD features an absorption onset in the UV range<sup>[99-101]</sup> and displays a low quantum yield without sensitizer.<sup>[77, 87-89, 92]</sup> Therefore, derivatization of the molecular framework allows for enhanced efficiencies of the photoconversion at a better overlap<sup>[86]</sup> with the solar spectrum.<sup>[82, 109, 128, 322]</sup> A plethora of synthetically available derivatives was classified according to their different substitution patterns.<sup>[121, 123-127]</sup> In general, a reciprocal relation between the redshift of the absorption bands<sup>[82]</sup> and the storage capacity, due to an increase of the molecular mass, was observed.<sup>[323]</sup> Theoretical modelling supported the search for kinetically stable NBD molecules of interest.<sup>[134-136, 324]</sup> Regarding their size and electronic qualities, many 2,3-disubstituted NBD derivatives<sup>[101, 102, 129-133]</sup> appear as promising candidates.

The energy-releasing cycloreversion from the particular QC to NBD derivative has to proceed in a controlled and efficient manner. For that, the back conversion can be initiated by

a thermal,<sup>[83, 106]</sup> catalytic,<sup>[137, 140]</sup> or electrochemical trigger.<sup>[144, 147]</sup> Various transition metals are known to be catalytically active towards the rearrangement reactions of cyclic organic molecules.<sup>[108, 138]</sup> While the energetic barrier for the isomerization is decreased between radical species,<sup>[145, 146]</sup> photoelectrochemical approaches<sup>[149]</sup> yield higher selectivities with less electrode fouling.<sup>[148]</sup> Furthermore, the concept of coupling MOST molecules to a suitable semiconductor electrode aims to release the stored energy in form of electricity instead of heat.<sup>[149]</sup>

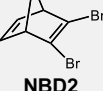
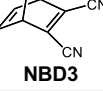
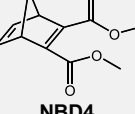
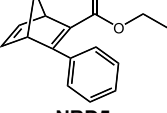
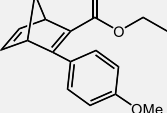
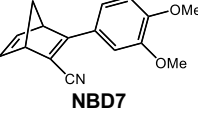
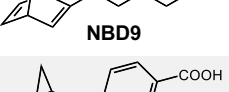
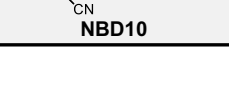
To begin with, findings on the unsubstituted NBD/QC system were condensed, including its electrochemical characterization<sup>[149]</sup> and the surface chemistry of both isomers on different catalyst materials. Specifically, the adsorption and reactivity of NBD on Pt(111) was assessed in multiple publications,<sup>[161-163]</sup> whereupon both NBD and its photoisomer QC were investigated in a multi-method (XPS, UPS, IRRAS, DFT) study for the first time.<sup>[164]</sup> In addition, photoelectrochemical IRRAS (PEC-IRRAS) experiments with a Pt(111) working electrode in the liquid phase combined the photoconversion from NBD to QC and the electrochemically triggered back conversion, so that information on the reversibility of the system was obtained.<sup>[165]</sup> IRRAS measurements in UHV confirmed the light-induced conversion from NBD to QC on Pt(111) using Michler's ketone as sensitizer.<sup>[325]</sup> Analogously, the reaction behavior of the NBD/QC pair was deduced on Ni(111) by synchrotron radiation-based XPS and UPS measurements, supported by DFT calculations.<sup>[166]</sup>

Having discussed the unsubstituted NBD/QC molecules, selected 2,3-disubstituted derivatives were regarded, categorized into symmetric and asymmetric compounds. As outlined before, enhanced reaction properties are anticipated by means of appropriate substitution of the parent NBD structure. Besides, a different surface chemistry of the derivatives might yield increased activities and/or higher stability limits on the catalyst. Table 4.1 gives an overview of the considered NBD/QC-based systems on the respective surfaces. Data on the absorption onset, the triggered energy release, the stability, and the adsorption are specified if available; detailed results of the particular investigations can be found in the corresponding literature (see references).

As first model system, the reactivity of 2,3-dibromo-NBD/QC (**NBD2**) on Ni(111) was explored by XPS and UPS, whereby DFT calculations resolved the related adsorption motifs.<sup>[167]</sup> In a follow-up study, the 2,3-dicyano-NBD/QC (**NBD3**) couple was investigated on

Ni(111).<sup>[250]</sup> The influence of a heteroatom at the bridgehead position was analyzed for different ester-substituted oxa-NBD/QC pairs on Pt(111), including experiments on 2,3-bis(methylester)-oxa-NBD/QC (**NBD4**).<sup>[302]</sup>

**Table 4.1:** Listing of the considered NBD derivatives (with their respective absorption onset  $\lambda_{\text{Onset}}$ ) in combination with the surface to catalyze the energy release of the corresponding QC isomer under the stated conditions. Subject to availability, the adsorption geometries and stability limits are described. More information can be found in the associated references. Note that derivatized NBD molecules are written in bold. Adapted with permission from Ref. [318] under license CC BY-NC 4.0 DEED. Copyright (2024) John Wiley and Sons.

MOLECULES	$\lambda_{\text{Onset}}$	SURFACE	ENERGY RELEASE	ADSORPTION	STABILITY	REF.
 NBD	267 nm	Pt(111) + sensitizer (MK) Ni(111)	at 125 K or 0.32 $V_{\text{fc}}$ at ~168 K	$\eta^2:\eta^1$ n/a $\eta^2:\eta^2$	thermal: 190 K 96% selectivity thermal: 190 K	[164] [165] [166]
 <b>NBD2</b>	n/a	Ni(111)	at 170 K	“side-on” Br away	partial dissoc. (at 120 K), thermal: 190 K	[167]
 <b>NBD3</b>	345 nm	Ni(111)	at 175 – 260 K	$\eta^2:\eta^2$	thermal: 290 K	[250]
 <b>NBD4</b>	332 nm	Pt(111)	at 310 – 340 K $k = 5.3 \times 10^{-4} \text{ s}^{-1}$	“side-on”-like (bridge oxygen towards surface)	thermal: 380 K > 99% selective	[302]
 <b>NBD5</b>	359 nm	Pt(111) Ni(111) Au(111) HOPG	at 140 – 230 K / instantaneous for $\geq 0.5 V_{\text{fc}}$	no “side-on” oxygen-bound upright standing n/a	thermal: 300 K thermal: 160 K desorption: 250 K 60% selectivity	[270] [270] [290] [296]
 <b>NBD6</b>	380 nm	HOPG	for $\geq 0.3 V_{\text{fc}}$ completed at 0.4 $V_{\text{fc}}$	n/a	$\geq 99.3\%$ selectivity (electrochemical)	[296]
 <b>NBD7</b>	389 nm	Pt(111) HOPG Au(111)	0.02 – 0.92 $V_{\text{fc}}$ 0.02 – 0.82 $V_{\text{fc}}$ $k = 2 \times 10^{-4} \text{ m} \cdot \text{s}^{-1}$	n/a n/a n/a	> 99% reversible 99.8% reversible > 1000 cycles	[315] [316] [287]
 <b>NBD8</b>	310 nm	Au(111)	instantaneous (monolayer)	TOTA in plane, NBD anchored	desorption: 320 K (multi) 600 K (mono)	[288]
 <b>NBD9</b>	n/a	$\text{Co}_3\text{O}_4(111)$	n/a	anchored (chelating), flat/standing	desorption: 240 K (multi) thermal: 400 K	[327]
 <b>NBD10</b>	378 nm	$\text{Co}_3\text{O}_4(111)$	thermal barrier: 103 $\text{kJ mol}^{-1}$ (350 – 370 K)	anchored (chelating)	desorption: 280 K (multi) thermal: 570 K 98.5% reversible	[328] [329]

The asymmetric derivatives were ordered according to their type of initiating the cycloreversion reaction. First, studies with a catalytic trigger were presented: The energy release from the promising push-pull conjugated 2-carbethoxy-3-phenyl-NBD/QC (**NBD5**) pair<sup>[268, 269]</sup> was examined on several surfaces. Synchrotron radiation-based XPS measurements compared the reaction routes on Pt(111) and Ni(111), respectively.<sup>[270]</sup> In a combined liquid-phase and surface science study, the catalytic activity of gold was assessed for the same molecule system.<sup>[290]</sup> Applying an external potential was demonstrated to also induce the cycloreversion, ideally in terms of an autocatalytic reaction pathway; these electrochemical experiments were described next: The influence of the substitution on the energy release was evaluated with PEC-IRRAS spectra of structurally similar derivatives, namely, **NBD5** and **NBD6** that is extended by a methoxy moiety in comparison.<sup>[296]</sup> Moreover, the overall cyclability of 2-cyano-3-(3,4-dimethoxyphenyl)-NBD/QC (**NBD7**) was determined by PEC-IRRAS on Pt(111),<sup>[315]</sup> and subsequently on the HOPG electrode,<sup>[316]</sup> the dependence of the rate constant of the cycloreversion to **NBD7** on the applied potential was revealed on Au(111).<sup>[287]</sup>

Finally, studies on linking NBD molecules to the surface through suitable anchoring groups or platforms were summarized: Among others, trioxatriangulenium (TOTA)-functionalized NBD/QC derivatives (**NBD8**) were shown to be stable under ambient conditions.<sup>[326]</sup> Their ordering and interconversion was explored on Au(111) by use of IRRAS spectroscopy and supporting DFT calculations;<sup>[288]</sup> concerning the catalytic activity of gold for the isomerization, the correspondence to the literature-known single-triplet mechanism of azobenzenes<sup>[289]</sup> was checked. The adsorption and thermal stability of well-defined NBD films of 1-(2'-norbornadienyl)pentanoic acid (**NBD9**) was investigated in IRRAS experiments on Co<sub>3</sub>O<sub>4</sub>(111)/Ir(100).<sup>[327]</sup> The coupling of a switchable NBD unit, specifically 2-cyano-3-(4-carboxyphenyl)-NBD (**NBD10**), to the same semiconducting Co<sub>3</sub>O<sub>4</sub>(111) surface was surveyed regarding its stability, activation barriers, and reversibility;<sup>[328]</sup> furthermore, the system was probed by PEC-IRRAS in solution, whereby the anchored monolayer, prepared in UHV, was measured in the liquid electrolyte.<sup>[329]</sup>

The general technical feasibility of NBD/QC molecules for MOST applications has been stated in process analyses;<sup>[76, 330]</sup> yet, the efficiencies strongly depend on the utilized range of the incoming solar light and the quantum yield of the photoconversion, which is addressed by sophisticated molecular design. Liquid derivatives<sup>[131]</sup> that do not require additional solvents as well as molecules embedded in processable matrices<sup>[154, 155]</sup> feature particular advantages

for an implementation. Hybrid approaches complement the absorption profile of the MOST unit, e.g., by a solar water heating system<sup>[156]</sup> or phase-change material,<sup>[157]</sup> so that the overall efficiency is increased. The stored energy is most accessible in form of heat, while measurements under operation conditions demonstrated the macroscopic heat release from NBD-based systems to be possible.<sup>[153]</sup> Altogether, the appropriate tuning of the physico-chemical parameters<sup>[79]</sup> of the NBD/QC molecule pair enables its applicability.<sup>[56]</sup>

In conclusion, this review illustrated the development of the NBD/QC pair in view of its derivatization and the facile triggering of the energy release on different surfaces. Results of UHV and liquid-phase studies were presented, which involved the photoisomerization to the respective QC derivative and/or the cycloreversion back to the relaxed NBD isomer. That is, information on the adsorption behavior, deduced reaction mechanisms, and the cyclability of the particular molecules was obtained, assessing their practicality as potential MOST system.

---

*Adapted with permission from Ref. [318] under license CC BY-NC 4.0 DEED. Copyright (2024) John Wiley and Sons.*

## 5 Summary

The transition from an infrastructure based on fossil fuels to renewable energy sources is one of the most decisive challenges in the 21<sup>st</sup> century. Due to the intermittent character of solar and wind power, novel energy storage solutions are indispensable to compensate for energy-deficient periods. Alongside photovoltaic approaches, the utilization of sunlight can be realized to store energy in a chemical manner. So-called molecular solar thermal (MOST) systems are of interest, since light harvesting and intrinsic storage are directly combined in one-photon one-molecule processes. This concept makes use of the reversible isomerization between a suitable molecule pair that represents the respective energy-lean and -rich state. Upon irradiation, the photoconversion into the strained isomer is induced, and later the energy-releasing back reaction to the relaxed compound is catalytically triggered on demand. By means of heterogeneous catalysis, a closed energy storage cycle can be proposed for MOST molecules (energy storage, adsorption, energy release, desorption).

In particular, the valence isomers norbornadiene (NBD) and quadricyclane (QC) exhibit advantageous properties for MOST applications: Next to a high energy storage capacity, the photoisomer features a reasonable stability; however, the absorption profile of unsubstituted NBD, with an onset in the UV range, does not coincide sufficiently with the incoming solar spectrum. To overcome this issue, derivatization of the NBD framework with appropriate substituents allows for a redshift of the absorption bands and therefore an enhanced overlap, yielding higher photoconversion efficiencies. Still, the trade-off is an increased molecular weight, resulting in lower energy storage densities. To date, a plethora of synthetically available derivatives is known. Especially, the 2,3-disubstitution of NBD appears viable in terms of large-scale applications.

Surface science investigations support the search for promising molecule and catalyst design. Information on adsorption motifs and thermally induced reaction pathways of interesting NBD/QC derivatives on different materials gives important insights for a knowledge-driven optimization of the respective systems. Thus, in the context of this thesis, fundamental model catalytic studies of several tailored molecules were conducted in a well-

defined ultra-high vacuum (UHV) environment. Specifically, synchrotron radiation-based X-ray photoelectron spectroscopy (XPS) was utilized as surface-sensitive technique. Hereby, the adsorption of the compounds on the catalytic surfaces was observed *in situ* allowing for the identification of spectroscopic fingerprints of the distinct species. Subsequent temperature-programmed measurements unraveled the reaction behavior at elevated temperatures, providing mechanistic findings. Primarily, the feasibility of the cycloreversion from the strained QC derivative to its relaxed NBD isomer was assessed. The extent of this back conversion conditions the practicality of a certain MOST pair. Moreover, the stability boundaries of the considered molecules were determined and, if possible, the decomposition routes specified. The interaction strength between surface species and substrate was available by observation and quantification of desorption processes.

The surface chemistry of the molecule pair 2,3-dicyano-NBD/QC was investigated on Ni(111), whereby (CN)<sub>2</sub>-NBD features a redshifted absorption onset of more than 40 nm, compared to NBD. XP spectra acquired during exposure to (CN)<sub>2</sub>-NBD at 130 K revealed its characteristic line shape and confirmed an intact adsorption without dissociation at low temperatures. The energy-rich (CN)<sub>2</sub>-QC was also stable under these experimental conditions and clearly distinguishable from (CN)<sub>2</sub>-NBD. The energy release in the course of the cycloreversion reaction from (CN)<sub>2</sub>-QC to (CN)<sub>2</sub>-NBD was monitored between 175 and 260 K. Heating to 290 K marked the thermal stability limit of the molecular framework, exceeding that of unsubstituted NBD by about 100 K. At higher temperatures, the detachment of the cyano moieties and the formation of C-H fragments was proposed. Above 400 K, carbide and nitride species were finally observed next to amorphous carbon structures.

The 2-carbethoxy-3-phenyl-derivatization of NBD/QC (PENBD/PEQC) is known to result in advantageous properties regarding application as MOST system: Compared to the parent molecules, the adsorption onset of PENBD is redshifted to 359 nm, while the isomerization proceeds at high quantum yields without any sensitizer, and the photoisomer PEQC exhibits an extraordinarily long half-life. High-resolution XPS investigations on this promising molecule pair were carried out on Pt(111) and Ni(111). The quantitative evaluation of the temperature-programmed XPS (TPXPS) experiments revealed the specific reaction pathways: Utilizing Pt(111) as catalyst surface, the cycloreversion from PEQC to PENBD took place between 140 and 230 K; no side product formation indicated a complete conversion. Unlike to unsubstituted QC on Pt(111), the energy release was accessible at higher temperatures in

---

a controlled manner. Besides, the stability of PENBD was much higher, as the detection of carbon monoxide (CO) constituted the beginning of its fragmentation only above 300 K. On Ni(111), the isomerization to PENBD was not achieved at any temperature, since individual decomposition routes already set in at 160 to 180 K. Notably, in the PENBD experiment, only 10% of the surface species remained after heating to 300 K, namely CO and carbonaceous residues. For PEQC, atomic oxygen was formed above 180 K alongside these decomposition products.

Findings on the kinetics of isomerization reactions stated a very high catalytic effect for gold surfaces. That is, the introduced PENBD/PEQC pair was also surveyed by XPS on a gold film, prepared by physical vapor deposition (PVD) on Pt(111). The adsorption of PENBD and PEQC was conducted at 110 K in dedicated experiments. Still, the collected XP line shapes did not display remarkable differences reasoning the existence of equivalent surface species. Therefore, the instantaneous cycloreversion from PEQC to PENBD was concluded, confirming the high energy release rate induced by gold. Starting the heating ramp of the TPXPS experiment, subtle changes in the XP spectra above 135 K were attributed to a rearrangement of PENBD to more stable adsorption geometries. Above 250 K, the entire PENBD has desorbed molecularly; minor residues on the surface were due to decomposition to a small extent, promoted by defects in the gold film.

Ester-substituted oxa-NBD/QC molecule pairs were investigated on Pt(111) to assess the influence of a heteroatom at the bridgehead within the framework. Functionalization at this position was found to enhance the photoconversion and affects the energy storage density. Moreover, the bridging methylene group of NBD was particularly involved in previous decomposition routes, so that an increased thermal stability of bridge-functionalized NBDs was anticipated. The interaction of hetero-NBD/QC compounds with the Pt(111) catalyst surface was studied in XPS experiments of 2,3-bis(methylester)-NBD/QC (O-NBD/QC) and the extended 2,3-bis(benzylester) derivatives (exO-NBD/QC). The reaction pathways of O-NBD/QC implied rearrangement steps of the molecules on the surface, before the cycloreversion from O-QC to O-NBD took place between 310 and 340 K in a quantitative manner. A remarkable thermal stability limit of 380 K was determined; heating further gave rise to C-H fragments and eventually carbide. The energy release from the extended exO-QC was not observed in the corresponding TPXPS experiment. Instead, simultaneously to the decline of the surface coverage, first changes in the exO-NBD/QC XP spectra were monitored starting at 135 K; the

attribution to CO was indicative of an early decomposition onset, whereby the fragmentation resulted in benzyloxy- and oxa-NBD/QC-like species. The further evolution of CO above 250 or 270 K suggested the existence of phenyl species; beyond 370 K, unspecified C-H fragments and carbide structures emerged.

In conclusion, this thesis comprises fundamental model studies on auspicious NBD/QC derivatives by means of synchrotron radiation-based XPS in order to promote the progress from the unsubstituted parent molecules towards MOSTs tailored by molecular design. To obtain optimal performance in the energy release, the catalytic activity of different materials was assessed. Altogether, information on adsorption motifs, desorption processes, and the interaction strength with the substrate was gained. The general feasibility of the energy release in a specific temperature range was examined in detail. Additionally, the respective stability limits of the molecules were identified, which particularly determine the practicality of the considered systems. In this way, factors to optimize the overall efficiency of derivatized NBD/QC pairs were addressed in terms of a fully reversible energy storage cycle.

## 6 Zusammenfassung

Der Wandel von einer auf fossilen Brennstoffen basierenden Infrastruktur zu erneuerbaren Energiequellen stellt eine der größten Herausforderungen des 21. Jahrhunderts dar. Aufgrund des diskontinuierlichen Charakters von Solar- und Windkraft sind neuartige Energiespeicherlösungen unabdingbar, um energiedefizitäre Zeiträume zu kompensieren. Neben photovoltaischen Lösungen kann Sonnenenergie auf chemische Weise gespeichert werden. Sogenannte molekulare solarthermische Systeme (MOST) sind von Interesse, welche Energiegewinnung und intrinsische Speicherung direkt in Ein-Photon-Ein-Molekül-Prozessen kombinieren. Dieses Konzept nutzt die reversible Isomerisierung zwischen einem geeigneten Molekülpaar, das den jeweiligen energiearmen und -reichen Zustand repräsentiert. Durch Bestrahlung erfolgt die Photoumwandlung in das verspannte Isomer und zu einem späteren Zeitpunkt wird bei Bedarf die energiefreisetzende Rückreaktion zur spannungsfreien Verbindung katalytisch induziert. Mittels heterogener Katalyse kann ein geschlossener Energiespeicherzyklus für MOST-Moleküle realisiert werden (Energiespeicherung, Adsorption, Energiefreisetzung, Desorption).

Im Besonderen weisen die Valenzisomere Norbornadien (NBD) und Quadricyclan (QC) vorteilhafte Eigenschaften für MOST-Anwendungen auf: Neben einer hohen Energiespeicherkapazität zeichnet sich das Photoisomer durch eine adäquate Stabilität aus; allerdings stimmt das Absorptionsprofil von unsubstituiertem NBD, mit einem Beginn im UV-Bereich, nicht ausreichend mit dem Spektrum der Sonne überein. Zur Lösung dieses Problems ermöglicht die Derivatisierung des NBD-Grundgerüsts mit geeigneten Substituenten eine Rotverschiebung der Absorptionsbanden und damit eine vergrößerte Überlappung, wodurch höhere Effizienzen bei der Photoumwandlung erzielt werden. Dabei ist ein Kompromiss mit dem erhöhten Molekulargewicht und den daraus resultierenden niedrigeren Energiespeicherdichten zu finden. Bisher ist eine Vielzahl an synthetisch verfügbaren Derivaten bekannt. Vor allem die 2,3-Disubstituierung von NBD erscheint praktikabel im Sinne einer Anwendung im großtechnischen Maßstab.

Oberflächenuntersuchungen unterstützen die Suche nach vielversprechenden Molekülen und entsprechenden Katalysatoren. Informationen über die Adsorptionsmotive und thermisch induzierte Reaktionspfade interessanter NBD/QC-Derivate auf verschiedenen Materialien geben wichtige Erkenntnisse für eine wissensbasierte Optimierung der jeweiligen Systeme. Deshalb wurden im Rahmen dieser Dissertation grundlegende modellkatalytische Studien von mehreren maßgeschneiderten Molekülen in einer wohldefinierten Ultrahochvakuum-Umgebung durchgeführt. Dabei wurde Synchrotronstrahlung-basierte Röntgenphotoelektronenspektroskopie als oberflächensensitive Methode genutzt, um die Adsorption der Verbindungen auf den katalytischen Oberflächen *in situ* zu beobachten; auf diese Weise konnten spektroskopische Fingerabdrücke der einzelnen Spezies identifiziert werden. Anschließende Temperatur-programmierte Messungen klärten das Reaktionsverhalten bei erhöhten Temperaturen auf, womit mechanistische Befunde erhalten wurden. Vorrangig wurde die Durchführbarkeit der Cycloreversion vom verspannten QC-Derivat zum spannungsfreien NBD-Isomer beurteilt. Das Ausmaß dieser Rückumwandlung bedingt die praktische Anwendbarkeit des jeweiligen MOST-Paars. Zudem wurden die Stabilitätsgrenzen der betrachteten Moleküle bestimmt und, wenn möglich, die Zersetzungswege spezifiziert. Die Beobachtung und Quantifizierung von Desorptionsprozessen ermöglichte Aussagen über die Interaktionsstärke zwischen den Oberflächenspezies und dem Substrat.

Die Oberflächenchemie des Molekülpaars 2,3-Dicyano-NBD/QC wurde auf Ni(111) untersucht, wobei  $(\text{CN})_2\text{-NBD}$  sich durch einen rotverschobenen Absorptionsbeginn von mehr als 40 nm im Vergleich zu NBD auszeichnet. Die XP-Spektren, welche während der Dosierung von  $(\text{CN})_2\text{-NBD}$  bei 130 K aufgenommen wurden, zeigten dessen charakteristisches Linienprofil und bestätigten eine intakte Adsorption ohne Dissoziation bei niedrigen Temperaturen. Das energiereiche  $(\text{CN})_2\text{-QC}$  war unter diesen experimentellen Bedingungen ebenfalls stabil und eindeutig von  $(\text{CN})_2\text{-NBD}$  unterscheidbar. Die Energiefreisetzung im Zuge der Cycloreversion-Reaktion von  $(\text{CN})_2\text{-QC}$  zu  $(\text{CN})_2\text{-NBD}$  wurde zwischen 175 und 260 K festgestellt. Die thermische Stabilitätsgrenze lag bei 290 K und übertraf somit jene von unsubstituiertem NBD um ungefähr 100 K. Bei höheren Temperaturen erfolgte die Abspaltung der Cyano-Gruppen und die Bildung von C-H-Fragmenten. Oberhalb von 400 K waren schließlich Carbid- und Nitrid-Spezies neben amorphen Kohlenstoffstrukturen beobachtbar.

Die 2-Carboethoxy-3-phenyl-Derivatisierung von NBD/QC (PENBD/PEQC) ist bekannt für vorteilhafte Eigenschaften bezüglich ihrer Anwendung als MOST-System: Verglichen mit den Ursprungsmolekülen ist der Absorptionsbeginn von PENBD zu 359 nm rotverschoben, während die Isomerisierung unter hohen Quantenausbeuten ohne Sensibilisatoren abläuft und das Photoisomer PEQC eine außergewöhnlich lange Halbwertszeit aufweist. Hochaufgelöste XPS-Untersuchungen dieses vielversprechenden Molekülpaars wurden auf Pt(111) und Ni(111) durchgeführt. Die quantitative Auswertung der Temperatur-programmierten XPS (TPXPS)-Experimente offenbarte die jeweiligen Reaktionspfade: Bei Verwendung von Pt(111) als Katalysatoroberfläche fand die Cycloreversion von PEQC zu PENBD zwischen 140 und 230 K statt; die Abwesenheit von Nebenprodukten deutete dabei auf eine komplette Umwandlung hin. Im Gegensatz zu unsubstituiertem QC auf Pt(111) war die Energiefreisetzung bei höheren Temperaturen auf eine kontrollierte Weise zugänglich. Außerdem war die Stabilität von PENBD um einiges höher, da erst die Detektion von Kohlenstoffmonoxid (CO) über 300 K auf dessen Fragmentierung hinwies. Auf Ni(111) wurde die Isomerisierung zu PENBD bei keiner Temperatur erreicht, da individuelle Zerfallswege schon bei 160 bis 180 K einsetzten. Auffallend im PENBD-Experiment war, dass nach Heizen auf 300 K nur 10 % der Spezies auf der Oberfläche verblieben, nämlich CO und kohlenstoffhaltige Rückstände. Für PEQC wurde neben diesen Zersetzungsprodukten atomarer Sauerstoff oberhalb von 180 K gebildet.

Untersuchungen zur Kinetik von Isomerisierungsreaktionen zeigten eine sehr hohe katalytische Wirkung von Goldoberflächen. Daher wurde das vorgestellte PENBD/PEQC-Paar auch mittels XPS auf einem Goldfilm charakterisiert, der durch physikalische Gasphasenabscheidung auf Pt(111) präpariert wurde. Die Adsorption von PENBD und PEQC erfolgte bei 110 K in dedizierten Experimenten. Dennoch wiesen die ermittelten XP-Linienprofile keine bemerkenswerten Unterschiede auf, was die Existenz von äquivalenten Oberflächenspezies nahelegte. Die Schlussfolgerung war deshalb die unmittelbare Cycloreversion von PEQC zu PENBD, was die hohe Rate der Energiefreisetzung durch Gold bestätigte. Nach Starten der Heizrampe im TPXPS-Experiment wurden geringfügige Änderungen in den XP-Spektren, beginnend bei 135 K, einer Umlagerung von PENBD in stabilere Adsorptionsgeometrien zugeschrieben. Oberhalb von 250 K war die molekulare Desorption des gesamten PENBD abgeschlossen; Defekte im Goldfilm begünstigten die Zersetzung in geringem Umfang, wodurch kleinere Rückstände auf der Oberfläche überblieben.

Ester-substituierte Oxa-NBD/QC-Molekülpaare wurden auf Pt(111) untersucht, um den Einfluss eines Heteroatoms im Brückenkopf des Grundgerüsts zu beurteilen. Die Funktionalisierung an dieser Position zeigte eine begünstigte Photoumwandlung und beeinflusst die Energiespeicherdichte. Darüber hinaus war die überbrückende Methylengruppe besonders an zuvor aufgeklärten Zersetzungswegen beteiligt, so dass eine erhöhte thermische Stabilität für brückenfunktionalisierte NBDs erwartet wurde. Die Wechselwirkung von Hetero-NBD/QC-Verbindungen mit der Pt(111)-Katalysatoroberfläche wurde in XPS-Experimenten von 2,3-Bis(methylester)-NBD/QC (O-NBD/QC) und den erweiterten 2,3-Bis(benzylester)-Derivaten (exO-NBD/QC) erforscht. In den Reaktionspfaden von O-NBD/QC traten Umlagerungsschritte der Moleküle auf der Oberfläche auf, bevor die Cycloreversion von O-QC zu O-NBD zwischen 310 und 340 K in quantitativem Umfang stattfand. Eine bemerkenswerte thermische Stabilität von 380 K wurde festgestellt; weiteres Hochheizen führte zu C-H-Fragmenten und schließlich Carbid. Die Energiefreisetzung vom erweiterten exO-QC wurde im dazugehörigen TPXPS-Experiment nicht beobachtet. Stattdessen waren gleichzeitig zur Abnahme der Oberflächenbedeckung, beginnend bei 135 K, erste Veränderungen in den exO-NBD/QC-XP-Spektren ersichtlich; die Zuordnung zu CO wies auf einen frühen Zerfallsbeginn hin, wobei die Fragmentierung in Benzyloxid- und Oxa-NBD/QC-ähnlichen Spezies resultierte. Die weitere Entstehung von CO über 250 bzw. 270 K legte die Existenz von Phenyl-Spezies nahe; oberhalb von 370 K entstanden unspezifizierte C-H-Fragmente und Carbid-Strukturen.

Insgesamt umfasst diese Dissertation grundlegende Modellstudien zu vielversprechenden NBD/QC-Derivaten mittels Synchrotronstrahlung-basierten XPS, um die Entwicklung von den unsubstituierten Ursprungsmolekülen hin zum molekularen Design von MOSTs voranzutreiben. Die Aktivität verschiedener Katalysatormaterialien wurde hinsichtlich einer optimalen Energiefreisetzung bewertet. Zusammenfassend wurden Informationen über Adsorptionmotive, Desorptionsprozesse und die Stärke der Wechselwirkung mit dem Substrat erhalten. Die allgemeine Realisierbarkeit der Energiefreisetzung in einem spezifischen Temperaturbereich wurde detailliert untersucht. Zusätzlich entscheiden die ermittelten Stabilitätsgrenzen der jeweiligen Moleküle maßgeblich über die praktische Anwendbarkeit der betrachteten Systeme. Auf diesem Weg wurden Faktoren zur Optimierung der Gesamteffizienz von derivatisierten NBD/QC-Paaren im Sinne eines vollständig reversiblen Energiespeicherzyklus adressiert.

## 7 Bibliography

- [1] C. Rosenzweig, D. Karoly, M. Vicarelli, P. Neofotis, Q. Wu, G. Casassa, A. Menzel, T. L. Root, N. Estrella, B. Seguin, P. Tryjanowski, C. Liu, S. Rawlins, A. Imeson, *Nature* **2008**, *453*, 353-357.
- [2] F. Piontek, L. Drouet, J. Emmerling, T. Kompas, A. Méjean, C. Otto, J. Rising, B. Soergel, N. Taconet, M. Tavoni, *Nat. Clim. Change* **2021**, *11*, 563-572.
- [3] M. Hübler, G. Klepper, S. Peterson, *Ecol. Econ.* **2008**, *68*, 381-393.
- [4] B. S. Levy, J. A. Patz, *Ann. Glob. Health* **2015**, *81*, 310-322.
- [5] S. Sippel, N. Meinshausen, E. M. Fischer, E. Székely, R. Knutti, *Nat. Clim. Change* **2020**, *10*, 35-41.
- [6] S. Zhou, B. Yu, Y. Zhang, *Sci. Adv.* **2023**, *9*, eabo1638.
- [7] S. Arrhenius, *Philos. Mag.* **1896**, *41*, 237-276.
- [8] J. Uppenbrink, *Science* **1996**, *272*, 1122-1122.
- [9] Z. Liu, Z. Deng, S. Davis, P. Ciais, *Nat. Rev. Earth Environ.* **2023**, *4*, 205-206.
- [10] N. S. Lewis, D. G. Nocera, *Proc. Natl. Acad. Sci. U.S.A.* **2006**, *103*, 15729-15735.
- [11] Fraunhofer-Gesellschaft zur Förderung der angewandten Forschung e.V., Fraunhofer-Institut für Solare Energiesysteme ISE, Freiburg, *Energy-Charts*, <https://www.energy-charts.info> (accessed on 03.03.2023).
- [12] J. Delbeke, A. Runge-Metzger, Y. Slingenberg, J. Werksman, in *Towards a Climate-Neutral Europe: Curbing the Trend* (Eds.: J. Delbeke, P. Vis), Routledge, London, **2019**, pp. 24-45.
- [13] S. N. Seo, *Reg. Sci. Policy Pract.* **2017**, *9*, 121-140.
- [14] A. J. Weaver, K. Zickfeld, A. Montenegro, M. Eby, *Geophys. Res. Lett.* **2007**, *34*, L19703.
- [15] M. Meinshausen, N. Meinshausen, W. Hare, S. C. Raper, K. Frieler, R. Knutti, D. J. Frame, M. R. Allen, *Nature* **2009**, *458*, 1158-1162.
- [16] H. L. van Soest, M. G. J. den Elzen, D. P. van Vuuren, *Nat. Commun.* **2021**, *12*, 2140.
- [17] AGEBA AG Energiebilanzen e.V., *Energy Consumption in Germany in 2022*, <https://ag-energiebilanzen.de> (accessed on 29.08.2023).
- [18] S. Shafiee, E. Topal, *Energy Policy* **2009**, *37*, 181-189.
- [19] M. Höök, X. Tang, *Energy Policy* **2013**, *52*, 797-809.
- [20] D. Shindell, C. J. Smith, *Nature* **2019**, *573*, 408-411.
- [21] J. Kotcher, E. Maibach, W. T. Choi, *BMC Public Health* **2019**, *19*, 1079.
- [22] L. W. Davis, *J. Econ. Perspect.* **2012**, *26*, 49-66.

- [23] D. Jahn, S. Korolczuk, *Environ. Politics* **2012**, *21*, 159-164.
- [24] D. Gielen, F. Boshell, D. Saygin, M. D. Bazilian, N. Wagner, R. Gorini, *Energy Strategy Rev.* **2019**, *24*, 38-50.
- [25] C. Breyer, S. Khalili, D. Bogdanov, M. Ram, A. S. Oyewo, A. Aghahosseini, A. Gulagi, A. A. Solomon, D. Keiner, G. Lopez, P. A. Østergaard, H. Lund, B. V. Mathiesen, M. Z. Jacobson, M. Victoria, S. Teske, T. Pregger, V. Fthenakis, M. Raugei, H. Holttinen, U. Bardi, A. Hoekstra, B. K. Sovacool, *IEEE Access* **2022**, *10*, 78176-78218.
- [26] G. Kopp, J. L. Lean, *Geophys. Res. Lett.* **2011**, *38*, L01706.
- [27] G. W. Crabtree, N. S. Lewis, *Physics Today* **2007**, *60*, 37-42.
- [28] C. G. Granqvist, *Adv. Mater.* **2003**, *15*, 1789-1803.
- [29] S. R. Wenham, M. A. Green, *Prog. Photovolt.: Res. Appl.* **1996**, *4*, 3-33.
- [30] D. Wöhrle, D. Meissner, *Adv. Mater.* **1991**, *3*, 129-138.
- [31] J. Gong, C. Li, M. R. Wasielewski, *Chem. Soc. Rev.* **2019**, *48*, 1862-1864.
- [32] M. A. Green, E. D. Dunlop, M. Yoshita, N. Kopidakis, K. Bothe, G. Siefer, X. Hao, *Prog. Photovolt.: Res. Appl.* **2023**, *31*, 651-663.
- [33] A. K. Singh, R. R. Singh, in *Innovations in Power and Advanced Computing Technologies (i-PACT)*, IEEE, Kuala Lumpur, Malaysia, **2021**, pp. 1-6.
- [34] M. S. Chowdhury, K. S. Rahman, T. Chowdhury, N. Nuthammachot, K. Techato, M. Akhtaruzzaman, S. K. Tiong, K. Sopian, N. Amin, *Energy Strategy Rev.* **2020**, *27*, 100431.
- [35] I. J. Pérez-Arriaga, C. Batlle, *Econ. Energy Environ. Policy* **2012**, *1*, 3-18.
- [36] J. P. Barton, D. G. Infield, *IEEE Trans. Energy Convers.* **2004**, *19*, 441-448.
- [37] H. Zsiborács, N. H. Baranyai, A. Vincze, L. Zentkó, Z. Birkner, K. Máté, G. Pintér, *Electronics* **2019**, *8*, 729.
- [38] R. J. Brodd, K. R. Bullock, R. A. Leising, R. L. Middaugh, J. R. Miller, E. Takeuchi, *J. Electrochem. Soc.* **2004**, *151*, K1.
- [39] S. Hameer, J. L. van Niekerk, *Int. J. Energy Res.* **2015**, *39*, 1179-1195.
- [40] C. Aoxia, P. K. Sen, in *IEEE Industry Applications Society Annual Meeting*, IEEE, Portland, OR, USA, **2016**, pp. 1-10.
- [41] Y. Sun, Z. Zhao, M. Yang, D. Jia, W. Pei, B. Xu, *CSEE J. Power Energy Syst.* **2019**, *6*, 160-173.
- [42] A. R. Dehghani-Saniij, E. Tharumalingam, M. B. Dusseault, R. Fraser, *Renew. Sustain. Energy Rev.* **2019**, *104*, 192-208.
- [43] C. Thies, K. Kieckhäfer, T. S. Spengler, M. S. Sodhi, *Procedia CIRP* **2019**, *80*, 292-297.
- [44] F. Schüth, *Chem. Ing. Tech.* **2011**, *83*, 1984-1993.
- [45] V. Balzani, A. Credi, M. Venturi, *ChemSusChem* **2008**, *1*, 26-58.

- [46] K. Moth-Poulsen, D. Coso, K. Börjesson, N. Vinokurov, S. K. Meier, A. Majumdar, K. P. C. Vollhardt, R. A. Segalman, *Energy Environ. Sci.* **2012**, *5*, 8534–8537.
- [47] A. Lennartson, K. Moth-Poulsen, in *Molecular Devices for Solar Energy Conversion and Storage* (Eds.: H. Tian, G. Boschloo, A. Hagfeldt), Springer Nature, Singapore, **2018**, pp. 327-352.
- [48] K. Moth-Poulsen, in *Organic Synthesis and Molecular Engineering* (Ed.: M. B. Nielsen), John Wiley and Sons, Hoboken, New Jersey, **2013**, pp. 179-196.
- [49] K. Börjesson, A. Lennartson, K. Moth-Poulsen, *ACS Sustain. Chem. Eng.* **2013**, *1*, 585-590.
- [50] T. J. Kucharski, Y. C. Tian, S. Akbulatov, R. Boulatov, *Energy Environ. Sci.* **2011**, *4*, 4449-4472.
- [51] A. Lennartson, A. Roffey, K. Moth-Poulsen, *Tetrahedron Lett.* **2015**, *56*, 1457-1465.
- [52] C. L. Sun, C. Wang, R. Boulatov, *ChemPhotoChem* **2019**, *3*, 268-283.
- [53] Q. Qiu, Y. Shi, G. G. D. Han, *J. Mater. Chem. C* **2021**, *9*, 11444-11463.
- [54] Z. Wang, P. Erhart, T. Li, Z.-Y. Zhang, D. Sampedro, Z. Hu, H. A. Wegner, O. Brummel, J. Libuda, M. B. Nielsen, K. Moth-Poulsen, *Joule* **2021**, *5*, 3116-3136.
- [55] A. Gimenez-Gomez, L. Magson, B. Peñin, N. Sanosa, J. Soilán, R. Losantos, D. Sampedro, *Photochem* **2022**, *2*, 694-716.
- [56] Z. Wang, H. Hölzel, K. Moth-Poulsen, *Chem. Soc. Rev.* **2022**, *51*, 7313-7326.
- [57] G. N. Lewis, T. T. Magel, D. Lipkin, *J. Am. Chem. Soc.* **1940**, *62*, 2973-2980.
- [58] D. Schulte-Frohlinde, H. Blume, H. Güsten, *J. Phys. Chem.* **1962**, *66*, 2486-2491.
- [59] D. H. Waldeck, *Chem. Rev.* **1991**, *91*, 415-436.
- [60] C. Bastianelli, V. Caia, G. Cum, R. Gallo, V. Mancini, *J. Chem. Soc. Perkin Trans. 2* **1991**, 679-683.
- [61] H. Taoda, K. Hayakawa, K. Kawase, H. Yamakita, *J. Chem. Eng. Jpn.* **1987**, *20*, 265-270.
- [62] A. R. Dias, M. E. Minas Da Piedade, J. A. Martinho Simões, J. A. Simoni, C. Teixeira, H. P. Diogo, Y. Meng-Yan, G. Pilcher, *J. Chem. Thermodyn.* **1992**, *24*, 439-447.
- [63] A. Goulet-Hanssens, M. Utecht, D. Mutruc, E. Titov, J. Schwarz, L. Grubert, D. Bleger, P. Saalfrank, S. Hecht, *J. Am. Chem. Soc.* **2017**, *139*, 335-341.
- [64] H. M. Bandara, S. C. Burdette, *Chem. Soc. Rev.* **2012**, *41*, 1809-1825.
- [65] K. Masutani, M. A. Morikawa, N. Kimizuka, *Chem. Commun.* **2014**, *50*, 15803-15806.
- [66] Z. Wang, R. Losantos, D. Sampedro, M. Morikawa, K. Börjesson, N. Kimizuka, K. Moth-Poulsen, *J. Mater. Chem. A* **2019**, *7*, 15042-15047.
- [67] H. D. Becker, *Chem. Rev.* **1993**, *93*, 145-172.
- [68] G. Jones, T. E. Reinhardt, W. R. Bergmark, *Sol. Energy* **1978**, *20*, 241-248.
- [69] H. Bouas-Laurent, J.-P. Desvergne, A. Castellan, R. Lapouyade, *Chem. Soc. Rev.* **2000**, *29*, 43-55.
- [70] K. P. C. Vollhardt, T. W. Weidman, *J. Am. Chem. Soc.* **1983**, *105*, 1676-1677.
- [71] R. Boese, J. K. Cammack, A. J. Matzger, K. Pflug, W. B. Tolman, K. P. C. Vollhardt, T. W. Weidman, *J. Am. Chem. Soc.* **1997**, *119*, 6757-6773.

- [72] Y. Kanai, V. Srinivasan, S. K. Meier, K. P. Vollhardt, J. C. Grossman, *Angew. Chem. Int. Ed.* **2010**, *49*, 8926-8929.
- [73] K. Börjesson, D. Cósó, V. Gray, J. C. Grossman, J. Guan, C. B. Harris, N. Hertkorn, Z. Hou, Y. Kanai, D. Lee, J. P. Lomont, A. Majumdar, S. K. Meier, K. Moth-Poulsen, R. L. Myrabo, S. C. Nguyen, R. A. Segalman, V. Srinivasan, W. B. Tolman, N. Vinokurov, K. P. Vollhardt, T. W. Weidman, *Chem. Eur. J.* **2014**, *20*, 15587-15604.
- [74] A. Lennartson, A. Lundin, K. Börjesson, V. Gray, K. Moth-Poulsen, *Dalton Trans.* **2016**, *45*, 8740-8744.
- [75] J. Orrego-Hernández, H. Hölzel, Z. Wang, M. Quant, K. Moth-Poulsen, in *Molecular Photoswitches, Vol. 1* (Ed.: Z. L. Pianowski), Wiley-VCH, Weinheim, **2022**, pp. 350-378.
- [76] C. Philippopoulos, D. Economou, C. Economou, J. Marangozis, *Ind. Eng. Chem. Res.* **1983**, *22*, 627-633.
- [77] V. A. Bren', A. D. Dubonosov, V. I. Minkin, V. A. Chernoiyanov, *Russ. Chem. Rev.* **1991**, *60*, 451-469.
- [78] A. D. Dubonosov, V. A. Bren, V. A. Chernoiyanov, *Russ. Chem. Rev.* **2002**, *71*, 917-927.
- [79] J. Orrego-Hernández, A. Dreos, K. Moth-Poulsen, *Acc. Chem. Res.* **2020**, *53*, 1478-1487.
- [80] G. Jones, S.-H. Chiang, P. T. Xuan, *J. Photochem.* **1979**, *10*, 1-18.
- [81] H.-D. Scharf, J. Fleischhauer, H. Leismann, I. Ressler, W. Schleker, R. Weitz, *Angew. Chem. Int. Ed.* **1979**, *18*, 652-662.
- [82] Z.-i. Yoshida, *J. Photochem.* **1985**, *29*, 27-40.
- [83] D. S. Kabakoff, J. C. G. Buenzli, J. F. M. Oth, W. B. Hammond, J. A. Berson, *J. Am. Chem. Soc.* **1975**, *97*, 1510-1512.
- [84] X. W. An, Y. D. Xie, *Thermochim. Acta* **1993**, *220*, 17-25.
- [85] M. J. Kuisma, A. M. Lundin, K. Moth-Poulsen, P. Hyldgaard, P. Erhart, *J. Phys. Chem. C* **2016**, *120*, 3635-3645.
- [86] D. M. Gates, *Science* **1966**, *151*, 523-529.
- [87] S. Miki, Y. Asako, Z.-i. Yoshida, *Chem. Lett.* **1987**, *16*, 195-198.
- [88] G. S. Hammond, P. Wyatt, C. D. DeBoer, N. J. Turro, *J. Am. Chem. Soc.* **1964**, *86*, 2532-2533.
- [89] T. Arai, T. Oguchi, T. Wakabayashi, M. Tsuchiya, Y. Nishimura, S. Oishi, H. Sakuragi, K. Tokumaru, *Bull. Chem. Soc. Jpn.* **1987**, *60*, 2937-2943.
- [90] H. Taoda, K. Hayakawa, K. Kawase, *J. Chem. Eng. Jpn.* **1987**, *20*, 335-338.
- [91] S. Murov, G. S. Hammond, *J. Phys. Chem.* **1968**, *72*, 3797-3801.
- [92] A. Cuppoletti, J. P. Dinnocenzo, J. L. Goodman, I. R. Gould, *J. Phys. Chem. A* **1999**, *103*, 11253-11256.
- [93] N. J. Turro, W. R. Cherry, M. F. Mirbach, M. J. Mirbach, *J. Am. Chem. Soc.* **1977**, *99*, 7388-7390.

- 
- [94] A. M. Helms, R. A. Caldwell, *J. Am. Chem. Soc.* **1995**, *117*, 358-361.
- [95] S. Lahiry, C. Haldar, *Sol. Energy* **1986**, *37*, 71-73.
- [96] L. Pan, J.-J. Zou, X. Zhang, L. Wang, *Ind. Eng. Chem. Res.* **2010**, *49*, 8526-8531.
- [97] D. J. Fife, W. M. Moore, K. W. Morse, *J. Am. Chem. Soc.* **1985**, *107*, 7077-7083.
- [98] P. A. Grutsch, C. Kutal, *J. Am. Chem. Soc.* **1986**, *108*, 3108-3110.
- [99] W. L. Dilling, *Chem. Rev.* **1966**, *66*, 373-393.
- [100] Y. Harel, A. W. Adamson, C. Kutal, P. A. Grutsch, K. Yasufuku, *J. Phys. Chem.* **1987**, *91*, 901-904.
- [101] M. Quant, A. Lennartson, A. Dreos, M. Kuisma, P. Erhart, K. Börjesson, K. Moth-Poulsen, *Chem. Eur. J.* **2016**, *22*, 13265-13274.
- [102] M. Quant, A. Hamrin, A. Lennartson, P. Erhart, K. Moth-Poulsen, *J. Phys. Chem. C* **2019**, *123*, 7081-7087.
- [103] R. Hoffmann, R. B. Woodward, *J. Am. Chem. Soc.* **1965**, *87*, 2046-2048.
- [104] R. B. Woodward, R. Hoffmann, *Angew. Chem. Int. Ed.* **1969**, *8*, 781-853.
- [105] C. Qin, Z. Zhao, S. R. Davis, *J. Mol. Struct.* **2005**, *728*, 67-70.
- [106] H. M. Frey, *J. Chem. Soc.* **1964**, 365-367.
- [107] G. S. Hammond, N. J. Turro, A. Fischer, *J. Am. Chem. Soc.* **1961**, *83*, 4674-4675.
- [108] H. Hogeveen, H. C. Volger, *J. Am. Chem. Soc.* **1967**, *89*, 2486-2487.
- [109] O. Diels, K. Alder, *Liebigs Ann.* **1931**, *490*, 236-242.
- [110] J. Hyman, Belgian Patent BE 498176, **1951**.
- [111] L. Schmerling, J. P. Luvisi, R. W. Welch, *J. Am. Chem. Soc.* **1956**, *78*, 2819-2821.
- [112] S. J. Cristol, R. P. Arganbright, G. D. Brindell, R. M. Heitz, *J. Am. Chem. Soc.* **1957**, *79*, 6035-6039.
- [113] J. Hine, J. A. Brown, L. H. Zalkow, W. E. Gardner, M. Hine, *J. Am. Chem. Soc.* **1954**, *77*, 594-598.
- [114] A. F. Plate, M. A. Pryanishnikova, *Bull. Acad. Sci. USSR, Div. Chem. Sci.* **1956**, *5*, 753-754.
- [115] L. Brjussowa, *Chem. Zentralblatt* **1936**, *107*, 2385-2386.
- [116] M. Lipp, *Ber. Dtsch. Chem. Ges.* **1941**, *74*, 1-6.
- [117] S. J. Cristol, *Tetrahedron* **1986**, *42*, 1617-1619.
- [118] Y. Hirshberg, E. Fischer, *J. Chem. Soc.* **1953**, 629-636.
- [119] C. D. Smith, *Org. Synth.* **1971**, *51*, 133-136.
- [120] W. G. Dauben, R. L. Cargill, *Tetrahedron* **1961**, *15*, 197-201.
- [121] K. Jorner, A. Dreos, R. Emanuelsson, O. El Bakouri, I. Fdez. Galván, K. Börjesson, F. Feixas, R. Lindh, B. Zietz, K. Moth-Poulsen, H. Ottosson, *J. Mater. Chem. A* **2017**, *5*, 12369-12378.
- [122] E. Vessally, *J. Iran. Chem. Soc.* **2009**, *6*, 99-103.
- [123] H. Prinzbach, *Pure Appl. Chem.* **1968**, *16*, 17-46.
- [124] M. Mansø, A. U. Petersen, Z. Wang, P. Erhart, M. B. Nielsen, K. Moth-Poulsen, *Nat. Commun.* **2018**, *9*, 1945.
-

- [125] M. Mansø, B. E. Tebikachew, K. Moth-Poulsen, M. B. Nielsen, *Org. Biomol. Chem.* **2018**, *16*, 5585-5590.
- [126] A. D. Dubonosov, S. V. Galichev, V. A. Chernoiyanov, V. A. Bren, V. I. Minkin, *Russ. J. Org. Chem.* **2001**, *37*, 67-71.
- [127] M. D. Kilde, M. Mansø, N. Ree, A. U. Petersen, K. Moth-Poulsen, K. V. Mikkelsen, M. B. Nielsen, *Org. Biomol. Chem.* **2019**, *17*, 7735-7746.
- [128] G. Kaupp, H. Prinzbach, *Helv. Chim. Acta* **1969**, *52*, 956-966.
- [129] V. Gray, A. Lennartson, P. Ratanaalert, K. Börjesson, K. Moth-Poulsen, *Chem. Commun.* **2014**, *50*, 5330-5332.
- [130] M. Jevric, A. U. Petersen, M. Mansø, S. Kumar Singh, Z. Wang, A. Dreos, C. Sumbly, M. B. Nielsen, K. Börjesson, P. Erhart, K. Moth-Poulsen, *Chem. Eur. J.* **2018**, *24*, 12767-12772.
- [131] A. Dreos, Z. Wang, J. Udmark, A. Ström, P. Erhart, K. Börjesson, M. B. Nielsen, K. Moth-Poulsen, *Adv. Energy Mater.* **2018**, *8*, 1703401.
- [132] M. Jevric, Z. Wang, A. U. Petersen, M. Mansø, C. J. Sumbly, M. B. Nielsen, K. Moth-Poulsen, *Eur. J. Org. Chem.* **2019**, *2019*, 2354-2361.
- [133] M. Mansø, A. U. Petersen, K. Moth-Poulsen, M. B. Nielsen, *Org. Biomol. Chem.* **2020**, *18*, 2113-2119.
- [134] M. Kuisma, A. Lundin, K. Moth-Poulsen, P. Hyldgaard, P. Erhart, *ChemSusChem* **2016**, *9*, 1786-1794.
- [135] J. L. Elholm, A. E. Hillers-Bendtsen, H. Hölzel, K. Moth-Poulsen, K. V. Mikkelsen, *Phys. Chem. Chem. Phys.* **2022**, *24*, 28956-28964.
- [136] N. Ree, M. Koerstz, K. V. Mikkelsen, J. H. Jensen, *J. Chem. Phys.* **2021**, *155*, 184105.
- [137] K. C. Bishop, *Chem. Rev.* **1976**, *76*, 461-486.
- [138] R. B. King, S. Ikai, *Inorg. Chem.* **1979**, *18*, 949-954.
- [139] J. Manassen, *J. Catal.* **1970**, *18*, 38-45.
- [140] M. J. Chen, H. M. Feder, *Inorg. Chem.* **1979**, *18*, 1864-1869.
- [141] F. D. Mango, J. H. Schachtschneider, *J. Am. Chem. Soc.* **1967**, *89*, 2484-2486.
- [142] G. F. Koser, P. R. Pappas, S.-M. Yu, *Tetrahedron Lett.* **1973**, *14*, 4943-4946.
- [143] L. Cassar, J. Halpern, *Chem. Commun.* **1970**, 1082-1083.
- [144] P. G. Gassman, R. Yamaguchi, G. F. Koser, *J. Org. Chem.* **1978**, *43*, 4392-4393.
- [145] E. Haselbach, T. Bally, Z. Lanyiova, P. Baertschi, *Helv. Chim. Acta* **1979**, *62*, 583-592.
- [146] J. L. Gębicki, J. Gębicki, J. Mayer, *J. Radiat. Phys. Chem.* **1987**, *30*, 165-167.
- [147] K. Yasufuku, K. Takahashi, C. Kutal, *Tetrahedron Lett.* **1984**, *25*, 4893-4896.
- [148] P. G. Gassman, J. W. Hershberger, *J. Org. Chem.* **1987**, *52*, 1337-1339.

- [149] O. Brummel, D. Besold, T. Döpfer, Y. Wu, S. Bochmann, F. Lazzari, F. Waidhas, U. Bauer, P. Bachmann, C. Papp, H.-P. Steinrück, A. Görling, J. Libuda, J. Bachmann, *ChemSusChem* **2016**, *9*, 1424-1432.
- [150] Z. Wang, H. Moïse, M. Cacciarini, M. B. Nielsen, M. A. Morikawa, N. Kimizuka, K. Moth-Poulsen, *Adv. Sci.* **2021**, *8*, 2103060.
- [151] S. Miki, Y. Asako, M. Morimoto, T. Ohno, Z.-i. Yoshida, T. Maruyama, M. Fukuoka, T. Takada, *Bull. Chem. Soc. Jpn.* **1988**, *61*, 973-981.
- [152] S. Miki, T. Maruyama, T. Ohno, T. Tohma, S.-i. Toyama, Z.-i. Yoshida, *Chem. Lett.* **1988**, *17*, 861-864.
- [153] Z. Wang, A. Roffey, R. Losantos, A. Lennartson, M. Jevric, A. U. Petersen, M. Quant, A. Dreos, X. Wen, D. Sampedro, K. Börjesson, K. Moth-Poulsen, *Energy Environ. Sci.* **2019**, *12*, 187-193.
- [154] A. U. Petersen, A. I. Hofmann, M. Fillols, M. Mansø, M. Jevric, Z. Wang, C. J. Sumby, C. Müller, K. Moth-Poulsen, *Adv. Sci.* **2019**, *6*, 1900367.
- [155] Z. Refaa, A. Hofmann, M. F. Castro, J. O. Hernandez, Z. Wang, H. Hölzel, J. W. Andreasen, K. Moth-Poulsen, A. S. Kalagasidis, *Appl. Energy* **2022**, *310*, 118541.
- [156] A. Dreos, K. Börjesson, Z. Wang, A. Roffey, Z. Norwood, D. Kushnir, K. Moth-Poulsen, *Energy Environ. Sci.* **2017**, *10*, 728-734.
- [157] V. Kashyap, S. Sakunkaewkasem, P. Jafari, M. Nazari, B. Eslami, S. Nazifi, P. Irajizad, M. D. Marquez, T. R. Lee, H. Ghasemi, *Joule* **2019**, *3*, 3100-3111.
- [158] Z. Wang, Z. Wu, Z. Hu, J. Orrego-Hernández, E. Mu, Z.-Y. Zhang, M. Jevric, Y. Liu, X. Fu, F. Wang, T. Li, K. Moth-Poulsen, *Cell Rep. Phys. Sci.* **2022**, *3*, 100789.
- [159] J. Orrego-Hernández, H. Hölzel, M. Quant, Z. Wang, K. Moth-Poulsen, *Eur. J. Org. Chem.* **2021**, *2021*, 5337-5342.
- [160] G. Ertl, *Angew. Chem. Int. Ed.* **2008**, *47*, 3524-3535.
- [161] E. L. Muetterties, *Pure Appl. Chem.* **1982**, *54*, 83-96.
- [162] M. C. Tsai, J. Stein, C. M. Friend, E. L. Muetterties, *J. Am. Chem. Soc.* **1982**, *104*, 3533-3534.
- [163] M. J. Hostetler, R. G. Nuzzo, G. S. Girolami, L. H. Dubois, *Organometallics* **1995**, *14*, 3377-3384.
- [164] U. Bauer, S. Mohr, T. Döpfer, P. Bachmann, F. Späth, F. Düll, M. Schwarz, O. Brummel, L. Fromm, U. Pinkert, A. Görling, A. Hirsch, J. Bachmann, H.-P. Steinrück, J. Libuda, C. Papp, *Chem. Eur. J.* **2017**, *23*, 1613-1622.
- [165] O. Brummel, F. Waidhas, U. Bauer, Y. Wu, S. Bochmann, H.-P. Steinrück, C. Papp, J. Bachmann, J. Libuda, *J. Phys. Chem. Lett.* **2017**, *8*, 2819-2825.
- [166] U. Bauer, L. Fromm, C. Weiß, P. Bachmann, F. Späth, F. Düll, J. Steinhauer, W. Hieringer, A. Görling, A. Hirsch, H.-P. Steinrück, C. Papp, *J. Phys. Chem. C* **2019**, *123*, 7654-7664.

- [167] U. Bauer, L. Fromm, C. Weiß, F. Späth, P. Bachmann, F. Düll, J. Steinhauer, S. Matysik, A. Pominov, A. Görling, A. Hirsch, H.-P. Steinrück, C. Papp, *J. Chem. Phys.* **2019**, *150*, 184706.
- [168] K. Siegbahn, C. Nordling, A. Fahlman, R. Nordberg, K. Hamrin, J. Hedman, G. Johansson, T. Bergmark, S.-E. Karlsson, I. Lindgren, B. Lindberg, *ESCA: Atomic, Molecular and Solid State Structure Studied by means of Electron Spectroscopy*, Almqvist & Wiksell, Uppsala, **1967**.
- [169] C. Papp, H.-P. Steinrück, *Surf. Sci. Rep.* **2013**, *68*, 446-487.
- [170] H. P. Bonzel, C. Kleint, *Prog. Surf. Sci.* **1995**, *49*, 107-153.
- [171] P. van der Heide, *X-ray Photoelectron Spectroscopy: An introduction to Principles and Practices*, John Wiley and Sons, Hoboken, New Jersey, **2012**.
- [172] H. Hertz, *Ann. Phys.* **1887**, *267*, 983-1000.
- [173] W. Hallwachs, *Ann. Phys.* **1888**, *269*, 301-312.
- [174] P. Lenard, *Ann. Phys.* **1900**, *307*, 359-375.
- [175] P. Lenard, *Ann. Phys.* **1902**, *313*, 149-198.
- [176] A. Einstein, *Ann. Phys.* **1905**, *322*, 132-148.
- [177] K. Siegbahn, K. Edvarson, *Nucl. Phys.* **1956**, *1*, 137-159.
- [178] K. Siegbahn, *J. Electron. Spectrosc. Relat. Phenom.* **1974**, *5*, 3-97.
- [179] K. Siegbahn, *Pure Appl. Chem.* **1976**, *48*, 77-97.
- [180] K. Siegbahn, *Rev. Mod. Phys.* **1982**, *54*, 709-728.
- [181] N. H. Turner, J. A. Schreifels, *Anal. Chem.* **1996**, *68*, 309-332.
- [182] C. S. Fadley, *J. Electron. Spectrosc. Relat. Phenom.* **2010**, *178-179*, 2-32.
- [183] P. S. Bagus, E. S. Ilton, C. J. Nelin, *Surf. Sci. Rep.* **2013**, *68*, 273-304.
- [184] C. R. Brundle, A. D. Baker, *Electron Spectroscopy: Theory, Techniques and Applications, Vol. 2*, Academic Press, London, New York, **1978**.
- [185] D. Briggs, M. P. Seah, *Practical Surface Analysis: Auger and X-Ray Photoelectron Spectroscopy*, 2nd ed., John Wiley and Sons, Chichester, West Sussex, **1990**.
- [186] S. Hüfner, *Photoelectron Spectroscopy: Principles and Applications*, 3rd ed., Springer-Verlag, Berlin, Heidelberg, **2003**.
- [187] K. Oura, V. Lifshits, A. Saranin, A. Zotov, M. Katayama, *Surface science: An introduction*, Springer-Verlag, Berlin, Heidelberg, **2003**.
- [188] S. Hüfner, *Very High Resolution Photoelectron Spectroscopy*, Springer-Verlag, Berlin, Heidelberg, **2007**.
- [189] K. W. Kolasinski, *Surface Science: Foundations of Catalysis and Nanoscience*, 3rd ed., John Wiley and Sons, Chichester, West Sussex, **2012**.
- [190] D. P. Woodruff, *Modern Techniques of Surface Science*, 3rd ed., Cambridge University Press, Cambridge, **2016**.

- 
- [191] F. A. Stevie, C. L. Donley, *J. Vac. Sci. Technol. A* **2020**, *38*, 063204.
- [192] T. Koopmans, *Physica* **1934**, *1*, 104-113.
- [193] W. Heisenberg, *Z. Phys.* **1927**, *43*, 172-198.
- [194] D. Coster, R. D. L. Kronig, *Physica* **1935**, *2*, 13-24.
- [195] C. C. Chang, *Surf. Sci.* **1971**, *25*, 53-79.
- [196] P. J. Potts, P. C. Webb, *J. Geochem. Explor.* **1992**, *44*, 251-296.
- [197] J. F. Moulder, W. F. Stickle, P. E. Sobol, K. D. Bomben, *Handbook of X-ray Photoelectron Spectroscopy: A Reference Book of Standard Spectra for Identification and Interpretation of XPS Data*, Physical Electronics, Eden Prairie, Minnesota, **1995**.
- [198] U. Gelius, *Phys. Scr.* **1974**, *9*, 133-147.
- [199] W. F. Egelhoff, *Surf. Sci. Rep.* **1987**, *6*, 253-415.
- [200] U. Gelius, E. Basilier, S. Svensson, T. Bergmark, K. Siegbahn, *J. Electron. Spectrosc. Relat. Phenom.* **1973**, *2*, 405-434.
- [201] N. Mårtensson, A. Nilsson, *J. Electron Spectrosc. Relat. Phenom.* **1990**, *52*, 1-46.
- [202] H. Tillborg, A. Nilsson, N. Mårtensson, *J. Electron. Spectrosc. Relat. Phenom.* **1993**, *62*, 73-93.
- [203] A. Föhlisch, J. Hasselström, O. Karis, D. Menzel, N. Mårtensson, A. Nilsson, *J. Electron. Spectrosc. Relat. Phenom.* **1999**, *101-103*, 303-308.
- [204] G. Wedler, H.-J. Freund, *Lehrbuch der Physikalischen Chemie*, 6th ed., Wiley-VCH, Weinheim, **2012**.
- [205] H.-P. Steinrück, T. Fuhrmann, C. Papp, B. Tränkenschuh, R. Denecke, *J. Chem. Phys.* **2006**, *125*, 204706.
- [206] C. J. Powell, A. Jablonski, *Nucl. Instrum. Methods Phys. Res. A* **2009**, *601*, 54-65.
- [207] M. P. Seah, W. A. Dench, *Surf. Interface Anal.* **1979**, *1*, 2-11.
- [208] M. P. Seah, *Surf. Interface Anal.* **1980**, *2*, 222-239.
- [209] M. P. Seah, M. T. Anthony, *Surf. Interface Anal.* **1984**, *6*, 230-241.
- [210] R. F. Reilman, A. Msezane, S. T. Manson, *J. Electron. Spectrosc. Relat. Phenom.* **1976**, *8*, 389-394.
- [211] D. P. Woodruff, *Surf. Sci.* **1994**, *299-300*, 183-198.
- [212] D. Woodruff, *Surf. Sci. Rep.* **2007**, *62*, 1-38.
- [213] C. S. Fadley, *Prog. Surf. Sci.* **1984**, *16*, 275-388.
- [214] B. D. Patterson, *Am. J. Phys.* **2011**, *79*, 1046-1052.
- [215] J. Als-Nielsen, D. McMorrow, *Elements of Modern X-ray Physics*, 2nd ed., John Wiley and Sons, Chichester, West Sussex, **2011**.
- [216] P. Willmott, *An Introduction to Synchrotron Radiation: Techniques and Applications*, John Wiley and Sons, Chichester, West Sussex, **2011**.
- [217] J. Stöhr, *NEXAFS Spectroscopy*, Springer-Verlag, Berlin, Heidelberg, **1992**.
-

- [218] E. M. McMillan, *Phys. Rev.* **1945**, *68*, 143-144.
- [219] H. Wiedemann, *Particle Accelerator Physics*, 4th ed., Springer International Publishing, Cham, **2015**.
- [220] J. D. Jackson, *Klassische Elektrodynamik*, 5th ed., De Gruyter, Berlin, Boston, **2014**.
- [221] K. Wille, *Rep. Prog. Phys.* **1991**, *54*, 1005-1067.
- [222] J. Falta, T. Möller, *Forschung mit Synchrotronstrahlung: Eine Einführung in die Grundlagen und Anwendungen*, Vieweg+Teubner Verlag, Wiesbaden, **2010**.
- [223] S. Mobilio, F. Boscherini, C. Meneghini, *Synchrotron Radiation: Basics, Methods and Applications*, Springer-Verlag, Berlin, Heidelberg, **2015**.
- [224] G. Brown, K. Halbach, J. Harris, H. Winick, *Nucl. Instrum. Methods Phys. Res.* **1983**, *208*, 65-77.
- [225] K. J. Kim, *Nucl. Instrum. Methods Phys. Res.* **1984**, *219*, 425-429.
- [226] W. B. Peatman, *Gratings, Mirrors and Slits: Beamline Design for Soft X-Ray Synchrotron Radiation Sources*, Routledge, London, **1997**.
- [227] R. Denecke, M. Kinne, C. M. Whelan, H.-P. Steinrück, *Surf. Rev. Lett.* **2002**, *09*, 797-801.
- [228] M. Kinne, Ph.D. thesis, Friedrich-Alexander-Universität Erlangen-Nürnberg (Erlangen), **2004**.
- [229] C. Gleichweit, Ph.D. thesis, Friedrich-Alexander-Universität Erlangen-Nürnberg (Erlangen), **2015**.
- [230] D. Roy, D. Tremblay, *Rep. Prog. Phys.* **1990**, *53*, 1621-1674.
- [231] H. Ibach, *Electron Spectroscopy for Surface Analysis*, Springer-Verlag, Berlin, Heidelberg, **1997**.
- [232] F. Hadjarab, J. L. Erskine, *J. Electron. Spectrosc. Relat. Phenom.* **1985**, *36*, 227-243.
- [233] H. Bubert, J. C. Rivière, W. S. M. Werner, in *Surface and Thin Film Analysis* (Eds.: G. Friedbacher, H. Bubert), Wiley-VCH, Weinheim, **2011**, pp. 7-41.
- [234] Helmholtz-Zentrum Berlin für Materialien und Energie, *JLSRF* **2016**, *2*, A72.
- [235] C. C. Leon, J. G. Lee, S. T. Ceyer, *J. Phys. Chem. C* **2014**, *118*, 29043-29057.
- [236] J. W. A. Sachtler, G. A. Somorjai, *J. Catal.* **1983**, *81*, 77-79.
- [237] B. Vogt, B. Schmiedeskamp, U. Heinzmann, *Z. Phys. B Con. Mat.* **1990**, *80*, 359-364.
- [238] E. R. Cohen, T. Cvitaš, J. G. Frey, B. Holmström, K. Kuchitsu, R. Marquardt, I. Mills, F. Pavese, M. Quack, J. Stohner, H. L. Strauss, M. Takami, A. J. Thor, *Quantities, Units and Symbols in Physical Chemistry*, 3rd ed., RSC Publishing, Cambridge, **2007**.
- [239] A. Baraldi, G. Comelli, S. Lizzit, D. Cocco, G. Paolucci, R. Rosei, *Surf. Sci.* **1996**, *367*, L67-L72.
- [240] D. A. Shirley, *Phys. Rev. B* **1972**, *5*, 4709-4714.
- [241] S. Tougaard, *Surf. Interface Anal.* **1988**, *11*, 453-472.
- [242] S. Doniach, M. Šunjić, *J. Phys. C: Solid State Phys.* **1970**, *3*, 285-291.
- [243] W. Zhao, S. M. Kozlov, O. Höfert, K. Gotterbarm, M. P. A. Lorenz, F. Viñes, C. Papp, A. Görling, H.-P. Steinrück, *J. Phys. Chem. Lett.* **2011**, *2*, 759-764.

- [244] G. Odahara, S. Otani, C. Oshima, M. Suzuki, T. Yasue, T. Koshikawa, *Surf. Sci.* **2011**, *605*, 1095-1098.
- [245] R. Addou, A. Dahal, P. Sutter, M. Batzill, *Appl. Phys. Lett.* **2012**, *100*, 021601.
- [246] M. Kinne, T. Fuhrmann, C. M. Whelan, J. F. Zhu, J. Pantförder, M. Probst, G. Held, R. Denecke, H.-P. Steinrück, *J. Chem. Phys.* **2002**, *117*, 10852-10859.
- [247] O. Björneholm, A. Nilsson, H. Tillborg, P. Bennich, A. Sandell, B. Hernnäs, C. Puglia, N. Mårtensson, *Surf. Sci.* **1994**, *315*, L983-L989.
- [248] F. Bondino, G. Comelli, F. Esch, A. Locatelli, A. Baraldi, S. Lizzit, G. Paolucci, R. Rosei, *Surf. Sci.* **2000**, *459*, L467-L474.
- [249] A. Cudok, H. Froitzheim, M. Schulze, *Phys. Rev. B* **1993**, *47*, 13682-13686.
- [250] F. Hemauer, U. Bauer, L. Fromm, C. Weiß, A. Leng, P. Bachmann, F. Düll, J. Steinhauer, V. Schwaab, R. Grzonka, A. Hirsch, A. Görling, H.-P. Steinrück, C. Papp, *ChemPhysChem* **2022**, *23*, e202200199.
- [251] D. P. Woodruff, A. M. Bradshaw, *Rep. Prog. Phys.* **1994**, *57*, 1029-1080.
- [252] I. Chorkendorff, J. N. Russell, J. T. Yates, *J. Chem. Phys.* **1987**, *86*, 4692-4700.
- [253] S. X. Huang, D. A. Fischer, J. L. Gland, *J. Phys. Chem.* **1996**, *100*, 13629-13635.
- [254] S. Lehwald, H. Ibach, *Surf. Sci.* **1979**, *89*, 425-445.
- [255] R. Haerle, E. Riedo, A. Pasquarello, A. Baldereschi, *Phys. Rev. B* **2001**, *65*, 045101.
- [256] J. Diaz, G. Paolicelli, S. Ferrer, F. Comin, *Phys. Rev. B* **1996**, *54*, 8064-8069.
- [257] P. K. Chu, L. Li, *Mater. Chem. Phys.* **2006**, *96*, 253-277.
- [258] C. Ronning, H. Feldermann, R. Merk, H. Hofsäss, P. Reinke, J. U. Thiele, *Phys. Rev. B* **1998**, *58*, 2207-2215.
- [259] A. Wiltner, C. Linsmeier, *phys. stat. sol. (a)* **2004**, *201*, 881-887.
- [260] M. Wei, Q. Fu, Y. Yang, W. Wei, E. Crumlin, H. Bluhm, X. H. Bao, *J. Phys. Chem. C* **2015**, *119*, 13590-13597.
- [261] R. Gouttebaron, S. Bourgeois, M. Perdureau, *Surf. Sci.* **2000**, *458*, 239-246.
- [262] T. Nakayama, K. Inamura, Y. Inoue, S. Ikeda, K. Kishi, *Surf. Sci.* **1987**, *179*, 47-58.
- [263] M. J. Grunze, J. Fühler, M. Neumann, C. R. Brundle, D. J. Auerbach, J. Behm, *Surf. Sci.* **1984**, *139*, 109-120.
- [264] C. N. R. Rao, G. Ranga Rao, *Surf. Sci. Rep.* **1991**, *13*, 223-263.
- [265] W. F. Egelhoff, *Phys. Rev. B* **1984**, *29*, 3681-3683.
- [266] K. Kishi, Y. Ehara, *Surf. Sci.* **1986**, *176*, 567-577.
- [267] J. C. Hemminger, E. L. Muetterties, G. A. Somorjai, *J. Am. Chem. Soc.* **1979**, *101*, 62-67.
- [268] P. Lorenz, T. Luchs, A. Hirsch, *Chem. Eur. J.* **2021**, *27*, 4993-5002.
- [269] T. Luchs, P. Lorenz, A. Hirsch, *ChemPhotoChem* **2020**, *4*, 52-58.

- [270] F. Hemauer, V. Schwaab, E. M. Freiberger, N. J. Waleska, A. Leng, C. Weiß, J. Steinhauer, F. Düll, P. Bachmann, A. Hirsch, H.-P. Steinrück, C. Papp, *Chem. Eur. J.* **2023**, *29*, e202203759.
- [271] F. Bournel, C. Laffon, P. Parent, G. Tourillon, *Surf. Sci.* **1996**, *350*, 60-78.
- [272] R. Zhang, A. J. Hensley, J. S. McEwen, S. Wickert, E. Darlatt, K. Fischer, M. Schoppke, R. Denecke, R. Streber, M. Lorenz, C. Papp, H.-P. Steinrück, *Phys. Chem. Chem. Phys.* **2013**, *15*, 20662-20671.
- [273] G. B. Fisher, J. L. Gland, *Surf. Sci.* **1980**, *94*, 446-455.
- [274] C. Papp, T. Fuhrmann, B. Tränkenschuh, R. Denecke, H.-P. Steinrück, *Phys. Rev. B* **2006**, *73*, 235426.
- [275] M. Castonguay, J. R. Roy, P. H. McBreen, *Langmuir* **2000**, *16*, 8306-8310.
- [276] E. Zahidi, M. Castonguay, P. McBreen, *J. Am. Chem. Soc.* **1994**, *116*, 5847-5856.
- [277] C. Papp, R. Denecke, H.-P. Steinrück, *Langmuir* **2007**, *23*, 5541-5547.
- [278] G. Held, J. Schuler, W. Sklarek, H.-P. Steinrück, *Surf. Sci.* **1998**, *398*, 154-171.
- [279] M. Castonguay, J. R. Roy, A. Rochefort, P. H. McBreen, *J. Am. Chem. Soc.* **2000**, *122*, 518-524.
- [280] W. Kuch, M. Schulze, W. Schnurnberger, K. Bolwin, *Surf. Sci.* **1993**, *287-288*, 600-604.
- [281] T. Pache, H.-P. Steinrück, W. Huber, D. Menzel, *Surf. Sci.* **1989**, *224*, 195-214.
- [282] J. Ontaneda, R. E. J. Nicklin, A. Cornish, A. Roldan, R. Grau-Crespo, G. Held, *J. Phys. Chem. C* **2016**, *120*, 27490-27499.
- [283] E. Zahidi, M. Castonguay, P. H. McBreen, *J. Phys. Chem.* **1995**, *99*, 17906-17916.
- [284] J. Wang, M. Castonguay, J. R. Roy, E. Zahidi, P. H. McBreen, *J. Phys. Chem. B* **1999**, *103*, 4382-4386.
- [285] Y. Bai, D. Kirvassilis, L. Xu, M. Mavrikakis, *Surf. Sci.* **2019**, *679*, 240-253.
- [286] M. K. Rajumon, K. Prabhakaran, C. N. R. Rao, *Surf. Sci.* **1990**, *233*, L237-L242.
- [287] E. Franz, C. Stumm, F. Waidhas, M. Bertram, M. Jevric, J. Orrego-Hernández, H. Hölzel, K. Moth-Poulsen, O. Brummel, J. Libuda, *ACS Catal.* **2022**, *12*, 13418-13425.
- [288] R. Eschenbacher, T. Xu, E. Franz, R. Löw, T. Moje, L. Fromm, A. Görling, O. Brummel, R. Herges, J. Libuda, *Nano Energy* **2022**, *95*, 107007.
- [289] A. Schlimm, R. Löw, T. Rusch, F. Röhricht, T. Strunskus, T. Tellkamp, F. Sönnichsen, U. Manthe, O. Magnussen, F. Tuczek, R. Herges, *Angew. Chem. Int. Ed.* **2019**, *58*, 6574-6578.
- [290] R. Eschenbacher, F. Hemauer, E. Franz, A. Leng, V. Schwaab, N. J. Waleska-Wellnhofer, E. M. Freiberger, L. Fromm, T. Xu, A. Görling, A. Hirsch, H.-P. Steinrück, C. Papp, O. Brummel, J. Libuda, *ChemPhotoChem* **2024**, *8*, e202300155.
- [291] M. A. van Spronsen, K.-J. Weststrate, A. den Dunnen, M. E. van Reijzen, C. Hahn, L. B. F. Juurlink, *J. Phys. Chem. C* **2016**, *120*, 8693-8703.
- [292] B. D. Kay, K. R. Lykke, J. R. Creighton, S. J. Ward, *J. Chem. Phys.* **1989**, *91*, 5120-5121.

- [293] R. G. Quiller, T. A. Baker, X. Deng, M. E. Colling, B. K. Min, C. M. Friend, *J. Chem. Phys.* **2008**, *129*, 064702.
- [294] J. Luthin, C. Linsmeier, *Surf. Sci.* **2000**, *454-456*, 78-82.
- [295] J. A. Herron, J. Scaranto, P. Ferrin, S. Li, M. Mavrikakis, *ACS Catalysis* **2014**, *4*, 4434-4445.
- [296] E. Franz, D. Krappmann, L. Fromm, T. Luchs, A. Görling, A. Hirsch, O. Brummel, J. Libuda, *ChemSusChem* **2022**, *15*, e202201483.
- [297] F. Hoffmann, *Surf. Sci. Rep.* **1983**, *3*, 107-192.
- [298] H. A. Pearce, N. Sheppard, *Surf. Sci.* **1976**, *59*, 205-217.
- [299] R. G. Greenler, D. R. Snider, D. Witt, R. S. Sorbello, *Surf. Sci.* **1982**, *118*, 415-428.
- [300] T. Iwasita, F. C. Nart, *Prog. Surf. Sci.* **1997**, *55*, 271-340.
- [301] E. L. Pace, L. J. Noe, *J. Chem. Phys.* **1968**, *49*, 5317-5325.
- [302] F. Hemauer, D. Krappmann, V. Schwaab, Z. Hussain, E. M. Freiberger, N. J. Waleska-Wellnhofer, E. Franz, F. Hampel, O. Brummel, J. Libuda, A. Hirsch, H.-P. Steinrück, C. Papp, *J. Chem. Phys.* **2023**, *159*, 074703.
- [303] R. I. Kvon, S. V. Koscheev, A. I. Boronin, *J. Mol. Catal. A: Chem.* **2000**, *158*, 297-300.
- [304] I. Matolínová, V. Johánek, J. Mysliveček, K. C. Prince, T. Skála, M. Škoda, N. Tsud, M. Vorokhta, V. Matolín, *Surf. Interface Anal.* **2011**, *43*, 1325-1331.
- [305] C. Witt, M.-C. Schmidt, C. Schröder, S. Schauermann, B. Hartke, *J. Phys. Chem. C* **2021**, *125*, 26167-26179.
- [306] G. Sinha, O. Heikkinen, M. Vestberg, L. Mether, K. Nordlund, J. Lahtinen, *Surf. Sci.* **2014**, *620*, 9-16.
- [307] T. Bürgi, F. Atamny, R. Schlögl, A. Baiker, *J. Phys. Chem. B* **2000**, *104*, 5953-5960.
- [308] K. M. Thom, J. G. Ekerdt, *Surf. Sci.* **2009**, *603*, 921-932.
- [309] S. Sundaresan, K. R. Kaza, *Surf. Sci.* **1985**, *160*, 103-121.
- [310] H. Ihm, J. M. White, *J. Phys. Chem. B* **2000**, *104*, 6202-6211.
- [311] H. Cabibil, H. Ihm, J. M. White, *Surf. Sci.* **2000**, *447*, 91-104.
- [312] C. T. Campbell, G. Ertl, H. Kuipers, J. Segner, *Surf. Sci.* **1981**, *107*, 207-219.
- [313] P. Radloff, G. Mitchell, C. Greenlief, J. White, C. Mims, *Surf. Sci.* **1987**, *183*, 377-402.
- [314] K. Rendulic, B. Sexton, *J. Catal.* **1982**, *78*, 126-135.
- [315] F. Waidhas, M. Jevric, L. Fromm, M. Bertram, A. Görling, K. Moth-Poulsen, O. Brummel, J. Libuda, *Nano Energy* **2019**, *63*, 103872.
- [316] F. Waidhas, M. Jevric, M. Bosch, T. Yang, E. Franz, Z. Liu, J. Bachmann, K. Moth-Poulsen, O. Brummel, J. Libuda, *J. Mater. Chem. A* **2020**, *8*, 15658-15664.
- [317] E. Franz, J. Jung, A. Kunz, H. A. Wegner, O. Brummel, D. Mollenhauer, J. Libuda, *J. Phys. Chem. Lett.* **2023**, *14*, 1470-1477.

- [318] F. Hemaue, H.-P. Steinrück, C. Papp, *ChemPhysChem* **2024**, *25*, e202300806.
- [319] S. J. Cristol, R. L. Snell, *J. Am. Chem. Soc.* **1954**, *76*, 5000.
- [320] S. J. Cristol, R. L. Snell, *J. Am. Chem. Soc.* **1958**, *80*, 1950-1952.
- [321] H. Bouas-Laurent, H. Dürr, *Pure Appl. Chem.* **2001**, *73*, 639-665.
- [322] K. J. Spivack, J. V. Walker, M. J. Sanford, B. R. Rupert, A. R. Ehle, J. M. Tocyloski, A. N. Jahn, L. M. Shaak, O. Obianyo, K. M. Usher, F. E. Goodson, *J. Org. Chem.* **2017**, *82*, 1301-1315.
- [323] P. Lainé, V. Marvaud, A. Gourdon, J.-P. Launay, R. Argazzi, C.-A. Bignozzi, *Inorg. Chem.* **1996**, *35*, 711-714.
- [324] M. Nucci, M. Marazzi, L. M. Frutos, *ACS Sustainable Chem. Eng.* **2019**, *7*, 19496-19504.
- [325] M. Schwarz, C. Schuschke, T. N. Silva, S. Mohr, F. Waidhas, O. Brummel, J. Libuda, *Rev. Sci. Instrum.* **2019**, *90*, 024105.
- [326] R. Löw, T. Rusch, T. Moje, F. Rohricht, O. M. Magnussen, R. Herges, *Beilstein J. Org. Chem.* **2019**, *15*, 1815-1821.
- [327] M. Schwarz, S. Mohr, T. Xu, T. Döpfer, C. Weiß, K. Civale, A. Hirsch, A. Görling, J. Libuda, *J. Phys. Chem. C* **2017**, *121*, 11508-11518.
- [328] C. Schuschke, C. Hohner, M. Jevric, A. Ugleholdt Petersen, Z. Wang, M. Schwarz, M. Kettner, F. Waidhas, L. Fromm, C. J. Sumbly, A. Görling, O. Brummel, K. Moth-Poulsen, J. Libuda, *Nat. Commun.* **2019**, *10*, 2384.
- [329] M. Bertram, F. Waidhas, M. Jevric, L. Fromm, C. Schuschke, M. Kastenmeier, A. Görling, K. Moth-Poulsen, O. Brummel, J. Libuda, *J. Chem. Phys.* **2020**, *152*, 044708.
- [330] C. Philippopoulos, J. Marangozis, *Ind. Eng. Chem. Prod. Res. Dev.* **1984**, *23*, 458-466.

---

## Acknowledgments – Danksagung

An dieser Stelle möchte ich denjenigen Personen Dank aussprechen, welche die Anfertigung meiner Dissertation ermöglicht haben und mich während meines Promotionsvorhabens unterstützt haben:

Mein besonderer Dank gilt zunächst Prof. Hans-Peter Steinrück für die Möglichkeit der Absolvierung meiner Doktorarbeit an seinem Lehrstuhl (FAU, Physikalische Chemie II). Als Teil hiervon konnte ich von dem äußerst angenehmen und ausgesprochen kollegialen als auch produktiven Arbeitsumfeld profitieren, wobei alle Arbeitsabläufe stets hervorragend organisiert waren. In allen wissenschaftlichen Belangen und darüber hinaus trugen konstruktive und gleichzeitig motivierende Diskussionen mit ihm maßgeblich zum erfolgreichen Abschluss der Projekte bei.

Gleichermaßen möchte ich Prof. Christian Papp meine Wertschätzung für die kompetente und umfassende Betreuung ausdrücken. Der aufschlussreiche und voranbringende Austausch mit ihm war unabdingbar für die Auswertung und Veröffentlichung der wissenschaftlichen Daten. Dabei waren seine hilfreichen Korrekturen und ideenreichen Vorschläge unverzichtbarer Bestandteil für ein bestmögliches Resultat. Für die Planung und Absprache der Experimente, insbesondere während Strahlzeit am Synchrotron, stand er jederzeit zur Verfügung. Auch danke ich für die Anstellung in seinem vorherigen und entstehenden Arbeitskreis (FU, Angewandte Physikalische Chemie).

Die erste Einarbeitung in die Thematik und Methodik verdanke ich Dr. Phiona Bachmann im Rahmen meiner zugrundeliegenden Masterarbeit, während Dr. Udo Bauer mir die thematische Bearbeitung erleichterte. Für kleinere Programmierhilfen bin ich Alexander Wolfram dankbar. Neben wissenschaftlichen Gesprächen stand mir mein Kollege Valentin Schwaab als Freund immer zur Seite.

Die Arbeit und Messungen am Synchrotron, einschließlich des Transports und der Montage der Anlage, erfordern zusätzlich zu Disziplin und Organisation in erster Linie Teamfähigkeit. In den zahlreichen Messzeiten war ein Zusammenhalt in der Synchrotrongruppe tags und nachts gegeben. Für die tatkräftige Unterstützung möchte ich mich ausdrücklich bei meinen Kolleginnen und Kollegen Natalie Waleska-Wellnhofer, Eva Marie Freiburger, Valentin Schwaab und Marius Steinmetz sowie den ehemaligen Mitgliedern Dr. Udo Bauer, Dr. Phiona Bachmann, Dr. Fabian Düll und Dr. Johann Steinhauer bedanken.

Im Zuge der fruchtbaren Kooperationen gilt zudem mein Dank den Inhabern und Mitarbeitern der entsprechenden Lehrstühle: Die essenziellen Synthesen der neuartigen und nichttrivialen Derivate wurden von Dr. Cornelius Weiß, Andreas Leng und Daniel Krappmann unter

---

Prof. Andreas Hirsch (FAU, Organische Chemie II) realisiert. Komplementäre infrarotspektroskopische Experimente wurden von Roman Eschenbacher, Evanie Franz und Zarah Hussain mit Beteiligung von Dr. Tao Xu und Dr. Olaf Brummel unter Prof. Jörg Libuda (FAU, Katalytische Grenzflächenforschung) durchgeführt und ergänzten bedeutsam die Erkenntnisse mehrerer vorgestellter Studien. Unterstützende Dichtefunktionaltheorie-Rechnungen wurden von Dr. Lukas Fromm unter Prof. Andreas Görling (FAU, Theoretische Chemie) bereitgestellt. Die Aufklärung der aufgezeigten Kristallstruktur erfolgte von Dr. Frank Hampel unter Prof. Henry Dube (FAU, Organische Chemie I). Vielen Dank für die Beiträge in den jeweiligen Veröffentlichungen.

Des Weiteren bedanke ich mich für die Zusammenarbeit mit Robert Grzonka und Vanessa Geller, welche ihre Bachelorarbeiten unter meiner Betreuung anfertigten, sowie Mattis Goßler und Zarah Hussain im Rahmen ihres Praktikums bei mir. Außerdem wurde dankenswerterweise die Koordination universitärer Angelegenheiten von Dr. Florian Maier, Akad. Dir. und Dr. Andreas Bayer, Akad. ORat übernommen. Überdies halfen die technischen Angestellten der Fortgeschrittenen-Praktika der Physikalischen Chemie zuvorkommend bei der studentischen Betreuung.

Nicht zuletzt sind die Expertise und das Mitwirken derjenigen zu nennen, welche den wissenschaftlichen Betrieb überhaupt erst möglich machen: Bezüglich aller Probleme technischer Natur waren Dipl.-Ing. Bernd Kreß (Vakuum-Technik) und Hans-Peter Bäumler (Elektronik) die ersten Ansprechpartner, wobei auf ihre umfangreiche Hilfe stets Verlass war. Weiterer Dank gilt Friedhold Wölfel als Leiter der Mechanikwerkstatt und dessen Team sowie Norman Anja Schmidt (IT-Administration). Unerlässlich waren ebenso die Sekretärinnen Susana Kreß, Andrea Meixner-Wolf und Christiane Karasev (FU Berlin).

Auch allen restlichen Mitgliedern des Lehrstuhls für Physikalische Chemie II gebührt Dank für die gegenseitige Unterstützung und Schaffung der außerordentlichen Arbeitsatmosphäre. Bei dieser Gelegenheit bedanke ich mich weiterhin bei den Gutachtern, Prüfern und allen zuständigen Universitätsorganen im Verlauf der Promotion.

Abschließend möchte ich mich herzlich bei meiner Familie bedanken, welche mir meine universitäre Ausbildung ermöglicht hat und mich in allen Lebenslagen und jeglicher Hinsicht bedingungslos unterstützt. Danke an meine Eltern, meine Schwester, meinen Schwager und meine Partnerin.

---

## Appendix

### A.1 Publication [P1] – (CN)<sub>2</sub>-NBD/QC on Ni(111)

*Surface Chemistry of the Molecular Solar Thermal Energy Storage System 2,3-Dicyano-Norbornadiene/Quadricyclane on Ni(111)*

Felix Hemauer, Udo Bauer, Lukas Fromm, Cornelius Weiß, Andreas Leng, Philipp Bachmann, Fabian Düll, Johann Steinhauer, Valentin Schwaab, Robert Grzonka, Andreas Hirsch, Andreas Görling, Hans-Peter Steinrück, and Christian Papp

*ChemPhysChem* **2022**, *23*, e202200199 (<https://doi.org/10.1002/cphc.202200199>), plus Cover Profile (<https://doi.org/10.1002/cphc.202200552>), and Front Cover 16/2022 (<https://doi.org/10.1002/cphc.202200553>).

Reprinted with permission from Ref. [250] under license CC BY-NC-ND 4.0 DEED. Copyright (2022) John Wiley and Sons.

### A.2 Publication [P2] – PENBD/PEQC on Pt(111) and Ni(111)

*Surface Studies on the Energy Release of the MOST System 2-Carboxy-3-Phenyl-Norbornadiene/Quadricyclane (PENBD/PEQC) on Pt(111) and Ni(111)*

Felix Hemauer, Valentin Schwaab, Eva Marie Freiberger, Natalie J. Waleska, Andreas Leng, Cornelius Weiß, Johann Steinhauer, Fabian Düll, Philipp Bachmann, Andreas Hirsch, Hans-Peter Steinrück, and Christian Papp

*Chem. Eur. J.* **2023**, *29*, e202203759 (<https://doi.org/10.1002/chem.202203759>), plus Cover Feature 25/2023 (<https://doi.org/10.1002/chem.202300994>).

Reprinted with permission from Ref. [270] under license CC BY 4.0 DEED. Copyright (2023) John Wiley and Sons.

### A.3 Publication [P3] – PENBD/PEQC on Au

*Au-Catalyzed Energy Release in a Molecular Solar Thermal (MOST) System: A Combined Liquid-Phase and Surface Science Study*

Roman Eschenbacher<sup>+</sup>, Felix Hemauer<sup>+</sup>, Evanie Franz, Andreas Leng, Valentin Schwaab, Natalie J. Waleska-Wellenhofer, Eva Marie Freiberger, Lukas Fromm, Tao Xu, Andreas Görling, Andreas Hirsch, Hans-Peter Steinrück, Christian Papp, Olaf Brummel, and Jörg Libuda

[<sup>+</sup>] These authors contributed equally.

*ChemPhotoChem* **2024**, *8*, e202300155 (<https://doi.org/10.1002/cptc.202300155>).

Reprinted with permission from Ref. [290] under license CC BY 4.0 DEED. Copyright (2023) John Wiley and Sons.

---

## A.4 Publication [P4] – O-NBD/QC and exO-NBD/QC on Pt(111)

*Surface science and liquid phase investigations of oxanorbornadiene/oxaquadricyclane ester derivatives as molecular solar thermal energy storage systems on Pt(111)*

Felix Hemauer, Daniel Krappmann, Valentin Schwaab, Zarah Hussain, Eva Marie Freiburger, Natalie J. Waleska-Wellnhofer, Evanie Franz, Frank Hampel, Olaf Brummel, Jörg Libuda, Andreas Hirsch, Hans-Peter Steinrück, and Christian Papp

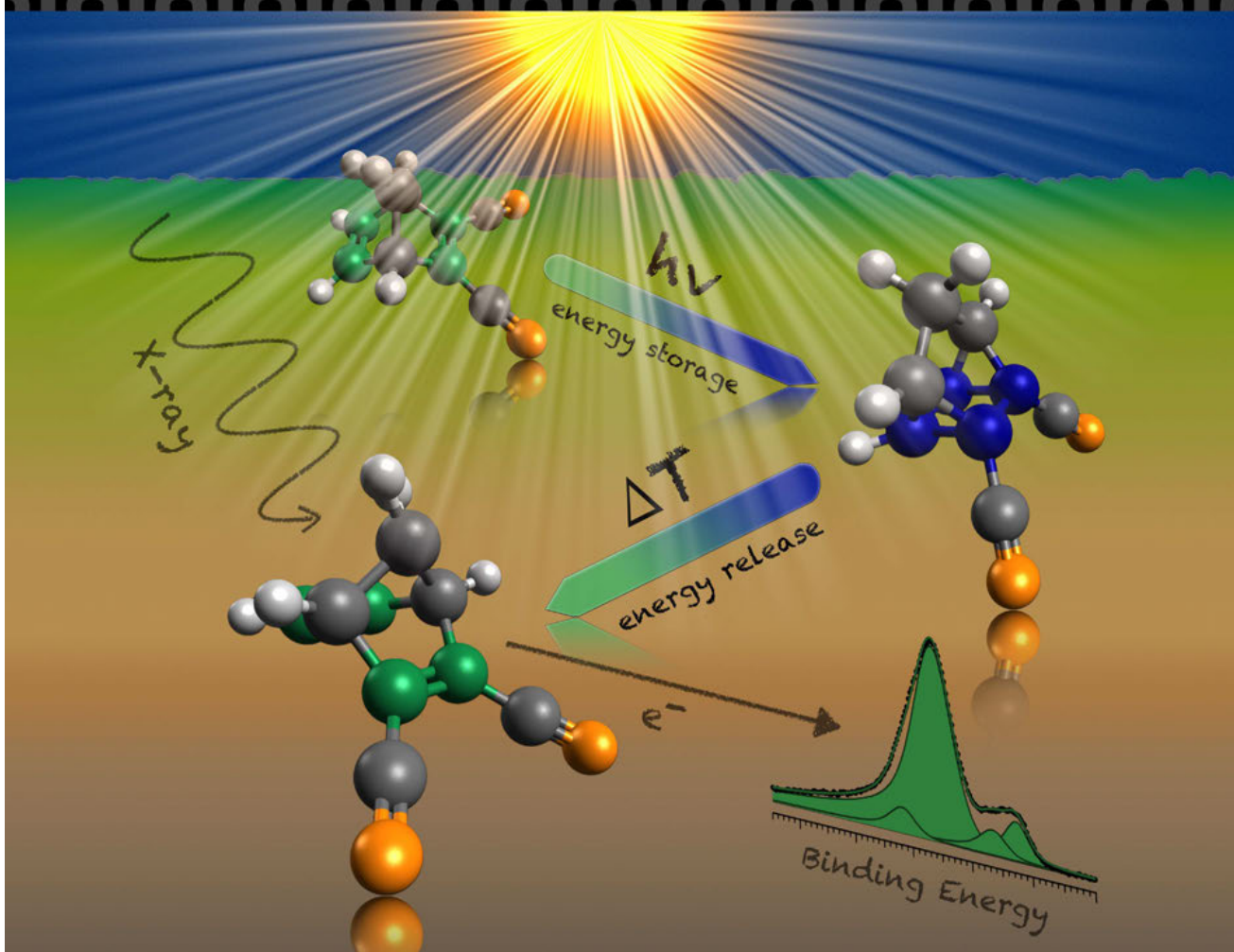
*J. Chem. Phys.* **2023**, 159, 074703 (<https://doi.org/10.1063/5.0158124>).

*Copyright (2023) AIP Publishing. This article may be downloaded for personal use only. Any other use requires prior permission of the author and AIP Publishing. This article appeared in J. Chem. Phys. 159, 074703 (2023) and may be found at <https://doi.org/10.1063/5.0158124>.*

**Front Cover:**

*Christian Papp and co-workers*

Surface Chemistry of the Molecular Solar Thermal Energy Storage System 2,3-Dicyano-Norbornadiene/  
Quadricyclane on Ni(111)





# Surface Chemistry of the Molecular Solar Thermal Energy Storage System 2,3-Dicyano-Norbornadiene/Quadricyclane on Ni(111)



Felix Hemauer



Prof. Dr. Andreas Hirsch



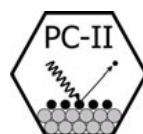
Prof. Dr. Andreas Görling



Prof. Dr. Hans-Peter Steinrück



Prof. Dr. Christian Papp



www.chemie.nat.fau.de

The front cover artwork is provided by the group of Prof. Dr. Christian Papp at Physical Chemistry II of FAU Erlangen-Nürnberg and FU Berlin. The image shows the isomerization reaction of the molecule pair 2,3-dicyano-norbornadiene/quadricyclane as potential molecular solar thermal (MOST) energy storage system. Read the full text of the Research Article at 10.1002/cphc.202200199.

### What prompted you to investigate this topic?

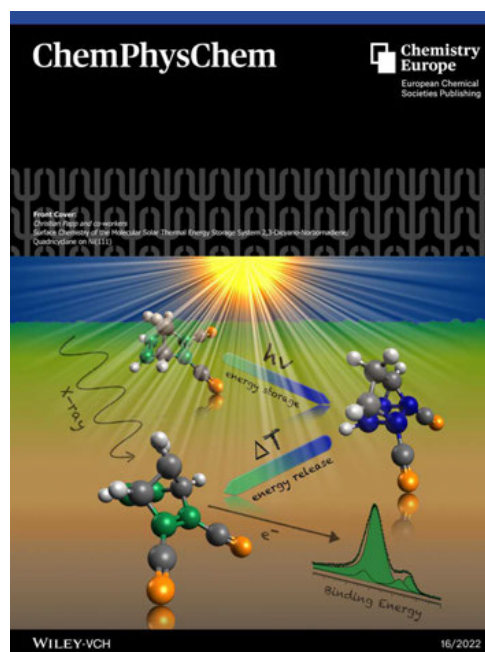
The necessity for green energy sources has never been higher. However, with the intermittent character of many regenerable energy sources such as solar energy, novel energy storage solutions have to be promoted. In this context, molecular solar thermal (MOST) systems provide the advantage of combining the light-harvesting process with storage as molecular strain. Towards large-scale applications, heterogeneous catalytic pathways need to be explored; we thus address the surface chemistry of promising derivatives.

### What other topics are you working on at the moment?

The research of the group of Prof. Dr. Christian Papp is focused on the fundamental understanding of surface processes by in situ techniques. Current topics are the concept of liquid organic hydrogen carriers for future energy storage, the growth and chemical modification of 2D materials for future electronics and the investigation of liquid metals/alloys in catalysis.

### How did each team member/collaborator contribute to the work?

The group of Prof. Dr. Christian Papp at the chair of Prof. Dr. Hans-Peter Steinrück was responsible for the synchrotron radi-



ation-based XPS measurements of the molecule pair. The synthesis of the derivatives was done by the group of Prof. Dr. Andreas Hirsch, while the performed DFT calculations were carried out in the group of Prof. Dr. Andreas Görling.

#### **Acknowledgements**

The work was supported by the Cluster of Excellence 'Engineering of Advanced Materials' and the Deutsche Forschungsgemein-

schaft (DFG) – Project No. 392607742. We thank Helmholtz-Zentrum Berlin for the allocation of synchrotron radiation beamtime and the BESSY II staff for support during beamtime.



# Surface Chemistry of the Molecular Solar Thermal Energy Storage System 2,3-Dicyano-Norbornadiene/Quadricyclane on Ni(111)

Felix Hemauer,<sup>[a]</sup> Udo Bauer,<sup>[a]</sup> Lukas Fromm,<sup>[b]</sup> Cornelius Weiß,<sup>[c]</sup> Andreas Leng,<sup>[c]</sup> Philipp Bachmann,<sup>[a]</sup> Fabian Düll,<sup>[a]</sup> Johann Steinhauer,<sup>[a]</sup> Valentin Schwaab,<sup>[a]</sup> Robert Grzonka,<sup>[a]</sup> Andreas Hirsch,<sup>[c]</sup> Andreas Görling,<sup>[b, d]</sup> Hans-Peter Steinrück,<sup>[a, d]</sup> and Christian Papp<sup>\*[a, d, e]</sup>

Molecular solar thermal (MOST) systems are a promising approach for the introduction of sustainable energy storage solutions. We investigated the feasibility of the dicyano-substituted norbornadiene/quadricyclane molecule pair on Ni(111) for catalytic model studies. This derivatization is known to lead to a desired bathochromic shift of the absorption maximum of the parent compound. In our experiments further favorable properties were found: At low temperatures, both molecules adsorb intact without any dissociation. *In situ* temperature-programmed HR-XPS experiments reveal the conversion of (CN)<sub>2</sub>-quadricyclane to (CN)<sub>2</sub>-norbornadiene under energy release between 175 and 260 K. The absence of other

surface species due to side reactions indicates full isomerization. Further heating leads to the decomposition of the molecular framework into smaller carbonaceous fragments above 290 K and finally to amorphous structures, carbide and nitride above 400 K. DFT calculations gave insights into the adsorption geometries. (CN)<sub>2</sub>-norbornadiene is expected to interact stronger with the surface, with flat configurations being favorable. (CN)<sub>2</sub>-quadricyclane exhibits smaller adsorption energies with negligible differences for flat and side-on geometries. Simulated XP spectra are in good agreement with experimental findings further supporting the specific spectroscopic fingerprints for both valence isomers.

## Introduction

With dwindling fossil fuels,<sup>[1]</sup> proceeding global warming,<sup>[2]</sup> and associated growing awareness for environmental issues, the need for green energy sources has never been higher. In

addition, the worldwide energy demand is expected to exceed 27.6 TW in 2050 being more than twice the amount of 2001.<sup>[3]</sup> In this picture, solar power appears as a promising candidate for clean energy production. However, due to its intermittent character and climatic dependency, strong mismatches between load and supply arise temporally and geographically. This leads to the necessity for not only sustainable energy sources but also the development of novel energy storage technologies, ideally directly combined with the light-harvesting process.

Next to photovoltaic and electrochemical approaches, it is also possible to capture and store solar energy in a chemical manner. So-called molecular solar thermal (MOST) energy systems employ the photoconversion of an energy-lean parent molecule to an energy-rich compound in a metastable state.<sup>[4]</sup> In a reversible isomerization, the energy is stored through a rearrangement of chemical bonds and the thereby introduced strain. On demand, the backward reaction can be triggered in a catalytic or thermal way leading to the release of the stored energy. For reasonable applicability, numerous requirements have to be fulfilled: The quantum yield of the energy storage steps should be as high as possible with an absorption maximum in the range of visible light; moreover, the photo-isomer must not be converted back by irradiation. Long storage times are desirable as well as high gravimetric energy densities; the latter are ensured by a low molecular weight in combination with a strong endothermic reaction profile.

Reported examples for MOST systems include stilbenes,<sup>[5]</sup> azobenzenes,<sup>[6]</sup> anthracenes,<sup>[7]</sup> or fulvalene-tetracarbonyl-

[a] F. Hemauer, Dr. U. Bauer, Dr. P. Bachmann, Dr. F. Düll, J. Steinhauer, V. Schwaab, R. Grzonka, Prof. Dr. H.-P. Steinrück, Dr. C. Papp  
Lehrstuhl für Physikalische Chemie II,  
Friedrich-Alexander-Universität Erlangen-Nürnberg  
Egerlandstr. 3, 91058 Erlangen, Germany

[b] Dr. L. Fromm, Prof. Dr. A. Görling  
Lehrstuhl für Theoretische Chemie,  
Friedrich-Alexander-Universität Erlangen-Nürnberg  
Egerlandstr. 3, 91058 Erlangen, Germany

[c] C. Weiß, A. Leng, Prof. Dr. A. Hirsch  
Lehrstuhl für Organische Chemie II,  
Friedrich-Alexander-Universität Erlangen-Nürnberg  
Nikolaus-Fiebiger-Str. 10, 91058 Erlangen, Germany

[d] Prof. Dr. A. Görling, Prof. Dr. H.-P. Steinrück, Dr. C. Papp  
Erlangen Catalysis Resource Center (ECRC),  
Friedrich-Alexander-Universität Erlangen-Nürnberg  
Egerlandstr. 3, 91058 Erlangen, Germany

[e] Dr. C. Papp  
Physikalische und Theoretische Chemie, Freie Universität Berlin  
Arnimallee 22, 14195 Berlin, Germany  
E-mail: christian.papp@fau.de

Supporting information for this article is available on the WWW under <https://doi.org/10.1002/cphc.202200199>

© 2022 The Authors. ChemPhysChem published by Wiley-VCH GmbH. This is an open access article under the terms of the Creative Commons Attribution Non-Commercial NoDerivs License, which permits use and distribution in any medium, provided the original work is properly cited, the use is non-commercial and no modifications or adaptations are made.



pump-thaw cycles, were adsorbed on the surface through the vapor pressure of the organic substances; the exposure is given in Langmuir ( $1 \text{ L} = 10^{-6} \text{ Torr}\times\text{s}$ ). The XP spectra were continuously recorded with a typical time of about 10–15 s for each spectrum during adsorption and heating. In order to avoid reactions or decomposition induced by X-ray irradiation (see Figure S6), the sample was shifted to a new position after each acquired spectrum. For data evaluation, the Fermi level was used as reference for all binding energies. The quantitative analysis is done by fitting of the signals: After subtraction of a linear background, contributions in the C 1s and N 1s spectra were fitted with peaks, described by Doniach-Šunjić functions<sup>[21]</sup> convoluted with Gaussian profiles. The coverage was determined by comparison to layers with known coverage; one monolayer (ML) corresponds to one atom per surface atom. Carbon coverages were calibrated with respect to a graphene layer<sup>[22]</sup> which contains two carbon atoms per nickel atom (2 ML); the amount of nitrogen on the surface is equivalent to 2/9 of the carbon coverage, according to the stoichiometric ratio within the molecules.

## Molecule Synthesis

### 2,3DibromoNorbornadiene

In a flamedried SCHLENK flask, norbornadiene (15.0 g; 163 mmol) and potassium *t*-butoxide (9.43 g; 84.0 mmol) were dissolved in 100 ml of dry and degassed THF under nitrogen atmosphere. The dispersion was cooled to  $-78^\circ\text{C}$  and *n*-butyl lithium (2.5 M in hexane; 33.2 ml; 83.0 mmol) was added dropwise over a period of 1.5 h. The mixture was warmed to  $-40^\circ\text{C}$  and stirred for 30 min. Afterwards it was cooled again to  $-78^\circ\text{C}$  and 1,2-dibromoethane (3.62 ml; 42.0 mmol) was slowly added via a syringe. Once the addition was completed, the solution was warmed to  $-40^\circ\text{C}$  and stirred for 1 h. Before the remaining 1,2-dibromoethane (10.9 ml; 126 mmol) was slowly added, the mixture was cooled again to  $-78^\circ\text{C}$ . The combined reagents were then stirred for 2 h at  $-40^\circ\text{C}$  and for additional 2 h at room temperature. The reaction was quenched by adding 100 ml of saturated  $\text{NH}_4\text{Cl}_{(\text{aq})}$  and extracted with MTBE ( $4 \times 100 \text{ ml}$ ). The combined organic phases were sequentially washed with water (100 ml) and brine (100 ml) and dried over  $\text{MgSO}_4$ . After the solvent was removed under reduced pressure, the crude was distilled (1st fraction:  $60^\circ\text{C}$ , 12 mbar, 1,2-dibromoethane; 2nd fraction:  $65^\circ\text{C}$ , 8 mbar, 2-bromonorbornadiene; 3rd fraction:  $80^\circ\text{C}$ – $100^\circ\text{C}$ , 6 mbar, 2,3-dibromonorbornadiene) to give the product as a colorless oil (6.73 g; 26.9 mmol; yield = 34%).

$^1\text{H-NMR}$  ( $\text{CDCl}_3$ , 400 MHz):  $\delta = 6.89$  (t,  $J = 2 \text{ Hz}$ , 2 H); 3.62 (t,  $J = 2 \text{ Hz}$ , 2 H); 2.45 (dt,  $J = 6.4 \text{ Hz}$ , 1 H); 2.18 (dt,  $J = 6.0 \text{ Hz}$ , 1 H) ppm.

$^{13}\text{C-NMR}$  ( $\text{CDCl}_3$ , 100 MHz):  $\delta = 141.3$ ; 133.1; 72.0; 58.6 ppm.

HRMS (APPI): calc. for  $\text{C}_7\text{H}_8\text{Br}_2$  [M]:  $m/z = 247.8836$ ; exp. 247.8835.

### 2,3DicyanoNorbornadiene

In a flamedried SCHLENK flask, 2,3-dibromonorbornadiene (2.00 g; 8.00 mmol) was dissolved in 20 ml of dry DMF under a nitrogen atmosphere. After the addition of  $\text{CuCN}$  (680 mg; 7.59 mmol), the dispersion was heated to  $120^\circ\text{C}$  and stirred for 2.5 h. Once the solution cooled to room temperature it was diluted with water and extracted with  $\text{EtOAc}$  ( $4 \times 100 \text{ ml}$ ). Due to the formation of a black slurry, the separation of the phases is highly time consuming but can be facilitated by the addition of aqueous ammonia. The combined organic phases were sequentially washed with large amounts of water and brine and then dried over  $\text{MgSO}_4$ . After

removing the solvent under reduced pressure, the crude was received as a yellowish oil, which was purified by column chromatography ( $\text{SiO}_2$ ; hexane : DCM/1:4  $R_f = 0.60$ ). 2,3-Dicyanonorbornadiene was isolated as a colorless oil (275 mg; 1.93 mmol; yield = 24%).

$^1\text{H-NMR}$  ( $\text{CDCl}_3$ , 300 MHz):  $\delta = 6.92$  (t,  $J = 1.8 \text{ Hz}$ , 2 H); 4.03 (quint,  $J = 2.1 \text{ Hz}$ , 2 H); 2.40 (dt,  $J = 7.5 \text{ Hz}$ , 1.5 Hz; 1 H); 2.33 (dt,  $J = 7.5 \text{ Hz}$ , 1.5 Hz, 1 H) ppm [see Figure S7].

$^{13}\text{C-NMR}$  ( $\text{CDCl}_3$ , 100 MHz):  $\delta = 141.6$ ; 141.3; 113.1; 74.9; 55.5 ppm [see Figure S8].

MS (ESI): calc. for  $\text{C}_9\text{H}_6\text{N}_2$  [ $\text{M} + \text{H}^+$ ]:  $m/z = 143.0609$ ; exp. 143.1069.

### 2,3DicyanoQuadracyclane

2,3-Dicyanonorbornadiene (100 mg; 0.703 mmol) was dissolved in 200 ml of pump-frozen methanol and irradiated for 3 h with a mercury vapor lamp. Once the solvent was removed under reduced pressure, the remaining yellow oil was purified by column chromatography ( $\text{SiO}_2$ ; hexane : DCM/1:4  $R_f = 0.27$ ). The product was isolated as a white solid (71 mg; 0.499 mmol; yield = 71%).

$^1\text{H-NMR}$  ( $\text{CDCl}_3$ , 300 MHz):  $\delta = 2.71$ – $2.68$  (m, 2 H); 2.50 (dt,  $J = 12.8 \text{ Hz}$ , 1.4 Hz; 1 H); 2.41– $2.38$  (m, 2 H); 2.30 (dt,  $J = 12.4 \text{ Hz}$ , 1.4 Hz; 1 H) ppm [see Figure S9].

$^{13}\text{C-NMR}$  ( $\text{CDCl}_3$ , 100 MHz):  $\delta = 116.1$ ; 32.7; 32.2; 25.7; 12.8 ppm [see Figure S10].

## DFT Calculations

All ab initio calculations were performed with the Vienna Ab initio Simulation Package (VASP) Version 5.4.1,<sup>[23]</sup> employing the projector-augmented wave method (PAW)<sup>[24]</sup> with a plane wave basis cutoff of 450 eV. The Perdew-Burke-Ernzerhof exchange correlation functional was used<sup>[25]</sup> together with a Methfessel-Paxton<sup>[26]</sup> smearing with a broadening width of 0.2 eV. To account for long-range intermolecular interactions, the zero damping DFT-D3 dispersion force correction scheme by Grimme was utilized.<sup>[27]</sup> The systems were calculated within a supercell approach where slabs of six Ni layers are separated by a 20 Å vacuum layer. Three of the atomic layers were fully relaxed while the other three were kept fixed to the bulk geometry with a lattice constant of 3.51 Å. To allow for non-interacting adsorbates, a 4 by 4 orthogonal unit cell was chosen to represent the surface. Brillouin zone integration was sampled with a  $4 \times 4 \times 1$  Monkhorst-Pack grid.<sup>[28]</sup> Geometries were optimized until all forces were smaller than 0.01 eV/Å. Adsorption energies were calculated as total energy differences with  $E_{\text{Ads}} = E_{\text{gas}} + E_{\text{surf}} - E_{\text{sys}}$  with the total energy of the molecule in the gas phase  $E_{\text{gas}}$ , of the clean metal surface  $E_{\text{surf}}$ , and the adsorbate system  $E_{\text{sys}}$  leading to higher adsorption energies for more stable geometries. XP spectra were modeled by calculations of relative core level shifts with the method of Slater's transition state,<sup>[29]</sup> which includes final state effects (ICORELEVEL = 2, CLZ = 0.5)<sup>[30]</sup> exciting half an electron into the vacuum.

## Results and Discussion

The adsorption and thermal evolution of  $(\text{CN})_2\text{-NBD}$  and  $(\text{CN})_2\text{-QC}$  on Ni(111) was followed *in situ* by measuring XP spectra of the C 1s and N 1s regions. In the following, the data for the two core levels are discussed separately in two sections. For easier monitoring of the conversion and surface reactions, we

concentrate on submonolayer coverages. At this coverage, information on adsorption geometries is better accessible, especially by comparison with performed DFT calculations. Complementary results with multilayer exposures are found in the supporting information.

### XP Spectra of the C 1s Region

First, the adsorption of  $(\text{CN})_2\text{-NBD}$  at 130 K is discussed. The C 1s spectra recorded during the adsorption experiments of  $(\text{CN})_2\text{-NBD}$  are depicted as waterfall plots in Figure 2a.

The exposure of 0.24 L led to a total carbon coverage of 0.26 ML. Starting from zero coverage (Figure 2a, black bold spectrum), a characteristic line shape of the XP spectra evolves upon dosing, which can be reproduced by four peaks with constant binding energies at 285.2, 284.6, 283.6 and 283.2 eV (Figure 2c, green). While the corresponding spectral shape represents the unique spectroscopic fingerprint of the molecule, it is difficult to assign contributions to individual carbon atoms, due to the complexity of the adsorbed species and the likely coexistence of different adsorption geometries. Interestingly, the obtained spectral shape differs considerably from that

of the parent molecule NBD,<sup>[13]</sup> (see Figure S4a and S4d) as  $(\text{CN})_2\text{-NBD}$  features contributions at lower as well as higher binding energies. These differences are attributed to the change in the molecular structure and various adsorption geometries originating from the functionalization of the NBD framework. They also indicate that adsorption occurs in a non-dissociative manner; this suggestion is confirmed by DFT calculations of the intact molecule (see below), as the expected line shape resembles the experimental data. In addition, information of the complementary N 1s region, which are discussed later, shows no indication for fragmentation at adsorption temperature. Contributions by multilayer signals are excluded, since the corresponding signals at 285.5, 287.2, 285.6 and 284.7 eV are only observed for higher surface coverages (see Figure S2a).

The thermal evolution of  $(\text{CN})_2\text{-NBD}$  on Ni(111) is investigated by TPXPS. Selected C 1s spectra are depicted in Figure 2b, along with color-coded fits of specific reaction intermediates in Figure 2c. The quantitative analysis of all spectra collected during the TPXPS experiment is provided in Figure 3a giving the amount and the temperature ranges of the respective surface species.

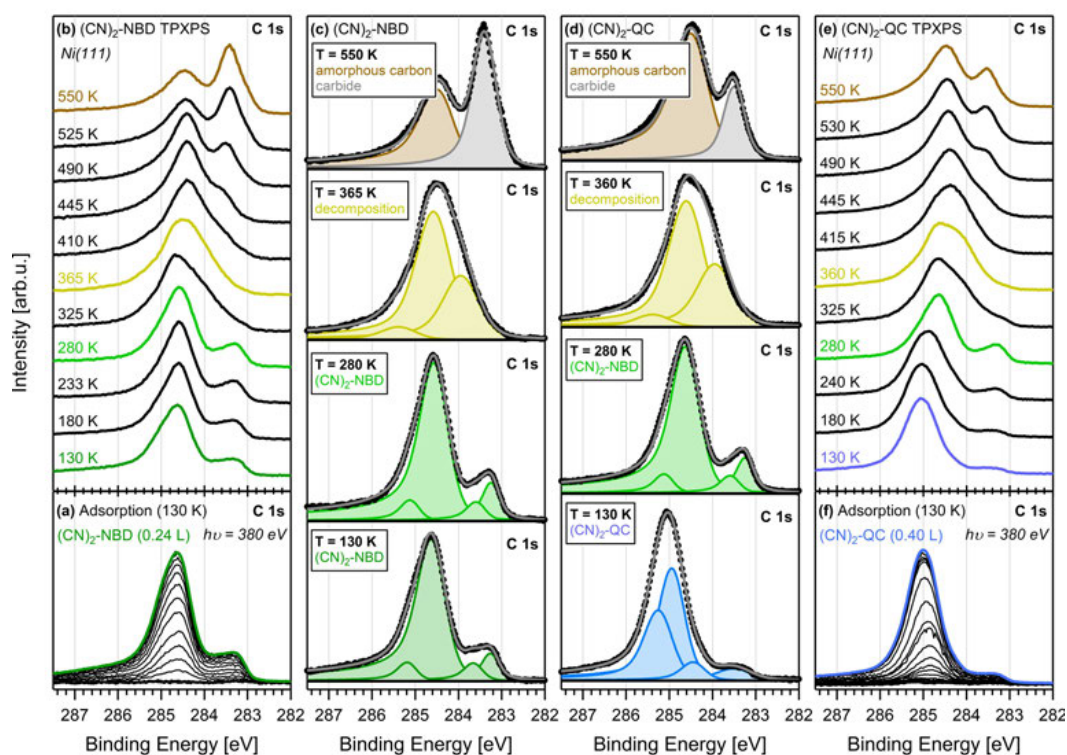


**Figure 2.** (a, f) Selected C 1s spectra of  $(\text{CN})_2\text{-NBD}$  and  $(\text{CN})_2\text{-QC}$  on Ni(111), collected during adsorption at 130 K; (b, e) subsequent TPXPS spectra (waterfall plot) during heating to 550 K; (c, d) comparison of distinct surface species for both molecules at equivalent temperatures with corresponding color-coded fits.

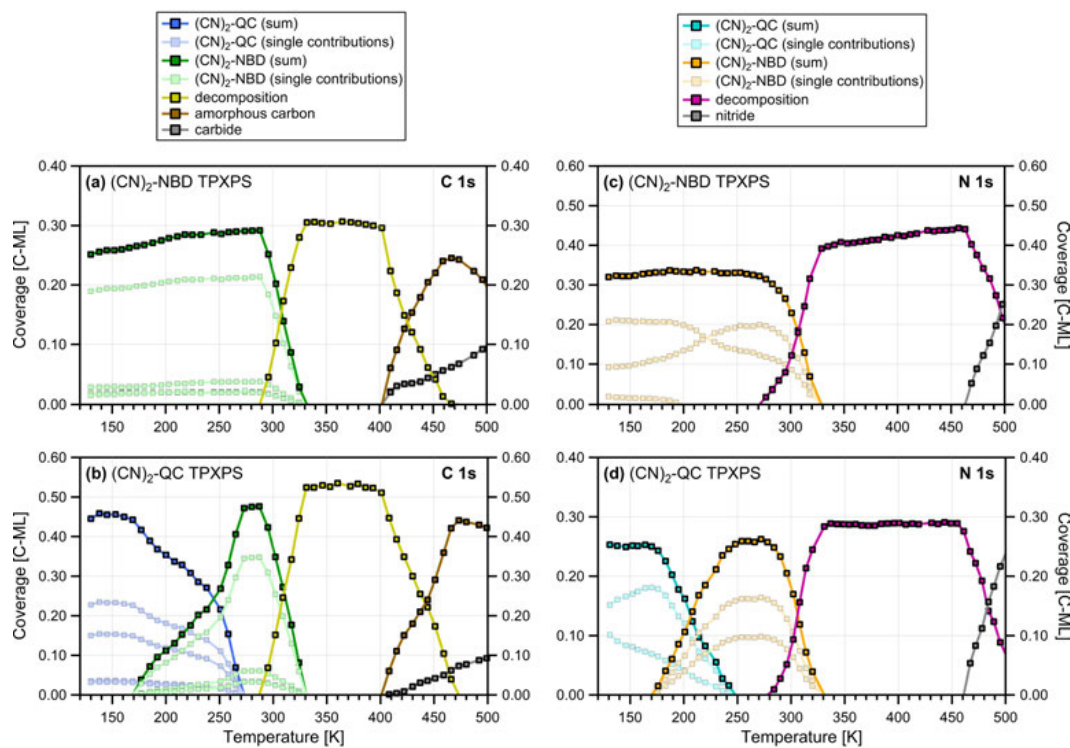


**Figure 3.** Quantitative analysis of the TPXP spectra of  $(\text{CN})_2\text{-NBD}$  and  $(\text{CN})_2\text{-QC}$ , collected with a heating rate of 0.5 K/s: (a, b) C 1s region, (c, d) N 1s region; light colors indicate contributions of single peaks to respective signal.

Below 170 K, there are only minor changes of the spectral line shape. Upon further heating to 280 K, we observe an increase of the overall carbon coverage by 16% (see Figure 3a), but no shifts of the individual peak energies (Figure 2c). Interestingly, the intensity ratio of the two higher energy peaks at 285.1 and 284.5 eV remain constant, while the two lower energy peaks at 283.6 and 283.2 eV change less than 25% in their relative intensities. From the absence of peak shifts, we conclude that no reaction has yet occurred, but instead only a rearrangement of  $(\text{CN})_2\text{-NBD}$  on the surface takes place. Supplying thermal energy to the system enables mobility and facilitates transitions into thermodynamically more favored configurations. This rearrangement also explains the mentioned change in total intensity due to alterations of the attenuation behavior of the photoelectrons<sup>[31]</sup> and/or contributions by differences in photoelectron diffraction resulting from various adsorption geometries.<sup>[32]</sup>

Beginning at a temperature of  $\sim 290$  K, a general broadening of the spectral line shape is observed, and the low binding energy feature characteristic of  $(\text{CN})_2\text{-NBD}$  vanishes. This observation suggests the presence of a new surface species, which is fitted with three peaks at 284.5, 284.3 and 283.9 eV (Figure 2c, yellow). This species is attributed to the

reaction of  $(\text{CN})_2\text{-NBD}$  to carbon fragments ( $\text{C}_x\text{H}_y$ ). Thermal decomposition and further dehydrogenation is common for hydrocarbons on nickel surfaces.<sup>[33]</sup> In comparison to previously investigated model systems,  $(\text{CN})_2\text{-NBD}$  exhibits the highest thermal stability with the decomposition onset at 290 K: Whereas both, unsubstituted  $\text{NBD}^{[13]}$  and  $(\text{Br})_2\text{-NBD}^{[17]}$  react to benzene and methylidyne already at 190 and 195 K, respectively, none of these reaction products are identified for  $(\text{CN})_2\text{-NBD}$  in the course of the temperature-programmed experiment here. Thus, the dicyano-substituted molecule stays intact for almost 100 K higher temperatures. Starting at  $\sim 400$  K, subsequent decomposition steps take place leading to amorphous carbon,<sup>[34]</sup> yielding a peak at 284.4 eV, and carbide,<sup>[22a,35]</sup> giving a signal at 283.4 eV (Figure 2c, brown and gray).

Next, we address the adsorption and thermal evolution of  $(\text{CN})_2\text{-QC}$  on Ni(111). The adsorption of  $(\text{CN})_2\text{-QC}$  at 130 K up to an exposure of 0.40 L was followed by XPS (Figure 2a), yielding a carbon coverage of 0.40 ML. The characteristic line shape of the XP spectra is fitted with four peaks at binding energies of 285.2, 284.9, 284.4 and 283.5 eV (Figure 2d, blue). Again, no assignment to distinct carbon atoms is given due to the complexity of the adsorption system, but the peaks can serve as a spectral fingerprint. As in the case of  $(\text{CN})_2\text{-NBD}$ , the

comparison of  $(\text{CN})_2\text{-QC}$  with unsubstituted  $\text{QC}^{[13]}$  reveals a deviating line shape (see Figure S5a and S5d): While  $(\text{CN})_2\text{-QC}$  displays major contributions above 285 eV, pure QC has a distinct peak at 283.4 eV. When comparing the two dicyano-substituted molecules, that is,  $(\text{CN})_2\text{-NBD}$  and  $(\text{CN})_2\text{-QC}$ , we observe very different spectra: Not only the binding energies of the four peaks used for fitting do not match, but also their relative intensities differ strongly. The differences between the spectra of  $(\text{CN})_2\text{-QC}$  to those of unsubstituted QC and  $(\text{CN})_2\text{-NBD}$  suggest a non-dissociative adsorption without conversion at low temperatures; this presumption is verified in the following discussion of the observed quantitative back reaction of  $(\text{CN})_2\text{-QC}$  to  $(\text{CN})_2\text{-NBD}$ . We can also rule out contributions from  $(\text{CN})_2\text{-QC}$  multilayers, which would show three peaks at 287.4, 286.2, and 284.8 eV (see Figure S2f).

The thermal evolution of the valence isomer  $(\text{CN})_2\text{-QC}$  is shown in Figure 2e, along with the quantitative analysis in Figure 3b. For the peak fitting, the intensity ratios of the fitted peaks at 285.2, 284.9, 284.4 and 283.5 eV were kept fixed. Up to 175 K, no changes of the binding energy positions are observed. At higher temperatures, changes of the spectral fingerprint become visible, indicative of the onset of the conversion of  $(\text{CN})_2\text{-QC}$  to  $(\text{CN})_2\text{-NBD}$ . The peaks related to  $(\text{CN})_2\text{-QC}$  drop in intensity and have completely vanished at  $\sim 270$  K; simultaneously,  $(\text{CN})_2\text{-NBD}$  has become the solely detected species. The comparison of the fitted C 1s TPXP spectra of  $(\text{CN})_2\text{-NBD}$  in Figure 2c and  $(\text{CN})_2\text{-QC}$  in Figure 2d confirms the isomerization of  $(\text{CN})_2\text{-QC}$  to  $(\text{CN})_2\text{-NBD}$ : At 280 K, the spectra from both TPXPS series (Figure 2c and 2d, green) are fitted with the same parameters; their identical appearance proves the presence of an equivalent surface species; the only minor difference is a shift of the main peak by less than 0.1 eV to higher binding energy for  $(\text{CN})_2\text{-QC}$ , which is within the accuracy of measurement and evaluation. The formed  $(\text{CN})_2\text{-NBD}$  has a maximum coverage of 0.48 ML at 270 K. The absence of other surface species indicates full conversion. Although the

temperature range from 175 to 260 K for the isomerization of  $(\text{CN})_2\text{-QC}$  to  $(\text{CN})_2\text{-NBD}$  is rather large (see Figure 3b), the relatively high onset for the reaction is of advantage for applications towards ambient conditions. The further thermal evolution is expected to be analogous to the  $(\text{CN})_2\text{-NBD}$  experiment. Indeed, at 290 K, identical decomposition signals are found (Figure 2d, yellow), due to dissociation into  $\text{C}_x\text{H}_y$  fragments.<sup>[33]</sup> Finally, when heating to above 400 K, amorphous carbon structures<sup>[34]</sup> and contributions by carbide<sup>[22a,35]</sup> are observed (Figure 2d, brown and gray), as in the case of  $(\text{CN})_2\text{-NBD}$ .

As next step, we performed DFT calculations in order to understand the interactions of the molecular pair with the surface and to obtain insights into the spectral fingerprints. Similar to previous results of NBD adsorption on surfaces, different adsorption motifs are conceivable.<sup>[12–13]</sup> For this reason, a flat ( $\eta^2:\eta^2$ ) geometry, in which NBD is bound via both its double bonds to the surface, and a side-on ( $\eta^2:\eta^1$ ) geometry, in which only one double bond and the  $\text{CH}_2$  bridgehead are bound to the surface, were regarded. In addition to these two basic motifs, different positions relative to the surface were considered. The most stable geometries are depicted in Figure 4.

As reported previously, the bond of NBD via the  $\text{C}=\text{C}$  double bond to the surface is a strong interaction leading to very stable structures. Therefore, for  $(\text{CN})_2\text{-NBD}$ , a “flat-like” adsorption via both double bonds (structure 4a–4c) is preferred and yields higher adsorption energies of about 3.6 to up to 4.0 eV, compared to values ranging from 1.4 eV for geometries with CN-groups pointing away from the surface to  $\sim 2.1$  eV for the side-on adsorption motif (structure 4d). Unlike in the case of the  $(\text{Br})_2\text{-NBD}$ ,<sup>[17]</sup> the CN-groups are not as bulky as the bromine atoms and offer more flexibility. In this way, they do not hinder the NBD moiety to interact with both  $\text{C}=\text{C}$  double bonds with the surface. Still, there are slight differences regarding the position of the molecule on the surface. In case of the “flat-like”

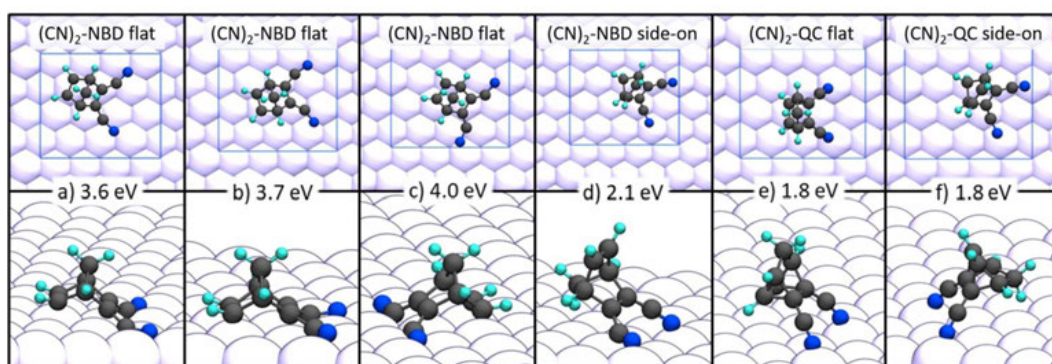


**Figure 4.** Adsorption geometries calculated with DFT: (a–c) different geometries for a flat adsorbed  $(\text{CN})_2\text{-NBD}$ , (d) side-on adsorbed  $(\text{CN})_2\text{-NBD}$ , (e) flat adsorbed  $(\text{CN})_2\text{-QC}$ , (f) side-on adsorbed  $(\text{CN})_2\text{-QC}$ ; corresponding adsorption energies are given; carbon atoms depicted in black, hydrogen in turquoise, nitrogen in blue, nickel surface in white, unit cells are indicated by a blue rectangle.

adsorption, we observe a preference for a CN adsorption in a bridge-like adsorption (structure 4a–4c). Furthermore, the most stable structure (4c) is bound with the C=C double bond without the CN-groups to two surface atoms and additionally on the other side with the CN-groups to a single Ni atom. The CN-groups are bending outwards to occupy their preferred bridge position. This structure is with 4.0 eV about 0.3 eV more stable than the rest of the structures.

During the adsorption process at low temperature, it is very likely that the  $(\text{CN})_2\text{-NBD}$  molecules stick randomly to the surface in one of the several possible geometries and stay in this way. Thus, a mixture of different structures is present. Heating the sample then provides enough energy to overcome the barrier for flipping and moving the molecules from, e.g., the less stable side-on to the more stable flat geometry, which explains the change of the spectral features in the temperature range from 130–175 K.

For  $(\text{CN})_2\text{-QC}$ , the adsorption in both orientations (structure 4e and 4f) is with 1.8 eV similarly stable. Thus, we assume a mixed adsorption. Because of the other bonding situation in QC with no double bonds, the interaction with the surface is different. The molecule is rather compact and offers mainly the

CN-groups to interact with the surface. Therefore, in both stable geometries the nitrogen atoms of the CN-groups are bound to surface nickel atoms in an on-top position. The difference between the two geometries (4e, 4f) is that in the “flat-like” geometry two hydrogen atoms of the strained four-membered ring are weakly interacting with the surface, whereas in the side-on geometry the  $\text{CH}_2$  group is doing so. In both cases, this is a weak dispersion interaction, explaining the small energy differences.

Calculations of the relative core level shifts for the different geometries (see Figure 5) corroborate the presence of unreacted  $(\text{CN})_2\text{-QC}$  on the surface. The spectra show higher binding energies for the QC derivative, which is also observed in the experiments. In general, a good correspondence of the calculated to the experimental spectra is found. But unfortunately, it is not possible to make a clear assignment to the structures. The shoulder at low binding energies can be assigned to the strongly interacting C=C double bond. Because of the lack of this interaction in the QC derivative, this spectral feature is not present. Additionally, this is the feature increasing in intensity during the proposed rearrangement from the side-on to the flat geometry.

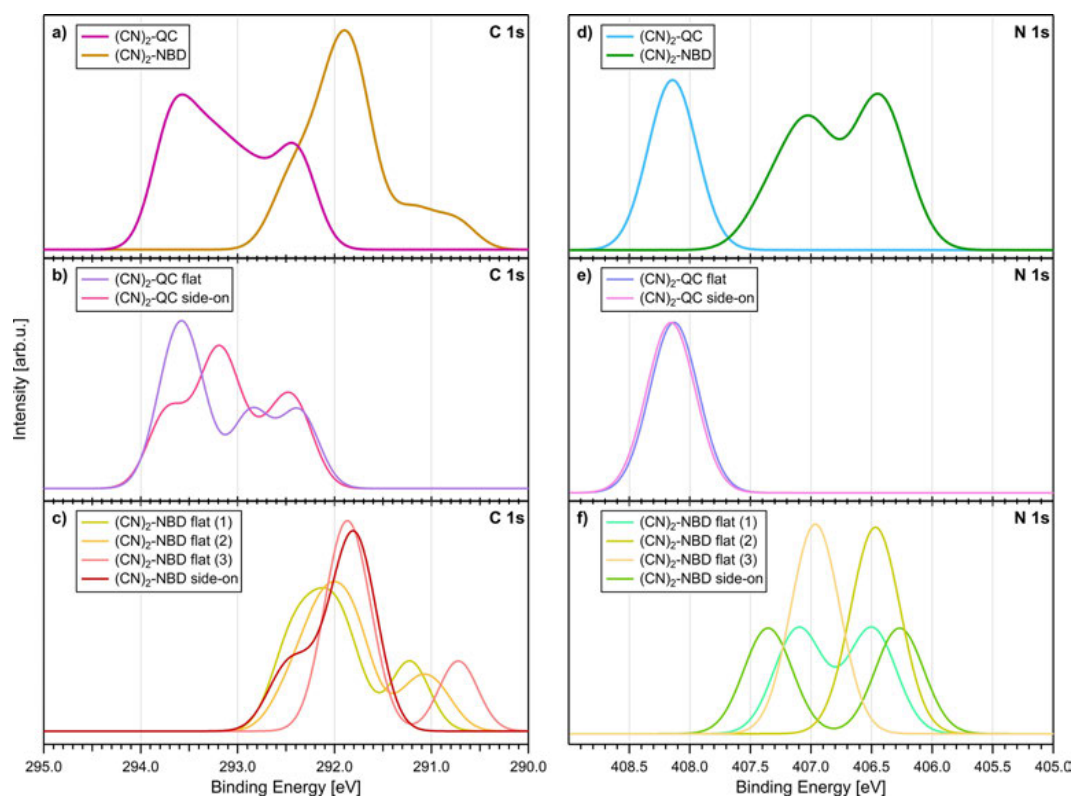


**Figure 5.** Representation of calculated XP spectra: (a–c) depiction of C 1s region results, whereby (a) gives a comparison of  $(\text{CN})_2\text{-NBD}$  and  $(\text{CN})_2\text{-QC}$  as total sum of (b,c) single contributions of different adsorption geometries; (d–f) depiction of N 1s region results of the molecule pair with (d) sum of respective signals and (e,f) spectra of single adsorption geometries; all spectra were generated by Gaussian functions with a width of 0.02 eV.

## XP Spectra of the N 1s Region

Complementary information on the adsorption and thermal evolution is obtained from XP spectra of the N 1s region. The N 1s spectra acquired during exposure of the Ni(111) surface to  $(\text{CN})_2\text{-NBD}$  and  $(\text{CN})_2\text{-QC}$  are depicted in Figure 6a and 6f, respectively. For  $(\text{CN})_2\text{-NBD}$ , an asymmetric peak evolves at 397.9 eV with a broad shoulder towards higher binding energy, yielding a total carbon coverage of 0.32 ML after a dosage of 0.34 L. In order to obtain a reasonable fit, three peaks at 399.5, 398.3 and 397.8 eV had to be used (Figure 6c, orange). This is rather surprising, since it was expected that both nitrogen atoms in the symmetric molecular framework of  $(\text{CN})_2\text{-NBD}$  show an equivalent behavior, which would imply the existence of only one peak. Multilayer formation is ruled out by comparison to the spectrum of multilayers with larger exposure, which show two peaks at 400.2 and 399.1 eV (see Figure S3a). Instead, we attribute the necessity of three peaks to various adsorption sites and/or geometries. In contrast to the structurally related dibromo-substituted  $(\text{Br})_2\text{-NBD}$  and  $(\text{Br})_2\text{-QC}$ ,<sup>[17]</sup> there are no indications that fragmentation takes place upon adsorption. Notably, the observed binding energies do not match those characteristic of atomic nitrogen ( $\sim 397$  eV)<sup>[36]</sup> or cyanide fragments ( $\sim 397.5$  eV) on nickel.<sup>[37]</sup>

Representative XP spectra of the thermal evolution are shown in Figure 6b, along with color-coded fits of specific reaction intermediates in Figure 6c. The quantitative analysis of all spectra collected during the TPXPS experiment is provided in Figure 3c. As the nitrogen atoms are part of the cyano groups attached to the NBD/QC framework, it is expected that changes of the adsorption geometries have a more pronounced effect in the N 1s than in the C 1s spectra. On the other hand, effects in the spectra of the conversion reaction are assumed to be less distinct in the N 1s region. At the start of the heating ramp, the peak at 397.8 eV exhibits the highest intensity (0.21 ML). Upon heating, the peak at 398.3 eV grows at the expense of the two other two peaks. At  $\sim 190$  K, the peak at 399.5 eV has vanished, and at 230 K the peak at 398.3 eV surpasses that at 397.8 eV becoming the dominant surface species at 270 K; simultaneously, the two remaining peaks shift by 0.07 eV towards lower binding energies, while the overall coverage stays roughly constant until 270 K (see Figure 3c). The change and even inversion in relative intensities as well as the small peaks shifts are attributed to rearrangement steps occurring upon heating from low temperatures of 130 K, as also discussed for the C 1s region. The rearrangement is finished until  $\sim 270$  K. (Figure 6c, light orange). Starting at  $\sim 280$  K, the peak with the maximum at 398.3 eV vanishes until 330 K, and a new asymmetric peak evolves at 397.6 eV (Figure 6c, purple), which is assigned to

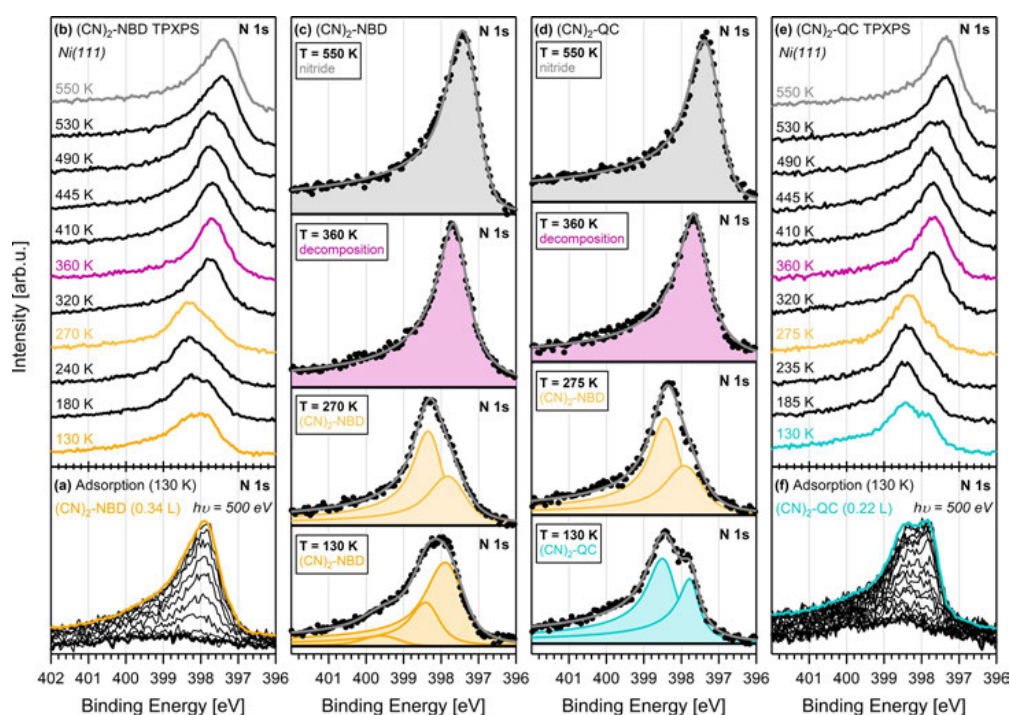


**Figure 6.** (a, f) Selected N 1s spectra of  $(\text{CN})_2\text{-NBD}$  and  $(\text{CN})_2\text{-QC}$  on Ni(111), collected during adsorption at 130 K; (b, e) subsequent TPXPS spectra (waterfall plot) during heating to 550 K; (c, d) comparison of distinct surface species for both molecules at equivalent temperatures with corresponding color-coded fits.

decomposition products. This observation is in good agreement with the temperature onset identified in the C 1s spectra. The cleavage of the carbon bond between cyano group and NBD framework results into the detachment of the cyano moieties.<sup>[37–38]</sup> This new spectral shape maintains from 330 to 460 K. The slight increase in coverage by about 10% is explained by different diffraction behavior of the formed compounds depending on their orientation on the surface.<sup>[32]</sup> Further heating gives rise to a broad, asymmetric signal developing at 470 K, which is fitted with one asymmetric peak at 397.3 eV (Figure 6c, gray). According to literature, this final signal is assigned to nitride emerging upon CN fragmentation.<sup>[33a,36]</sup>

The N 1s spectra collected during the adsorption of the valence isomer (CN)<sub>2</sub>-QC are depicted in Figure 6f; the black bold spectrum at the bottom was acquired prior to exposure, while its slightly curved background indicates minor impurities on the surface. During dosing, a characteristic line shape evolves, which was fitted with two asymmetric peaks at 398.4 and 397.7 eV (Figure 6d, turquoise). For the largest exposure of 0.22 L, a carbon coverage of 0.25 ML was obtained. Analogous to (CN)<sub>2</sub>-NBD, the two peaks are attributed to different adsorption sites and/or geometries on the surface. Contributions from multilayers are not found by comparison to the spectrum of multilayers with two peaks at 400.2 and 399.7 eV (see Figure S3f). Even though the peak maxima of (CN)<sub>2</sub>-NBD and (CN)<sub>2</sub>-QC have almost identical binding energies, the characteristic line shapes serve as fingerprint for the respective molecule. This is due to the different intensity ratios and number of the fitted peaks, which make the molecule pair clearly distinguishable also in the N 1s region.

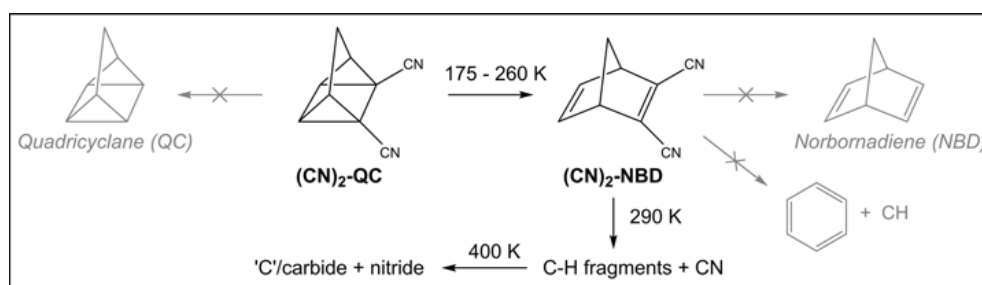
Selected XP spectra of the TPXPS experiment of (CN)<sub>2</sub>-QC are depicted in Figure 6e, along with color-coded fits in Figure 6d; the quantification is given in Figure 3d. Up to 170 K, the total coverage remains constant. The peak at 398.4 eV increases until this temperature to a maximum of 0.18 ML at the expense of the peak at 397.7 eV, which is linearly declining (see Figure 3d). The temperature of 170 K also marks the onset of the evolution of a more narrow signal, which can be fitted with exactly the same parameters as for (CN)<sub>2</sub>-NBD. Hence, the conversion of (CN)<sub>2</sub>-QC to (CN)<sub>2</sub>-NBD is confirmed in the N 1s

spectra at the same temperature as in the C 1s spectra. At 250 K, the isomerization is completed, yielding (CN)<sub>2</sub>-NBD as only surface species (Figure 6d, light orange). From this temperature on, an analogous reaction pathway is observed for (CN)<sub>2</sub>-QC and (CN)<sub>2</sub>-NBD. Above ~280 K, the same fragmentation product is detected with a peak at 397.6 eV (Figure 6d, purple) attributed to cleaved cyano groups on the surface.<sup>[37–38]</sup> Above 470 K, the formation of nitride as final decomposition product is deduced from the asymmetric peak at 397.3 eV (Figure 6d, gray).<sup>[33a,36]</sup>

## Conclusions

We investigated the surface chemistry of dicyano-norbornadiene/quadricyclane on Ni(111) with HR-XPS, supported by DFT calculations. The adsorption of (CN)<sub>2</sub>-NBD and (CN)<sub>2</sub>-QC yields distinguishable spectroscopic fingerprints in the C 1s and N 1s regions, which are characteristic of the respective molecule. In addition, no indications for dissociation upon adsorption are found. Results from DFT calculations show that the adsorption in flat geometries ( $\eta^2:\eta^2$ ) is energetically favored for (CN)<sub>2</sub>-NBD, whereas the weaker bound (CN)<sub>2</sub>-QC displays minor energetic differences in different adsorption motifs. During adsorption at low temperature, the activation barrier to find the lowest energy is not overcome, leading to a mixture of different adsorption geometries. When supplying thermal energy to the system, we propose a rearrangement step for (CN)<sub>2</sub>-NBD into its most favorable geometry. Simulated XP spectra confirm the spectroscopic differences of (CN)<sub>2</sub>-NBD and (CN)<sub>2</sub>-QC.

Starting at 175 K, the conversion of (CN)<sub>2</sub>-QC to (CN)<sub>2</sub>-NBD is spectroscopically observed, while (CN)<sub>2</sub>-NBD is the solely detectable surface species at 260 K. Upon heating above 290 K, the molecular framework of (CN)<sub>2</sub>-NBD decomposes with the detachment of the cyano moiety. Above 400 K, amorphous carbon structures, carbide and nitride are formed (see Scheme 1). In contrast to parent NBD and dibromo-substituted NBD on Ni(111), benzene and methylidyne as decomposition intermediates are not formed during thermal evolution. In comparison, the dicyano-substituted system seems superior with an about 100 K higher onset of decomposition.<sup>[13,17]</sup> Thus,



**Scheme 1.** Proposed reaction pathway of (CN)<sub>2</sub>-QC on Ni(111): onset of cycloreversion reaction to (CN)<sub>2</sub>-NBD at 175 K, being completed at 260 K; beginning decomposition into C–H fragments and CN for temperatures above 290 K; final observation of amorphous carbon, carbide and nitride species.

our study demonstrates that the reactivity of the norbornadiene/quadracyclane system can be strongly influenced by the choice of the functional group, with the cyano moieties being electronically similar to halides, but smaller and more flexible. The successful monitoring of the cyclorversion reaction and the high thermal stability gives the general practicality of the surveyed model system as promising candidate for future MOST applications.

### Acknowledgements

The work was supported by the Cluster of Excellence 'Engineering of Advanced Materials' and the Deutsche Forschungsgemeinschaft (DFG) – Project No. 392607742. We thank Helmholtz-Zentrum Berlin for the allocation of synchrotron radiation beamtime and the BESSY II staff for support during beamtime. Open Access funding enabled and organized by Projekt DEAL.

### Conflict of Interest

The authors declare no conflict of interest.

### Data Availability Statement

The data that support the findings of this study are available from the corresponding author upon reasonable request.

**Keywords:** catalysis · energy storage · MOST system · photoelectron spectroscopy · surface reactions

- [1] a) M. Höök, X. Tang, *Energy Policy* **2013**, *52*, 797–809; b) British Petroleum, *Statistical Review of World Energy* **2020**, 69.
- [2] M. Meinshausen, N. Meinshausen, W. Hare, S. C. Raper, K. Frieler, R. Knutti, D. J. Frame, M. R. Allen, *Nature* **2009**, *458*, 1158–1162.
- [3] N. S. Lewis, D. G. Nocera, *Proc. Natl. Acad. Sci. USA* **2006**, *103*, 15729–15735.
- [4] a) A. Lennartson, A. Roffey, K. Moth-Poulsen, *Tetrahedron Lett.* **2015**, *56*, 1457–1465; b) K. Moth-Poulsen, D. Coso, K. Börjesson, N. Vinokurov, S. K. Meier, A. Majumdar, K. P. C. Vollhardt, R. A. Segalman, *Energy Environ. Sci.* **2012**, *5*; c) K. Börjesson, A. Lennartson, K. Moth-Poulsen, *ACS Sustainable Chem. Eng.* **2013**, *1*, 585–590; d) T. J. Kucharski, Y. C. Tian, S. Akbulatov, R. Boulatov, *Energy Environ. Sci.* **2011**, *4*, 4449–4472; e) C. L. Sun, C. Wang, R. Boulatov, *ChemPhotoChem* **2019**, *3*, 268–283; f) Z. Wang, A. Roffey, R. Losantos, A. Lennartson, M. Jevric, A. U. Petersen, M. Quant, A. Dreos, X. Wen, D. Sampedro, K. Börjesson, K. Moth-Poulsen, *Energy Environ. Sci.* **2019**, *12*, 187–193.
- [5] a) D. Schulte-Frohlinde, H. Blume, H. Güsten, *J. Phys. Chem.* **1962**, *66*, 2486–2491; b) D. H. Waldeck, *Chem. Rev.* **1991**, *91*, 415–436; c) C. Bastianelli, V. Caia, G. Cum, R. Gallo, V. Mancini, *J. Chem. Soc. Perkin Trans. 2* **1991**, 679–683.
- [6] a) H. Taoda, K. Hayakawa, K. Kawase, H. Yamakita, *J. Chem. Eng. Jpn.* **1987**, *20*, 265–270; b) H. M. Bandara, S. C. Burdette, *Chem. Soc. Rev.* **2012**, *41*, 1809–1825; c) A. M. Kolpak, J. C. Grossman, *Nano Lett.* **2011**, *11*, 3156–3162; d) K. Masutani, M. A. Morikawa, N. Kimizuka, *Chem. Commun.* **2014**, *50*, 15803–15806; e) Z. Wang, R. Losantos, D. Sampedro, M. Morikawa, K. Börjesson, N. Kimizuka, K. Moth-Poulsen, *J. Mater. Chem. A* **2019**, *7*, 15042–15047.
- [7] a) G. Jones, T. E. Reinhardt, W. R. Bergmark, *Sol. Energy* **1978**, *20*, 241–248; b) J. F. Xu, Y. Z. Chen, L. Z. Wu, C. H. Tung, Q. Z. Yang, *Org. Lett.* **2013**, *15*, 6148–6151.
- [8] a) K. P. C. Vollhardt, T. W. Weidman, *J. Am. Chem. Soc.* **1983**, *105*, 1676–1677; b) R. Boese, J. K. Cammack, A. J. Matzger, K. Pflug, W. B. Tolman, K. P. C. Vollhardt, T. W. Weidman, *J. Am. Chem. Soc.* **1997**, *119*, 6757–6773; c) Y. Kanai, V. Srinivasan, S. K. Meier, K. P. Vollhardt, J. C. Grossman, *Angew. Chem. Int. Ed.* **2010**, *49*, 8926–8929; *Angew. Chem.* **2010**, *122*, 9110–9113; d) K. Börjesson, D. Coso, V. Gray, J. C. Grossman, J. Guan, C. B. Harris, N. Hertkorn, Z. Hou, Y. Kanai, D. Lee, J. P. Lomont, A. Majumdar, S. K. Meier, K. Moth-Poulsen, R. L. Myrabo, S. C. Nguyen, R. A. Segalman, V. Srinivasan, W. B. Tolman, N. Vinokurov, K. P. Vollhardt, T. W. Weidman, *Chem. Eur. J.* **2014**, *20*, 15587–15604; e) A. Lennartson, A. Lundin, K. Börjesson, V. Gray, K. Moth-Poulsen, *Dalton Trans.* **2016**, *45*, 8740–8744.
- [9] X. W. An, Y. D. Xie, *Thermochim. Acta* **1993**, *220*, 17–25.
- [10] H. Taoda, K. Hayakawa, K. Kawase, *J. Chem. Eng. Jpn.* **1987**, *20*, 335–338.
- [11] G. S. Hammond, N. J. Turro, A. Fischer, *J. Am. Chem. Soc.* **1961**, *83*, 4674–4675.
- [12] U. Bauer, S. Mohr, T. Dopfer, P. Bachmann, F. Späth, F. Düll, M. Schwarz, O. Brummel, L. Fromm, U. Pinkert, A. Görling, A. Hirsch, J. Bachmann, H.-P. Steinrück, J. Libuda, C. Papp, *Chem. Eur. J.* **2017**, *23*, 1613–1622.
- [13] U. Bauer, L. Fromm, C. Weiß, P. Bachmann, F. Späth, F. Düll, J. Steinhauer, W. Hieberger, A. Görling, A. Hirsch, H.-P. Steinrück, C. Papp, *J. Phys. Chem. C* **2018**, *123*, 7654–7664.
- [14] M. Quant, A. Lennartson, A. Dreos, M. Kuisma, P. Erhart, K. Börjesson, K. Moth-Poulsen, *Chem. Eur. J.* **2016**, *22*, 13265–13274.
- [15] a) V. A. Bren', A. D. Dubonosov, V. I. Minkin, V. A. Chernouvanov, *Russ. Chem. Rev.* **1991**, *60*, 451–469; b) A. D. Dubonosov, V. A. Bren, V. A. Chernouvanov, *Russ. Chem. Rev.* **2002**, *71*, 917–927.
- [16] a) V. Gray, A. Lennartson, P. Ratanalert, K. Börjesson, K. Moth-Poulsen, *Chem. Commun.* **2014**, *50*, 5330–5332; b) K. Jorner, A. Dreos, R. Emanuelsson, O. El Bakouri, I. Fdez. Galván, K. Börjesson, F. Feixas, R. Lindh, B. Zietz, K. Moth-Poulsen, H. Ottosson, *J. Mater. Chem. A* **2017**, *5*, 12369–12378; c) A. Dreos, Z. Wang, J. Udmark, A. Ström, P. Erhart, K. Börjesson, M. B. Nielsen, K. Moth-Poulsen, *Adv. Energy Mater.* **2018**, *8*; d) M. Jevric, A. U. Petersen, M. Mansø, S. Kumar Singh, Z. Wang, A. Dreos, C. Sumbly, M. B. Nielsen, K. Börjesson, P. Erhart, K. Moth-Poulsen, *Chem. Eur. J.* **2018**, *24*, 12767–12772; e) M. Mansø, A. U. Petersen, Z. Wang, P. Erhart, M. B. Nielsen, K. Moth-Poulsen, *Nat. Commun.* **2018**, *9*, 1945; f) M. Mansø, B. E. Tebikachew, K. Moth-Poulsen, M. B. Nielsen, *Org. Biomol. Chem.* **2018**, *16*, 5585–5590; g) M. D. Kilde, M. Mansø, N. Ree, A. U. Petersen, K. Moth-Poulsen, K. V. Mikkelsen, M. B. Nielsen, *Org. Biomol. Chem.* **2019**, *17*, 7735–7746; h) M. Mansø, L. Fernandez, Z. Wang, K. Moth-Poulsen, M. B. Nielsen, *Molecules* **2020**, *25*; i) J. Orrego-Hernández, A. Dreos, K. Moth-Poulsen, *Acc. Chem. Res.* **2020**, *53*, 1478–1487.
- [17] U. Bauer, L. Fromm, C. Weiss, F. Späth, P. Bachmann, F. Düll, J. Steinhauer, S. Matysik, A. Pominov, A. Görling, A. Hirsch, H.-P. Steinrück, C. Papp, *J. Chem. Phys.* **2019**, *150*, 184706.
- [18] a) Y. Harel, A. W. Adamson, C. Kutal, P. A. Grutsch, K. Yasufuku, *J. Phys. Chem.* **1987**, *91*, 901–904; b) W. L. Dilling, *Chem. Rev.* **1966**, *66*, 373–393; c) Z.-i. Yoshida, *J. Photochem.* **1985**, *29*, 27–40.
- [19] R. Denecke, M. Kinne, C. M. Whelan, H.-P. Steinrück, *Surf. Rev. Lett.* **2002**, *09*, 797–801.
- [20] a) C. Papp, H.-P. Steinrück, *Surf. Sci. Rep.* **2013**, *68*, 446–487; b) A. Baraldi, G. Comelli, S. Lizzit, D. Cocco, G. Paolucci, R. Rosei, *Surf. Sci.* **1996**, *367*, L67–L72.
- [21] S. Doniach, M. Sunjic, *J. Phys. C* **1970**, *3*, 285–291.
- [22] a) W. Zhao, S. M. Kozlov, O. Höfert, K. Gotterbarm, M. P. A. Lorenz, F. Viñes, C. Papp, A. Görling, H.-P. Steinrück, *J. Phys. Chem. Lett.* **2011**, *2*, 759–764; b) R. Addou, A. Dahal, P. Sutter, M. Batzill, *Appl. Phys. Lett.* **2012**, *100*, 021601.
- [23] a) G. Kresse, J. Hafner, *Phys. Rev. B* **1993**, *47*, 558–561; b) G. Kresse, J. Furthmüller, *Comput. Mater. Sci.* **1996**, *6*, 15–50; c) G. Kresse, J. Furthmüller, *Phys. Rev. B* **1996**, *54*, 11169–11186.
- [24] G. Kresse, D. Joubert, *Phys. Rev. B* **1999**, *59*, 1758–1775.
- [25] J. P. Perdew, K. Burke, M. Ernzerhof, *Phys. Rev. Lett.* **1996**, *77*, 3865–3868.
- [26] M. Methfessel, A. T. Paxton, *Phys. Rev. B* **1989**, *40*, 3616–3621.
- [27] S. Grimme, J. Antony, S. Ehrlich, H. Krieg, *J. Chem. Phys.* **2010**, *132*, 154104.
- [28] H. J. Monkhorst, J. D. Pack, *Phys. Rev. B* **1976**, *13*, 5188–5192.
- [29] a) J. C. Slater, in *Advances in Quantum Chemistry*, Vol. 6 (Ed.: P.-O. Löwdin), Academic Press, **1972**, pp. 1–92; b) J. F. Janak, *Phys. Rev. B* **1978**, *18*, 7165–7168.
- [30] L. Köhler, G. Kresse, *Phys. Rev. B* **2004**, *70*.
- [31] C. J. Powell, A. Jablonski, *Nucl. Instrum. Methods Phys. Res. Sect. A* **2009**, *601*, 54–65.

- [32] D. P. Woodruff, A. M. Bradshaw, *Rep. Prog. Phys.* **1994**, *57*, 1029–1080.
- [33] a) I. Chorkendorff, J. N. Russell, J. T. Yates, *J. Chem. Phys.* **1987**, *86*, 4692–4700; b) S. X. Huang, D. A. Fischer, J. L. Gland, *J. Phys. Chem.* **1996**, *100*, 13629–13635; c) S. Lehwald, H. Ibach, *Surf. Sci.* **1979**, *89*, 425–445; d) C. Papp, R. Denecke, H.-P. Steinrück, *Langmuir* **2007**, *23*, 5541–5547.
- [34] a) R. Haerle, E. Riedo, A. Pasquarello, A. Baldereschi, *Phys. Rev. B* **2001**, *65*, 045101; b) J. Diaz, G. Paolicelli, S. Ferrer, F. Comin, *Phys. Rev. B* **1996**, *54*, 8064–8069; c) P. K. Chu, L. Li, *Mater. Chem. Phys.* **2006**, *96*, 253–277; d) C. Ronning, H. Feldermann, R. Merk, H. Hofsäss, P. Reinke, J. U. Thiele, *Phys. Rev. B* **1998**, *58*, 2207–2215.
- [35] a) A. Wiltner, C. Linsmeier, *Phys. Status Solidi* **2004**, *201*, 881–887; b) M. Wei, Q. Fu, Y. Yang, W. Wei, E. Crumlin, H. Bluhm, X. H. Bao, *J. Phys. Chem. C* **2015**, *119*, 13590–13597.
- [36] a) M. J. Grunze, J. Fühler, M. Neumann, C. R. Brundle, D. J. Auerbach, J. Behm, *Surf. Sci.* **1984**, *139*, 109–120; b) C. N. R. Rao, G. Ranga Rao, *Surf. Sci. Rep.* **1991**, *13*, 223–263; c) W. F. Egelhoff, *Phys. Rev. B* **1984**, *29*, 3681–3683.
- [37] a) R. Gouttebaron, S. Bourgeois, M. Perdureau, *Surf. Sci.* **2000**, *458*, 239–246; b) T. Nakayama, K. Inamura, Y. Inoue, S. Ikeda, K. Kishi, *Surf. Sci.* **1987**, *179*, 47–58.
- [38] a) K. Kishi, Y. Ehara, *Surf. Sci.* **1986**, *176*, 567–577; b) J. C. Hemminger, E. L. Muetterties, G. A. Somorjai, *J. Am. Chem. Soc.* **1979**, *101*, 62–67.

Manuscript received: March 24, 2022  
Revised manuscript received: May 23, 2022  
Accepted manuscript online: May 25, 2022  
Version of record online: June 29, 2022

# ChemPhysChem

## Supporting Information

### **Surface Chemistry of the Molecular Solar Thermal Energy Storage System 2,3-Dicyano-Norbornadiene/Quadricyclane on Ni(111)**

Felix Hemauer, Udo Bauer, Lukas Fromm, Cornelius Weiß, Andreas Leng, Philipp Bachmann, Fabian Düll, Johann Steinhauer, Valentin Schwaab, Robert Grzonka, Andreas Hirsch, Andreas Görling, Hans-Peter Steinrück, and Christian Papp\*

### Multilayer experiments of $(\text{CN})_2\text{-NBD}$ and $(\text{CN})_2\text{-QC}$

Multilayer experiments were performed to obtain further insights and to give additional proof for the conversion of  $(\text{CN})_2\text{-QC}$  to  $(\text{CN})_2\text{-NBD}$ . In these experiments, multilayers of both molecules were adsorbed at 130 K. The comparison of the respective spectral line shapes to those of submonolayers adsorbed at 130 K on Ni(111) (see main manuscript) is depicted in Figure S1. The multilayers of the two molecules show a very characteristic molecule-specific shape, which in both cases can clearly be differentiated from the submonolayer region by additional peaks at higher binding energies.

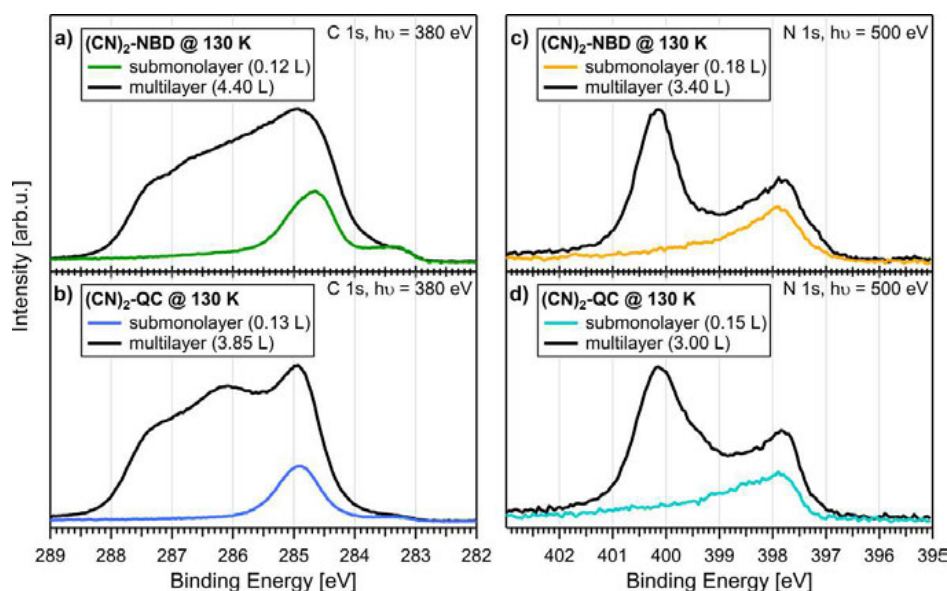


**Figure S1:** Depiction of acquired submono- and multilayer spectra at adsorption temperature of 130 K for (a, c)  $(\text{CN})_2\text{-NBD}$  and (b, d)  $(\text{CN})_2\text{-QC}$  in the respective core region; the characteristic line shape evolves features at higher binding energy side for multilayer exposures.

As a next step, temperature-programmed experiments were carried out. The desorption temperature of the multilayers is identified for both molecules to be about  $\sim 250$  K; above this temperature saturated monolayers remain on the surface. The C 1s multilayer spectra of  $(\text{CN})_2\text{-NBD}$  and  $(\text{CN})_2\text{-QC}$  show very characteristic differences measured right after adsorption (see Figure S2a and S2f). However, the comparison of the spectra of the two molecules after heating to 275 K gives an identical spectral shape, which is fitted with four peaks at 284.9, 284.3, 283.8 and 283.2 eV with a constant relative ratio (Figure S2b and S2e, light green). This again indicates complete conversion of  $(\text{CN})_2\text{-NBD}$  to  $(\text{CN})_2\text{-QC}$  at this temperature.

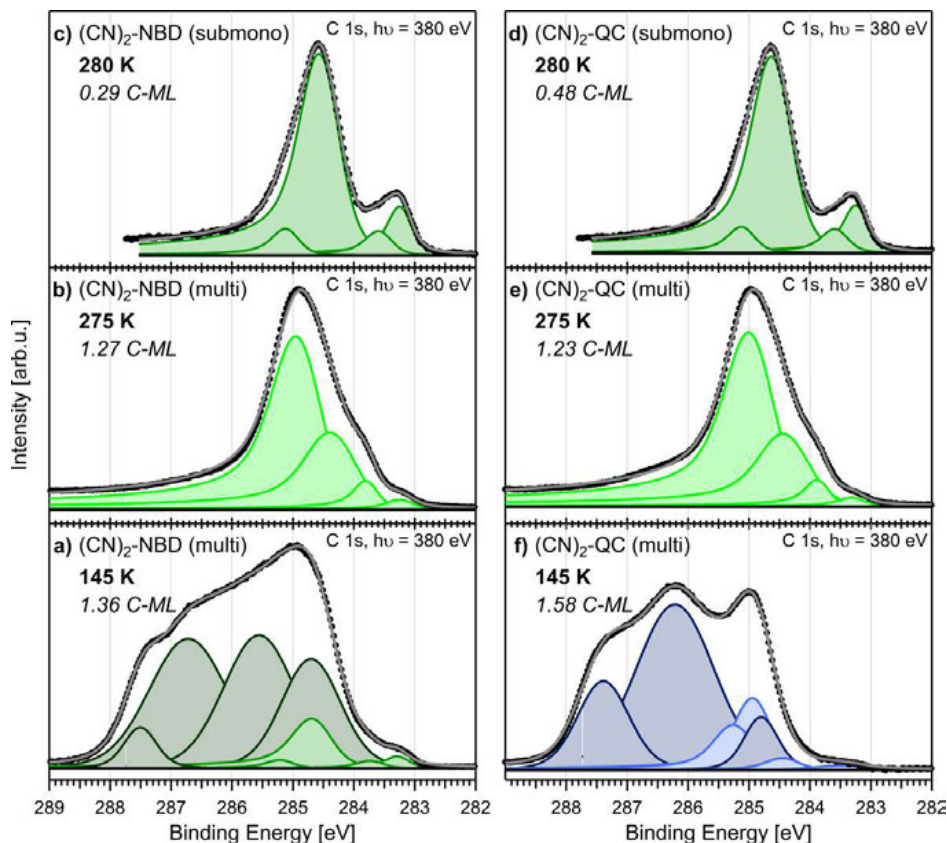
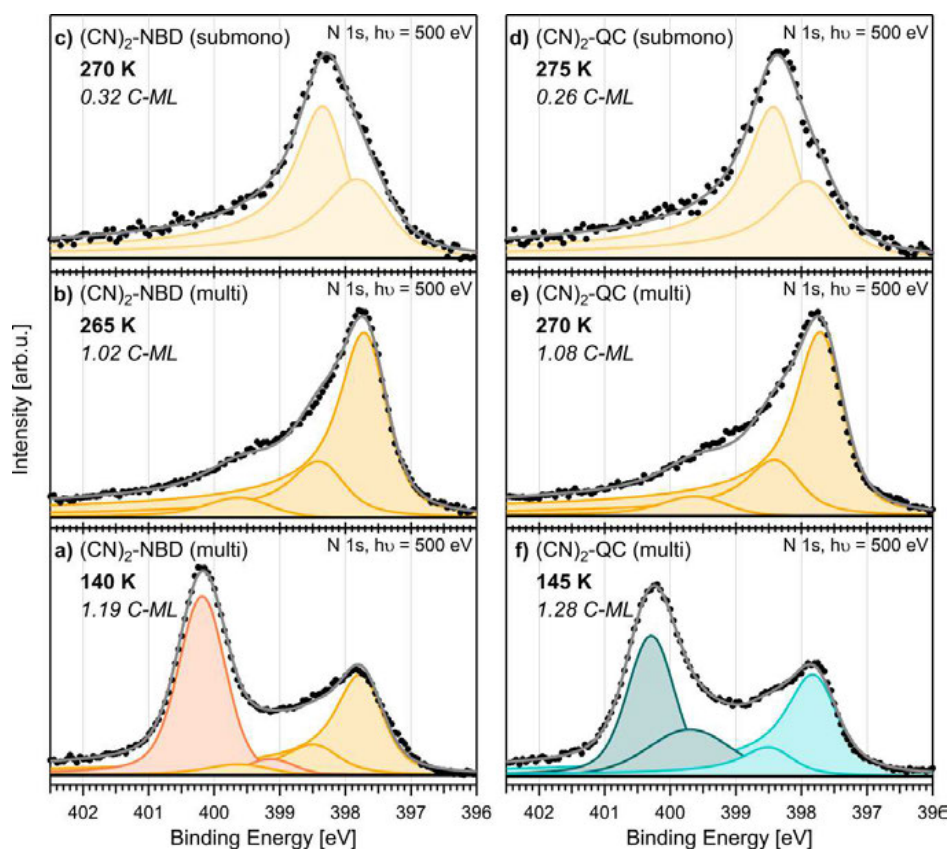


**Figure S2:** XP spectra of multilayer experiments of (a)  $(\text{CN})_2\text{-NBD}$  and (f)  $(\text{CN})_2\text{-QC}$  in the C 1s region after adsorption with color-coded fits (dark colors represent multilayer peaks); (b, e) comparison of spectra at 275 K confirms conversion of  $(\text{CN})_2\text{-QC}$  to  $(\text{CN})_2\text{-NBD}$  resulting in the same surface species (light green); (c, d) differences to equivalent spectra of submonolayer experiments (green).

Notably, compared to the submonolayer experiments at this temperature (see Figure S2c and S2d), the positions of the fitted peaks deviate up to 0.3 eV, and the line shape of the spectra obtained after heating the multilayer to 275 K is overall broader with additional intensity at  $\sim 284$  eV in comparison to submonolayer exposures heated to the same temperatures. These differences are explained by the higher surface coverage, by which stronger intermolecular interactions are expected and not all molecules can rearrange to the most stable configuration.

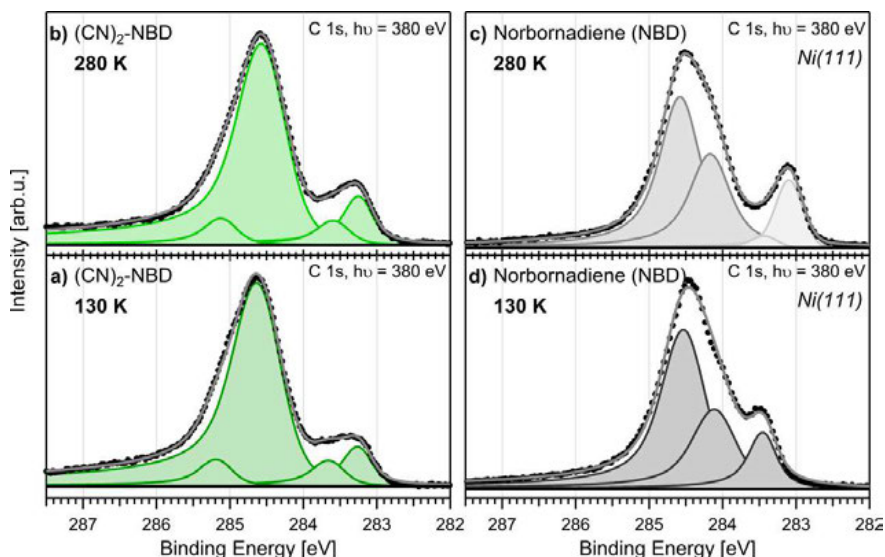
The findings in the N 1s region display the same behavior. The characteristic spectra of  $(\text{CN})_2\text{-NBD}$  and  $(\text{CN})_2\text{-QC}$  with their distinct multilayer features serve as fingerprint (see Figure S3a and S3f). However, after heating to  $\sim 270$  K, their spectral

differences are gone, and the three fitted peaks at 399.6, 398.3 and 397.6 eV are identical for both molecules (Figure S3b and S3e, orange). As before, the spectra obtained after heating the multilayer to 275 K do not match those of the submonolayer at equivalent temperatures (see Figure S3c and S3d). In comparison, they are shifted to lower binding energies by about 0.6 eV and possess a higher asymmetry towards higher binding energy side. The underlying reason is again the larger surface coverage and the results of that. Nevertheless, the isomerization reaction of  $(\text{CN})_2\text{-QC}$  to  $(\text{CN})_2\text{-NBD}$  is also clearly observed in these additional experiments.

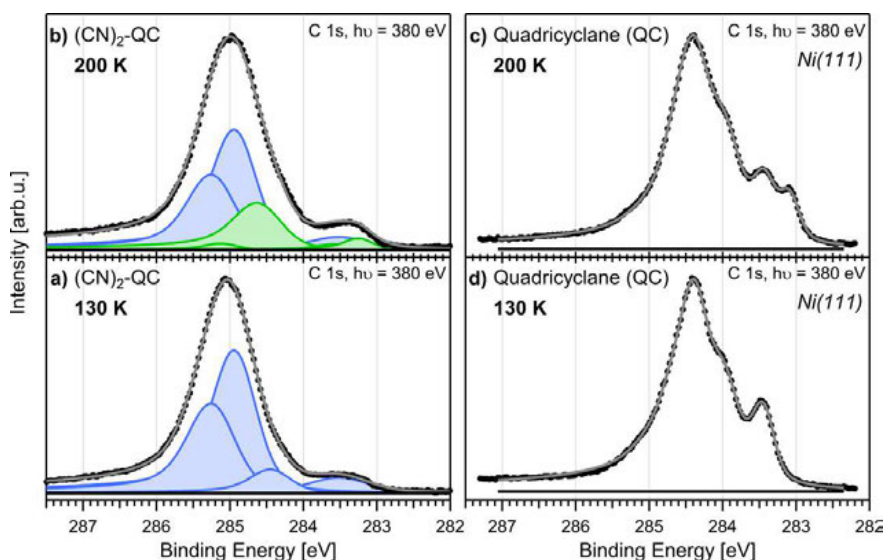


**Figure S3:** XP spectra of multilayer experiments of (a)  $(\text{CN})_2\text{-NBD}$  and (f)  $(\text{CN})_2\text{-QC}$  in the N 1s region after adsorption with color-coded fits (dark colors represent multilayer peaks); (b, e) comparison of spectra at ~270 K confirms conversion of  $(\text{CN})_2\text{-QC}$  to  $(\text{CN})_2\text{-NBD}$  resulting in the same surface species (orange); (c, d) differences to equivalent spectra of submonolayer experiments (light orange).

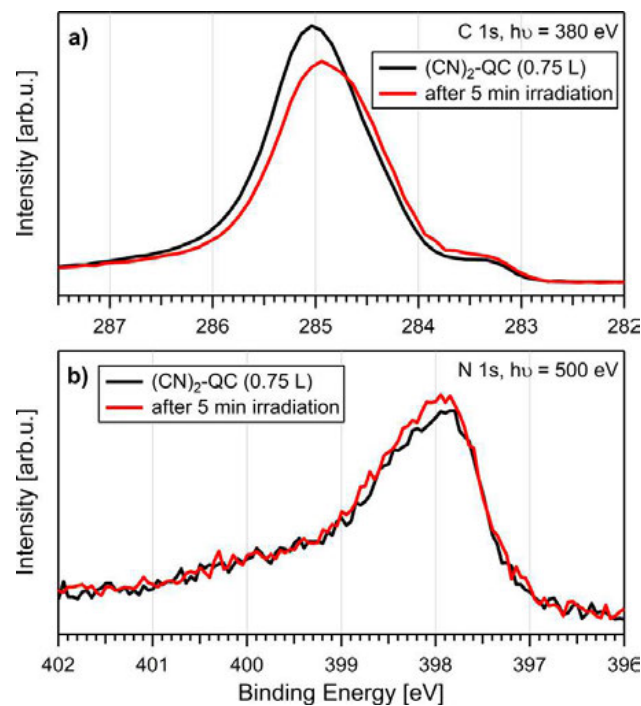
**Comparison of  $(\text{CN})_2\text{-NBD}$  and  $(\text{CN})_2\text{-QC}$  with unsubstituted NBD and QC**



**Figure S4:** Comparison of XP spectra of  $(\text{CN})_2\text{-NBD}$  with unsubstituted norbornadiene on Ni(111) in the C 1s region at (a, d) adsorption temperature and (b, c) 280 K; whereas  $(\text{CN})_2\text{-NBD}$  (green) displays only minor changes in the intensity ratio of the fitted peaks, NBD (dark gray) has already reacted to benzene (gray) and methylidyne (light gray).



**Figure S5:** Comparison of XP spectra of  $(\text{CN})_2\text{-QC}$  with unsubstituted quadricyclane on Ni(111) in the C 1s region at (a, d) adsorption temperature and (b, c) 200 K; whereas  $(\text{CN})_2\text{-QC}$  (blue) displays the partial conversion to  $(\text{CN})_2\text{-NBD}$  (green), the line shape of  $(\text{CN})_2\text{-QC}$  does not resemble that of QC at elevated temperature.

**Beam damage test of  $(\text{CN})_2\text{-QC}$** 

**Figure S6:** Representation of XPS spectra of  $(\text{CN})_2\text{-QC}$  measured (black) prior to and (red) after irradiation with X-rays for five minutes; the excitation energy was chosen to 380 and 500 eV for the respective core level. (a) In the C 1s region, the spectral shape of  $(\text{CN})_2\text{-QC}$  assimilates that of  $(\text{CN})_2\text{-NBD}$  by a shift of the main peak towards lower binding energy and a broadening of the shoulder. (b) The N 1s region exhibits minor changes in its spectral shape as the effects of the conversion are not as pronounced herein.

**NMR spectra of (CN)<sub>2</sub>-NBD and (CN)<sub>2</sub>-OC**

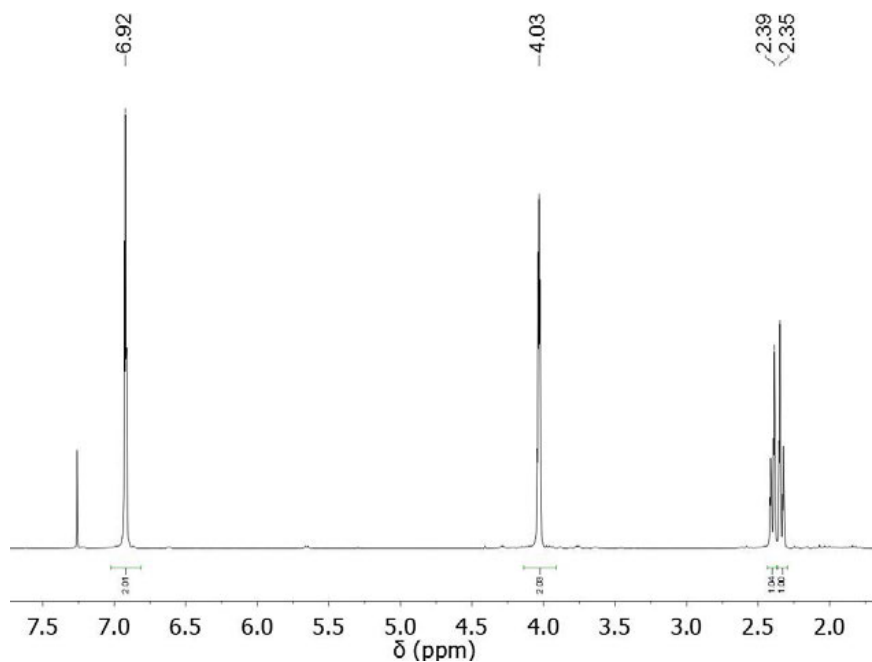


**Figure S7:** *1H-NMR spectrum of 2,3-Dicyano-NBD (CDCl<sub>3</sub>; 300 MHz)*

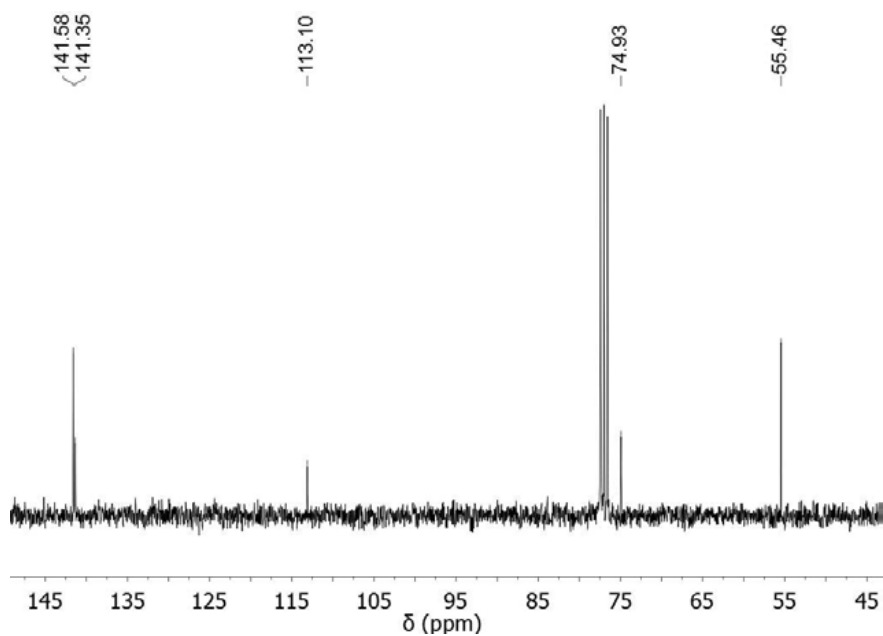


**Figure S8:** *13C-NMR spectrum of 2,3-Dicyano-NBD (CDCl<sub>3</sub>; 300 MHz)*

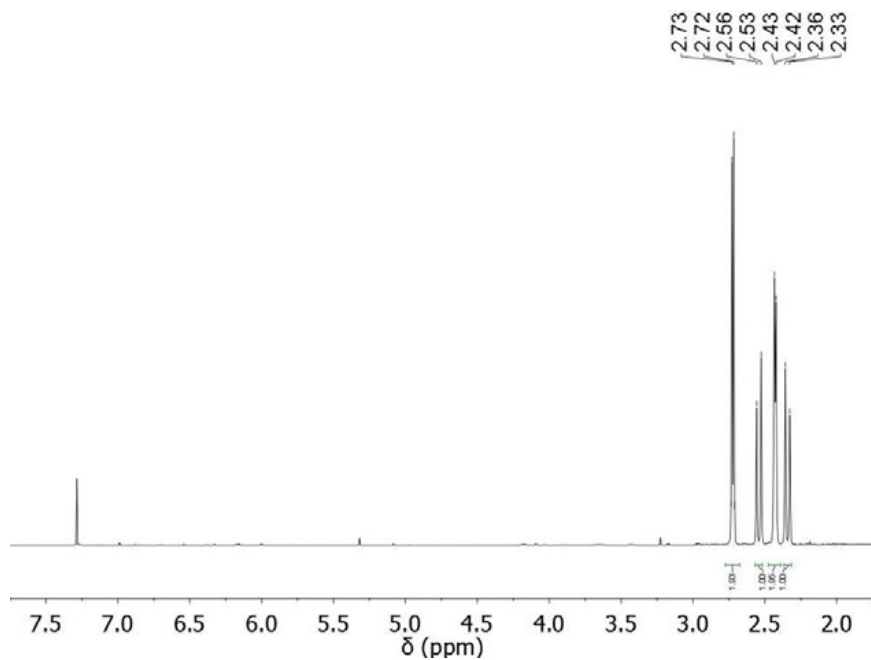


Figure S9:  $^1\text{H-NMR}$  spectrum of 2,3-Dicyano-QC ( $\text{CDCl}_3$ ; 400 MHz)

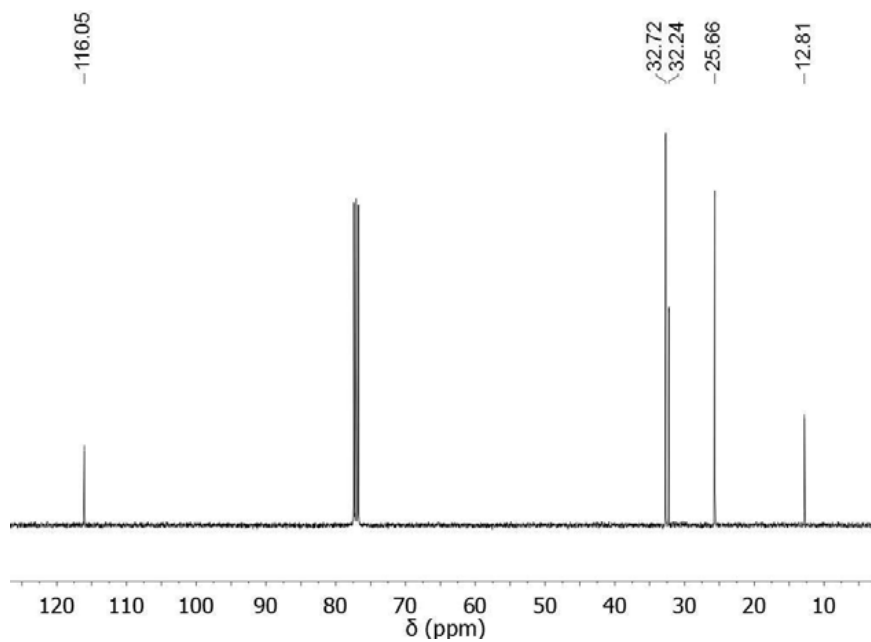


Figure S10:  $^{13}\text{C-NMR}$  spectrum of 2,3-Dicyano-QC ( $\text{CDCl}_3$ ; 400 MHz)

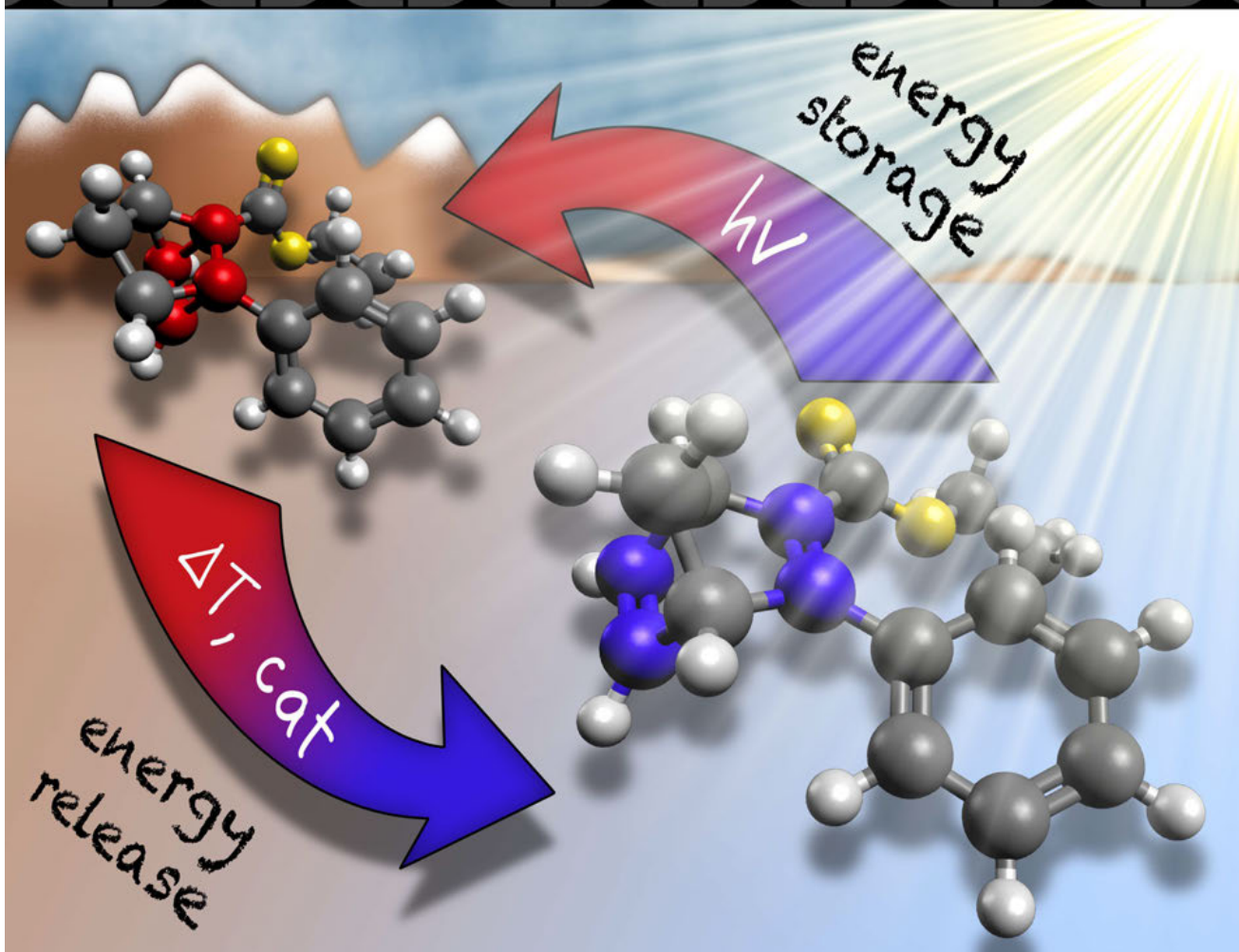
# Chemistry A European Journal

 **Chemistry  
Europe**  
European Chemical  
Societies Publishing

**Cover Feature:**

*C. Papp and co-workers*

Surface Studies on the Energy Release of the MOST System 2-Carboxy-3-Phenyl-Norbornadiene/Quadracyclane (PENBD/PEQC) on Pt(111) and Ni(111)



WILEY-VCH

25/2023



# Surface Studies on the Energy Release of the MOST System 2-Carboethoxy-3-Phenyl-Norbornadiene/Quadricyclane (PENBD/PEQC) on Pt(111) and Ni(111)

Felix Hemauer,<sup>[a]</sup> Valentin Schwaab,<sup>[a]</sup> Eva Marie Freiberger,<sup>[a]</sup> Natalie J. Waleska,<sup>[a]</sup> Andreas Leng,<sup>[b]</sup> Cornelius Weiß,<sup>[b]</sup> Johann Steinhauer,<sup>[a]</sup> Fabian Düll,<sup>[a]</sup> Philipp Bachmann,<sup>[a]</sup> Andreas Hirsch,<sup>[b]</sup> Hans-Peter Steinrück,<sup>[a, c]</sup> and Christian Papp<sup>\*[a, c, d]</sup>

**Abstract:** Novel energy-storage solutions are necessary for the transition from fossil to renewable energy sources. Auspicious candidates are so-called molecular solar thermal (MOST) systems. In our study, we investigate the surface chemistry of a derivatized norbornadiene/quadricyclane molecule pair. By using suitable push-pull substituents, a bathochromic shift of the absorption onset is achieved, allowing a greater overlap with the solar spectrum. Specifically, the adsorption and thermally induced reactions of 2-carboethoxy-3-phenyl-norbornadiene/quadricyclane are assessed on Pt(111) and Ni(111) as model catalyst surfaces by synchrotron radiation-based X-ray photoelectron spectroscopy (XPS). Comparison of the respective XP spectra enables the distinction of the energy-rich molecule from its energy-lean counterpart and allows qualitative information on the

adsorption motifs to be derived. Monitoring the quantitative cycloreversion between 140 and 230 K spectroscopically demonstrates the release of the stored energy to be successfully triggered on Pt(111). Heating to above 300 K leads to fragmentation of the molecular framework. On Ni(111), no conversion of the energy-rich compound takes place. The individual decomposition pathways of the two isomers begin at 160 and 180 K, respectively. Pronounced desorption of almost the entire surface coverage only occurs for the energy-lean molecule on Ni(111) above 280 K; this suggests weakly bound species. The correlation between adsorption motif and desorption behavior is important for applications of MOST systems in heterogeneously catalyzed processes.

## Introduction

The structural transition to renewable energy sources is one of the most decisive challenges of the 21st century. With a share

of more than 76% of the primary energy consumption in Germany in 2021,<sup>[1]</sup> there is still a major dependence on fossil fuels. Moreover, the future of nuclear power generation is questionable due to safety concerns and political decisions.<sup>[2]</sup> Thus, green energy production is without alternative. However, in addition to geographical factors and seasonal fluctuations, there is no constant renewable power generation throughout a day. This intermittent character is especially pronounced for wind and solar energy. The resulting mismatch between load and demand of energy requires novel storing solutions.

One approach to tackle both energy production and energy storage are so-called molecular solar thermal (MOST) systems.<sup>[3]</sup> Unlike to photovoltaic devices, solar energy is captured and stored in a chemical manner. The energy-lean parent compound is converted to its energy-rich valence isomer by irradiation. In this process, a rearrangement of chemical bonds leads to strain within the molecular framework. Triggered thermally or catalytically, the back reaction releases the energetic difference on demand. The energy density strongly depends on the molecular weight and the reaction enthalpy of the photoconversion. Moreover, the absorption maximum of the energy-lean compound should coincide with the solar spectrum. Reversibility of the overall storage cycle and thermal stability also determine the feasibility of the considered systems.

[a] F. Hemauer, V. Schwaab, E. M. Freiberger, N. J. Waleska, Dr. J. Steinhauer, Dr. F. Düll, Dr. P. Bachmann, Prof. Dr. H.-P. Steinrück, Prof. Dr. C. Papp  
Lehrstuhl für Physikalische Chemie II  
Friedrich-Alexander-Universität Erlangen-Nürnberg  
Egerlandstr. 3, 91058 Erlangen (Germany)  
E-mail: christian.papp@fau.de

[b] A. Leng, Dr. C. Weiß, Prof. Dr. A. Hirsch  
Lehrstuhl für Organische Chemie II  
Friedrich-Alexander-Universität Erlangen-Nürnberg  
Nikolaus-Fiebiger-Str. 10, 91058 Erlangen (Germany)

[c] Prof. Dr. H.-P. Steinrück, Prof. Dr. C. Papp  
Erlangen Center for Interface Research and Catalysis (ECRC)  
Friedrich-Alexander-Universität Erlangen-Nürnberg  
Egerlandstr. 3, 91058 Erlangen (Germany)

[d] Prof. Dr. C. Papp  
Physikalische und Theoretische Chemie  
Freie Universität Berlin  
Arnimallee 22, 14195 Berlin (Germany)

Supporting information for this article is available on the WWW under <https://doi.org/10.1002/chem.202203759>

© 2023 The Authors. Chemistry – A European Journal published by Wiley-VCH GmbH. This is an open access article under the terms of the Creative Commons Attribution License, which permits use, distribution and reproduction in any medium, provided the original work is properly cited.

Various compound classes have been suggested for MOST applications in literature. These include different azobenzenes,<sup>[4]</sup> stilbenes,<sup>[5]</sup> or fulvalene-tetracarbonyl-diruthenium<sup>[6]</sup> based systems. Herein, we investigate derivatives of the molecule pair norbornadiene (NBD) and quadricyclane (QC). The parent compounds are well known for several decades<sup>[7]</sup> and exhibit promising storage properties with a sufficient quantum yield for the photoconversion,<sup>[8]</sup> a reasonable long-term stability,<sup>[9]</sup> and a high reaction enthalpy of  $89 \text{ kJ mol}^{-1}$ .<sup>[10]</sup> However, the absorption onset of unsubstituted NBD at  $\sim 267 \text{ nm}$ <sup>[11]</sup> has to be shifted to higher wavelengths for a better overlap with the solar spectrum.<sup>[12]</sup> Functionalization of the molecular framework leads to the desired bathochromic shift, but increases the molecular weight and, therefore, reduces the storage capacity. In addition, requirements concerning the thermal stability and facile isomerization into its energy-rich counterpart have still to be fulfilled. By now, numerous derivatives are available from synthesis.<sup>[11,13]</sup>

Insights into the surface chemistry at molecular scale during heterogeneously catalyzed processes provide crucial information for the path to real-life applications of the proposed model systems. Next to demonstrating successful isomerization and a triggered back reaction, stability boundaries and the interaction strength with the surface must be assessed. Our group investigated the cycloreversion reaction of unsubstituted QC to NBD and its thermal evolution on different catalyst surfaces. We found a high reactivity on Pt(111),<sup>[14]</sup> such that the conversion to NBD took place at temperatures below 125 K. On Ni(111),<sup>[15]</sup> the onset of the reaction of QC to NBD was determined to be  $\sim 168 \text{ K}$ . The decomposition of NBD set in at about 190 K in both cases. In addition, first derivatives were studied on Ni(111). Results for 2,3-dibromonorbornadiene and its isomer<sup>[16]</sup> showed a partial dissociation of the bromine moieties at  $\sim 120 \text{ K}$ . Nevertheless, the cycloreversion occurred at 170 K, while the subsequent reaction was equivalent to that found for the unsubstituted system. For 2,3-dicyano-norbornadiene and the corresponding isomer,<sup>[17]</sup> we observed intact adsorption at 130 K. The conversion reaction to the NBD derivative was monitored between 175 and 260 K, while thermal stability was given up to 290 K.

In this work, we discuss the adsorption and reaction behavior of 2-carbethoxy-3-phenyl-norbornadiene/quadricyclane (Figure 1), which is addressed in the following as phenylester-NBD/QC (PENBD/PEQC), on Pt(111) and Ni(111). With its push-pull substituents, the absorption onset of this NBD derivate at  $359 \text{ nm}$ <sup>[18]</sup> is favorable, while the molecular mass is still reasonable with  $240.3 \text{ g mol}^{-1}$ . Synchrotron radiation-based X-ray photoelectron spectroscopy allows for in-situ measurements during adsorption. Temperature-programmed XPS (TPXPS) experiments were conducted to gain insights into the reaction pathway of both compounds on the two surfaces. In this way, we provide results on the feasibility of triggering the cycloreversion, and information about the thermal stability and decomposition. Thereby, another molecular design of norbornadiene/quadricyclane systems is evaluated.

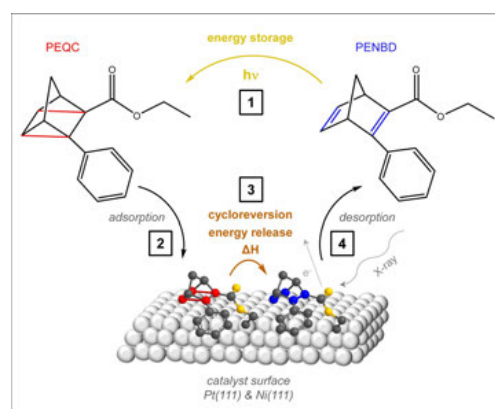


**Figure 1.** Scheme of the overall energy storage cycle of PENBD/PEQC as a proposed molecular solar thermal system: 1) Solar energy is captured and stored through irradiation of PENBD and isomerization to PEQC. 2) Adsorption of PEQC on a suitable catalyst material to trigger 3) the cycloreversion reaction back to PENBD under the release of energy on demand. 4) Desorption of the intact molecule for ideal total reversibility. XPS experiments conducted under UHV conditions are indicated by representation of the photoelectric effect.

## Results and Discussion

The feasibility of the molecule pair 2-carbethoxy-3-phenyl-norbornadiene/quadricyclane (PENBD/PEQC) as a MOST system is addressed on different model catalyst surfaces, namely Pt(111) and Ni(111). In our study, we discuss in-situ HR-XPS measurements of the thermal evolution. In all experiments, the coverage was chosen to be in the sub-monolayer range to trace the reaction pathway without influence by possible physisorbed layers, which do not take part in the reaction. In the following, first C 1s spectra are evaluated, and the complementary O 1s region is described thereafter.

### PENBD/PEQC on Pt(111): C 1s region

We start with discussing the adsorption of PEQC and PENBD on Pt(111) at 125 K. Figure 2a depicts the evolution of the C 1s spectra with characteristic line shape upon exposing the clean surface (gray spectrum) to the energy-rich, strained PEQC. An exposure of 3.7 L resulted in a carbon coverage of 0.39 ML (red). The adsorption of the energy-lean counterpart PENBD is shown in Figure 2f; in this case, an exposure of 2.4 L at 125 K led to a coverage of 0.25 ML (blue). After the adsorption experiments, the temperature-programmed experiments were conducted by applying a constant heating rate ( $\beta = 0.5 \text{ K s}^{-1}$ ), while acquiring XP spectra continuously. Figure 2b depicts selected spectra of PEQC of the thermal evolution, and in Figure 2e the corresponding data of PENBD is shown. All XP spectra of the adsorption and TPXPS experiments are provided as density plots (Figure S2 in the Supporting Information). For a quantitative analysis of the adsorption and reaction behavior,

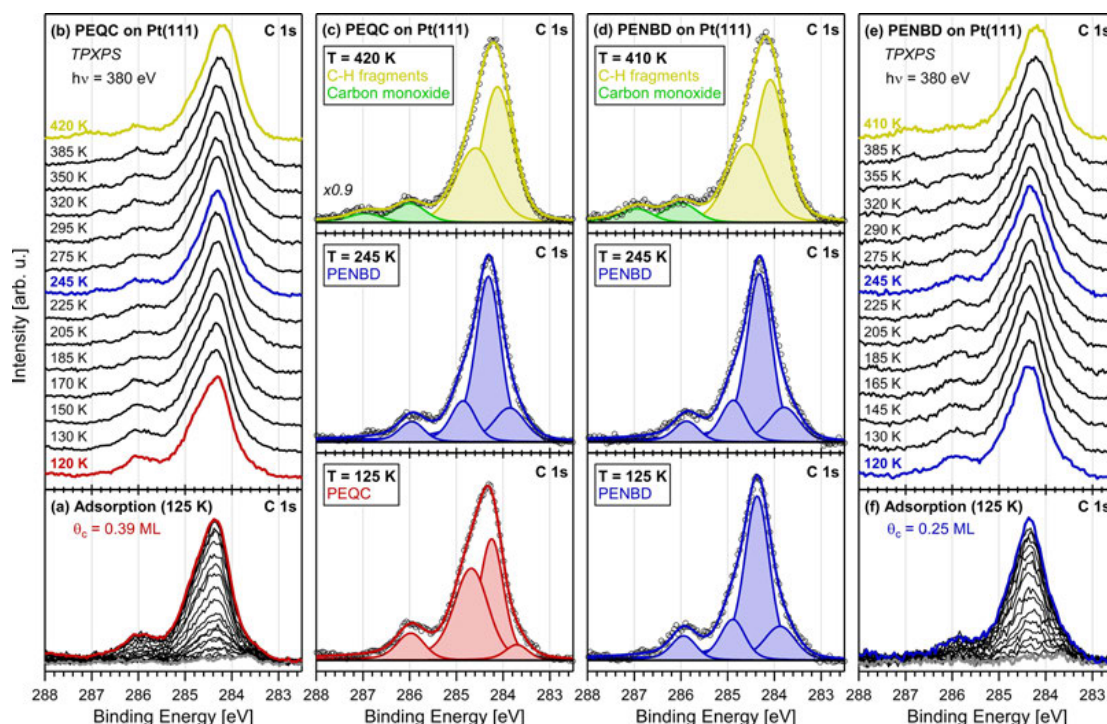


**Figure 2.** XP spectra of a) PEQC and f) PENBD in the C 1s region upon adsorption at low temperature on Pt(111); their characteristic line shapes enable the molecules to be distinguished. The thermal evolution during temperature-programmed XPS (TPXPS) experiments is depicted for selected spectra of b) PEQC and e) PENBD as waterfall plots; c), d) spectra shown with fits are highlighted.

the data for both molecules have been fitted with a suitable fit model (see Table S1 for parameters).

We begin with the analysis of the data for adsorption of the energy-rich PEQC on Pt(111). Representative XP spectra along with their color-coded fits are shown in Figure 2c. At 125 K, the C 1s spectrum of PEQC (red) is fitted with four peaks at 283.7, 284.2, 284.7 and 286.0 eV with a fixed relative intensity ratio (1:8:8:2). Due to the large number of chemically very similar carbon atoms within the molecular structure and different possible orientations on the surface, the overlapping peaks cannot be assigned to individual carbon atoms in the molecules. The XP spectra rather serve as fingerprint of the investigated molecule. Nevertheless, we assume that the carbon atoms adjacent to the oxygen atoms of the ester moiety contribute to the peaks at higher binding energy.<sup>[19]</sup> The other peaks fall in the binding energy range known for unsubstituted quadricyclane on Pt(111) between 283.5 and 284 eV,<sup>[14]</sup> and benzene on Pt(111) between 284 to 285 eV.<sup>[20]</sup>

The result of peak fitting for the energy-lean PENBD is shown in Figure 2d for different representative temperatures. After adsorption of PENBD at 125 K (blue), at first sight, an overall similar line shape is detected as for PEQC. This is not surprising, as both molecular structures deviate by only two C–C bonds within the extended framework. However, closer

inspection showed that quite different fit parameters have to be employed. Most notably is the difference of the relative intensity ratio (1:4:1:0.6) for PENBD, in comparison to PEQC (see above). While again four peaks describe the envelope of the measured spectra, the peaks are shifted to lower binding energies by 100 to 200 meV in comparison to PEQC, yielding values of 283.9, 284.4, 284.9 and 285.9 eV. In addition, the peak widths are different, that is, the peak at 283.9 eV is by 190 meV broader, whereas that at 284.9 eV is by 220 meV more narrow. As outlined above, a direct assignment of the respective signals to single atoms is not possible. Nevertheless, we again propose that the peak at highest binding energy correlates to the carbon atoms close to the ester group. Similar subtle differences in the spectral appearance have also been found for unsubstituted NBD/QC on Pt(111).<sup>[14]</sup> In summary, molecular adsorption of both PEQC and PENBD is observed, with each showing a distinct spectral fingerprint.

Next, we address the C 1s spectra during thermal evolution of PEQC on Pt(111). In Figure 2b, the waterfall plot shows selected spectra upon heating, and Figure 2c displays the peak fitting for the spectra at 125, 245 and 420 K. The corresponding quantitative analysis of all spectra of the heating series yields the coverage of the surface species in carbon MLs as a function of temperature in Figure 3; in addition, the proposed reaction

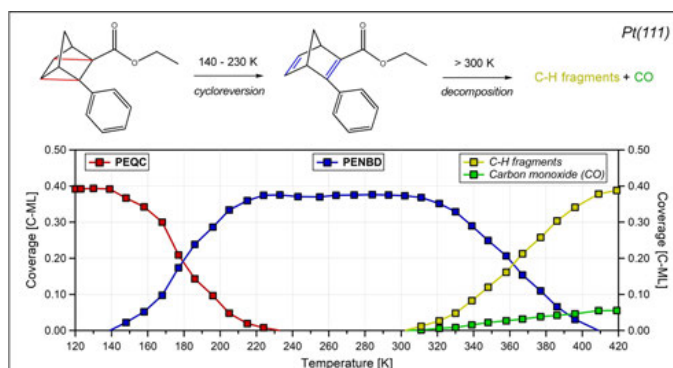


**Figure 3.** Quantitative analysis of the temperature-programmed XPS (TPXPS) experiment of PEQC in the C 1s region on Pt(111) coverage in carbon monolayers as a function of temperature: onset of the back reaction of PEQC to PENBD at 140 K, PENBD as solely surface species above 230 K, and decomposition into C–H fragments and CO when heating higher than 300 K;  $\beta = 0.5 \text{ K}^{-1}$ .

pathway of PEQC on Pt(111) is illustrated. The spectral appearance of PEQC stays unchanged until 140 K. Thereafter, the shoulder at  $\sim 285 \text{ eV}$  loses intensity and the height of the maximum at  $\sim 284.4 \text{ eV}$  increases. Overall, a transformation towards the line shape of PENBD at 125 K (Figure 2d, bottom) occurs. From the identical fit parameters at 245 K, we conclude that equivalent surface species exist. The onset of the cycloreversion reaction of PEQC to PENBD is at 140 K. Above this temperature, the surface coverage of PEQC is declining to the same extent as that of PENBD is increasing, while the total carbon amount remains constant. At 180 K, the amount of PENBD passes that of PEQC, and above 230 K, only PENBD is present on the surface (Figure 3). The unchanged total surface coverage and the absence of additional peaks indicate that no side reactions or desorption takes place and a quantitative conversion of PEQC to PENBD occurs. The observations for PEQC are in contrast to those for unsubstituted QC, which undergoes a direct back reaction to NBD upon adsorption on Pt(111) already at 125 K.<sup>[14]</sup> Therefore, steric and electronic influences by the push/pull-ligands and a different adsorption geometry hinder the catalytic activity on Pt(111) for the energy-rich PEQC derivative, so that a controlled conversion to energy-lean PENBD is observed at higher temperatures. Upon further heating, an analogous reaction behavior is found as for the PENBD experiment (see below).

The thermal evolution of PENBD can be analyzed from the TPXP spectra in Figure 2e and the selected fits in Figure 2d. Up to 300 K, no changes of the spectral line shape of PENBD are observed. Both the widths as well as the relative intensities remain constant; minor deviations of the peak positions by less than 100 meV towards lower binding energies are within the accuracy of measurement and evaluation. This observation indicates that the thermal stability of PENBD is relatively high, considering the fact that for unsubstituted NBD on Pt(111) already at 190 K the dissociation of a hydrogen atom from the bridgehead methyl group occurs.<sup>[14]</sup> This comparison suggests a different adsorption behavior of PENBD with no “side-on”

geometry, implying that the bridgehead methyl group of the NBD unit does not point towards the surface. Above 300 K, a broadening of the main signal is found, which is fitted with two peaks at 284.1 and 284.6 eV (yellow). This indicates the onset of the decomposition of the molecular framework into unspecified C–H fragments as common dissociation products of hydrocarbons at elevated temperatures.<sup>[14,21]</sup> The two remaining peaks at higher binding energies, 286.0 and 286.9 eV (green) are ascribed to emerging carbon monoxide (CO), in accordance to literature values for bridge and on-top adsorption sites on Pt(111).<sup>[22]</sup> The amount of detected CO (Figure 3) matches the expected proportion of 12.5% (1/8) of the total fit area, implying the quantitative formation of two equivalents of CO for each decomposed molecule.

The complementary O 1s spectra of PEQC and PENBD on Pt(111) are given in Figure S1. However, due to coadsorption of water, the low oxygen content of the molecules and resulting rather low signal-to-noise ratio, less information can be derived. Moreover, the spectral differences of PEQC and PENBD are less pronounced in the O 1s spectra, since the structural differences only affect two pairs of carbon atoms within the NBD/QC framework, which are remote to the ester moiety. Thus, no distinction is possible in the O 1s region. Nonetheless, the stability boundaries are verified and the presence of carbon monoxide, in bridge and on-top position, is confirmed.

#### PENBD/PEQC on Ni(111): C 1s region

For comparison, we also addressed the adsorption and thermal evolution of PEQC and PENBD on Ni(111). The data is depicted and evaluated analogously to the Pt(111) experiments. The corresponding density plots of all measured XP spectra are given in Figure S3. Figure 4a shows the spectra during exposure of Ni(111) to the energy-rich, strained PEQC at 115 K leading to a characteristic line shape; the exposure of 1.4 L yielded 0.29 ML (red spectrum). Small intensities prior to the dosage (gray) are

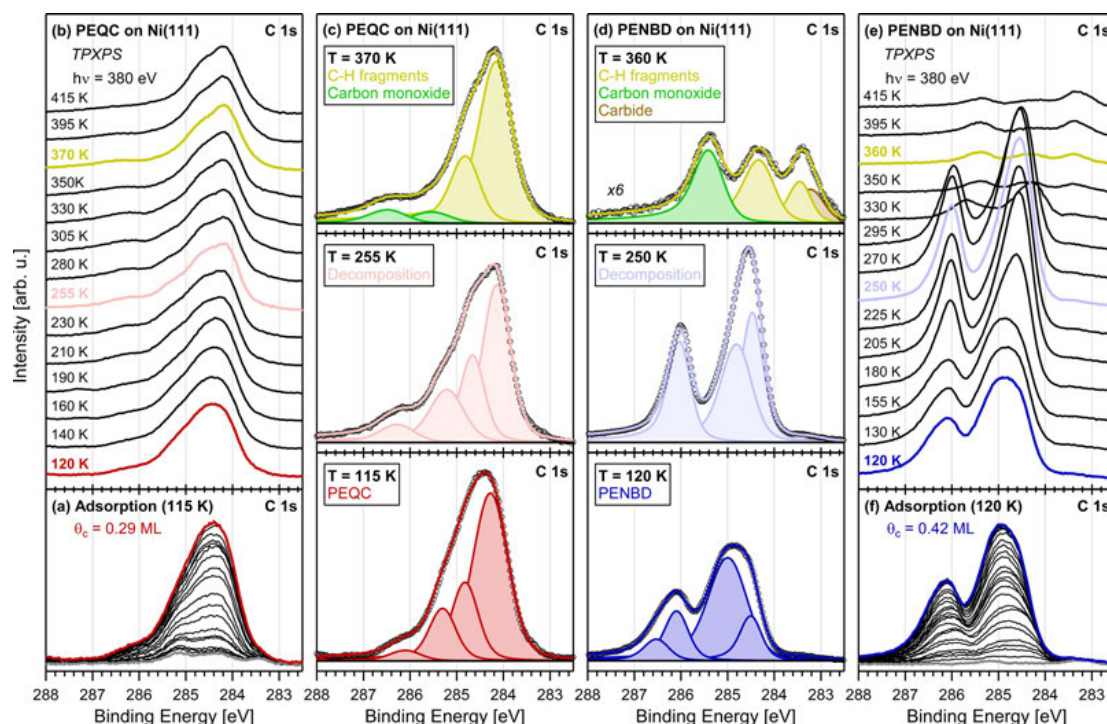


**Figure 4.** XP spectra of a) PEQC and f) PENBD in the C 1s region upon adsorption at low temperature on Ni(111); their characteristic line shapes enable the molecules to be distinguished. The thermal evolution during temperature-programmed XPS (TPXPS) experiments is depicted for selected spectra of b) PEQC and e) PENBD as waterfall plots; c), d) spectra shown with fits are highlighted.

due to preadsorption of residual PEQC molecules in the chamber. The adsorption of the energy-lean PENBD at 120 K is depicted in Figure 4f (blue); here an exposure of 1.9 L resulted in a coverage of 0.42 ML. The subsequent TPXPS experiments of PEQC and PENBD are shown in Figure 4b and 4e, respectively. Again, the data was fitted for quantitative analysis (see Table S2 for parameters). Selected spectra of PEQC and PENBD along with their color-coded fits are shown in Figure 4c and d, respectively. The quantitative analyses of the thermal evolution are provided in Figure 5, wherein the coverages of the surface species are plotted against the temperature.

The spectrum after adsorption of PEQC on Ni(111) at 115 K (red) is fitted with four peaks at 284.3, 284.8, 285.3 and 286.1 eV with constant relative intensity ratio (10:3.7:2.5:0.7). As was the case for Pt(111), no direct assignment of the fitted peaks to single atoms within the molecular framework is possible, but the line shape serves as spectroscopic fingerprint of the investigated molecule. In literature, signals of unsubstituted QC on Ni(111) have been observed between 283.5 and 284.5 eV,<sup>[15]</sup> and those of benzene at slightly higher binding energies.<sup>[23]</sup> Thus, a convolution of these contributions plus those of the ester moiety up to 286.1 eV are in line with the observed spectrum of PEQC. Notably, while binding energy positions are comparable to the values of PEQC on Pt(111) (see above), their

relative intensities are different and the FWHM is higher on Ni(111).

After adsorption of PENBD on Ni(111) at 120 K, the C 1s spectrum in Figure 4d (blue) displays a very different line shape from that of PEQC, with two separated strong signals. Fitting yields four peaks at 284.5, 285.0, 286.1 and 286.5 eV, with fixed relative intensity ratio (1:3.7:1.2:0.5); the peaks are individually shifted by up to 800 meV towards higher binding energies and show other widths compared to PEQC/Ni(111). The minor contribution at 283.2 eV (1.2% of total intensity) is assigned to carbide,<sup>[24]</sup> which is present on the surface prior to the adsorption and does not change during the experiment. Again, no attribution to single atoms is possible from the fitted peaks. Since there are only slight structural differences between PEQC and PENBD, it is surprising to find such strongly differing spectral shapes after adsorption on Ni(111), unlike to the situation on Pt(111). Next to different electronic influences of the substrate, an additional cause for this behavior is the possible coexistence of different adsorption geometries of PEQC and PENBD, which will be discussed later in the O 1s section.

The thermal evolution of PEQC on Ni(111) is shown in the waterfall plot in Figure 4b, along with selected fits in Figure 4c; the quantitative analysis of all data is given in Figure 5a. Line

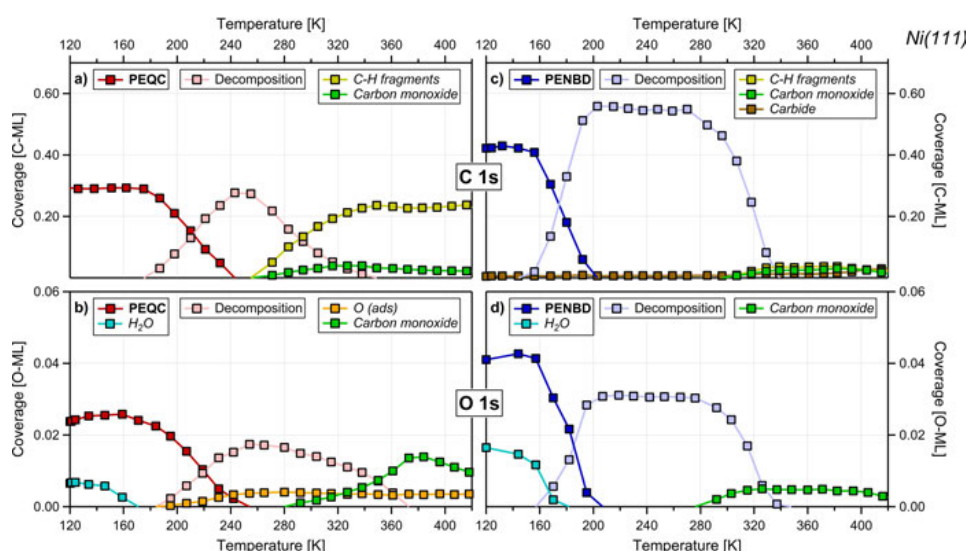


**Figure 5.** Quantitative analysis of the TPXPS experiments on Ni(111) of a) PEQC in the C 1s region, b) PEQC in the O 1s region, c) PENBD in the C 1s region, and d) PENBD in the O 1s region. Respective surface species are color coded, and their coverages are given in corresponding monolayers as a function of temperature;  $\beta = 0.5 \text{ K s}^{-1}$ .

shape and coverage remain unchanged, until above 180 K small changes in the spectral appearance and an overall shift to lower binding energies are observed, indicating a transformation of the surface species that is complete at  $\sim 240 \text{ K}$ ; four new peaks at 284.1, 284.6, 285.2 and 286.3 eV are employed in order to obtain a satisfying fit (Figure 4c, light red). Three are shifted to lower binding energies by up to 200 meV, and only the peak at 286.3 eV shifts to higher binding energies by 200 meV. In addition, the relative intensity ratios change, in particular yielding a lower intensity for the peak with the lowest binding energy due to a more narrow line shape. Therefore, a rearrangement of the molecule on the surface, similar to what has been reported for dicyanonorbadiene,<sup>[17]</sup> and/or decomposition reactions<sup>[25]</sup> are proposed. Compared to PENBD at equivalent temperatures, the line shape differs significantly. This is true for every spectrum during the thermal evolution of the molecular pair indicating no cycloreversion of PEQC to PENBD or even the presence of identical surface species at any temperature on Ni(111). Instead, individual decomposition routes are found. The stability boundaries are similar to unsubstituted and dibromo-substituted NBD/QC on nickel.<sup>[15–16]</sup>

Upon further heating PEQC to above 270 K, another characteristic change of the line shape is seen. The spectra are fitted by four new peaks at 284.1, 284.8, 285.5 and 286.4 eV (Figure 4c), with no change in total coverage (Figure 5a) and thus no desorption, which is in contrast to the behavior of PENBD (see below). The peaks at 285.5 and 286.4 eV (green) are ascribed to CO on bridge site and on top site, respectively; small shifts to higher binding energies compared to clean Ni(111) are attributed to coadsorption of hydrogen and

oxygen.<sup>[26]</sup> As for PEQC/Pt(111), two equivalents of CO are formed for each decomposed PEQC molecule, since the fit area of CO ( $\sim 12\%$ ; Figure 5a) agrees with the stoichiometric ratio of 1/8. The two remaining peaks at 284.1 and 284.8 eV are due to residual unspecified C–H fragments on the surface.<sup>[27]</sup>

The thermal evolution of PENBD on Ni(111) is shown in the waterfall plot in Figure 4e and selected fits in Figure 4d. The line shape and coverage (Figure 4e) remains unchanged up to 160 K. Thereafter, the spectroscopic appearance shows a pronounced change, and the C 1s spectra are now fitted with three new peaks at 284.5, 284.8 and 286 eV (Figure 4d, light blue). Thus, this temperature marks the onset of the first reaction step. Simultaneously, we find a significant change in the O 1s region (see below). These observations indicate a decomposition of the molecular framework, likely with a detachment of the ester moiety.<sup>[28]</sup> In contrast to unsubstituted NBD and dibromo-substituted NBD on Ni(111),<sup>[15–16]</sup> there are no indications for the formation of methylidyne or benzene.<sup>[23,29]</sup> Interestingly, the total carbon amount rises by 30% to 0.56 ML at 205 K, when the signals of intact PENBD have vanished. Since no additional carbon was supplied to the surface, we attribute this observation to a lower attenuation of the photoelectrons due to the reaction step and/or different photoelectron diffraction conditions for the distributed fragments in comparison to the bulky molecule (note the high surface sensitivity and multiple scattering effects at the chosen low kinetic energy of the photoelectrons of  $\sim 100 \text{ eV}$ ).<sup>[30]</sup> Starting at 280 K, a pronounced decrease of the total coverage to a residual coverage of 0.06 ML at 340 K is observed in Figure 5c (that is, a decline of more than 87%), indicative of nearly complete

desorption of all surface species. This strong desorption is rather uncommon for extended hydrocarbon molecules. We explain this behavior by a weak interaction of the decomposition fragments with the nickel surface. With support of the O 1s data (see below), a less stable adsorption motif of PENBD is proposed. Next to the present carbide at 283.2 eV, the remaining signal above 340 K is fitted with three peaks at 283.4, 284.3 and 285.4 eV (Figure 4d). While the latter peak (green) is assigned to CO in bridge position,<sup>[26]</sup> the other two peaks (yellow) are attributed to C–H fragments.<sup>[27]</sup>

#### PENBD/PEQC on Ni(111): O 1s region

Complementary information on adsorption and reaction of PEQC and PENBD on Ni(111) is obtained from TPXPS in the O 1s region. All XP spectra are depicted as density plots in Figure S3. The spectra collected during adsorption of the energy-rich PEQC at 120 K are shown in Figure 6a; an exposure of 1.1 L yielded a final coverage of 0.19 carbon ML (red spectrum). Prior to the adsorption (gray), contributions due to preadsorption from residual PEQC in the chamber are visible. The spectra during adsorption of the energy-lean PENBD are shown in Figure 6f; here, an exposure of 1.5 L yielded 0.32 carbon ML

(blue). The subsequent TPXPS measurements are depicted as waterfall plots in Figure 6b for PEQC and Figure 6e for PENBD. Analogous to the C 1s experiment, the spectra are fitted for quantitative analysis (see Table S2 for parameters).

Figure 6c depicts the O 1s spectra of PEQC on Ni(111) at selected temperatures along with their color-coded fits. The quantification of the data is given in Figure 5b. After adsorption at 120 K (red), two distinct signals are observed. For the fit model, three peaks at 531.7, 533.1 and 533.3 eV are employed to reproduce the line shape. Since the total carbon coverage stays constant up to ~250 K (Figure 5a) but the total oxygen O 1s coverage decreases by almost 30%, we conclude that coadsorbed water contributes to the O 1s signal. We attribute the peak at 533.1 eV in Figure 6c (turquoise) to water, as its binding energy and desorption temperature match literature values on Ni(111).<sup>[31]</sup> The two peaks at 531.7 and 533.3 eV (red) are assigned to PEQC, as expected for two inequivalent oxygen atoms in the molecule; accordingly, the areas of both peaks are identical. The peak at 533.3 eV stems from the ether oxygen (C–O–C) within the ester moiety, and the peak at 531.7 eV from the carbonyl oxygen (C=O). Notably, the latter one exhibits a narrower peak width by 625 meV, which is explained by the more constrained flexibility of the double bound oxygen atom. The binding energy difference of 1.6 eV of both oxygen atoms

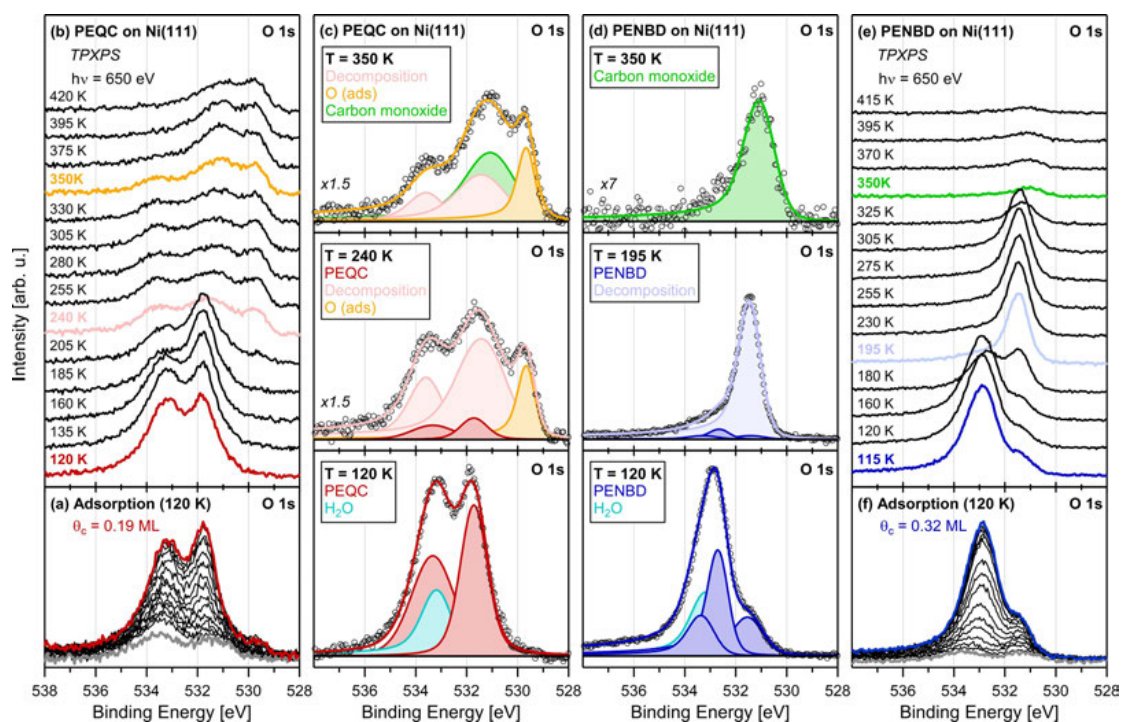


**Figure 6.** XP spectra of a) PEQC and f) PENBD in the O 1s region upon adsorption at low temperature on Ni(111). The thermal evolution during temperature-programmed XPS (TPXPS) experiments is depicted for selected spectra of b) PEQC and e) PENBD as waterfall plots; c, d) representative surface species are given with their corresponding color-coded fits, respectively.

is in agreement with ester derivatives adsorbed on single crystal surfaces.<sup>[19,28,32]</sup>

For PENBD on Ni(111), the fit to the spectrum after adsorption at 120 K is shown in Figure 6d (blue). Again, the coadsorption of water was unavoidable during exposure yielding a peak at 533.1 eV (turquoise).<sup>[31]</sup> The spectrum is fitted with three additional peaks at 531.5, 532.7 and 533.3 eV (blue), with a fixed relative intensity ratio (1:2:1). The positions are shifted to lower binding energies by up to 600 meV in comparison to PEQC. Along to the results of Ontaneda et al.,<sup>[32]</sup> we attribute this to a stronger interaction of the oxygen atoms with the surface. Interestingly, on Pt(111) hardly any difference is observed in the O 1s spectra of PEQC and PENBD at 125 K (Figure S1). With only minor structural differences between PEQC and PENBD, remote to the oxygen atoms, different adsorption motifs of the molecules are expected. As PEQC features higher O 1s binding energies, the oxygen atoms of the ester group are likely to be not bound to the surface;<sup>[32]</sup> instead, stable adsorption by the QC framework and phenyl moiety is suggested. In contrast, for PENBD, we propose an “oxygen bound” geometry with the ester group pointing towards the surface. Our fits indicate two different binding fashions: The binding with two oxygen atoms to the surface leads to a very similar chemical environment for both atoms and is attributed to the peak at 532.7 eV; on the other hand, the two peaks at 531.5 and 533.3 eV, with identical fit area, are due to a binding and non-binding oxygen atom.<sup>[32]</sup> Notably, various rotational isomers of esters are known on Ni(111)<sup>[33]</sup> enabling different binding motifs. The pronounced desorption of PENBD on Ni(111) for relatively low temperatures of 270 K (Figure 5c) is attributed to the weaker Ni-oxygen interaction<sup>[34]</sup> compared to the Ni-carbon bond for PEQC. Our results thus indicate that the derivatization with extended ligands can determine the adsorption behavior of the molecule pair and hereby leads to very different desorption properties and decomposition pathways upon heating, which is addressed in the following.

The thermal evolution of PEQC on Ni(111) in the O 1s region is shown in Figure 6b as waterfall plot, along with selected fits in Figure 6c; the quantitative analysis is given in Figure 5b. Analogous to the PENBD experiment (see below), the water contributions desorb between 140 and 180 K, so that the intensity of the PEQC peaks increase slightly due to less damping. Starting at 180 K, a narrow peak appears at 529.6 eV, which is assigned to atomic oxygen on Ni(111) (orange).<sup>[25a,26,35]</sup> At the same time, two new peaks at 531.3 and 533.5 eV indicate the onset of the decomposition of PEQC (rose). This observation matches the conclusions derived from the C 1s experiment (see above). Heating to above 280 K gives rise to an additional peak at 531.0 eV (green), which is assigned to CO on a bridge site,<sup>[26]</sup> in line with the findings in the C 1s region.

The TPXPS experiment of PENBD on Ni(111) in the O 1s region is depicted in Figure 6e along with selected fits in Figure 6d, and the quantitative analysis in Figure 5d. Between 140 and 180 K, coadsorbed water desorbs, which is in agreement with findings in literature.<sup>[31b]</sup> Above 160 K, a new peak evolves at 531.4 eV (light blue). This clear shift of 1.3 eV of the main signal towards lower binding energy matches the spectral

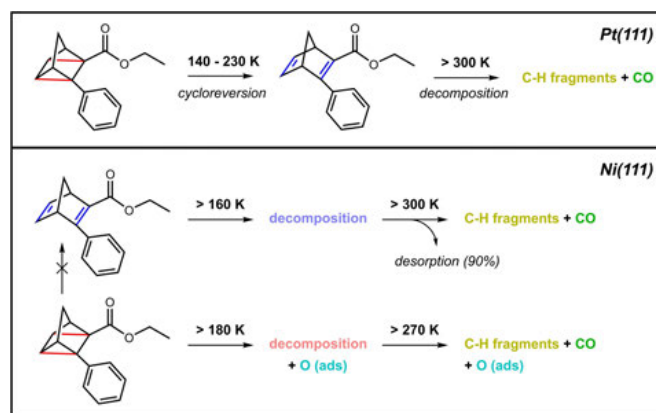
changes in the C 1s region at equivalent temperatures (see above). Therefore, a first reaction step is proposed which includes the oxygen atoms. Likely, this step is the detachment or fragmentation of the ester moiety.<sup>[25b]</sup> The decrease of about 25% of the oxygen coverage in comparison to the initial PENBD (note that for the carbon region an according increase is detected, see above) is attributed to different attenuation and diffraction conditions depending on the adsorption geometry of the newly formed species.<sup>[30]</sup> Starting at 280 K, a new peak emerges at 531.0 eV (Figure 6d, green), which fits to literature values of CO on Ni(111) in bridge position.<sup>[26]</sup> Simultaneously, the majority of the O 1s signal vanishes leaving only 16% of the previous surface coverage (Figure 5d), in very good agreement with the corresponding C 1s experiment (13% of total intensity remaining, see above).

## Conclusion

We have investigated the surface chemistry of 2-carboxy-3-phenyl-norbornadiene/quadracyclane (PENBD/PEQC) on Pt(111) and Ni(111) by synchrotron radiation-based HR-XPS measurements. The adsorption of the two valence isomers and their thermal evolution was monitored in temperature-programmed experiments. For both surfaces, a spectroscopic distinction between the energy-rich PEQC and its energy-lean counterpart PENBD was possible upon exposure at temperatures between 115 and 125 K. On Pt(111), no “side-on” geometry is found for the molecule pair, as we observed no signs of the detachment of a hydrogen atom from the bridgehead methyl group. On Ni(111), the very distinct spectral appearance of PEQC and PENBD in the C 1s and O 1s regions indicates different adsorption motifs. Whereas PEQC is expected to bind by the QC framework and phenyl moiety, PENBD is adsorbed weaker in an “oxygen-bound” fashion, with the ester group likely oriented towards the surface.

Reaction pathways for both valence isomers on the two surfaces (Scheme 1) are proposed based on a quantitative evaluation of the corresponding TPXPS experiments. For Pt(111) as model catalyst surface, the onset of the cycloreversion reaction of PEQC to PENBD is found at 140 K, with the conversion complete at 230 K. Decomposition of PENBD occurs only at 300 K, when decomposition products assigned to CO and C–H fragments emerge on the surface. Notably, PENBD on Pt(111) is much more stable than unsubstituted NBD, which decomposes even at 190 K. The back reaction of PEQC to PENBD cannot be triggered thermally on Ni(111). Instead, individual decomposition routes begin at 160 and 180 K. Interestingly, for PENBD on Ni(111), about 90% of the surface species desorbs above 300 K; this is explained by the “oxygen-bound” adsorption geometry, which only allows for a weak surface interaction. Minor contributions from CO and C–H fragments remain on the surface. For PEQC, when heating higher than 180 K, atomic oxygen is observed next to these decomposition products.

Thus, we have demonstrated the dependence of the reactivity of derivatized NBD/QC species on the catalyst surface used. On Pt(111), the successfully monitored cycloreversion reaction of PEQC to PENBD fulfills the most important requirement of a MOST



**Scheme 1.** Top: Proposed reaction pathway of PEQC on Pt(111). The cycloreversion reaction to PENBD occurs between 140 and 230 K with subsequent decomposition into C–H fragments and CO when the mixture is heated at > 300 K. Bottom: On Ni(111). There is no conversion of PEQC to PENBD, but individual decomposition steps begin at 160 and 180 K; there is pronounced desorption of PENBD above 300 K, and further fragmentation above 270 K for PEQC.

system; the experiments on Ni(111) provided insights into stability boundaries and desorption behavior of the derivatives, which is of interest for heterogeneously catalyzed processes to ensure a fully reversible energy storage cycle.

## Experimental Section

**X-ray photoelectron spectroscopy (XPS):** All experiments were carried out in a transportable ultra-high-vacuum (UHV) apparatus; the setup is described in detail elsewhere.<sup>[36]</sup> The analysis chamber houses a hemispherical electron analyzer (Omicron EA 125U7 HR), and an evaporator for organic compounds. Surface cleaning and preparation is conducted in a separate preparation chamber, which includes, among other typical surface science tools, a sputter gun and LEED optics. The XPS measurements were performed using synchrotron radiation at BESSY II of Helmholtz-Zentrum Berlin, at beamlines UE56/2-PGM1 and -PGM2. The light incidence angle was 50°, and the spectra were acquired at normal emission. With an excitation energy of 380 eV for the C 1s and 650 eV for the O 1s region, total energy resolutions of 180 and 250 meV were achieved, respectively.

Prior to each adsorption experiment, the Pt(111) and Ni(111) single crystals were checked for cleanliness by XPS. Ion bombardment ( $\text{Ar}^+$ ,  $E = 1.0$  keV,  $I_s \sim 2$   $\mu\text{A}$ ) was used to remove impurities on the surfaces, with subsequent annealing to 1200 K. Residual carbon contaminations were removed by oxygen exposure at 800 K. 2-Carboxy-3-phenyl-norbornadiene/quadricyclane were purified by freeze–pump–thaw procedures. Deposition of both compounds onto the surface at ~120 K took place through their vapor pressure, with the exposure given in Langmuir (1 L =  $10^{-6}$  Torr s). Coverages are denoted in ML (1 ML equals one adsorbed atom per surface atom), as determined by comparison to layers with well-defined coverage. These are the CO  $c(4 \times 2)$  superstructure on Pt(111)<sup>[22,37]</sup> with a carbon coverage of 0.5 ML, and the closed graphene layer on Ni(111)<sup>[38]</sup> with a carbon coverage of 2 ML; the oxygen coverages are then calculated using the stoichiometric factor of 1/8 in the molecular structure. Temperature-programmed experiments<sup>[21,39]</sup> were performed with a heating rate of  $\beta = 0.5$   $\text{K s}^{-1}$  up to 550 K, using a bifilar coiled filament behind the crystal. To minimize beam damage, that is, X-ray induced reactions,

we shifted the sample to a new position after every recorded spectrum. All XPS binding energies were referenced to the Fermi level, and a linear background was subtracted from the XP spectra. The quantitative analysis was performed by fitting the respective contributions in the XP spectra; the applied line shape is a convolution of Doniach–Sunjic<sup>[40]</sup> and Gaussian functions.

## Molecule synthesis

**2-Carboxy-3-phenyl-norbornadiene (PENBD):** Ethyl-3-phenylpropionate (5.55 g, 31.9 mmol, 1 equiv.) and cyclopentadiene (freshly cracked; 4.22 g, 63.8 mmol, 2 equiv.) were added to a pressure vial and the reaction was heated to 170 °C overnight, after degassing of the reaction mixture with argon for 5 min. Subsequently, the crude product was purified by fractionated vacuum distillation using a Vigreux column ( $b_p = 123$  °C at  $4.6 \times 10^{-2}$  mbar). PENBD was obtained as a colorless oil (4.59 g, 19.1 mmol, 60%).  $^1\text{H NMR}$  (400 MHz,  $\text{CDCl}_3$ , 25 °C):  $\delta = 7.54$ – $7.51$  (m, 2H), 7.38–7.29 (m, 3H), 7.01–6.99 (m, 1H), 6.94–6.92 (m, 1H), 4.14 (qd,  $J = 6.8, 0.8$  Hz, 2H), 4.08–4.06 (m, 1H), 3.87–3.85 (m, 1H), 2.26 (dt,  $J = 6.4, 1.6$  Hz, 1H), 2.06 (dt,  $J = 6.8, 1.6$  Hz, 1H), 1.22 (t,  $J = 7.1$  Hz, 3H) ppm; see Figure S4.

**2-Carboxy-3-phenyl-quadricyclane (PEQC):** PENBD (300 mg, 1.25 mmol) was dissolved in deuterated chloroform and irradiated with an UV-LED (Seoul Viosys, CUD1AF4D, 310 nm, 30 mW) overnight. Afterwards, the solvent was removed, and the crude product was purified by flash chromatography (hexane/EtOAc 9.5:0.5, v/v). PEQC was obtained as a white solid (294 mg, 1.23 mmol, 98%).  $^1\text{H NMR}$  (400 MHz,  $\text{CDCl}_3$ , 25 °C):  $\delta = 7.29$ – $7.23$  (m, 4H), 7.20–7.14 (m, 1H), 3.97 (qd,  $J = 7.2, 0.4$  Hz, 2H), 2.56–2.53 (m, 1H), 2.45–2.42 (m, 1H), 2.36 (dt,  $J = 11.6, 1.4$  Hz, 1H), 2.23–2.21 (m, 1H), 2.12 (dt,  $J = 11.6, 1.4$  Hz, 1H), 1.72–1.69 (m, 1H), 1.03 (t,  $J = 7.2$  Hz, 3H) ppm; see Figure S5.

## Acknowledgements

Support for this work was granted by the Deutsche Forschungsgemeinschaft (DFG) – Project no. 392607742 and the Cluster of Excellence “Engineering of Advanced Materials”. We thank

Helmholtz-Zentrum Berlin for the allocation of synchrotron radiation beamtime and the BESSY II staff for support during beamtime. Open Access funding enabled and organized by Projekt DEAL.

### Conflict of Interest

The authors declare no conflict of interest.

### Data Availability Statement

The data that support the findings of this study are available from the corresponding author upon reasonable request.

**Keywords:** catalysis · energy storage · MOST system · photoelectron spectroscopy · surface reactions

- [1] AGEBA AG Energiebilanzen e.V., *Energy Consumption in Germany in 2021*, [https://ag-energiebilanzen.de/wp-content/uploads/2022/06/AGEBA\\_Jahresbericht2020\\_20220613\\_engl\\_Web.pdf](https://ag-energiebilanzen.de/wp-content/uploads/2022/06/AGEBA_Jahresbericht2020_20220613_engl_Web.pdf) (retrieved 22.11.2022).
- [2] D. Jahn, S. Korolczuk, *Environ. Politics* **2012**, *21*, 159–164.
- [3] a) A. Lennartson, A. Roffey, K. Moth-Poulsen, *Tetrahedron Lett.* **2015**, *56*, 1457–1465; b) C. L. Sun, C. Wang, R. Boulatov, *ChemPhotoChem* **2019**, *3*, 268–283; c) Z. Wang, A. Roffey, R. Losantos, A. Lennartson, M. Jevric, A. U. Petersen, M. Quant, A. Dreos, X. Wen, D. Sampedro, K. Börjesson, K. Moth-Poulsen, *Energy Environ. Sci.* **2019**, *12*, 187–193; d) Z. Wang, P. Erhart, T. Li, Z.-Y. Zhang, D. Sampedro, Z. Hu, H. A. Wegner, O. Brummel, J. Libuda, M. B. Nielsen, K. Moth-Poulsen, *Joule* **2021**, *5*, 3116–3136; e) K. Börjesson, A. Lennartson, K. Moth-Poulsen, *ACS Sustainable Chem. Eng.* **2013**, *1*, 585–590; f) T. J. Kucharski, Y. C. Tian, S. Akbulatov, R. Boulatov, *Energy Environ. Sci.* **2011**, *4*, 4449–4472; g) K. Moth-Poulsen, D. Čoso, K. Börjesson, N. Vinokurov, S. K. Meier, A. Majumdar, K. P. C. Vollhardt, R. A. Segalman, *Energy Environ. Sci.* **2012**, *5*, 8534; h) Q. Qiu, Y. Shi, G. G. D. Han, *J. Mater. Chem. C* **2021**, *9*, 11444–11463.
- [4] a) H. Taoda, K. Hayakawa, K. Kawase, H. Yamakita, *J. Chem. Eng. Jpn.* **1987**, *20*, 265–270; b) Z. Wang, R. Losantos, D. Sampedro, M. Morikawa, K. Börjesson, N. Kimizuka, K. Moth-Poulsen, *J. Mater. Chem. A* **2019**, *7*, 15042–15047; c) H. M. Bandara, S. C. Burdette, *Chem. Soc. Rev.* **2012**, *41*, 1809–1825.
- [5] a) D. Schulte-Frohlinde, H. Blume, H. Güsten, *J. Phys. Chem.* **1962**, *66*, 2486–2491; b) C. Bastianelli, V. Caia, G. Cum, R. Gallo, V. Mancini, *J. Chem. Soc. Perkin Trans. 2* **1991**, 679–683.
- [6] a) K. Börjesson, D. Čoso, V. Gray, J. C. Grossman, J. Guan, C. B. Harris, N. Hertkorn, Z. Hou, Y. Kanai, D. Lee, J. P. Lomont, A. Majumdar, S. K. Meier, K. Moth-Poulsen, R. L. Myrabo, S. C. Nguyen, R. A. Segalman, V. Srinivasan, W. B. Tolman, N. Vinokurov, K. P. Vollhardt, T. W. Weidman, *Chem. Eur. J.* **2014**, *20*, 15587–15604; b) Y. Kanai, V. Srinivasan, S. K. Meier, K. P. Vollhardt, J. C. Grossman, *Angew. Chem. Int. Ed.* **2010**, *49*, 8926–8929; *Angew. Chem.* **2010**, *122*, 9110–9113.
- [7] G. S. Hammond, N. J. Turro, A. Fischer, *J. Am. Chem. Soc.* **1961**, *83*, 4674–4675.
- [8] H. Taoda, K. Hayakawa, K. Kawase, *J. Chem. Eng. Jpn.* **1987**, *20*, 335–338.
- [9] H. Hogeveen, H. C. Volger, *J. Am. Chem. Soc.* **1967**, *89*, 2486–2487.
- [10] X. W. An, Y. D. Xie, *Thermochim. Acta* **1993**, *220*, 17–25.
- [11] M. Quant, A. Lennartson, A. Dreos, M. Kuisma, P. Erhart, K. Börjesson, K. Moth-Poulsen, *Chem. Eur. J.* **2016**, *22*, 13265–13274.
- [12] a) A. D. Dubonosov, V. A. Bren, V. A. Chernouvanov, *Russ. Chem. Rev.* **2002**, *71*, 917–927; b) V. Gray, A. Lennartson, P. Ratanalert, K. Börjesson, K. Moth-Poulsen, *Chem. Commun.* **2014**, *50*, 5330–5332; c) M. Mansø, B. E. Tebikachew, K. Moth-Poulsen, M. B. Nielsen, *Org. Biomol. Chem.* **2018**, *16*, 5585–5590.
- [13] a) K. Jorner, A. Dreos, R. Emanuelsson, O. El Bakouri, I. Fdez. Galván, K. Börjesson, F. Feixas, R. Lindh, B. Zietz, K. Moth-Poulsen, H. Ottosson, *J. Mater. Chem. A* **2017**, *5*, 12369–12378; b) M. Jevric, A. U. Petersen, M. Mansø, S. Kumar Singh, Z. Wang, A. Dreos, C. Sumbly, M. B. Nielsen, K. Börjesson, P. Erhart, K. Moth-Poulsen, *Chem. Eur. J.* **2018**, *24*, 12767–12772; c) A. Dreos, Z. Wang, J. Udmark, A. Ström, P. Erhart, K. Börjesson, M. B. Nielsen, K. Moth-Poulsen, *Adv. Energy Mater.* **2018**, *8*, 1703401; d) M. Mansø, A. U. Petersen, Z. Wang, P. Erhart, M. B. Nielsen, K. Moth-Poulsen, *Nat. Commun.* **2018**, *9*, 1945; e) M. Mansø, L. Fernandez, Z. Wang, K. Moth-Poulsen, M. B. Nielsen, *Molecules* **2020**, *25*, 322; f) J. Orrego-Hernández, A. Dreos, K. Moth-Poulsen, *Acc. Chem. Res.* **2020**, *53*, 1478–1487; g) A. Kunz, H. A. Wegner, *ChemSystemsChem* **2020**, *3*, e2000035.
- [14] U. Bauer, S. Mohr, T. Dopfer, P. Bachmann, F. Späth, F. Düll, M. Schwarz, O. Brummel, L. Fromm, U. Pinkert, A. Görling, A. Hirsch, J. Bachmann, H.-P. Steinrück, J. Libuda, C. Papp, *Chem. Eur. J.* **2017**, *23*, 1613–1622.
- [15] U. Bauer, L. Fromm, C. Weiß, P. Bachmann, F. Späth, F. Düll, J. Steinhauer, W. Hieringer, A. Görling, A. Hirsch, H.-P. Steinrück, C. Papp, *J. Phys. Chem. C* **2018**, *123*, 7654–7664.
- [16] U. Bauer, L. Fromm, C. Weiß, F. Späth, P. Bachmann, F. Düll, J. Steinhauer, S. Matysik, A. Pominov, A. Görling, A. Hirsch, H.-P. Steinrück, C. Papp, *J. Chem. Phys.* **2019**, *150*, 184706.
- [17] F. Hemauer, U. Bauer, L. Fromm, C. Weiß, A. Leng, P. Bachmann, F. Düll, J. Steinhauer, V. Schwaab, R. Grzonka, A. Hirsch, A. Görling, H. P. Steinrück, C. Papp, *ChemPhysChem* **2022**, *23*, e202200199.
- [18] a) P. Lorenz, T. Luchs, A. Hirsch, *Chem. Eur. J.* **2021**, *27*, 4993–5002; b) W. Alex, P. Lorenz, C. Henkel, T. Clark, A. Hirsch, D. M. Guldi, *J. Am. Chem. Soc.* **2022**, *144*, 153–162.
- [19] F. Bourmel, C. Laffon, P. Parent, G. Tourillon, *Surf. Sci.* **1996**, *350*, 60–78.
- [20] R. Zhang, A. J. Hensley, J. S. McEwen, S. Wickert, E. Darlatt, K. Fischer, M. Schoppke, R. Denecke, R. Streber, M. Lorenz, C. Papp, H. P. Steinrück, *Phys. Chem. Chem. Phys.* **2013**, *15*, 20662–20671.
- [21] C. Papp, H.-P. Steinrück, *Surf. Sci. Rep.* **2013**, *68*, 446–487.
- [22] M. Kinne, T. Fuhrmann, C. M. Whelan, J. F. Zhu, J. Pantförder, M. Probst, G. Held, R. Denecke, H. P. Steinrück, *J. Chem. Phys.* **2002**, *117*, 10852–10859.
- [23] C. Papp, T. Fuhrmann, B. Tränkenschuh, R. Denecke, H. P. Steinrück, *Phys. Rev. B* **2006**, *73*, 235426.
- [24] A. Wiltner, C. Linsmeier, *Phys. Status Solidi* **2004**, *201*, 881–887.
- [25] a) M. Castonguay, J. R. Roy, P. H. McBreen, *Langmuir* **2000**, *16*, 8306–8310; b) E. Zahidi, M. Castonguay, P. McBreen, *J. Am. Chem. Soc.* **1994**, *116*, 5847–5856.
- [26] G. Held, J. Schuler, W. Sklarek, H. P. Steinrück, *Surf. Sci.* **1998**, *398*, 154–171.
- [27] a) S. Lehwald, H. Ibach, *Surf. Sci.* **1979**, *89*, 425–445; b) C. Papp, R. Denecke, H.-P. Steinrück, *Langmuir* **2007**, *23*, 5541–5547.
- [28] M. Castonguay, J. R. Roy, A. Rochefort, P. H. McBreen, *J. Am. Chem. Soc.* **2000**, *122*, 518–524.
- [29] H. P. Steinrück, T. Fuhrmann, C. Papp, B. Tränkenschuh, R. Denecke, *J. Chem. Phys.* **2006**, *125*, 204706.
- [30] a) C. J. Powell, A. Jablonski, *Nucl. Instrum. Methods Phys. Res. Sect. A* **2009**, *601*, 54–65; b) D. P. Woodruff, A. M. Bradshaw, *Rep. Prog. Phys.* **1994**, *57*, 1029–1080.
- [31] a) W. Kuch, M. Schulze, W. Schnurnberger, K. Bolwin, *Surf. Sci.* **1993**, *287–288*, 600–604; b) T. Pache, H. P. Steinrück, W. Huber, D. Menzel, *Surf. Sci.* **1989**, *224*, 195–214.
- [32] J. Ontaneda, R. E. J. Nicklin, A. Cornish, A. Roldan, R. Grau-Crespo, G. Held, *J. Phys. Chem. C* **2016**, *120*, 27490–27499.
- [33] a) E. Zahidi, M. Castonguay, P. H. McBreen, *J. Phys. Chem.* **1995**, *99*, 17906–17916; b) J. Wang, M. Castonguay, J. R. Roy, E. Zahidi, P. H. McBreen, *J. Phys. Chem. B* **1999**, *103*, 4382–4386.
- [34] Y. Bai, D. Kirvassilis, L. Xu, M. Mavrikakis, *Surf. Sci.* **2019**, *679*, 240–253.
- [35] M. K. Rajumon, K. Prabhakaran, C. N. R. Rao, *Surf. Sci.* **1990**, *233*, L237–L242.
- [36] R. Denecke, M. Kinne, C. M. Whelan, H.-P. Steinrück, *Surf. Rev. Lett.* **2002**, *09*, 797–801.
- [37] F. Bondino, G. Comelli, F. Esch, A. Locatelli, A. Baraldi, S. Lizzit, G. Paolucci, R. Rosei, *Surf. Sci.* **2000**, *459*, L467–L474.
- [38] a) W. Zhao, S. M. Kozlov, O. Höfert, K. Gotterbarm, M. P. A. Lorenz, F. Viñes, C. Papp, A. Görling, H.-P. Steinrück, *J. Phys. Chem. Lett.* **2011**, *2*, 759–764; b) R. Addou, A. Dahal, P. Sutter, M. Batzill, *Appl. Phys. Lett.* **2012**, *100*, 021601.
- [39] A. Baraldi, G. Comelli, S. Lizzit, D. Cocco, G. Paolucci, R. Rosei, *Surf. Sci.* **1996**, *367*, L67–L72.
- [40] S. Doniach, M. Sunjic, *J. Phys. C Solid State Phys.* **1970**, *3*, 285–291.

Manuscript received: December 1, 2022  
 Accepted manuscript online: February 25, 2023  
 Version of record online: March 23, 2023

# Chemistry–A European Journal

Supporting Information

## **Surface Studies on the Energy Release of the MOST System 2-Carboxy-3-Phenyl-Norbornadiene/Quadricyclane (PENBD/PEQC) on Pt(111) and Ni(111)**

Felix Hemauer, Valentin Schwaab, Eva Marie Freiburger, Natalie J. Waleska, Andreas Leng, Cornelius Weiß, Johann Steinhauer, Fabian Düll, Philipp Bachmann, Andreas Hirsch, Hans-Peter Steinrück, and Christian Papp\*

## [P2] – SUPPORTING INFORMATION

### Fit parameters for PENBD/PEQC on Pt(111)

**Table 1:** Used fit parameters for quantitative evaluation of respective molecule

Molecule	Core level	Peak #	Binding Energy / eV	Gaussian width / eV	Lorentzian width / eV	Asymmetry factor	
PEQC	C 1s	1	283.7	0.46	0.10	0.05	
		2	284.2	0.48	0.10	0.05	
		3	284.7	0.72	0.10	0.05	
		4	286.0	0.57	0.10	0.05	
	O 1s	1	531.4	1.24	0.10	0.00	
		2	532.8	1.24	0.10	0.00	
		H <sub>2</sub> O	532.2	1.08	0.10	0.10	
	PENBD	C 1s	1	283.9	0.65	0.10	0.05
			2	284.4	0.50	0.10	0.05
			3	284.9	0.50	0.10	0.05
4			285.9	0.50	0.10	0.05	
O 1s		1	531.4	1.24	0.10	0.00	
		2	532.8	1.24	0.10	0.00	
		H <sub>2</sub> O	532.2	1.08	0.10	0.10	

### Fit parameters for PENBD/PEQC on Ni(111)

**Table 2:** Used fit parameters for quantitative evaluation of respective molecule

Molecule	Core level	Peak #	Binding Energy / eV	Gaussian width / eV	Lorentzian width / eV	Asymmetry factor	
PEQC	C 1s	1	284.3	0.76	0.10	0.04	
		2	284.8	0.55	0.10	0.04	
		3	285.3	0.56	0.10	0.04	
		4	286.1	0.67	0.10	0.04	
	O 1s	1	531.7	0.87	0.20	0.00	
		2	533.3	1.50	0.20	0.00	
		H <sub>2</sub> O	533.1	1.20	0.10	0.12	
	PENBD	C 1s	1	284.5	0.42	0.10	0.06
			2	285.0	0.84	0.10	0.06
			3	286.1	0.47	0.10	0.06
4			286.5	0.50	0.10	0.06	
carbide			283.2	0.56	0.09	0.14	
O 1s		1	531.5	1.23	0.10	0.12	
		2	532.7	0.79	0.10	0.12	
		3	533.3	1.23	0.10	0.12	
			H <sub>2</sub> O	533.1	1.20	0.10	0.12

PENBD/PEQC on Pt(111) - O 1s region

We investigated the adsorption and thermal evolution of the molecular pair PEQC and PENBD on Pt(111) also in the O 1s region (see Table 2 for parameters). Figure S1a depicts the spectra during adsorption of PEQC at 125 K; an exposure of 3.3 L yielded a carbon coverage of 0.29 ML (red spectrum), which is comparable to the amount in the C 1s experiment. Due to the smaller stoichiometric number of oxygen atoms and a low cross section, the acquired O 1s are broader with a lower signal-to-noise ratio, compared to the C 1s results. The two peaks at 531.4 and 532.8 eV, with almost identical heights, are assigned to the two chemically different oxygen atoms within the ester moiety of the molecular framework.<sup>[1]</sup> Moreover, a significant amount of water is coadsorbed on the surface contributing at 532.2 eV (Figure S1c, turquoise), which is in accordance to literature.<sup>[2]</sup>

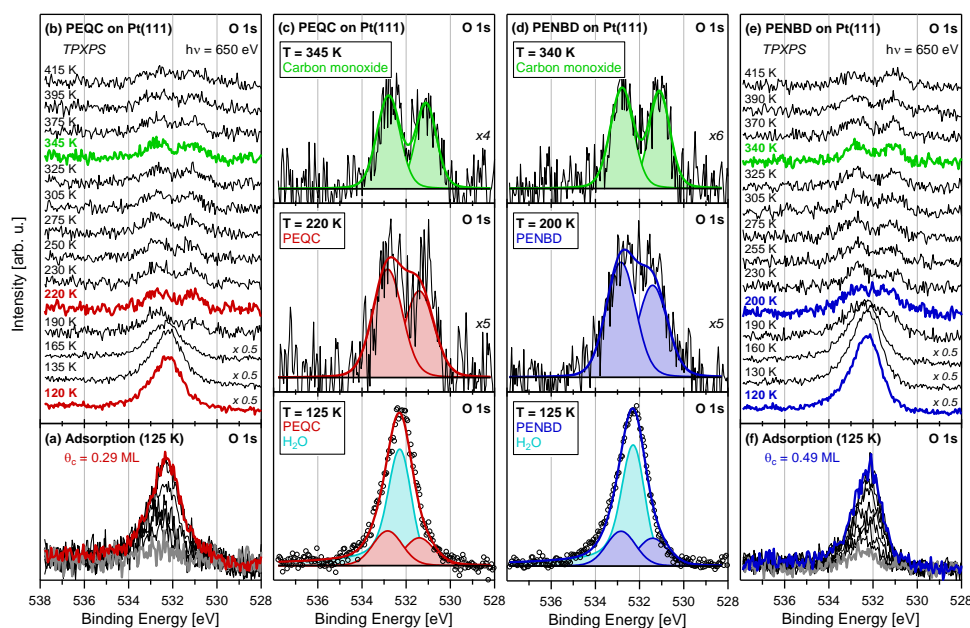


**Figure S1:** O 1s spectra of (a) PEQC and (f) PENBD upon adsorption at 125 K on Pt(111). Coadsorbed water overlaps with the molecular contributions to the line shape; a distinction of both molecules is not possible. The thermal evolution during temperature-programmed XPS (TPXPS) experiments is shown for selected spectra (averaged over three measurements) of (b) PEQC and (e) PENBD as waterfall plots; (c, d) representative spectra (averaged over three measurements) are highlighted in color.

The spectra collected during adsorption of PENBD are shown in Figure S1f; here, an exposure of 4.0 L led to a coverage of 0.49 ML (blue spectrum). The peaks next to the water contribution at 532.2 eV are fitted with the same fitting parameter as for PEQC. The spectral

distinction of the two valence isomers in the O 1s region is expected to be less pronounced, as the structural differences only affect carbon atoms, which are remote from the oxygen atoms. Moreover, the overlapping water signal and the rather poor signal-to-noise ratio make a differentiation of PEQC and PENBD in the O 1s region not possible.

The waterfall plots of the TPXPS experiments for PEQC and PENBD are given in Figure S1b and S1e, respectively. Each spectrum is averaged over three measurements to increase the statistics. Figure S1c and S1d shows representative color-coded fits at selected temperatures. Heating to temperatures higher than 155 K leads to the desorption of water from Pt(111),<sup>[2]</sup> so that at 190 K only signals of PEQC and PENBD remain. Upon further heating, no changes of the line shapes are monitored indicating no fragmentation of the ester group. Above 300 K, for both molecules, two signals emerge at 531.1 and 532.8 eV with slightly narrower widths (Figure S1c and S1d, green). This temperature range coincides with the decomposition onset observed in the C 1s experiments. Likewise, the signals are assigned to the evolution of carbon monoxide occupying bridge and on-top sites on the platinum surface.<sup>[3]</sup>

Density plots of PENBD/PEQC on Pt(111)

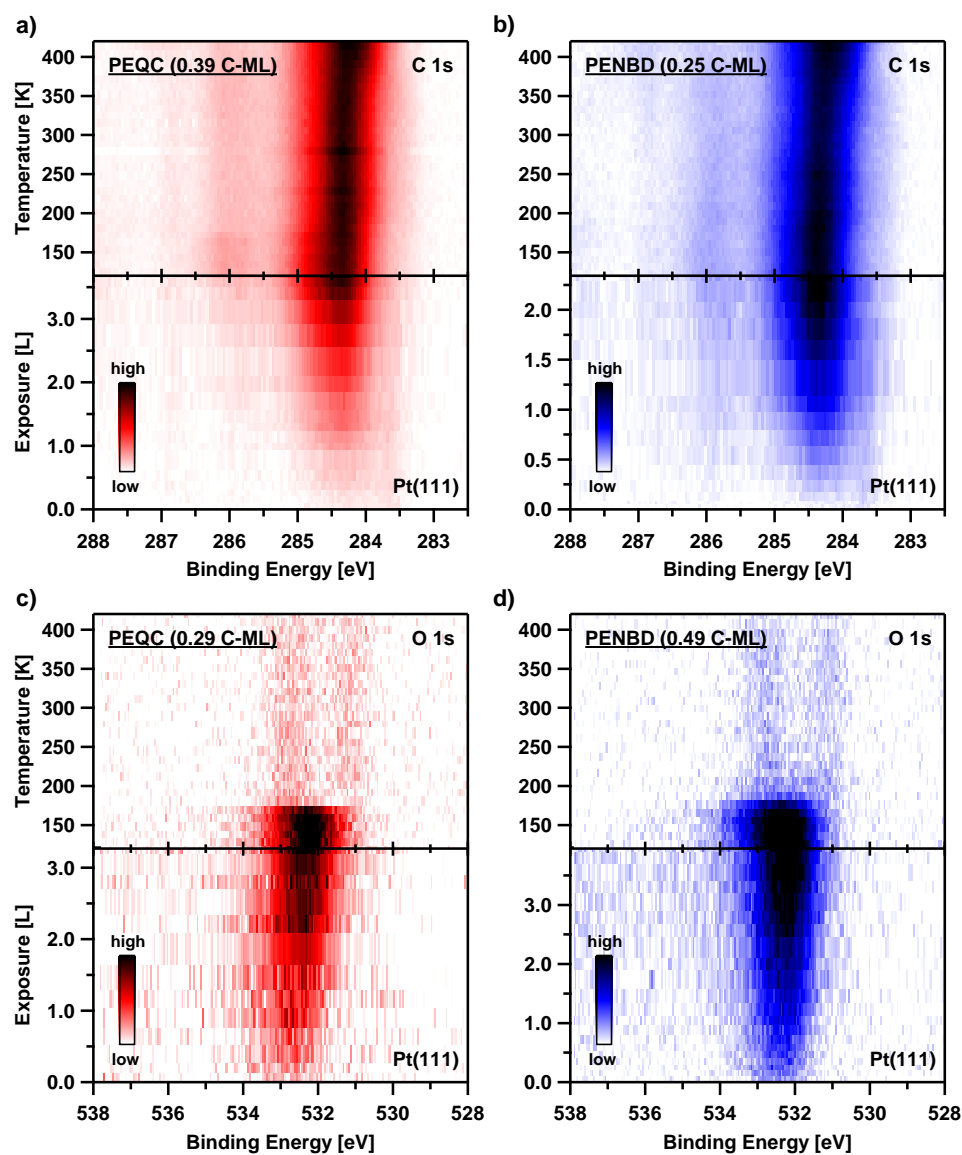


**Figure S2:** Representation of all recorded XP spectra as color-coded density plots during adsorption at 125 K and temperature-programmed experiments on Pt(111): a) PEQC in the C 1s region, b) PENBD in the C 1s region, c) PEQC in the O 1s region and d) PENBD in the O 1s region.

Density plots of PENBD/PEQC on Ni(111)

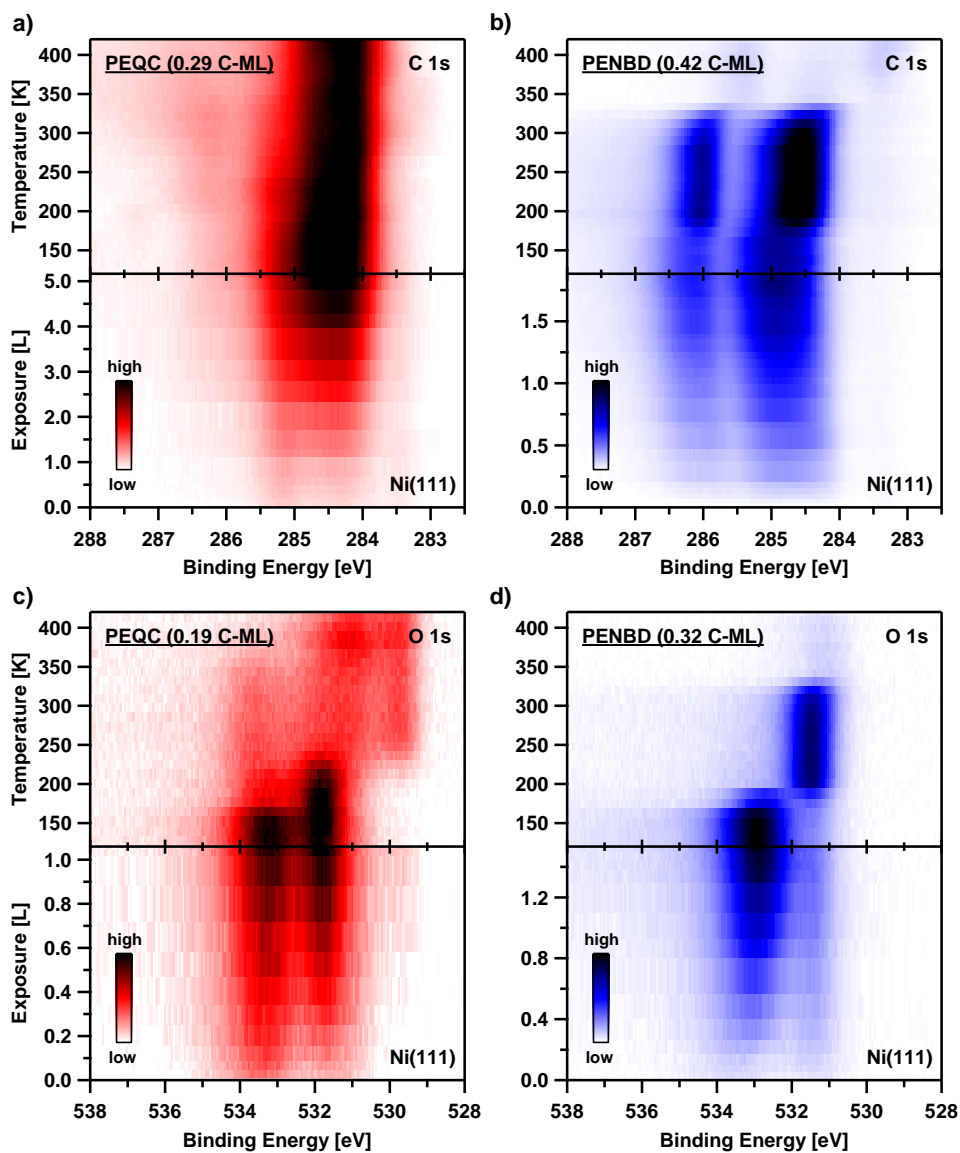


**Figure S3:** Representation of all recorded XP spectra as color-coded density plots during adsorption at ~120 K and temperature-programmed experiments on Ni(111): a) PEQC in the C 1s region, b) PENBD in the C 1s region, c) PEQC in the O 1s region and d) PENBD in the O 1s region.

NMR spectrum of PENBD

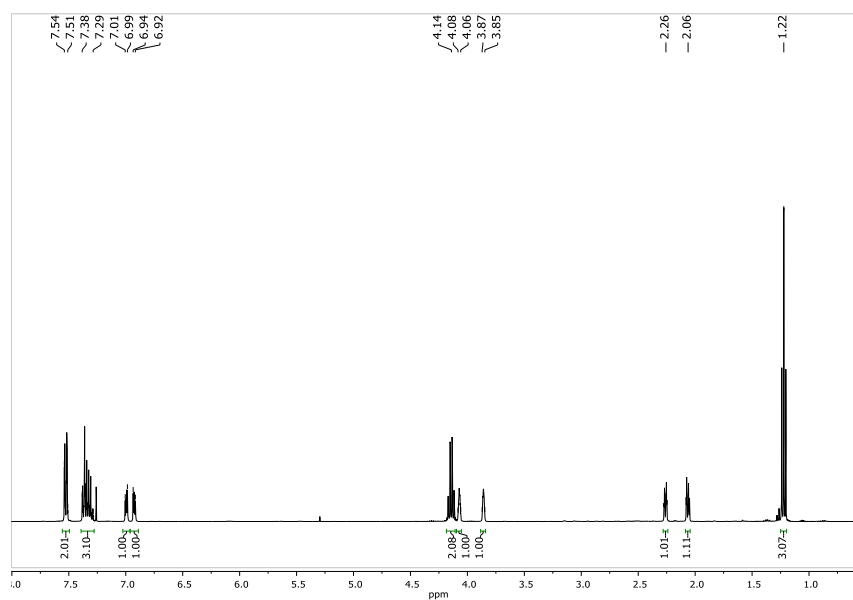


Figure S4: <sup>1</sup>H NMR spectrum (400 MHz, CDCl<sub>3</sub>, 25 °C) of PENBD.

NMR spectrum of PEQC

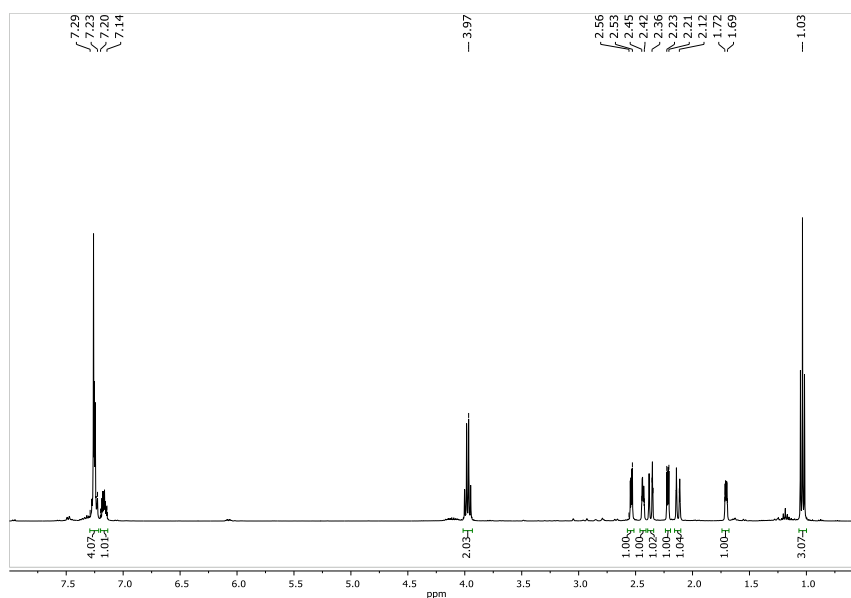


Figure S5: <sup>1</sup>H NMR spectrum (400 MHz, CDCl<sub>3</sub>, 25 °C) of PEQC.

Literature

- [1] F. Bournel, C. Laffon, P. Parent, G. Tourillon, *Surf. Sci.* **1996**, *350*, 60-78.
- [2] G. B. Fisher, J. L. Gland, *Surf. Sci.* **1980**, *94*, 446-455.
- [3] M. Kinne, T. Fuhrmann, C. M. Whelan, J. F. Zhu, J. Pantförder, M. Probst, G. Held, R. Denecke, H. P. Steinrück, *J. Chem. Phys.* **2002**, *117*, 10852-10859.



# Au-Catalyzed Energy Release in a Molecular Solar Thermal (MOST) System: A Combined Liquid-Phase and Surface Science Study

Roman Eschenbacher<sup>+, [a]</sup> Felix Hemauer<sup>+, [b]</sup> Evanie Franz,<sup>[a]</sup> Andreas Leng,<sup>[c]</sup> Valentin Schwaab,<sup>[b]</sup> Natalie J. Waleska-Wellnhofer,<sup>[b]</sup> Eva Marie Freiburger,<sup>[b]</sup> Lukas Fromm,<sup>[d]</sup> Tao Xu,<sup>[a]</sup> Andreas Görling,<sup>[d]</sup> Andreas Hirsch,<sup>[c]</sup> Hans-Peter Steinrück,<sup>[b]</sup> Christian Papp,<sup>[b, e]</sup> Olaf Brummel,<sup>\*[a]</sup> and Jörg Libuda<sup>[a]</sup>

Molecular solar thermal systems (MOSTs) are molecular systems based on couples of photoisomers (photoswitches), which combine solar energy conversion, storage, and release. In this work, we address the catalytically triggered energy release in the promising MOST couple phenylethylesternorbordiene/quadracyclane (PENBD/PEQC) on a Au(111) surface in a combined liquid-phase and surface science study. We investigated the system by photoelectrochemical infrared reflection absorption spectroscopy (PEC-IRRAS) in the liquid phase, conventional IRRAS and synchrotron radiation photoelectron spectroscopy (SRPES) in ultra-high vacuum (UHV). Au(111) is highly active towards catalytically triggered energy release. In the liquid phase, we did not observe any decomposition of the

photoswitch, no deactivation of the catalyst within 100 conversion cycles and we could tune the energy release rate of the heterogeneously catalyzed process by applying an external potential. In UHV, submonolayers of PEQC on Au(111) are back-converted to PENBD instantaneously, even at 110 K. Multilayers of PEQC are stable up to ~220 K. Above this temperature, the intrinsic mobility of the film is high enough that PEQC molecules come into direct contact with the Au(111) surface, which catalyzes the back-conversion. We suggest that this process occurs via a singlet-triplet mechanism induced by electronic coupling between the PEQC molecules and the Au(111) surface.

## Introduction

Besides the established technologies to harvest and store solar energy, such as photovoltaics, batteries, or power-to-X technologies, there are also very simple molecular approaches. One example are molecular solar thermal systems (MOSTs), which combine solar energy conversion, storage, and release using switchable photoisomers (photoswitches).<sup>[1–5]</sup> In this approach, an energy-lean isomer is converted photochemically in a one-photon one-molecule process into its metastable energy-rich isomer. In this way, the solar energy is stored chemically. The stored energy can be released as thermal energy when an appropriate trigger is applied. Different classes of photoswitches may serve as MOSTs, e.g., the E/Z-azobenzene couple (E/Z-AZO),<sup>[6–11]</sup> the dihydroazulene/vinylheptafulvene couple (DHA/VHF),<sup>[12–14]</sup> and the azaborine/BN-dewar couple (AB/ABD).<sup>[15]</sup> One of the most studied MOST systems, is the norbornadiene/quadracyclane pair (NBD/QC).<sup>[4,16–20]</sup> The pristine NBD/QC couple reaches an energy density of 100 kJ·mol<sup>-1</sup> (1 MJ·kg<sup>-1</sup>),<sup>[4]</sup> which is similar to state-of-the-art Li-ion batteries. However, NBD absorbs light only in a very small spectral region (below 300 nm)<sup>[4]</sup> of the solar spectrum (100 nm to 1 μm),<sup>[21]</sup> which limits its applicability. To overcome this issue, researchers developed a variety of different NBD/QC derivatives with additional push-pull ligands, which shift the absorption maximum to the red and enable a better match with the solar spectrum.<sup>[22–25]</sup>

[a] R. Eschenbacher,<sup>+</sup> E. Franz, Dr. T. Xu, Dr. O. Brummel, Prof. Dr. J. Libuda  
Interface Research and Catalysis  
Erlangen Center for Interface Research and Catalysis  
Friedrich-Alexander-Universität Erlangen-Nürnberg  
Egerlandstraße 3, 91058 Erlangen (Germany)  
E-mail: olaf.brummel@fau.de

[b] F. Hemauer,<sup>+</sup> V. Schwaab, N. J. Waleska-Wellnhofer, E. M. Freiburger,  
Prof. Dr. H.-P. Steinrück, Prof. Dr. C. Papp  
Lehrstuhl für Physikalische Chemie II  
Friedrich-Alexander-Universität Erlangen-Nürnberg  
Egerlandstraße 3, 91058 Erlangen (Germany)

[c] A. Leng, Prof. Dr. A. Hirsch  
Lehrstuhl für Organische Chemie II  
Friedrich-Alexander-Universität Erlangen-Nürnberg  
Nikolaus-Fiebiger-Straße 10, 91058 Erlangen (Germany)

[d] Dr. L. Fromm, Prof. Dr. A. Görling  
Lehrstuhl für Theoretische Chemie  
Friedrich-Alexander-Universität Erlangen-Nürnberg  
Egerlandstraße 3, 91058 Erlangen (Germany)

[e] Prof. Dr. C. Papp  
Angewandte Physikalische Chemie  
Freie Universität Berlin  
Arnimallee 22, 14195 Berlin (Germany)

[\*] These authors contributed equally to this work.

Supporting information for this article is available on the WWW under <https://doi.org/10.1002/cptc.202300155>

© 2023 The Authors. ChemPhotoChem published by Wiley-VCH GmbH. This is an open access article under the terms of the Creative Commons Attribution License, which permits use, distribution and reproduction in any medium, provided the original work is properly cited.

One aspect, which is equally important, but received less attention so far, is the controlled energy release in MOST systems.<sup>[4]</sup> The most promising approaches to trigger the energy release are by a heterogeneous catalyst<sup>[23,26–29]</sup> or by an electrochemical process.<sup>[6,30–34]</sup> In a recent study, we combined the advantages of both approaches. For a specific NBD/QC couple, we demonstrated that the catalytic activity of Au(111) is very high (exceeding the activity of Pt(111) by a factor of 200 in the liquid phase). In addition, we showed that the catalytic activity can be tuned by an externally applied potential. Here, it is important to note that the reaction was always triggered by a catalytic process and not by an electrochemical reaction.<sup>[35]</sup> In stability tests, the system remained operational over 1000 conversion cycles without any side product formation detected. Moreover, the observed loss in catalytic activity was less than 0.1% per cycle demonstrating the outstanding catalytic properties of Au(111).<sup>[35]</sup> For this study, the phenylethylester-substituted molecule pair PENBD/PEQC was chosen due to its promising properties concerning applicability as MOST system. The characterization after synthesis revealed not only a distinct redshift of the absorption onset of the NBD derivative to 359 nm with a reasonable quantum yield ( $\Phi_{\text{isom}} = 71\%$  without photosensitizer)<sup>[23]</sup> but also a very pronounced thermal stability of the PEQC isomer (half-life of 450 days at room temperature). In addition, these isomers provide a high energy storage capacity of  $367.5 \text{ kJ kg}^{-1}$ .<sup>[36]</sup> Moreover, the surface chemistry of both PENBD and PEQC has already been investigated by synchrotron radiation-based XPS on different catalyst surfaces, namely Pt(111) and Ni(111).<sup>[37]</sup> In addition, the electrocatalytically triggered energy release of PEQC on HOPG was observed in PEC-IRRAS experiments before.<sup>[34]</sup> Yet, the catalytic activity and/or selectivity of the energy-releasing cycloreversion reaction was not ideal on the catalyst materials considered previously. Therefore, we investigate the PENBD/PEQC system on gold surfaces in the present study.<sup>[35,38]</sup> We apply a multi-method approach combining surface science techniques (IRRAS, SRPES) for a mechanistic understanding and liquid-phase experiments (PEC-IRRAS) to assess the performance and cyclability under realistic conditions. To gain a deeper mechanistic understanding of the catalytic processes, surface science studies in ultra-high vacuum (UHV) are required.<sup>[39]</sup> In the field of MOSTs, surface science studies demonstrated that the back-conversion reaction strongly depends on the catalyst surface. Moreover, these studies provided a detailed picture of the adsorption behavior, rearrangement steps, the stability limits, and decomposition pathways.<sup>[37,38,40–43]</sup> On Ni(111), pristine QC is stable in the submonolayer up to temperatures of  $\sim 175 \text{ K}$ .<sup>[40]</sup> Functionalized QC was found to be stable even up to  $260 \text{ K}$ .<sup>[42]</sup> In contrast, Pt(111) and Au(111) are much more reactive.<sup>[11,35,37,43]</sup> In direct contact with these surfaces, submonolayers of QC derivatives convert back even at  $\sim 100 \text{ K}$ .<sup>[38]</sup> QC derivatives can only be stabilized in form of frozen multilayer films. It was proposed that the energy release on Au(111) is triggered by electronic coupling via a singlet-triplet mechanism. The gold substrate mediates an intersystem crossing between the singlets ( $S_0$ ) and triplets ( $T_1$ ) in the

relaxation process resulting into minimized activation barriers; the mixing of quantum states of gold and molecular states enhances the isomerization rate drastically and reduces the direct chemical involvement of the surface.<sup>[29]</sup> For a NBD derivative with a TOTA anchoring platform on Au(111), we already suggested that the energy release occurs only if there is a direct electronic coupling to the gold.<sup>[38]</sup>

To finally prove the role of the electronic coupling in a liquid system, it is necessary to study the same NBD derivative in both environments, i.e., in the liquid phase under electrochemical control and in UHV. Herein, we present the results of such work.

## Experimental

### Synthesis

**Phenylethylesternorbordiene (PENBD):** Freshly cracked cyclopentadiene (63.8 mmol, 4.22 g, 2 eq.) and ethyl-3-phenylpropionate (31.9 mmol, 5.55 g, 1 eq.) were degassed with argon and heated to  $180^\circ\text{C}$  overnight in a pressure vial. Afterwards, the mixture was purified via fractionated vacuum distillation using a Vigreux column (bp =  $123^\circ\text{C}$  at  $4.6 \times 10^{-2}$  mbar) yielding the desired product as colorless oil, which solidified while storing in the freezer ( $-20^\circ\text{C}$ ).

**Yield:** 4.59 g, 19.1 mmol, 60%.

**Phenylethylesterquadracyclane (PEQC):** For preparative photoisomerization, PENBD (300 mg, 1.25 mmol) was dissolved in CDCl<sub>3</sub> and irradiated in a quartz glass cuvette overnight, using a UV-LED (Seoul Viosys, CUD1AF4D, 310 nm, 30 mW). Subsequently, the crude product was purified via flash chromatography (hexane : EtOAc, 9.5 : 0.5) to obtain the title compound (294 mg, 1.23 mmol, 98%).

The UV/Vis spectra of both molecules were recorded on a J-815 CD spectropolarimeter from JASCO at  $21^\circ\text{C}$  in acetonitrile (HPLC grade) and are provided in Figure 1. For further details on the syntheses we refer to literature.<sup>[23]</sup>

### Liquid-phase experiments

**Cleaning of the equipment:** All PTFE and glassware was stored in a solution of NOCHROMIX® (Sigma Aldrich) and concentrated sulfuric acid (Merck, Emsure, 98%) overnight. Prior to the measurement, the equipment was rinsed 5 times with ultra-pure water (MilliQ Synergy UV,  $18.2 \text{ M}\Omega \text{ cm}$  at  $298 \text{ K}$ , TOC < 5 ppb) and boiled 3 times in Milli-Q water for at least 25 min. Finally, the equipment was dried in an evacuated desiccator overnight.

**Photoelectrochemical infrared reflection absorption spectroscopy (PEC-IRRAS):** All PEC-IRRAS spectra were recorded using a vacuum-based Fourier-transform infrared (FT-IR) spectrometer (Bruker, Vertex 80v) with evacuated optics and a liquid nitrogen-cooled mercury cadmium telluride (MCT) detector. We used a scanner velocity of  $240 \text{ kHz}$  and a resolution of  $8 \text{ cm}^{-1}$  leading to an acquisition time of 0.5 s per spectrum. The setup was equipped with a UV-LED (Seoul Viosys, CUD1AF4D, 310 nm, 30 mW) underneath a CaF<sub>2</sub> hemisphere (Korth,  $d = 25 \text{ mm}$ ), which served as IR and UV-transparent window. The detector was protected by a KRS-5 filter. For details on the PEC-IRRAS setup we refer to our previous work.<sup>[44]</sup>

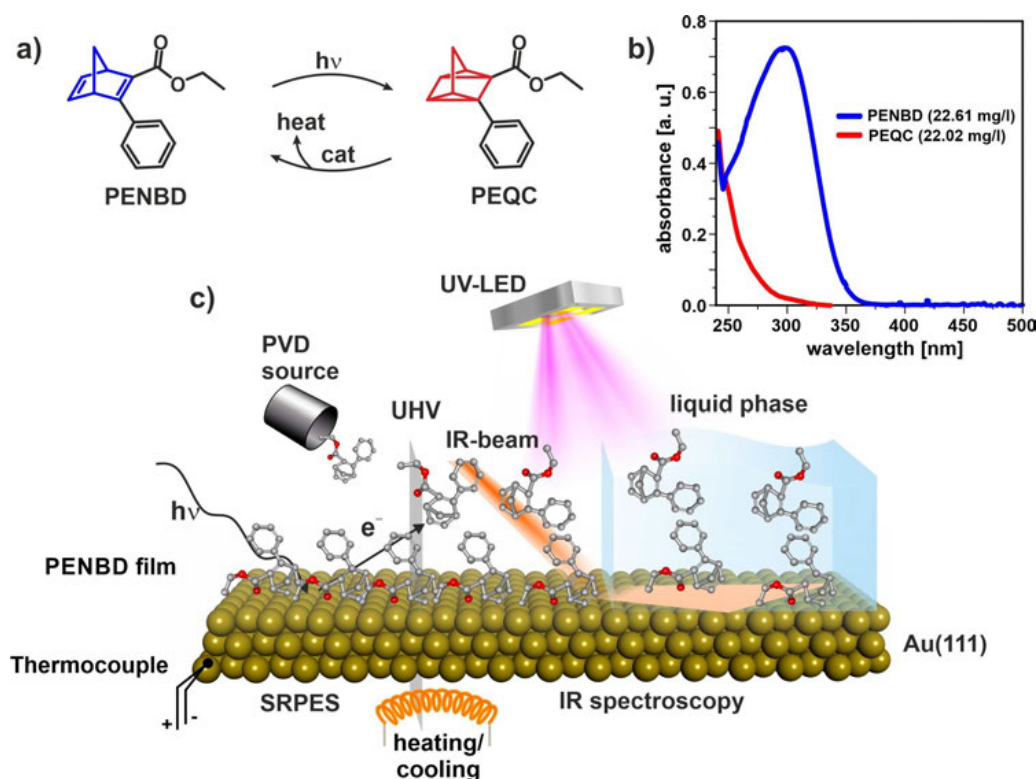


**Figure 1.** Schematic representation of the investigated system: a) Reaction scheme of the photochemical conversion and catalytically triggered back-conversion of PENBD/QC using Au(111) as catalyst; b) UV/Vis spectra of comparable concentrations of PENBD and PEQC; c) Overview of the different methods used in this study: SRPES (synchrotron radiation photoelectron spectroscopy), IR spectroscopy (infrared spectroscopy), PVD (physical vapor deposition) source, and UHV (ultra-high vacuum).

We cleaned the Au(111) single crystal (MaTeck, 99.999%,  $d = 10$  mm, roughness  $< 10$  nm, accuracy  $< 0.1^\circ$ ) in a freshly prepared piranha acid solution ( $\text{H}_2\text{SO}_4(\text{conc.}) : \text{H}_2\text{O}_2(30\%) : 2:1$ ). Afterwards, we rinsed the crystal thoroughly with ultrapure water (MilliQ synergy UV,  $18.2 \text{ M}\Omega\text{cm}$  at  $25^\circ\text{C}$ ,  $< 5$  ppb TOC) and annealed the crystal in the flame of a Bunsen burner at orange glow for 3 min.<sup>[45]</sup> We measured PEC-IRRAS spectra in reflectance mode using a thin-layer configuration. In all experiments, we used a solution of 10 mM PENBD with 0.1 M tetrabutylammoniumperchlorate (TBAP) (Sigma Aldrich, 99.0%) as supporting electrolyte in acetonitrile (MeCN) (Sigma-Aldrich, 99.999%). Potential control was provided by a commercial potentiostat (Gamry, Reference [600]) using a three-electrode configuration with a graphite rod as counter electrode and an  $\text{Ag}/\text{Ag}^+$  electrode (0.01 M  $\text{AgNO}_3$  with 0.1 M TBAP in MeCN) as reference electrode (RE). The calibration of the RE was performed in an external cell versus the cyclic voltammogram of ferrocene (Alfa Aesar, 99.5%). Note that in this work all potentials are referred to the redox potential of the ferrocene couple ( $V_{\text{Fc}}$ ).

#### Surface science experiments

**IRRAS experiment:** The sample cleaning and all IRRAS experiments were performed in an UHV setup with two sub-chambers and a base pressure of  $1.0 \times 10^{-10}$  mbar. The first sub-chamber is mainly

used for sample preparation and consists of an ion gun (Specs IQE 11/35), electron beam evaporators (Focus EFM3), a LEED optics (Specs ErLEED 150), a quartz crystal microbalance (QCM, Inficon SQM-160), a gas dosing system, and a quadrupole mass spectrometer (QMS, Blazers Quadstar 422). The second measuring sub-chamber is equipped with multiple home-built Knudsen-cells, a QMS (Hiden Analytical Hal 3F), and a programmable effusive beam. IR spectra were measured with a vacuum Fourier-transform infrared (FTIR) spectrometer (Bruker VERTEX 80v) together with a liquid nitrogen-cooled mercury cadmium telluride (MCT) detector.

**Sample preparation:** The Au(111) single crystal (MaTeck) was cleaned with  $\text{Ar}^+$  sputtering (Ar, Linde,  $> 99.9999\%$ ; 1.2 keV,  $8 \times 10^{-5}$  mbar, 60 min) and annealing (823 K in UHV; 10 min). LEED was used in order to check the structure of the sample.

**PVD of PENBD:** PENBD was evaporated from a glass reservoir. Prior deposition, the reservoir was evacuated via a rough pump. This reservoir is separated via a Swagelok valve from a home-built Knudsen cell, which is pumped by a separate high vacuum line. We monitored the uptake via IR spectra (rate of  $1 \text{ min-spectrum}^{-1}$ , spectral resolution of  $4 \text{ cm}^{-1}$ ). Each spectrum was referenced to the clean surface recorded before the deposition. The growth rate was adjusted via the pressure in the chamber ( $\sim 4.5 \times 10^{-8}$  mbar).

**Temperature programmed-IRRAS (TP-IRRAS or TP-IRAS):** We carried out the TP-IRRAS experiment by heating the sample with a

linear heating ramp ( $2\text{ K}\cdot\text{min}^{-1}$ ) while recording IRRA spectra ( $1\text{ min}\cdot\text{spectrum}^{-1}$ ) simultaneously. The dampening of IR signals at higher temperatures was adjusted using a procedure by T. Xu et al.<sup>[46]</sup> Absolute spectra are obtained by using the last IRRA spectrum (measuring time of 10 minutes) at the end of the heating ramp of 700 K as a reference. The relative TP-IRRAS plot ( $n = n_i/n_{i-1}$ ) was obtained by dividing each spectrum ( $n_i$ ) by the previous spectrum ( $n_{i-1}$ ).

**Photochemical conversion in UHV:** All photochemical experiments were performed in UHV using a home-built UV-source.<sup>[47]</sup> We used a high-power LED (Seoul Viosys, CUD1AF4D) with a peak wavelength of 310 nm and a typical forward voltage of 5.5 V. Power was supplied externally (PEAKTECH 6210) and we triggered the LED by a TTL signal from the spectrometer (Bruker OPUS 7.2).

**Synchrotron radiation photoelectron spectroscopy (SRPES):** The synchrotron radiation-based X-ray photoelectron spectroscopy experiments were conducted at beamline U49/2-PGM 1 of BESSY II (Helmholtz-Zentrum Berlin)<sup>[48]</sup> during multi-bunch top-up mode. All data were measured with a transportable ultra-high vacuum (UHV) apparatus, which is discussed in detail elsewhere.<sup>[49]</sup> The preparation of the sample was done in a dedicated chamber with typical surface science tools, such as a sputter gun, LEED optics, an electron beam evaporator, and a quartz crystal microbalance. The analysis chamber, separated by a gate valve, houses a quadrupole mass spectrometer, a hemispherical electron analyzer, and a directly attached evaporator for organic substances. XP spectra were recorded in normal emission ( $0^\circ$ ), and the angle of the incident light was  $50^\circ$ . The excitation energy of the photons was set to 380 and 650 eV, for probing the C 1s and O 1s regions, respectively, yielding resolutions of 150 meV (C 1s) and 250 meV (O 1s). All spectra were referenced to the Fermi level. For quantification, a linear background was subtracted and the signals were fitted with peaks consisting of a convolution of Gaussian and Doniach-Sunjić functions.<sup>[50]</sup> Coverages were calibrated by comparison with a saturated CO  $c(4 \times 2)$  superstructure on Pt(111),<sup>[51]</sup> which equals  $\theta_c = 0.5\text{ ML}$  (that is, one carbon atom per every second surface atom).

As substrate for the SRPES measurements, we used a thin Au film deposited on a Pt(111) crystal; specifically, we evaporated a layer of 30 Å gold and annealed subsequently at 770 K for 10 min.<sup>[52–54]</sup> Gold deposition was calibrated with the built-in QCM. The Pt(111) crystal was cleaned by ion bombardment ( $\text{Ar}^+$ ,  $E = 1.0\text{ keV}$ ,  $I_c \sim 8\text{ }\mu\text{A}$ ) and annealed to 1200 K. Carbon contaminations were removed by exposure to oxygen at 850 K. The organic substances were purified with freeze-pump-thaw cycles and exposed to the surface at 110 K by their vapor pressure; the exposure is given in Langmuir ( $1\text{ L} = 10^{-6}\text{ Torr}\cdot\text{s}$ ). Temperature-programmed experiments<sup>[55,56]</sup> up to 550 K were performed with a heating rate of  $0.5\text{ K}\cdot\text{s}^{-1}$ , utilizing a bifilar coiled filament behind the crystal. The sample was moved to a different position for every new spectrum to avoid beam damage effects by the intense X-ray radiation.

## Results and Discussion

In Figure 1a, we depict the investigated MOST system phenylethylesternorbornadiene (PENBD) and its metastable QC derivative (PEQC). Upon irradiation, PENBD converted to the strained PEQC, thus storing part of the energy of the photon. We triggered the thermal energy release using Au(111) as heterogeneous catalyst. The experimental methods used in this study are illustrated in Figure 1b. We investigated the

reaction kinetics, the reversibility, and the potential dependence of the energy-release reaction in the liquid phase by PEC-IRRAS. To obtain additional insights into the mechanism of back-conversion and desorption, we studied the behavior of submonolayers and multilayers of PENBD and PEQC by TP-SRPES and TP-IRRAS in UHV.

In Figure 2a and b, we show the IR spectra of PENBD and PEQC from gas-phase DFT calculations (top),<sup>[34]</sup> measurements in transmission mode at ambient pressure (middle)<sup>[34]</sup> and the multilayer IRRA spectra in UHV (bottom). We summarize the assignment of the IR bands in Table 1 and Table 2. We

**Table 1.** IR band positions of PENBD in transmission spectra (ambient pressure) and multilayer spectra (UHV), and assignment to vibrational modes.

Assignment	Wavenumber [ $\text{cm}^{-1}$ ]		
	DFT	Transmission IR	IRRAS
$\nu(\text{C}-\text{H})_{\text{as} + \text{s Phenyl}}$	3125 + 3116	2982	2983
$\nu(\text{C}-\text{H})_{\text{as Ester}}$	3055	2937	2940
$\nu(\text{C}-\text{H})_{\text{s Ester} + \text{NBD}}$	2974	2870	2869
$\nu(\text{C}=\text{O})_{\text{as Ester}}$	1683 <sup>[a]</sup>	1693	1703
$\nu(\text{C}-\text{C})_{\text{as Phenyl}} + \delta(\text{C}-\text{C})_{\text{NBD}}$	1592 <sup>[a]</sup> + 1563 <sup>[a]</sup>	1595 + 1558	1595 + 1558
$\nu(\text{C}-\text{C})_{\text{as Phenyl}}$	1478 <sup>[a]</sup>	1492	1493
$\delta(\text{C}-\text{C})_{\text{NBD}}$	1276 <sup>[a]</sup> + 1200 <sup>[a]</sup> + 1131 <sup>[a]</sup> + 1088 + 1059	1295 + 1236 + 1181 + 1100 + 1074	1296 + 1242 + 1191 + 1103 + 1076
$\nu(\text{C}-\text{C}-\text{O})_{\text{Ester}}$	1029	1022	1035
$\delta(\text{C}-\text{C})_{\text{Phenyl}} + \delta(\text{C}-\text{C})_{\text{NBD}}$	752 + 709 + 678	762 + 719 + 696	766 + 723 + 696

[a] Published in Ref. [34].

**Table 2.** IR band positions of PEQC in transmission spectra (ambient pressure) and multilayer spectra (UHV), and assignment to vibrational modes.

Assignment	Wavenumber [ $\text{cm}^{-1}$ ]		
	DFT	Transmission IR	IRRAS
$\nu(\text{C}-\text{H})_{\text{as} + \text{s Phenyl}}$	3125 + 3110	2987	2976
$\nu(\text{C}-\text{H})_{\text{as Ester}}$	3055	2929 + 2945	2933
$\nu(\text{C}-\text{H})_{\text{s Ester}}$	2973	2857	2862
$\nu(\text{C}=\text{O})_{\text{as Ester}}$	1711 <sup>[a]</sup>	1692	1716
$\nu(\text{C}-\text{C})_{\text{as Phenyl}}$	1601 <sup>[a]</sup>	1602	1604
$\nu(\text{C}-\text{C})_{\text{as Phenyl}}$	1490 <sup>[a]</sup>	1445	1446
$\nu(\text{C}-\text{C})_{\text{as Ester}}$	1379 <sup>[a]</sup> + 1361 <sup>[a]</sup>	1409 + 1377	1408 + 1381
$\delta(\text{C}-\text{C})_{\text{QC}}$	1282 + 1208 <sup>[a]</sup> + 1153 <sup>[a]</sup> + 1091 + 1025	1297 + 1236 + 1187 + 1122 + 1024	1304 + 1238 + 1113 + 1051 + 968
$\delta(\text{C}-\text{C})_{\text{Phenyl}} + \delta(\text{C}-\text{C})_{\text{QC}}$	899 + 849 + 743	811 + 757 + 702	810 + 760 + 697

[a] Published in Ref. [34].

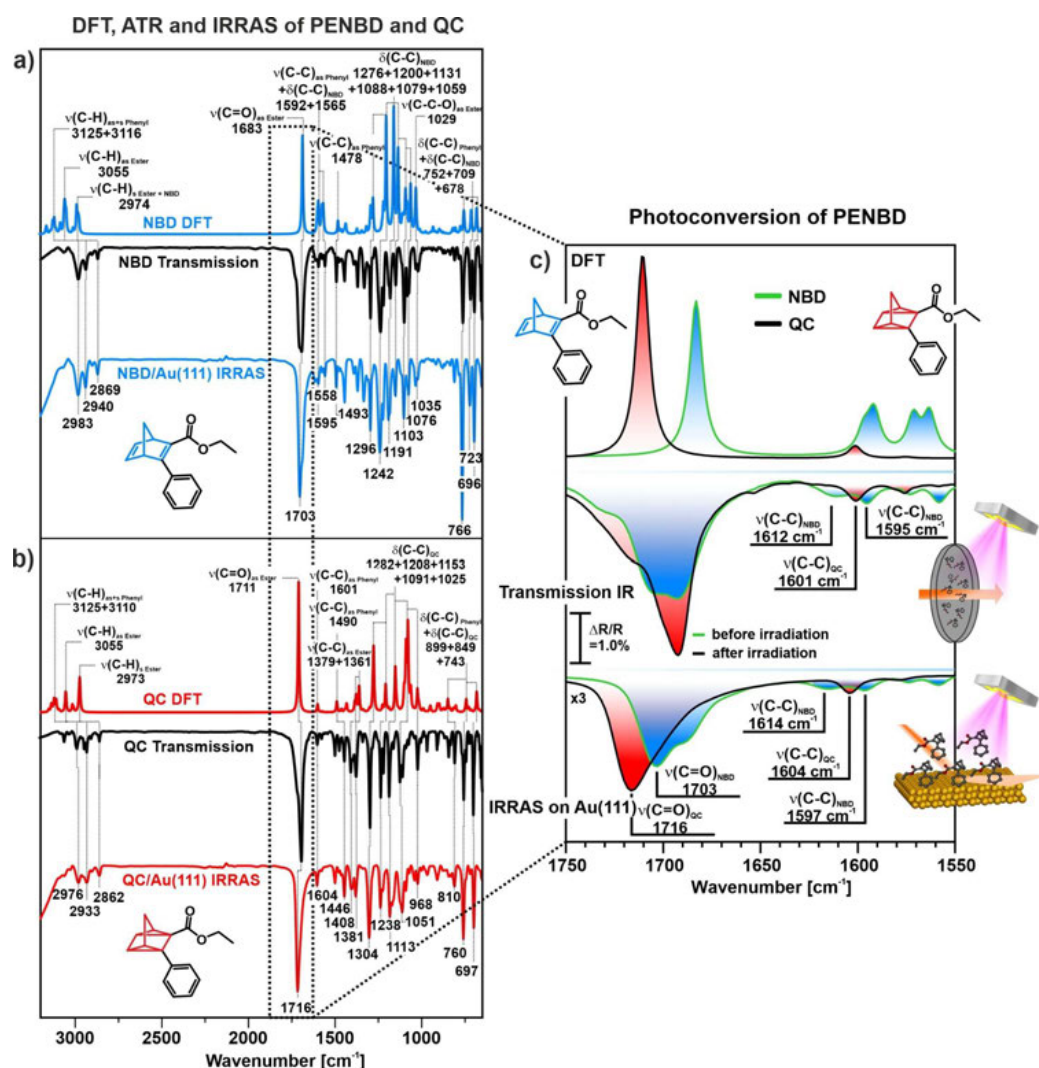


**Figure 2.** DFT calculated gas-phase IR, transmission IR in bulk solution, and multilayer IRRAS of a) PENBD and b) PEQC; c) Characteristic spectral region (1750 to 1550  $\text{cm}^{-1}$ ) before and after UV irradiation (128 scans (liquid phase), 256 s (UHV); see experimental) in identical order. DFT gas-phase spectra of PENBD (green spectrum with blue underlay) to PEQC (black spectrum with red underlay) as reference spectra (top); transmission IR spectra of PENBD/PEQC in KBr (middle) and IRRAS multilayer spectra on Au(111) at 110 K (bottom). Significant bands are labeled. DFT and transmission IR spectra are adapted with permission from Ref. [34] under terms of the CC-BY 4.0 license. Copyright (2022), the Authors, published by Wiley-VCH.

observed a good agreement between the calculated IR spectra, the transmission spectra under ambient conditions, and the multilayer spectra in UHV. This demonstrated that PENBD can be deposited by PVD without decomposition. The complete disappearance of the bands at 1614 and 1596  $\text{cm}^{-1}$ , specific for PENBD, as well as the appearance of the band at 1604  $\text{cm}^{-1}$ , specific for PEQC, after irradiation in UHV indicated that PENBD can be photochemically converted to PEQC in a quantitative manner even under surface science conditions.

#### PEC-IRRAS in liquid phase

We studied the photochemical conversion and the catalytically triggered back-conversion of PENBD/PEQC on Au(111) in the liquid phase *in situ* by PEC-IRRAS (see Figure 3a). During the reaction, we applied a potential of  $-0.7 V_{\text{fc}}$  to the Au electrode. Note that we could tune the reaction rate by the applied potential as demonstrated in our previous work.<sup>[35]</sup> The corresponding spectra at open circuit potential (OCP) are provided in the Supporting Information (see Figure SI 1). We

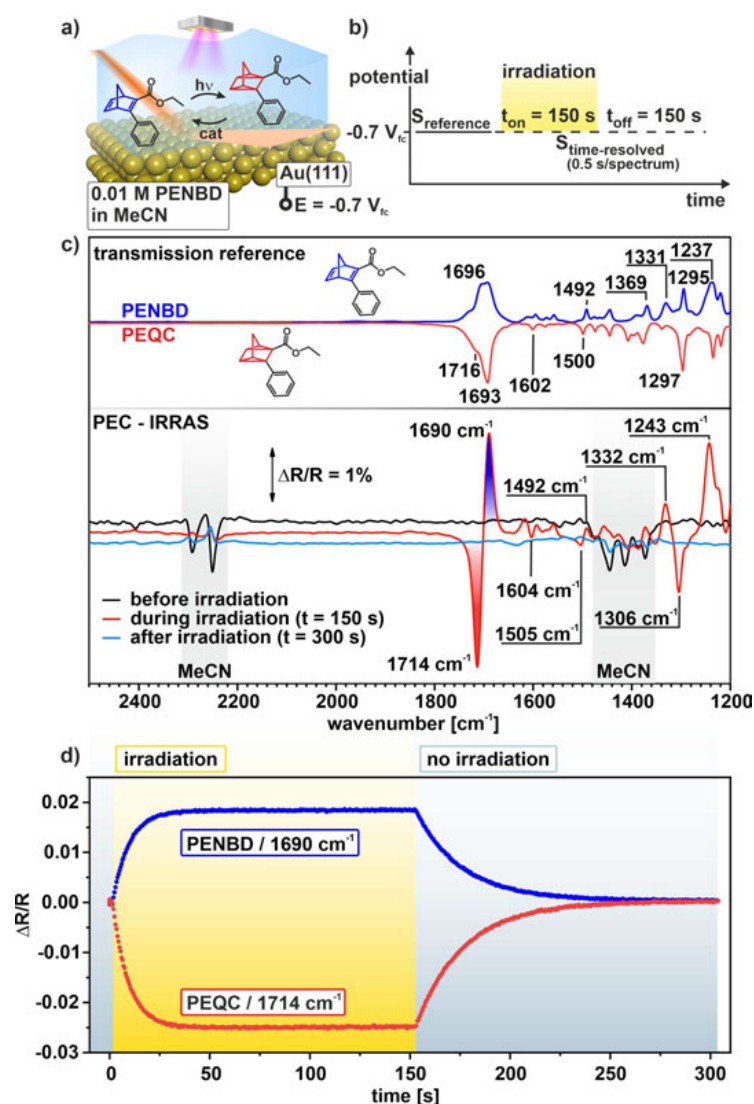


**Figure 3.** Photochemical conversion and catalytically triggered back-conversion of the PENBD/PEQC system in the liquid phase; a) Schematic representation of the energy storage and release; b) Experimental procedure; c) Transmission spectra of PENBD and PEQC and selected spectra before, during, and after irradiation measured during the *in situ* experiment; d) Peak intensity of the  $\nu(\text{CO})$  band of PENBD and PEQC during irradiation and catalytically triggered back-conversion; all spectra were acquired with 10 mM PENBD in 0.1 M  $\text{Bu}_4\text{NClO}_4$  in MeCN at  $-0.7 V_{fc}$ .

measured PEC-IRRA spectra in thin-layer configuration using a spacer of 25  $\mu\text{m}$  thickness. In this thin-layer configuration, the reactant exchange between the thin layer and the bulk solution is suppressed.<sup>[57]</sup> In previous work, we demonstrated that with this setup NBD diffusion from the thin layer to the bulk solution takes  $\sim 260$  min. As a light source we used a UV-LED with  $\lambda_{\text{max}} = 310$  nm (30 mW). A scheme of the experimental procedure is shown in Figure 3b. First, a reference spectrum and one additional spectrum were recorded before irradiation.

Next, IR spectra (acquisition time = 0.5 s) were recorded during and after the irradiation (300 s per cycle). Figure 3c upper part shows the transmission reference spectra of PENBD (blue) and PEQC (red). For the most intense band around  $1700 \text{ cm}^{-1}$ , the  $\nu(\text{CO})$  stretching vibration, conversion led to a band shift which gave rise to a s-shaped band in the difference spectra. We used the  $\nu(\text{CO})$  band as a spectroscopic marker to follow the conversion and back-conversion. In the bottom part of Figure 3c, we show three selected PEC-IRRA spectra. One

before irradiation, one during irradiation, and one after the LED was switched off. Before irradiation, we did not observe any bands of PENBD or PEQC in the difference spectra, indicating stable conditions. Note that small bands at 1450 and 2250  $\text{cm}^{-1}$  belong to the solvent acetonitrile<sup>[58]</sup> and indicated minimal changes of the layer thickness. During irradiation, we observed positive features for PENBD at 1690  $\text{cm}^{-1}$  ( $\nu(\text{CO})$ ), 1492  $\text{cm}^{-1}$  ( $\delta(\text{CH})_{\text{phenyl}}$ ), 1332  $\text{cm}^{-1}$  ( $\delta(\text{CH})_{\text{phenyl}}$ ), and 1243  $\text{cm}^{-1}$  ( $\delta(\text{CH})_{\text{NBD}}$ ). For PEQC, we observed negative bands at 1714  $\text{cm}^{-1}$  ( $\nu(\text{CO})$ ), 1604  $\text{cm}^{-1}$  ( $\nu(\text{CC})_{\text{phenyl}}$ ), 1505  $\text{cm}^{-1}$  ( $\delta(\text{CH})_{\text{phenyl}}$ ), and 1306  $\text{cm}^{-1}$  ( $\nu(\text{CC})_{\text{QC, ester}}$ ). Note that all spectra are difference spectra referred to the spectrum before irradiation. Therefore, positive bands (pointing upwards) indicate consumed species, while negative bands (pointing downwards) indicate formed species. The bands demonstrate the conversion of PENBD to PEQC upon irradiation. After irradiation, all bands vanished showing that all PEQC is back-converted to PENBD. In addition, we did not observe any other bands, which would indicate the formation of a side product. For a more detailed analysis, we will focus on the most intense bands, i. e., the  $\nu(\text{CO})$  bands. The intensity of these bands is plotted in Figure 3d. Upon irradiation, the intensity of both peaks increased very quickly and reached a plateau after  $\sim 50$  s ( $t_{1/2} = 7.5$  s). After the LED is switched off, the intensity rapidly decreased and vanished completely after  $\sim 150$  s ( $t_{1/2} = 17$  s). The increase in peak intensity during irradiation indicated photoconversion of PENBD to PEQC. As the Au(111) surface is present during irradiation, PEQC was continuously back-converted. After  $\sim 50$  s of irradiation, the system reached steady state condition. After switching off the LED, all PEQC was back-converted to PENBD. In previous work, we determined the rate constant for the back-conversion of 2-cyano-3-(3,4-dimethoxyphenyl)-NBD/QC on Au(111) to be  $5.8 \times 10^{-6} \text{ m}\cdot\text{s}^{-1}$  at  $-0.7 \text{ V}_{\text{fc}}$ .<sup>[35]</sup> As the half-life times of the conversion and back-conversion are very similar to the ones in the former study, we conclude that the reaction rate of the back-conversion on Au(111) is similar for both systems.

In the next step, we tested the cyclability of the system. We repeated the experiment described in Figure 3b for 100 times (Figure 4a). Note that we applied a potential of  $-0.7 \text{ V}_{\text{fc}}$  during the experiment. In Figure 4b and c, we depict the  $\nu(\text{CO})$  region recorded during the first and the last cycles (cycle 1–3 and cycle 100–103) and the intensities of the  $\nu(\text{CO})$  bands for different cycles (spectra from 2500 to 1200  $\text{cm}^{-1}$  are provided in Figure SI 2). Within the 100 storage cycles, PEQC was always back-converted completely to PENBD. We did not observe the formation of any side product. From this observation, we conclude that the system is fully reversible within the detection limits of our experiment. These results are in agreement with our previous work on the catalytic back-conversion of 2-cyano-3-(3,4-dimethoxyphenyl)-QC on Au(111).<sup>[35]</sup>

Finally, we inspected the stability of the reaction system. From our observation that the system is fully reversible, we conclude that the kinetics of the photochemical conversion are unaffected. Consequently, we can use the band intensity in the steady state to analyze the changes of the back-

conversion rate qualitatively. We observed that the peak intensity is nearly constant over the 100 cycles and even decreased slightly with increasing cycle number. From this observation, we conclude that the catalytic activity remained stable within the 100 conversion cycles. Notably, the activity of the Au(111) surface was even increasing slightly with more frequent cycling. We attribute this favorable effect to reductive decomposition of impurities or poisoning species, which are present in the beginning after sample preparation (the exact nature cannot be determined on the basis of the present experiments). In summary, our results demonstrate very high catalytic activity and selectivity of Au(111) for energy release in the PENBD/PEQC system in the liquid phase.

### Monolayer conversion with SRPES in UHV

In the next step, we address the catalytic energy release by surface science methods. We started with SRPES measurements of PEQC and PENBD at submonolayer coverages to obtain information on the activity of the compounds in direct contact with the gold surface and their reaction pathways upon heating. We followed the adsorption and thermal evolution of the photoswitches *in situ* in the C 1s and O 1s regions (see complete data sets in Figure SI 3 and SI 4). The catalyst surface was a gold film prepared by PVD and subsequent annealing<sup>[52]</sup> on a Pt(111) single crystal (see experimental section). This preparation led to a well-ordered surface structure<sup>[53]</sup> with a behavior in photoemission experiments identical to that of Au(111).<sup>[54]</sup>

Selected C 1s spectra are shown in Figure 5a. The red spectrum was acquired after exposure of the gold surface to PEQC at 110 K, yielding a total carbon coverage of 0.24 ML. In Figure 5b, we provide the corresponding quantitative analysis of the TP-SRPES experiment with PEQC, showing the carbon coverage as a function of temperature.

Interestingly, there were no pronounced differences in the spectral appearance when compared to PENBD (blue spectrum in Figure 5a) after adsorption of comparable amounts (0.32 ML) at 110 K, indicating the existence of equivalent surface species. The C 1s spectra of both PEQC and PENBD in Figure 5a featured a relatively broad signal with a main contribution at 284.3 eV and a distinct shoulder at 285.7 eV. In addition, smaller peaks at  $\sim 287.8$  eV were found in both spectra. While the NBD/QC framework and phenyl moiety without heteroatoms are expected to contribute to the main signal at 284.3 eV, carbon atoms in vicinity to the oxygen atoms of the ester group were likely to add intensity at higher binding energies. Our observations suggest that the reaction of PEQC to PENBD already took place immediately upon adsorption. We attribute this spontaneous conversion at 110 K to the high catalytic activity of the gold surface leading to an instantaneous cycloreversion to PENBD. Therefore, no PEQC was observed spectroscopically even at low temperatures. Spectra of the O 1s region also confirmed the conversion (see Figure SI 5). The direct reconversion of PEQC under cryogenic temperatures is in agreement with previous experiments on

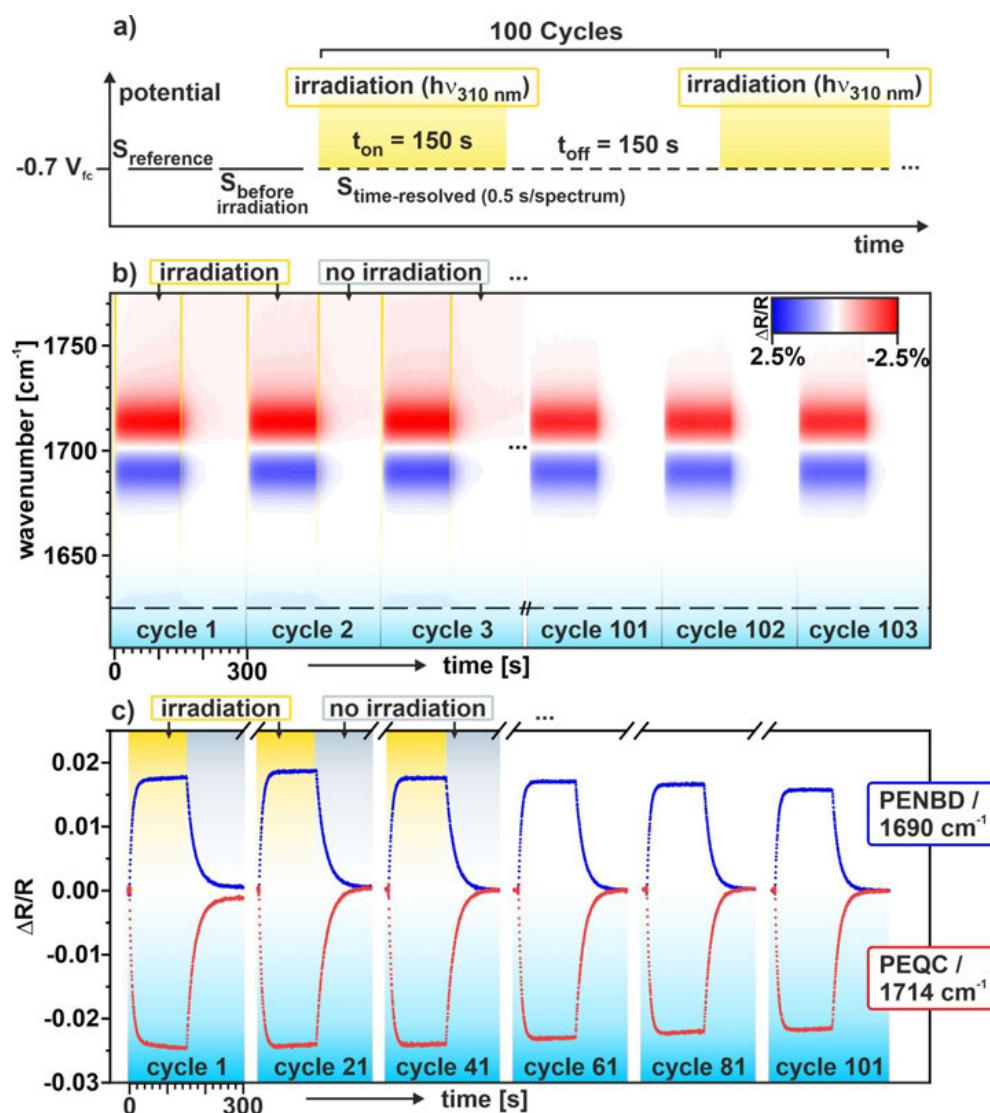


**Figure 4.** Stability of the PENBD-PEQC/Au(111) system probed over 100 storage and release cycles (between steady state and total back-conversion); a) Schematic presentation of the experimental procedure; b) Color plot of the  $\nu(\text{CO})$  region of the IR spectra recorded during cycle 1–3 and 101–103; c) Band intensity of  $\nu(\text{CO})$  bands of PENBD ( $1690 \text{ cm}^{-1}$ ) and PEQC ( $1714 \text{ cm}^{-1}$ ) during cycle 1, 21, 41, 61, 81, and 101.

Au(111), where the NBD/QC derivative was assembled on the Au(111) surface by means of a trioxatriangulene anchor platform.<sup>[38]</sup> We suggest that the reaction follows the same singlet-triplet mechanism as originally proposed by Herges, Magnussen, Tuzek, and co-workers for the catalytic back-conversion of azobenzene-based MOST photoswitches on Au(111).<sup>[29]</sup> The intersystem crossing between singlet and triplet states of the MOST molecules is mediated by the gold surface and represents a reaction pathway that minimizes the probability for uncontrolled side reactions. Figure SI 6

schematically depicts the energy landscape of the reaction system during the isomerization process.

In the following, we investigated the thermal behavior to obtain a more detailed view on the reaction behavior of PENBD. Starting at 135 K (see Figure SI 4 for details), a shift of the main signal at 284.3 eV occurred by about 150 meV towards higher binding energies. Simultaneously, the shoulders at the higher binding got considerably less intense and noticeably broader (light blue spectrum at 170 K in Figure 5a). This most striking change concerns the carbon atoms

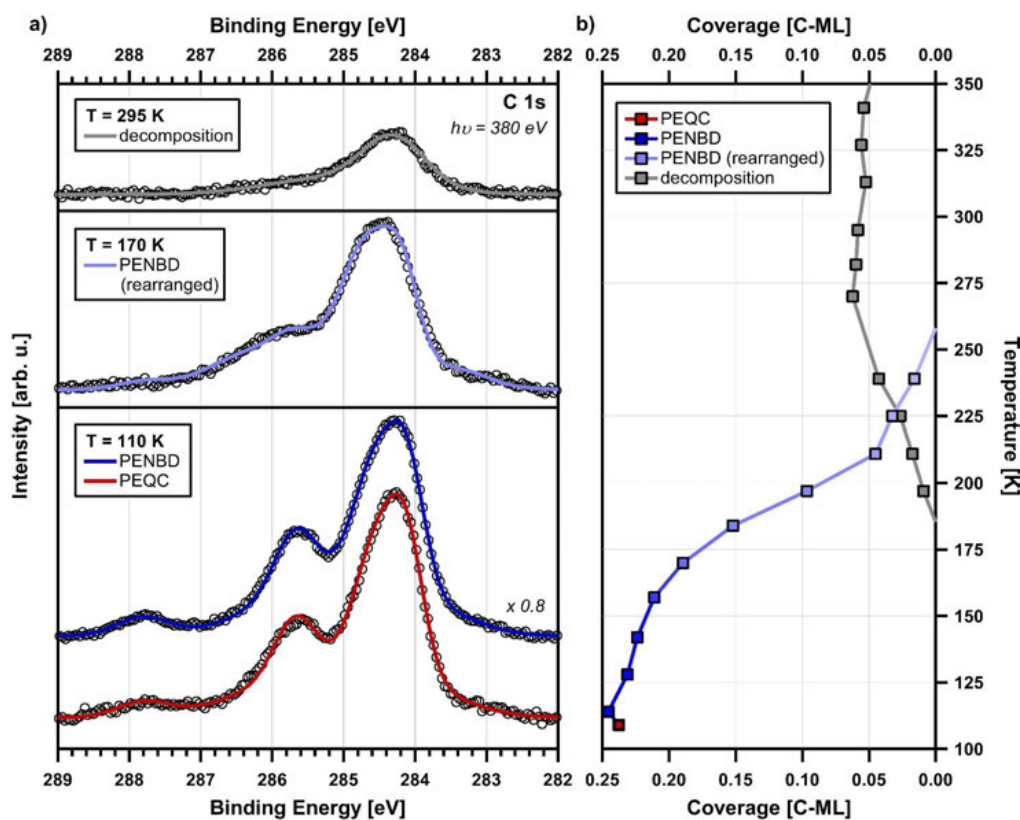


**Figure 5.** Selected SRPE spectra and quantitative analysis of the PEQC experiment; a) C 1s spectra at representative temperatures. There is no spectral distinction upon adsorption of PEQC and PENBD (rescaled) indicating an instantaneous cycloreversion reaction; rearrangement of PENBD occurs upon heating, and desorption of PENBD proceeds up to 250 K, with minor residues remaining on the surface (promoted by defects in gold film); b) Carbon coverage in monolayers upon thermal evolution.

influenced by the oxygen of the ester moiety, suggesting that the substituent can adopt different adsorption configurations. Since the spectral differences between 110 and 170 K were small, we propose that the molecules rearranged to a more stable adsorption geometry, as also observed for other NBD/QC systems.<sup>[37,42]</sup> While there was only a slight decline in carbon coverage below 150 K (less than 10%), a much more pronounced decrease was found up to 210 K (see Figure 5b). Beginning at 190 K, the line shape was described by an asymmetric peak at 284.3 eV (grey spectrum). This contribution is ascribed to carbonaceous fragments on the surface. These decomposition products were the only detected surface species above 250 K. The remaining coverage of ~0.05 ML, after the desorption of intact PENBD, was about 20% of the initial carbon amount. The obtained spectra at these temperatures match with literature values for carbide formation on polycrystalline gold.<sup>[59]</sup> This fragmentation was likely promoted by defects in the prepared gold films, as anticipated by theory for under-coordinated sites on gold.<sup>[60]</sup>

Our results demonstrate that the cycloreversion reaction on Au(111) took place at submonolayer coverages even at cryogenic temperatures of 110 K. Rearrangement of PENBD started at ~135 K, with the photoswitch adopting its most favorable adsorption geometry. Heating to >250 K, all PENBD has desorbed molecularly from the submonolayer, leaving minor residues on the surface due to decomposition at defects of the gold film.

#### Growth of mono and multilayer films of PENBD on Au(111)

The question remains, how the photoisomers behave at multilayer coverage. To address this question, we investigated the growth of PENBD films by IRRAS. We recorded time-resolved IRRAS spectra during deposition of PENBD on clean Au(111) at 110 K in UHV (see Figure 6). At submonolayer coverage, the most prominent signal was the  $\nu(\text{C}-\text{O})_{\text{Ester}}$  vibration at  $1052\text{ cm}^{-1}$  (Figure 6a and b). Note that only components of the dynamic dipole moment perpendicular to

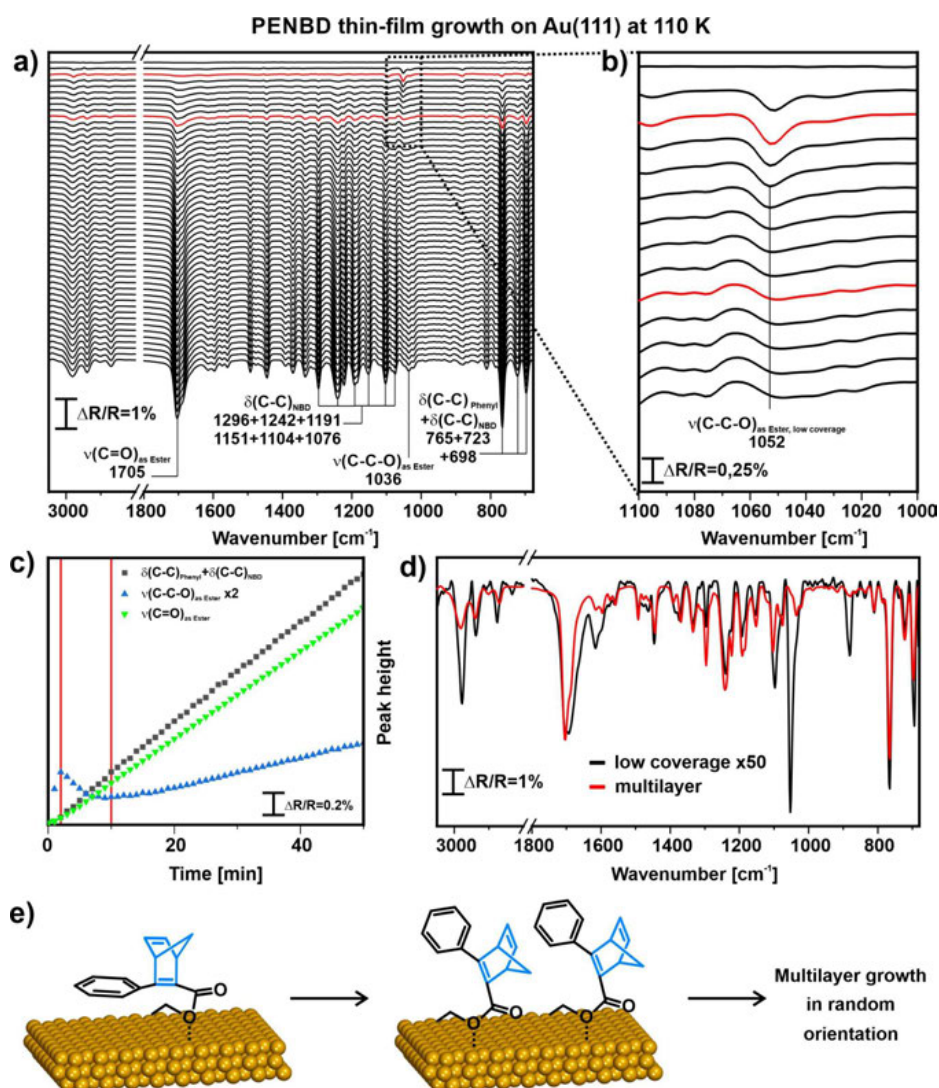


**Figure 6.** a) *In situ* IRRA spectra measured during PVD of PENBD on Au(111) at 110 K. For clarity, only the first 50 spectra are shown; b) Zoomed in portion of (a) at the  $\nu(\text{C}-\text{C}-\text{O})_{\text{as Ester}}$  band at low coverage; c) Integrated band intensity of selected vibrational modes plotted as a function of deposition time. The integrated bands are  $\delta(\text{C}-\text{C})_{\text{Phenyl}} + \delta(\text{C}-\text{C})_{\text{NBD}}$  (739 to 798  $\text{cm}^{-1}$ ),  $\nu(\text{C}-\text{C}-\text{O})_{\text{as Ester}}$  (997 to 1061  $\text{cm}^{-1}$ ), and  $\nu(\text{C}=\text{O})_{\text{as Ester}}$  (1637 to 1784  $\text{cm}^{-1}$ ); d) Comparison of the PENBD monolayer (scaled by 50 times) and the multilayer; e) Reorientation of PENBD in the (sub)monolayer.

the surface plane give rise to absorption due to the metal surface selection rule (MSSR).<sup>[61–63]</sup> Therefore, we conclude that the ester group of this PENBD molecule adsorbed in an upright-standing binding motif. With increasing coverage, the  $\nu(\text{C}-\text{C}-\text{O})_{\text{as Ester}}$  signal decreased in intensity and redshifted from 1052 to 1036  $\text{cm}^{-1}$  in the multilayer. This indicated change of orientation on the Au(111) surface. In parallel, new bands appeared close to the positions of the multilayer (see Table 1). In addition, we observed changes in the relative band intensities (see Figures 6c and d showing scaled spectra of the

monolayer at low coverage and of the multilayer). These changes in intensity indicated a reorientation of the adsorbed PENBD molecules (see Figure 6e). After the first 10 minutes, all bands grew linearly suggesting a random orientation of the adsorbing molecules in the multilayer.

## Thermal stability and back-conversion of PEQC in UHV

Finally, we converted the multilayer of PENBD photochemically and studied its back-conversion upon heating by TP-IRRAS (from 110 to 700 K). In the color plot in Figure 7a, we show the multilayer spectra with a background spectrum measured after desorption at 700 K. These spectra represent all species present on the surface (denoted as 'absolute spectra'). In the

color plot in Figure 7b, we show all spectra always using the previously recorded spectrum as background. These spectra represent the differential changes while heating ('differential' spectra). Positive bands indicate a loss of band intensity, while negative bands indicate a gain in band intensity.

From 110 to 150 K, we observed bands at the positions of the multilayer spectrum of PEQC. In this temperature range, the spectra did not change (no signals

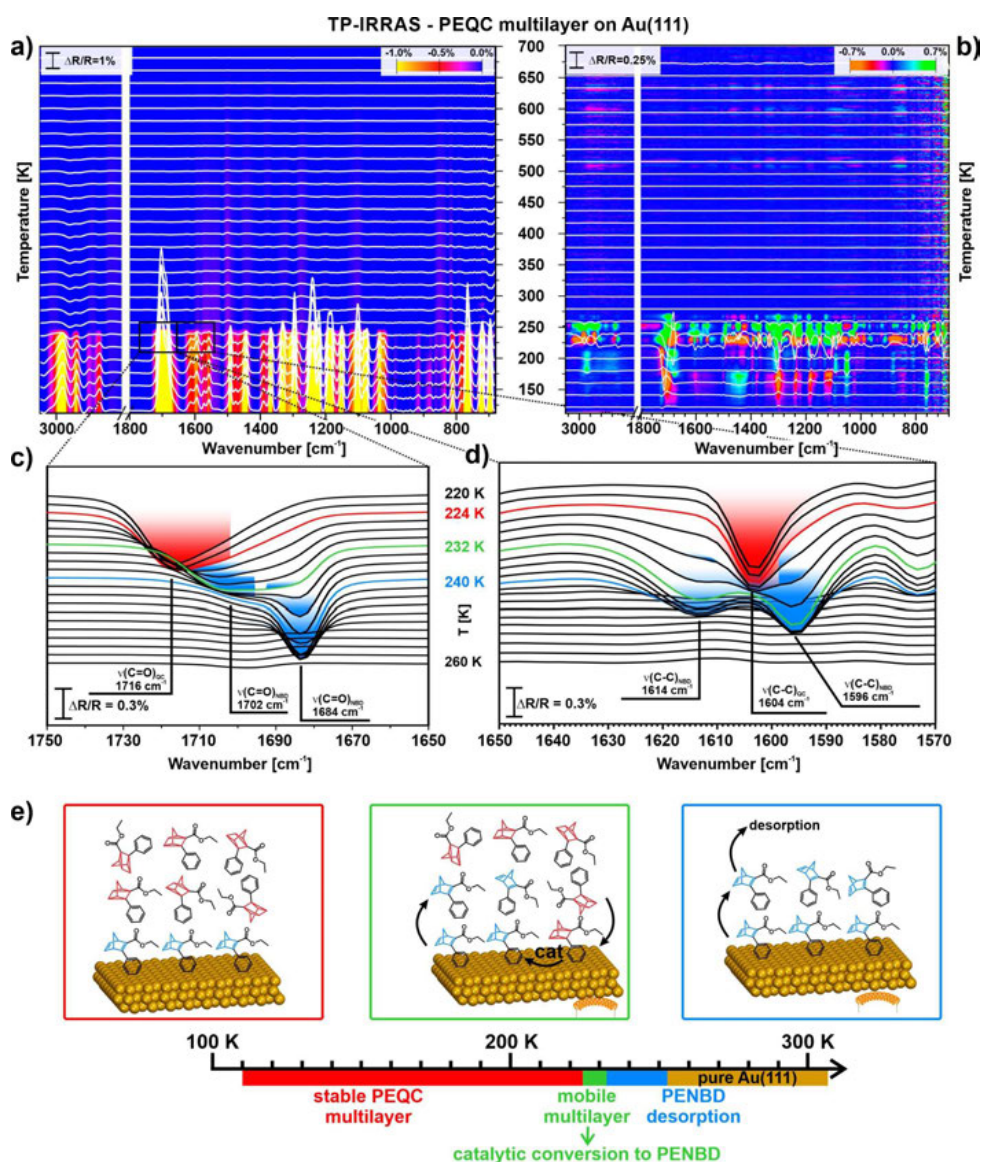


Figure 7. a) TP-IRRAS of a PEQC multilayer from 110 to 700 K plotted as absolute spectra in a color plot (see experimental); b) TP-IRRAS of a PEQC multilayer from 110 to 700 K plotted as relative spectra in a color plot (see experimental); c) Enlarged detail of the absolute spectra in the  $\nu(\text{C}=\text{O})_{\text{as}}$  region (1750 to 1650  $\text{cm}^{-1}$ ) from 220 to 260 K; d) Enlarged detail of the absolute spectra in the  $\nu(\text{C}-\text{C})_{\text{OC/NBD}}$  region (1650 to 1570  $\text{cm}^{-1}$ ); e) Schematic model of the catalytic back-conversion on the gold surface.

in the differential spectra). From 150 to 224 K, we observed changes in the band ratios (see differential spectra). From 224 to 232 K, the band at  $1716\text{ cm}^{-1}$  vanished, and two new bands appeared at  $1702\text{ cm}^{-1}$  and  $1684\text{ cm}^{-1}$ . The latter band became the dominant band at temperatures  $> 232\text{ K}$  (see inset in Figure 7c). In the region around  $1600\text{ cm}^{-1}$ , we observed that the band at  $1604\text{ cm}^{-1}$  vanished between 224 and 232 K, while two new bands appeared at  $1614$  and  $1596\text{ cm}^{-1}$  (inset 7d). Above 250 K, these bands disappeared.

The changes of band ratios between 150 and 224 K indicated a change of film morphology. The spectral changes in the temperature range between 224 and 232 K suggested that PEQC converts back to PENBD in a narrow temperature range. We propose that in this temperature region, the molecules in the film became mobile, so all PEQC species got in direct contact with the gold surface and were back-converted to PENBD. The loss of signal intensity above 232 K was attributed to the desorption of the multilayer. Note that the band at  $1684\text{ cm}^{-1}$  corresponds to the  $\nu(\text{C}=\text{O})$  mode of a molecule, which is in direct contact to the gold surface. Above 240 K, the PENBD monolayer started to desorb. We attribute the lower desorption temperature in the SRPES experiments to the different starting conditions (submonolayer coverage vs. multilayer coverage). In Figure 7e, we schematically depict the behavior at different temperatures. Up to 224 K, the multilayer of PEQC was stable and only some rearrangements in the frozen film took place. Between 224 and 232 K, the multilayer film became so mobile that all PEQC molecules came in contact with the Au(111) surface and were directly back-converted to PENBD. Above 232 and 240 K, the multilayer and monolayer desorbed, respectively.

## Conclusions

In summary, we studied the mechanism and reversibility of energy release from a norbornadiene-based molecular solar thermal (MOST) system combining liquid-phase and surface science experiments. Specifically, we studied the promising MOST system phenylethylesternorbornadiene/quadricyclane (PENBD/PEQC) on catalytically active Au(111) by photoelectrochemical infrared reflection absorption spectroscopy (PEC-IRRAS) in the liquid phase (reaction kinetics and reversibility), synchrotron radiation photoelectron spectroscopy (SRPES) in ultra-high vacuum (UHV) (mechanism, monolayer conversion), and UHV-based IRRAS (mechanism, bulk conversion).

Our main conclusions are summarized as follows:

- (1) Activity: The Au(111) surface triggers the energy release of PEQC in the liquid phase with very high activity. The back-conversion is fully completed within 150 s. The release rate of the heterogeneously catalyzed back-conversion of PEQC can be tuned by applying an external potential.
- (2) Reaction mechanism: In UHV, (sub)monolayers of PEQC, which are in contact with the Au(111) surface, convert directly back to PENBD, even at cryogenic temperatures (110 K). We attribute the back-conversion to the same singlet-triplet mechanism previously reported for other

photoswitches.<sup>[29,38]</sup> The reaction is induced by direct electronic coupling between the Au(111) surface and PEQC. In the multilayer, where the photoswitch is electronically decoupled from the Au(111) surface, PEQC is stable up to temperatures of 220 K. Above this temperature, the frozen film becomes mobile, all PEQC reaches the Au(111) surface, and is back-converted to PENBD.

- (3) Desorption: In UHV, we observe desorption of the multilayer at temperatures above 232 K (IRRAS). At submonolayer coverage, PENBD first rearranges at temperatures of  $\sim 135\text{ K}$  into the energetically most favorable adsorption geometry. At elevated temperatures of  $> 250\text{ K}$ , all PENBD has desorbed from the submonolayer, leaving minor residues on the surface promoted by defects in the gold film (SRPES).
- (4) Reversibility: In the liquid phase, the back-conversion on Au(111) is highly selective and within numerous conversion cycles we do not observe any decomposition. Within 100 cycles, no deactivation occurs and the activity of the Au(111) surface even increases slightly, possibly due to removal of contaminants.

Our multi-method study demonstrates the outstanding catalytic properties of gold as a heterogeneous catalyst for the energy release from NBD-based MOST systems and provides additional mechanistic information required for further knowledge-driven catalyst development.

## Supporting Information

The authors have cited additional references within the Supporting Information (Ref. [64–66]).

## Acknowledgements

The authors acknowledge financial support by the Deutsche Forschungsgemeinschaft (DFG) within the Research Unit FOR 5499 “Molecular Solar Energy Management – Chemistry of MOST Systems” (project 496207555) and project 392607742. The authors acknowledge additional support by the DFG (Collaborative Research Centre SFB 1452 – Catalysis at Liquid Interfaces, Research Unit FOR 1878 “Functional Molecular Structures on Complex Oxide Surfaces” (project 214951840) and further projects (431733372, 453560721, 322419553)), the German Federal ministry of Education and Research (BMBF, Project Combined Infrared and X-Ray Analytics of Energy Materials, CIXenergy 05 K19WE1), the Bavarian ministry of Economic Affairs, Regional Development and Energy, and the Cluster of Excellence “Engineering of Advanced Materials”. We thank Helmholtz-Zentrum Berlin for the allocation of synchrotron radiation beamtime and the BESSY II staff for support during beamtime. We also thank Yannick Wingerter from the group of Prof. Dr. Hirsch for measuring the UV/Vis spectra of PENBD and PEQC. Open Access funding enabled and organized by Projekt DEAL.

### Conflict of Interests

The authors declare no conflict of interest.

### Data Availability Statement

The data that support the findings of this study are presented in the Manuscript and the Supplementary Information. Source data are provided at Zenodo: DOI <https://zenodo.org/doi/10.5281/zenodo.10022604>.

**Keywords:** norbornadiene · photoswitches · quadricyclane · solar energy storage · surface chemistry

- [1] T. J. Kucharski, Y. Tian, S. Akbulatov, R. Boulatov, *Energy Environ. Sci.* **2011**, *4*, 4449–4472.
- [2] A. Lennartson, K. Moth-Poulsen, in *Molecular Devices for Solar Energy Conversion and Storage*, Springer, Singapore, **2018**, pp. 327–352.
- [3] Z. Wang, A. Roffey, R. Losantos, A. Lennartson, M. Jevric, A. U. Petersen, M. Quant, A. Dreos, X. Wen, D. Sampedro, K. Börjesson, K. Moth-Poulsen, *Energy Environ. Sci.* **2019**, *12*, 187–193.
- [4] Z. Wang, P. Erhart, T. Li, Z.-Y. Zhang, D. Sampedro, Z. Hu, H. A. Wegner, O. Brummel, J. Libuda, M. B. Nielsen, K. Moth-Poulsen, *Joule* **2021**, *5*, 3116–3136.
- [5] T. J. Kucharski, N. Ferralis, A. M. Kolpak, J. O. Zheng, D. G. Nocera, J. C. Grossman, *Nat. Chem.* **2014**, *6*, 441–447.
- [6] A. Goulet-Hanssens, M. Utecht, D. Mutruc, E. Titov, J. Schwarz, L. Grubert, D. Bléger, P. Saalfrank, S. Hecht, *J. Am. Chem. Soc.* **2017**, *139*, 335–341.
- [7] Z. F. Liu, K. Hashimoto, A. Fujishima, *Nature* **1990**, *347*, 658–660.
- [8] A. H. Heindl, H. A. Wegner, *Chem. A Eur. J.* **2020**, *26*, 13730–13737.
- [9] J. H. Griwatz, A. Kunz, H. A. Wegner, *Beilstein J. Org. Chem.* **2022**, *18*, 781–787.
- [10] E. Franz, A. Kunz, N. Oberhof, A. H. Heindl, M. Bertram, L. Fusek, N. Taccardi, P. Wasserscheid, A. Dreuw, H. A. Wegner, O. Brummel, J. Libuda, *ChemSusChem* **2022**, *15*, e202200958.
- [11] E. Franz, J. Jung, A. Kunz, H. A. Wegner, D. Mollenhauer, O. Brummel, J. Libuda, *J. Phys. Chem. Lett.* **2023**, *14*, 1470–1477.
- [12] S. L. Broman, M. B. Nielsen, *Phys. Chem. Chem. Phys.* **2014**, *16*, 21172–21182.
- [13] C. Schottler, S. K. Vegge, M. Cacciarini, M. B. Nielsen, *ChemPhotoChem* **2022**, *6*, e202200037.
- [14] M. D. Kilde, M. Mansø, N. Ree, A. U. Petersen, K. Moth-Poulsen, K. V. Mikkelsen, M. B. Nielsen, *Org. Biomol. Chem.* **2019**, *17*, 7735–7746.
- [15] K. Edel, X. Yang, J. S. A. Ishibashi, A. N. Lamm, C. Maichle-Mössmer, Z. X. Giustra, S. Y. Liu, H. F. Bettinger, *Angew. Chem. Int. Ed.* **2018**, *57*, 5296–5300.
- [16] A. D. Dubonosov, V. A. Bren, V. A. Chernoiyanov, *Russ. Chem. Rev.* **2002**, *71*, 917–927.
- [17] V. A. Bren', A. D. Dubonosov, V. I. Minkin, V. A. Chernoiyanov, *Russ. Chem. Rev.* **1991**, *60*, 451–469.
- [18] C. Schuschke, C. Hohner, M. Jevric, A. Ugleholdt Petersen, Z. Wang, M. Schwarz, M. Kettner, F. Waidhas, L. Fromm, C. J. Sumbly, A. Görling, O. Brummel, K. Moth-Poulsen, J. Libuda, *Nat. Commun.* **2019**, *10*, 1–10.
- [19] Z. Wang, H. Hölzel, K. Moth-Poulsen, *Chem. Soc. Rev.* **2022**, *51*, 7313–7326.
- [20] Z. Wang, Z. Wu, Z. Hu, J. Orrego-Hernández, E. Mu, Z. Y. Zhang, M. Jevric, Y. Liu, X. Fu, F. Wang, T. Li, K. Moth-Poulsen, *Cell Reports Phys. Sci.* **2022**, *3*, 100789.
- [21] "Solar radiation and photosynthetically active radiation," can be found under <http://www.fondriest.com/environmental-measurements/parameters/weather/photosynthetically-active-radiation>, **2014**. (accessed on 2023-03-09).
- [22] M. Jevric, A. U. Petersen, M. Mansø, S. Kumar Singh, Z. Wang, A. Dreos, C. Sumbly, M. B. Nielsen, K. Börjesson, P. Erhart, K. Moth-Poulsen, *Chem. A Eur. J.* **2018**, *24*, 12767–12772.
- [23] P. Lorenz, T. Luchs, A. Hirsch, *Chem. A Eur. J.* **2021**, *27*, 4993–5002.
- [24] M. Quant, A. Lennartson, A. Dreos, M. Kuisma, P. Erhart, K. Börjesson, K. Moth-Poulsen, *Chem. A Eur. J.* **2016**, *22*, 13265–13274.
- [25] J. Orrego-Hernández, A. Dreos, K. Moth-Poulsen, *Acc. Chem. Res.* **2020**, *53*, 1478–1487.
- [26] Ken-ichi Hirao, A. Yamashita, O. Yonemitsu, *Tetrahedron Lett.* **1988**, *29*, 4109–4112.
- [27] D. J. Fife, K. W. Morse, W. M. Moore, *J. Am. Chem. Soc.* **1983**, *105*, 7404–7407.
- [28] U. Jung, C. Schütt, O. Filinova, J. Kubitschke, R. Herges, O. Magnussen, *J. Phys. Chem. C* **2012**, *116*, 25943–25948.
- [29] A. Schlimm, R. Löw, T. Rusch, F. Röhrich, T. Strunskus, T. Tellkamp, F. Sönnichsen, U. Manthe, O. Magnussen, F. Tuzcek, R. Herges, *Angew. Chem. Int. Ed.* **2019**, *58*, 6574–6578.
- [30] J. L. Greenfield, M. A. Gerkman, R. S. L. Gibson, G. G. D. Han, M. J. Fuchter, *J. Am. Chem. Soc.* **2021**, *143*, 15250–15257.
- [31] F. Waidhas, M. Jevric, L. Fromm, M. Bertram, A. Görling, K. Moth-Poulsen, O. Brummel, J. Libuda, *Nano Energy* **2019**, *63*, 103872.
- [32] F. Waidhas, M. Jevric, M. Bosch, T. Yang, E. Franz, Z. Liu, J. Bachmann, K. Moth-Poulsen, O. Brummel, J. Libuda, *J. Mater. Chem. A* **2020**, *8*, 15658–15664.
- [33] O. Brummel, D. Besold, T. Döpfer, Y. Wu, S. Bochmann, F. Lazzari, F. Waidhas, U. Bauer, P. Bachmann, C. Papp, H.-P. Steinrück, A. Görling, J. Libuda, J. Bachmann, *ChemSusChem* **2016**, *9*, 1424–1432.
- [34] E. Franz, D. Krappmann, L. Fromm, T. Luchs, A. Görling, A. Hirsch, O. Brummel, J. Libuda, *ChemSusChem* **2022**, *15*, e202201483.
- [35] E. Franz, C. Stumm, F. Waidhas, M. Bertram, M. Jevric, J. Orrego-Hernández, H. Hölzel, K. Moth-Poulsen, O. Brummel, J. Libuda, *ACS Catal.* **2022**, *12*, 13418–13425.
- [36] T. Luchs, P. Lorenz, A. Hirsch, *ChemPhotoChem* **2020**, *4*, 52–58.
- [37] F. Hemaue, V. Schwaab, E. M. Freiberger, N. J. Waleska, A. Leng, C. Weiß, J. Steinhauer, F. Düll, P. Bachmann, A. Hirsch, H.-P. Steinrück, C. Papp, *Chem. A Eur. J.* **2023**, *29*, e202203759.
- [38] R. Eschenbacher, T. Xu, E. Franz, R. Löw, T. Moje, L. Fromm, A. Görling, O. Brummel, R. Herges, J. Libuda, *Nano Energy* **2022**, *95*, 107007.
- [39] G. Ertl, *Angew. Chem. Int. Ed.* **2008**, *47*, 3524–3535.
- [40] U. Bauer, L. Fromm, C. Weiß, P. Bachmann, F. Späth, F. Düll, J. Steinhauer, W. Hieringer, A. Görling, A. Hirsch, H.-P. Steinrück, C. Papp, *J. Phys. Chem. C* **2019**, *123*, 7654–7664.
- [41] U. Bauer, L. Fromm, C. Weiß, F. Späth, P. Bachmann, F. Düll, J. Steinhauer, S. Matysik, A. Pominov, A. Görling, A. Hirsch, H.-P. Steinrück, C. Papp, *J. Chem. Phys.* **2019**, *150*, 1847061–18470613.
- [42] F. Hemaue, U. Bauer, L. Fromm, C. Weiß, A. Leng, P. Bachmann, F. Düll, J. Steinhauer, V. Schwaab, R. Grzonka, A. Hirsch, A. Görling, H.-P. Steinrück, C. Papp, *ChemPhysChem* **2022**, *23*, e202200199.
- [43] U. Bauer, S. Mohr, T. Döpfer, P. Bachmann, F. Späth, F. Düll, M. Schwarz, O. Brummel, L. Fromm, U. Pinkert, A. Görling, A. Hirsch, J. Bachmann, H.-P. Steinrück, J. Libuda, C. Papp, *Chem. A Eur. J.* **2017**, *23*, 1613–1622.
- [44] O. Brummel, F. Waidhas, U. Bauer, Y. Wu, S. Bochmann, H.-P. Steinrück, C. Papp, J. Bachmann, J. Libuda, *J. Phys. Chem. Lett.* **2017**, *8*, 2819–2825.
- [45] L. A. Kibler, *Int. Soc. Electrochem.* **2003**, *1*–56.
- [46] T. Xu, M. Schwarz, K. Werner, S. Mohr, M. Amende, J. Libuda, *Phys. Chem. Chem. Phys.* **2016**, *18*, 10419–10427.
- [47] M. Schwarz, C. Schuschke, T. N. Silva, S. Mohr, F. Waidhas, O. Brummel, J. Libuda, *Rev. Sci. Instrum.* **2019**, *90*, 1–10.
- [48] Helmholtz-Zentrum Berlin für Materialien und Energie, *JLSRF* **2016**, *2*, A72.
- [49] R. Denecke, M. Kinne, C. M. Whelan, H.-P. Steinrück, *Surf. Rev. Lett.* **2002**, *9*, 797–801.
- [50] S. Doniach, M. Sunjic, *J. Phys. C Solid State Phys.* **1970**, *3*, 285–291.
- [51] M. Kinne, T. Fuhrmann, C. M. Whelan, J. F. Zhu, J. Pantförder, M. Probst, G. Held, R. Denecke, H.-P. Steinrück, *J. Chem. Phys.* **2002**, *117*, 10852–10859.
- [52] C. C. Leon, J. G. Lee, S. T. Ceyer, *J. Phys. Chem. C* **2014**, *118*, 29043–29057.
- [53] J. W. A. Sachtler, G. A. Somorjai, *J. Catal.* **1983**, *81*, 77–94.
- [54] B. Vogt, B. Schmiedeskamp, U. Heinzmann, *Zeitschrift für Phys. B Condens. Matter* **1990**, *80*, 359–364.
- [55] A. Baraldi, G. Comelli, S. Lizzit, D. Cocco, G. Paolucci, R. Rosei, *Surf. Sci.* **1996**, *367*, L62–L67.
- [56] C. Papp, H.-P. Steinrück, *Surf. Sci. Rep.* **2013**, *68*, 446–487.
- [57] T. Iwasita, F. C. Nart, *Prog. Surf. Sci.* **1997**, *55*, 271–340.
- [58] E. L. Pace, L. J. Noe, *J. Chem. Phys.* **1968**, *49*, 5317–5325.
- [59] J. Luthin, C. Linsmeier, *Surf. Sci.* **2000**, *454*, 78–82.
- [60] J. A. Herron, J. Scaranto, P. Ferrin, S. Li, M. Mavrikakis, *ACS Catal.* **2014**, *4*, 4434–4445.

- [61] F. M. Hoffmann, *Surf. Sci. Rep.* **1983**, *3*, 107–192.  
[62] H. A. Pearce, N. Sheppard, *Surf. Sci.* **1976**, *59*, 205–217.  
[63] R. G. Greenler, D. R. Snider, D. Witt, R. S. Sorbello, *Surf. Sci.* **1982**, *118*, 415–428.  
[64] M. A. Van Spronsen, K. J. Weststrate, A. Den Dunnen, M. E. Van Reijnen, C. Hahn, L. B. F. Juurlink, *J. Phys. Chem. C* **2016**, *120*, 8693–8703.  
[65] B. D. Kay, K. R. Lykke, J. R. Creighton, S. J. Ward, *J. Chem. Phys.* **1989**, *91*, 5120–5121.
- [66] R. G. Quiller, T. A. Baker, X. Deng, M. E. Colling, B. K. Min, C. M. Friend, *J. Chem. Phys.* **2008**, *129*, 0647021–0647029.

---

Manuscript received: October 20, 2023  
Revised manuscript received: October 25, 2023  
Accepted manuscript online: November 2, 2023  
Version of record online: November 21, 2023

# ChemPhotoChem

## Supporting Information

### **Au-Catalyzed Energy Release in a Molecular Solar Thermal (MOST) System: A Combined Liquid-Phase and Surface Science Study**

Roman Eschenbacher, Felix Hemauer, Evanie Franz, Andreas Leng, Valentin Schwaab, Natalie J. Waleska-Wellenhofer, Eva Marie Freiberger, Lukas Fromm, Tao Xu, Andreas Görling, Andreas Hirsch, Hans-Peter Steinrück, Christian Papp, Olaf Brummel,\* and Jörg Libuda

1. Conversion cycles at open circuit potential

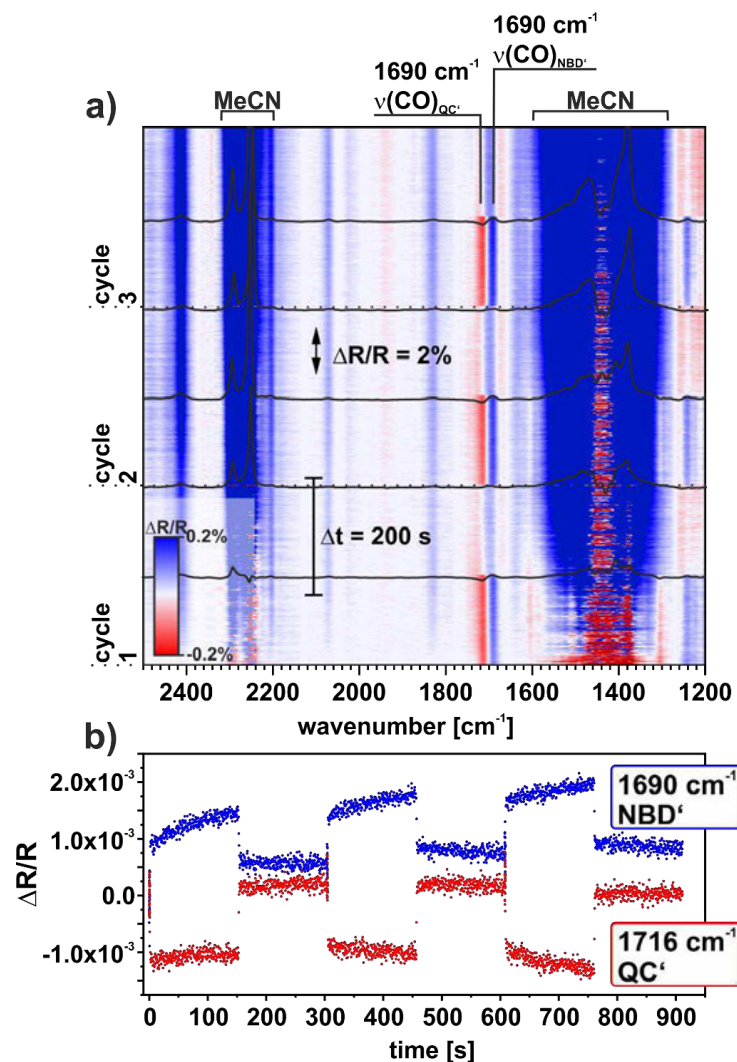


**Figure SI 1:** Reversibility test of the catalytically triggered PENBD/PEQC energy storage system on Au(111) in the liquid phase (MeCN at open circuit potential (OCP)); a) Color plot of 3 conversion and back-conversion cycles; b) Intensity plot vs time.

2. Full spectra of 100 conversion and back-conversion cycles

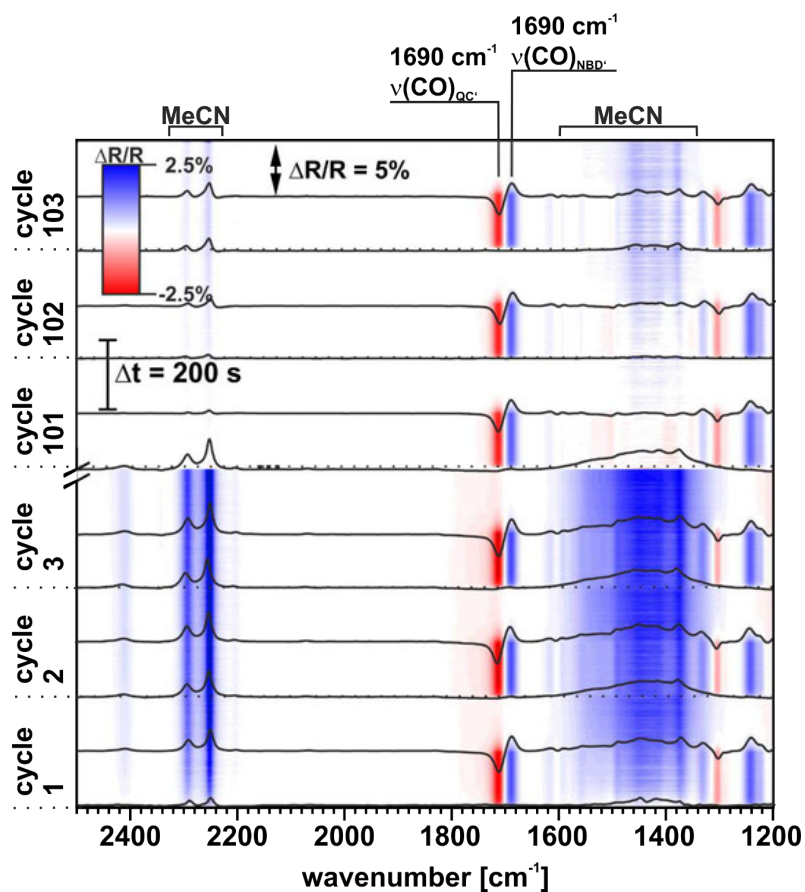
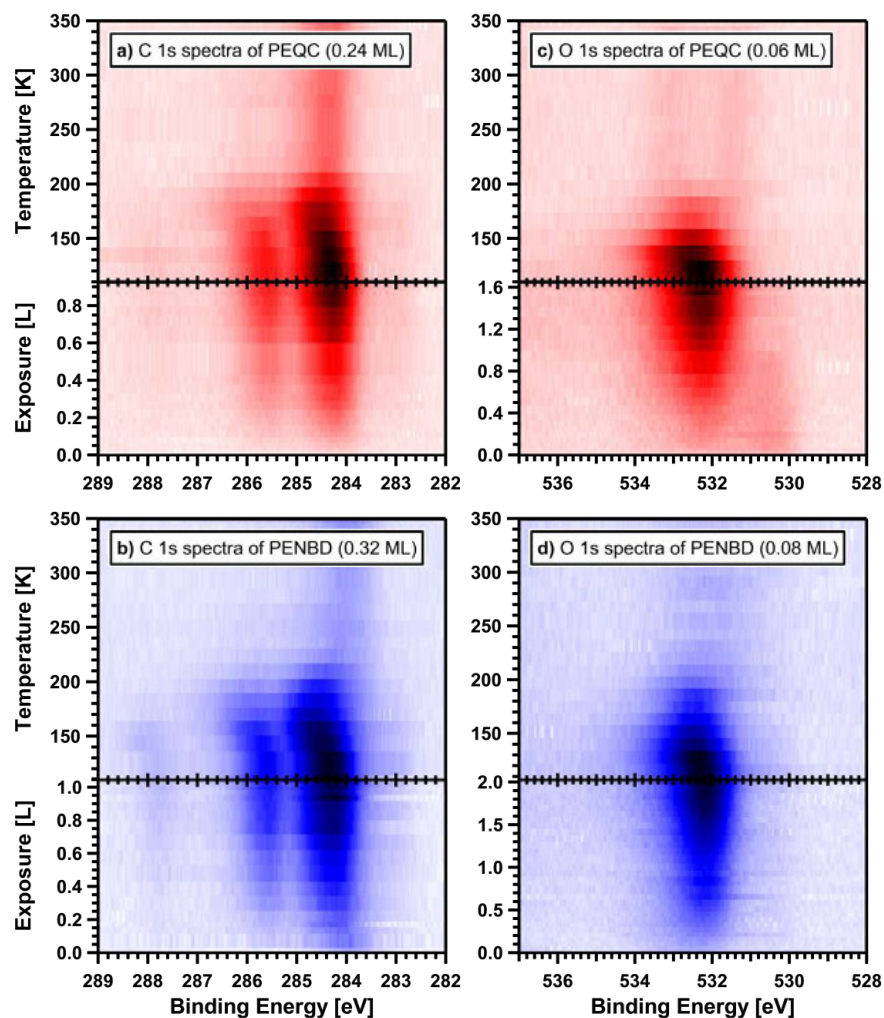


Figure SI 2: Spectra between 2500 and 1200  $\text{cm}^{-1}$  of 100 conversion cycles at  $-0.7 V_{\text{f}}$ . We provide the frequency region of the  $\nu(\text{CO})$  in Figure 4.

### 3. Density plots of SRPES experiments



**Figure SI 3:** Color-coded (blue being the highest intensity) density plots of the *in situ* SRPES experiments: a) C 1s spectra of PEQC (0.24 C-ML); b) C 1s spectra of PENBD (0.32 C-ML); c) O 1s spectra of PEQC (0.06 O-ML); and d) O 1s spectra of PENBD (0.08 O-ML); collected at photon energies of 380 eV (a, b) and 650 eV (c, d).

#### 4. Waterfall plots of SRPES experiments

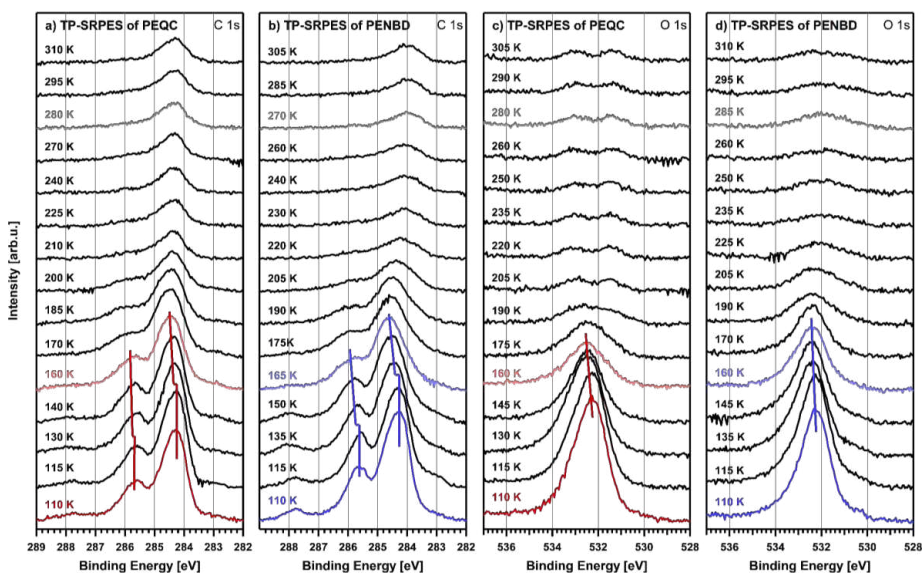


**Figure SI 4:** Temperature-programmed SRPES (TP-SRPES) experiments shown as waterfall plots: a) PEQC in C 1s region; b) PENBD in C 1s region; c) PEQC in O 1s region; and d) PENBD in O 1s region. Shifts of binding energy positions of signals are indicated by colored lines.

#### 5. SRPE spectra in O 1s region

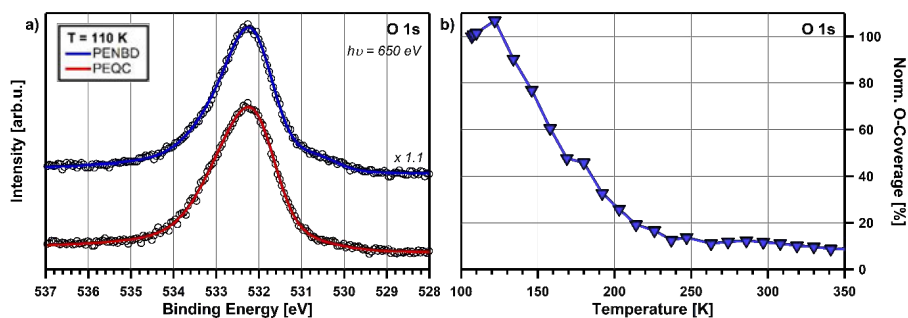


**Figure SI 5:** a) Comparison of the O 1s spectra of PEQC and PENBD (rescaled) after adsorption on Au/Pt(111) at 110 K; the same spectral appearance is observed for both molecules; minor deviations are explained by impurities of co-adsorbed water.<sup>[1]</sup> b) Normalized oxygen coverage as derived from O 1s spectra in Figure SI 3, collected during heating of the PENBD layer; a contribution of water desorption to the decrease of the O-coverage above 140 K cannot be completely excluded.<sup>[2,3]</sup>

## 6. Singlet-triplet mechanism

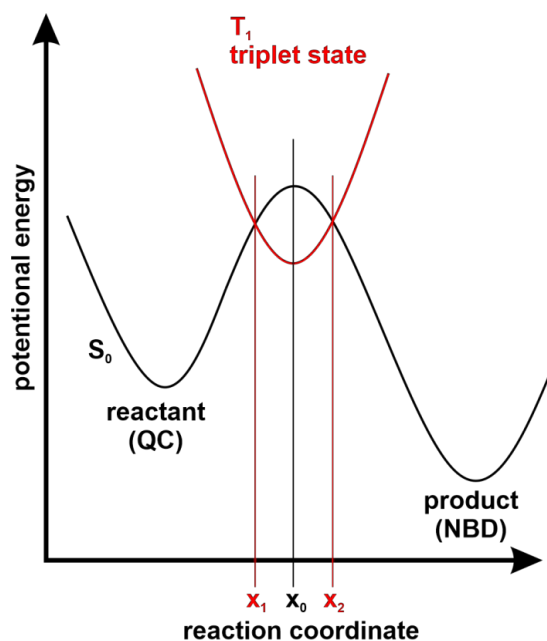


**Figure SI 6:** Schematic energy landscape of the reaction system during the isomerization process, according to the singlet-triplet mechanism, proposed by Schlimm et al.<sup>[4]</sup> Whereby  $S_0$  depicts the potential surface in the single state, separating reactant and product by an energetic barrier (with maximum at  $x_0$ ), parabola  $T_1$  represents the intermediate triplet state (with  $x_1$  and  $x_2$  as respective crossing points of the dividing surfaces).

By assessing the coupling between different electronic states, Schlimm et al.<sup>[4]</sup> investigated the mechanistic insights during the isomerization of different azobenzene-systems on Au(111) suggesting an electronic transition mediated by bulk gold, which resulted in a pronounced enhancement of the rate constants. Analogously, the reaction system of the switchable NBD/QC molecule pair can be considered. In the beginning, the reactant (for the back conversion: QC) is in the  $S_0$  singlet state. Through coupling with the gold catalyst, the intermediate transfer to the triplet state  $T_1$  of the adsorbate is facilitated. Thereafter, the product (NBD) reaches its singlet state  $S_0$  in an intersystem crossing (ISC) relaxation process. Here, the delocalization of the wavefunctions into the gold surface is essential, which is expressed by the respective spin density.

**References**

- [1] M. A. van Spronsen, K. J. Weststrate, A. den Dunnen, M. E. van Reijzen, C. Hahn, L. B. F. Juurlink, *J. Phys. Chem. C* **2016**, *120*, 8693–8703.
- [2] B. D. Kay, K. R. Lykke, J. R. Creighton, S. J. Ward, *J. Chem. Phys.* **1989**, *91*, 5120–5121.
- [3] R. G. Quiller, T. A. Baker, X. Deng, M. E. Colling, B. K. Min, C. M. Friend, *J. Chem. Phys.* **2008**, *129*, 064702-1-064702–9.
- [4] A. Schlimm, R. Löw, T. Rusch, F. Röhricht, T. Strunskus, T. Tellkamp, F. Sönnichsen, U. Manthe, O. Magnussen, F. Tuzcek, R. Herges, *Angew. Chemie* **2019**, *131*, 6646–6650.

This article may be downloaded for personal use only. Any other use requires prior permission of the author and AIP Publishing.  
 This article appeared in *J. Chem. Phys.* 159, 074703 (2023) and may be found at <https://doi.org/10.1063/5.0158124>.

# Surface science and liquid phase investigations of oxanorbornadiene/oxaquadricyclane ester derivatives as molecular solar thermal energy storage systems on Pt(111)

Cite as: *J. Chem. Phys.* 159, 074703 (2023); doi: 10.1063/5.0158124

Submitted: 15 May 2023 • Accepted: 31 July 2023 •

Published Online: 21 August 2023



Felix Hemauer,<sup>1</sup> Daniel Krappmann,<sup>2</sup> Valentin Schwaab,<sup>1</sup> Zarah Hussain,<sup>3</sup> Eva Marie Freiburger,<sup>1</sup> Natalie J. Waleska-Wellnhofer,<sup>1</sup> Evanie Franz,<sup>3</sup> Frank Hampel,<sup>4</sup> Olaf Brummel,<sup>3</sup> Jörg Libuda,<sup>3,5</sup> Andreas Hirsch,<sup>2</sup> Hans-Peter Steinrück,<sup>1,5</sup> and Christian Papp<sup>1,5,6,a)</sup>

## AFFILIATIONS

<sup>1</sup> Lehrstuhl für Physikalische Chemie II, Friedrich-Alexander-Universität Erlangen-Nürnberg, Egerlandstr. 3, 91058 Erlangen, Germany

<sup>2</sup> Lehrstuhl für Organische Chemie II, Friedrich-Alexander-Universität Erlangen-Nürnberg, Nikolaus-Fiebiger-Str. 10, 91058 Erlangen, Germany

<sup>3</sup> Lehrstuhl für Katalytische Grenzflächenforschung, Friedrich-Alexander-Universität Erlangen-Nürnberg, Egerlandstr. 3, 91058 Erlangen, Germany

<sup>4</sup> Lehrstuhl für Organische Chemie I, Friedrich-Alexander-Universität Erlangen-Nürnberg, Nikolaus-Fiebiger-Str. 10, 91058 Erlangen, Germany

<sup>5</sup> Erlangen Center for Interface Research and Catalysis (ECRC), Friedrich-Alexander-Universität Erlangen-Nürnberg, Egerlandstr. 3, 91058 Erlangen, Germany

<sup>6</sup> Physikalische und Theoretische Chemie, Freie Universität Berlin, Arnimallee 22, 14195 Berlin, Germany

<sup>a)</sup> Author to whom correspondence should be addressed: [christian.papp@fau.de](mailto:christian.papp@fau.de)

## ABSTRACT

The transition to renewable energy sources comes along with the search for new energy storage solutions. Molecular solar thermal systems directly harvest and store solar energy in a chemical manner. By a suitable molecular design, a higher overall efficiency can be achieved. In this study, we investigate the surface chemistry of oxa-norbornadiene/quadricyclane derivatives on a Pt(111) surface. Specifically, we focus on the energy storage and release properties of molecules that are substituted with ester moieties of different sizes. For our model catalytic approach, synchrotron radiation-based x-ray photoelectron spectroscopy measurements were conducted in ultra-high vacuum (UHV) and correlated with the catalytic behavior in the liquid phase monitored by photochemical infrared reflection absorption spectroscopy. The differences in their spectral appearance enabled us to unambiguously differentiate the energy-lean and energy-rich isomers and decomposition products. Next to qualitative information on the adsorption motifs, temperature-programmed experiments allowed for the observation of thermally induced reactions and the deduction of the related reaction pathways. We analyzed the selectivity of the cycloreversion reaction from the energy-rich quadricyclane derivative to its energy-lean norbornadiene isomer and competing processes, such as desorption and decomposition. For the 2,3-bis(methylester)-substitution, the cycloreversion reaction was found to occur between 310 and 340 K, while the thermal stability limit of the compounds was determined to be 380 K. The larger 2,3-bis(benzylester) derivatives have a lower apparent adsorption energy and a decomposition onset already at 135 K. In the liquid phase (in acetonitrile), we determined the rate constants for the cycloreversion reaction on Pt(111) to  $k = 5.3 \times 10^{-4} \text{ s}^{-1}$  for the 2,3-bis(methylester)-substitution and  $k = 6.3 \times 10^{-4} \text{ s}^{-1}$  for the 2,3-bis(benzylester) derivative. The selectivities were of >99% and 98% for the two molecules, respectively. The difference in the catalytic behavior of Pt(111) for both derivatives is less pronounced in the liquid phase than in UHV, which we attribute to the passivation of the Pt(111) surface by carbonaceous species under ambient conditions.

This article may be downloaded for personal use only. Any other use requires prior permission of the author and AIP Publishing.  
This article appeared in *J. Chem. Phys.* 159, 074703 (2023) and may be found at <https://doi.org/10.1063/5.0158124>.

**Supplementary Material for**

**Surface Science and Liquid Phase Investigations of**

**Oxanorbornadiene/Oxaquadricyclane**

**Ester Derivatives as Molecular Solar Thermal Energy**

**Storage Systems on Pt(111)**

Felix Hemauer,<sup>1</sup> Daniel Krappmann,<sup>2</sup> Valentin Schwaab,<sup>1</sup> Zarah Hussain,<sup>3</sup>  
Eva Marie Freiberger,<sup>1</sup> Natalie J. Waleska-Wellnhofer,<sup>1</sup> Evanie Franz,<sup>3</sup> Dr. Frank Hampel,<sup>4</sup>  
Dr. Olaf Brummel,<sup>3</sup> Prof. Dr. Jörg Libuda,<sup>3,5</sup> Prof. Dr. Andreas Hirsch,<sup>2</sup>  
Prof. Dr. Hans-Peter Steinrück,<sup>1,5</sup> and Prof. Dr. Christian Papp<sup>1,5,6,a)</sup>

<sup>1</sup>*Lehrstuhl für Physikalische Chemie II, Friedrich-Alexander-Universität Erlangen-Nürnberg,  
Egerlandstr. 3, 91058 Erlangen, Germany*

<sup>2</sup>*Lehrstuhl für Organische Chemie II, Friedrich-Alexander-Universität Erlangen-Nürnberg,  
Nikolaus-Fiebiger-Str. 10, 91058 Erlangen, Germany*

<sup>3</sup>*Lehrstuhl für Katalytische Grenzflächenforschung, Friedrich-Alexander-Universität  
Erlangen-Nürnberg, Egerlandstr. 3, 91058 Erlangen, Germany*

<sup>4</sup>*Lehrstuhl für Organische Chemie I, Friedrich-Alexander-Universität Erlangen-Nürnberg,  
Nikolaus-Fiebiger-Str. 10, 91058 Erlangen, Germany*

<sup>5</sup>*Erlangen Center for Interface Research and Catalysis (ECRC), Friedrich-Alexander-  
Universität Erlangen-Nürnberg, Egerlandstr. 3, 91058 Erlangen, Germany*

<sup>6</sup>*Physikalische und Theoretische Chemie, Freie Universität Berlin, Arnimallee 22, 14195  
Berlin, Germany*

<sup>a)</sup>Author to whom correspondence should be addressed: [christian.papp@fau.de](mailto:christian.papp@fau.de)